Dynamische aspecten van geavanceerde multi-sectie afstembare halfgeleiderlasers

Dynamic Aspects of Advanced Multi-Section Tunable Semiconductor Lasers

Bart Moeyersoon

Proefschrift tot het verkrijgen van de graad van
Doctor in de Toegepaste Wetenschappen: Elektrotechniek

Universiteit Gent
Vakgroep Informatietechnologie
Voorzitter: Prof. dr. ir. P. Lagasse
Faculteit Toegepaste Wetenschappen
Academiejaar 2004-2005

Promotoren:

Prof. dr. ir. G. Morthier	Universiteit Gent, INTEC
Prof. dr. ir. R. Baets	Universiteit Gent, INTEC

Examencommissie:

Prof. dr. ir. D. De Zutter, voorzitter	Universiteit Gent, INTEC
Dr. E. A. J. M. Bente	Technische Universiteit Eindhoven
Dr. ir. G. Sarlet	Syntune AB, Sweden
Prof. dr. P. Clauws	Universiteit Gent, Vaste-stofwetenschappen
Prof. dr. ir. D. Van Thourhout	Universiteit Gent, INTEC

Universiteit Gent
Faculteit Toegepaste Wetenschappen

Vakgroep Informatietechnologie (INTEC)
Sint-Pietersnieuwstraat 41
9000 Gent
BELGIUM

Tel.: +32-9-264.33.19
Fax: +32-9-264.35.93
http://www.intec.ugent.be

Preface - Voorwoord

Onderliggend werk zou nooit tot stand gekomen zijn zonder de steun en de inspanningen van heel wat mensen. Dit 'Voorwoord' —typisch het laatste stukje tekst dat wordt toegevoegd— is de geschikte plaats om hen te bedanken.

Ik wil vakgroepvoorzitter Prof. Lagasse bedanken voor de mogelijkheid om onderzoek te verrichten in een goed georganiseerde vakgroep met een uitstekende infrastructuur.

Een grote dankuwel gaat naar mijn promotoren Prof. Geert Morthier en Prof. Roel Baets voor de uitstekende begeleiding enerzijds en anderzijds toch de vrijheid die ik kreeg bij het uitvoeren van mijn onderzoek. Zonder jullie uitgebreide vakkennis en talrijke suggesties zou deze eerder–ingenieur–dan–wetenschapper heel wat meer moeite gehad hebben een doctoraat te behalen. Bedankt ook voor de deur die steeds openstond.

De sfeer binnen de fotonica groep is redelijk fantastisch te noemen, waarvoor dank, waarde collega's. Enkele mensen verdienen een aparte vermelding. Mijn grote opto–avontuur is begonnen toen ik samen met Dirk thesis deed onder begeleiding van Ronny. Mannen, bedankt voor de van meet af aan uitstekende samenwerking. Ronny wil ik ook nog eens apart bedanken voor het aangeven van het idee voor het prisma–filter. Bedankt Gert, voor de inwijding in de geheimen van de meetkamer en voor de begeleiding tijdens het voorlaatste jaar van mijn werk. Bedankt, bureaugenoten Frederik, Wim B, Peter, Wim W en Hannes, nu en dan doorspekt met een oude of een nieuwe Europeaan. Het was mij zeer aangenaam met jullie een bureau te delen en van tijd tot tijd het door het plafond lekkende regenwater te bestrijden of een verdwaalde duif naar buiten te helpen. Verder verdienen de mensen van de eerste

verdieping van het prachtige 39–gebouw (Dirk, Kris, Lieven, Peter en Ronny) een speciale vermelding voor hun moed en zelfopoffering voor het aanhoren van de muzikale uitspattingen van ondergetekende, voor de voortrekkersrol bij de organisatie van de zoveelste allerlaatste 39 barbecue en voor de afkoeling die zij de rest van de bewoners van ons niet–geklimatiseerde gebouw bij warm weer belangeloos boden. Bedankt ook aan alle collega's uit de 39 voor de aangename sfeer en voor de bij wijlen onvergetelijke koffiepauzes. Een man die onmisbaar is geworden voor de goede werking van de fotonica groep, is Hendrik. Bedankt om orde te scheppen in de chaos in de meetkamers, voor het vinden van die onvindbare component, voor de hulp bij het zoveelste computer probleem, enz. Respect! Verder heb ik ook het genoegen gehad enkele thesissen te mogen begeleiden. Bedankt, Kurt en Sam en Johan om mee de geheimen van de afstembare laser te helpen doorgronden. Wie zeker niet mogen vergeten worden, zijn het technisch en administratief personeel van de vakgroep. Drie van deze mensen in het bijzonder hebben een belangrijke rol gespeeld bij het tot stand komen van dit werk: bedankt Liesbet, voor het vele opdampwerk; bedankt Marc, voor je precisie soldeerwerk en bedankt Luc, voor de grote zorg en nauwkeurigheid waarmee je allerhande uitbreidingen voor de meetopstelling hebt gemaakt.

Het leven is meer dan werken alleen —gelukkig maar. Bedankt vriendjes en vriendinnetjes, voor jullie vriendschap en voor de nodige ontspanning van tijd tot tijd.

Graag wil ik ook mijn familie bedanken voor hun niet aflatende steun en interesse. In het bijzonder wil ik mijn ouders bedanken voor de steun en hulp op zovele gebieden die ze mij blijven geven.

Dit brengt me bij het thuisfront. Kamiel, je bijdrage aan het schrijven van dit proefschrift mag niet onderschat worden: met het grootste gemak kon je —waarschijnlijk onbewust— de vermoeidheid en de stress doen verdwijnen. Als kers op de taart gunde je je ouders tevens de nodige nachtrust. Eveline, dit is de enige plaats in dit boek waar ik de juiste woorden maar niet vind. Hoe te zeggen wat niet in woorden kan uitgedrukt worden? Bedankt om voor Kamiel en mij te zorgen tijdens die laatste maanden dat ik 's avonds en tijdens het weekend weer eens op het labo zat. Bedankt voor al die kleine en grote dingen die je stilaan onmisbaar maken in mijn bestaan.

Peace!

Bart Moeyersoon
Gent, Juni 2005

Contents

Nederlandstalige tekst

Dutch summary – Nederlandstalige Samenvatting

1. Inleiding

1.1 Optische telecommunicatie

Toepassingen zoals het verzenden van email, het uitwisselen van audio- en videobestanden zorgen nog steeds voor een sterke toename van het wereldwijde internet verkeer: in 2005 wordt een dagelijks trafiek van anderhalf miljoen Terabits (!) per dag voorzien en verwacht wordt dat dit exponentieel zal blijven groeien in de komende jaren [1]. Gelukkig kunnen deze enorme hoeveelheden data over de hele wereld getransporteerd worden door optische telecommunicatie netwerken gebaseerd op WDM–technologie [2, 3, 4, 5, 6, 7, 8]. WDM staat voor 'Wavelength Division Multiplexing' en houdt in dat meerdere optische signalen (elk met een verschillende golflengte) tot één optisch signaal gecombineerd worden en over dezelfde optische vezel verstuurd worden. Dit laat toe de gigantische bandbreedte van optische vezels (zo'n 25 THz) beter te benutten, wat tevens een aanzienlijk kostenbesparing inhoudt [9].

Aanvankelijk werd WDM enkel toegepast in punt–tot–punt verbindingen waarbij in elke netwerkknoop de data werd verwerkt door elektronische schakelapparatuur. Een evolutie naar volwaardige optische WDM–netwerken zonder intermediaire elektronische verwerking wordt echter verwacht [3, 4, 6, 7, 8, 10, 11]. Dergelijke netwerken zullen gebruik maken van golflengteroutering en het optisch schakelen van (groepen van) datapakketten. Verwacht wordt dat afstembare halfgeleiderlasers een belangrijke rol zullen spelen in toekomstige optische netwerktechnologieën [12, 13, 14].

1.2 Lichtbronnen voor telecommunicatie

1.2.1 Vereisten

Om gebruikt te kunnen worden als signaalbron in optische telecommunicatie netwerken, moeten (afstembare) laser diodes aan een aantal strenge specificaties voldoen. Zo moet hun uitgangsvermogen voldoende hoog zijn, voor lange–afstand netwerken typisch tussen 10 en 20 mW voor netwerken in metropolische gebieden volstaan vermogens tussen 2 en 5 mW [15, 16].

De lasers moeten ook beschikken over goede ruis– en spectrale eigenschappen. De ruiseigenschappen worden meestal gekarakteriseerd a.h.v. de relatieve intensiteitsruis (eng. 'Relative Intensity Noise' of RIN) en lijnbreedte [17, 18, 19]. De RIN is een maat voor de relatieve intensiteitsfluctuaties in het uitgangsvermogen, de lijnbreedte staat voor de spectrale breedte van de laser piek en is een maat voor de fase ruis van het laser signaal. De RIN ligt typisch beneden –120 dB/Hz. De lijnbreedte ligt typisch tussen 1 en 100 MHz. De spectrale eigenschappen worden beschreven a.h.v. de zijmodeonderdrukking (eng. 'Side Mode Suppression Ratio' of SMSR). Dit is een maat voor de spectrale zuiverheid van de laser. De SMSR wordt gedefinieerd als de verhouding van het vermogen van de hoofdmode en dat van de sterkste zijmode 40 dB.

Het is natuurlijk ook heel belangrijk dat de goede performantie van de laser behouden wordt zolang hij in gebruik is. Dit houdt in dat de laser een voldoende hoge betrouwbaarheid moet hebben.

1.2.2 Afstembare lasers

Afstembare halfgeleiderlasers bestaan typisch uit meerdere secties: een actieve secties die het vermogen levert en één of meerdere passieve secties die toelaten de laserfrequentie te veranderen [20, 21]. Er bestaan heel wat types afstembare lasers, elk met hun eigen specifieke opbouw en eigenschappen. Het basisprincipe is echter steeds hetzelfde: een actieve sectie levert het vermogen, één of meerdere reflector secties staan in voor de grove afstemming van de frequentie en een fase sectie staat in voor de fijne regeling van de frequentie. Daarom zal de eenvoudige drie–sectie gedistribueerde Bragg reflector (eng. Distributed Bragg Reflector of DBR) laser, bestaande uit een actieve sectie, een fase sectie en een reflector sectie, als voorbeeld gebruikt worden doorheen dit werk. om enkele belangrijke (dynamische) aspecten van multi-sectie afstembare halfgeleiderlasers te onderzoeken. De behaalde resultaten en de

conclusies die daaruit getrokken worden zijn meestal direct uitbreidbaar naar meer complexe afstembare lasers. Voor meer achtergrond i.v.m. afstembare laser, de afstemmechanises, de verschillende types enz., verwijzen we graag naar [20, 21].

Momenteel kunnen afstembare lasers vervaardigd worden met dezelfde specificaties als de vaste-frequentie lasers (de zogenaamde 'Distributed Feedback' of DFB lasers [19]) die normaal in optische netwerken gebruikt worden, en dit over hun volledige afstembereik [14]. Het gebruik van afstembare lasers i.p.v. vaste-frequentie lasers brengt een aantal belangrijke voordelen met zich mee. Ten eerste wordt het inventarisbeheer aanzienlijk vereenvoudigd omdat geen aparte DFB laser meer vereist is voor elk golflengtekanaal. Een ander voordeel is dat één afstembare laser kan gebruikt worden als reserve laser voor meerdere DFB lasers, wat een aanzienlijke kostenbesparing met zich meebrengt omdat niet voor elk golflengtekanaal een aparte reserve laser moet voorzien worden. Het gebruik van afstembare lasers verhoogt ook dit van het netwerk aanzienlijk: schommelingen in het dataverkeer kunnen eenvoudig opgevangen worden en nieuwe diensten kunnen dynamisch voorzien worden [15, 16]. Het meest belangrijke en ook meest uitdagende voordeel is echter dat nieuwe netwerktechnologieën gebaseerd op golflengteroutering en het optisch schakelen van (groepen van) datapakketten kunnen ontwikkeld worden dankzij afstembare lasers [12, 13, 14]. Mede hierdoor zal het zogenaamde volledig optisch netwerk ontwikkeld kunnen worden. Dit netwerk zal een grotere capaciteit, functionaliteit, schaalbaarheid en flexibiliteit hebben en zal transparant zijn voor modulatie– en coderingsformaten. Deze eigenschappen bieden de mogelijkheid op een eenvoudigere netwerk architectuur en kost–effectieve exploitatie van netwerken.

1.4 Uitdagingen - Doel van dit werk

Uit het bovenstaande is het duidelijk dat afstembare halfgeleiderlasers belangrijke kandidaten zijn voor veel nuttige toepassingen in huidige en toekomstige optische netwerken. Om echter aan de strenge eisen van een netwerkomgeving te voldoen, moeten bepaalde aspecten nog onderzocht en/of opgelost worden.

Een eerste aspect betreft het golflengteschakelgedrag van deze componenten. Voor optische schakel toepassingen zijn golflengte schakeltijden vereist van de orde van enkele nanoseconden. De golflengte van afstembare halfgeleiderlasers kan snel veranderd worden op een elek-

tronische manier, maar jammer genoeg treden hierbij problemen op op een grotere tijdsschaal (orde micro– of zelfs milliseconden) door de thermisch geïnduceerde golflengtedrift. In dit werk zullen we het golflengteschakelgedrag onderzoeken en oplossingen voorstellen om het te verbeteren.

Een ander aspect betreft de degradatie van (afstembare) halfgeleiderlasers. De betrouwbaarheidscriteria voor telecommunicatie netwerken zijn zeer streng. Uitgangsvermogen, golflengte en zijmode onderdrukking moeten op de vereiste waarden gehouden worden om signaal degradatie en overspraak te vermijden. Dit houdt o.a. in dat de relatie tussen deze grootheden enerzijds en de afstemstromen anderzijds altijd correct moet blijven. Degradatie van de afstemsecties kan echter een aanzienlijke verandering van de golflengte versus afstemstroom karakteristieken veroorzaken, wat leidt tot een verminderde golflengte (optische frequentie) nauwkeurigheid en een afname van de zijmode onderdrukking. Daarom is een procedure die –liefst op een geautomatiseerde manier– de afstemtabel kan actualiseren een vereiste opdat afstembare lasers in een telecommunicatie netwerk zouden kunnen gebruikt worden.

Dikwijls wordt een optische versterker geïntegreerd met een afstembare laser om het beschikbare uitgangsvermogen te vergroten. Er moest echter nog onderzocht worden wat de invloed hiervan is op belangrijke laser karakteristieken zoals de RIN, lijnbreedte en SMSR.

1.4 Structuur van de thesis

Het golflengteschakelgedrag van afstembare halfgeleiderlasers wordt onderzocht in hoofdstuk 2. Er zullen twee methodes voorgesteld worden dit gedrag te verbeteren. De ene methode is gebaseerd op pre–compensatie van de afstemstromen, de andere methode is gebaseerd op optische terugkoppeling via een periodiek referentie filter. Het zal aangetoond worden dat praktische implementatie van het terugkoppelingsschema moeilijk is met bestaande filters zonder dat de terugkoppeling de laser destabiliseert. Daartoe moest een nieuw filter ontwikkeld worden. Het ontwerp en de karakterisatie van dit filter wordt beschreven in hoofdstuk 3. In hoofdstuk 4 wordt numeriek en experimenteel aangetoond dat het golflengteschakelgedrag van afstembare halfgeleiderlasers kan verbeterd worden via optische terugkoppeling van het nieuw ontwikkelde filter.

In hoofdstuk 5 worden de verschillende degradatie mechanismen die optreden in afstembare lasers behandeld. Er worden technieken beschreven om de performantie van afstembare lasers te controleren. Verder zal ook een eenvoudige procedure beschreven worden die toelaat op een automatische manier de volledige afstemtabel van een gedegradeerde afstembare laser te actualiseren, en dit enkel op basis van de informatie die kan gehaald worden uit de verandering (door degradatie) in de afstemkarakteristieken van één golflengte kanaal.

De invloed van een geïntegreerde optische versterker op de RIN, lijnbreedte en SMSR van een (afstembare) halfgeleiderlaser wordt onderzocht in hoofdstuk 6.

De belangrijkste besluiten van dit werk worden tenslotte gepresenteerd in hoofdstuk 7.

1.5 Publicaties

Het werk uitgevoerd in het kader van dit proefschrift werd gepubliceerd (of ingezonden voor publicatie) in een aantal internationale vaktijdschriften:

1. B. Moeyersoon, G. Morthier, R. Bockstaele, R. Baets, "Improvement of the Wavelength Switching Behaviour of Semiconductor Tunable Lasers Through Optical Feedback from a Periodic Reference Filter based on a Novel Prism-Based Implementation of a Fox-Smith Resonator," accepted for publication in *IEEE Photonics Technology Letters*, October 2005.

2. B. Moeyersoon, G. Morthier, M. Zhao, "Degradation of the mode suppression in Single Mode Laser Diodes due to integrated optical amplifiers," *IEEE Journal of Quantum Electronics*, vol. 40, pp. 241–244, March 2004.

3. Ronan ODowd, Yonglin Yu , Gavin Mulvihill, Sean ODuill, G. Morthier, B. Moeyersoon, "Transmitters for two-tier optical datapacket labeling in advanced IP networks," accepted for publication in *IEE Proc. Optoelectronics, Special Issue Optoelectronic Devices*, Juni 2005.

4. G. Morthier, B. Moeyersoon, "Improvement of the direct modulation behaviour of semiconductor lasers by using a holding beam," *IEEE Photonics Technology Letters*, vol. 16, pp. 1616–1618, July 2004.

5. G. Morthier, B. Moeyersoon, "Intensity Noise and Linewidth of Laser Diodes with Integrated Semiconductor Optical Amplifier," *IEEE Photonics Technology Letters*, vol. 14, pp.1644–1646, December 2002.

6. G. Morthier, B. Moeyersoon, R. Baets, "A $\lambda/4$-shifted Sampled or Superstructure Grating Widely Tunable Twin-Guide Laser," *IEEE Photonics Technology Letters*, vol. 13, pp.1052–1054, October 2001.

De resultaten werden ook gepresenteerd op een aantal internationale conferenties. Hiervoor verwijzen we naar de Engelstalige tekst.

2. Golflengteschakelgedrag van afstembare laser diodes

In dit dit deel zullen we, na een korte inleiding, het golflengteschakelgedrag van afstembare lasers bespreken, alsook twee methodes voorstellen die kunnen gebruikt worden om dat gedrag te verbeteren. Deze twee methodes steunen op pre–compensatie van de afstemstromen enerzijds en optische terugkoppeling via een stabiel referentie filter anderzijds.

2.1 Inleiding

In de huidige telecommunicatienetwerken gebeurt het schakelen en routeren van de data in de knooppunten nog bijna uitsluitend op een elektronische manier. Dit betekent dat de inkomende optische datastromen eerst moeten worden omgezet naar het elektrisch domein en dat na het schakelen de omgekeerde bewerking moet gebeuren. Bovendien wordt de doorvoercapaciteit van een knooppunt zo beperkt door de maximaal haalbare snelheid van de elektronica die momenteel beperkt is tot zo'n 40 Gbit/s. Als men bedenkt dat de transmissiecapaciteit van een standaard optische vezel typisch 25 THz is, is het duidelijk dat op deze manier een belangrijke 'elektronische flessenhals' wordt gecreëerd. Om dit te vermijden en ook om een flexibelere en efficiënter gebruik van de enorme beschikbare bandbreedte van de WDM technologie te bereiken, wordt het verwacht dat toekomstige netwerk technologieën gebruikt zullen maken van golflengteroutering en het optisch schakelen van (groepen van) datapakketten [8]. Dit zal helpen

het zogenaamd 'volledig–optisch' netwerk te creëren. Dergelijke netwerken hebben een grotere capaciteit, functionaliteit, schaalbaarheid en flexibiliteit en zullen transparant zijn voor modulatie– en coderingsformaten. Al deze voordelen houden een potentieel voor een vereenvoudigde netwerk architectuur en koste efficiënte exploitatie van netwerken in zich. Het spreekt voor zich dat snel (orde nanoseconden) afstembare optische signaalbronnen één van de sleutelcomponenten zullen zijn voor de ontwikkeling van dergelijke technologie [12, 13]. Sommige afstembare halfgeleiderlasers zijn in staat zo snel te schakelen op een elektronische manier [22, 23, 24, 25, 26, 27, 28, 29, 30, 31, 32, 33], maar jammer genoeg treden hierbij problemen op op een grotere tijdsschaal (orde micro– of zelfs milliseconden) door de thermisch geïnduceerde golflengtedrift. Deze drift wordt veroorzaakt door de temperatuursverandering te wijten aan het schakelen van de afstemstromen [34, 35, 36, 37, 38, 39, 40, 41]. In de volgende secties zullen we deze drift kwantificeren alsook twee methodes voorstellen die gebruikt kunnen worden om deze drift tegen te werken.

2.2 Golflengteschakelgedrag van afstembare halfgeleiderlasers

De golflengte (of optische frequentie) van een afstembare halfgeleiderlaser kan op een vrij eenvoudige manier snel veranderd worden door één of meerdere van de afstemstromen te schakelen [23]. In de volgende drie secties zullen we achtereenvolgens een theoretisch model voor het golflengteschakelgedrag (kort) bespreken, simulatie resultaten verkregen via dit model tonen alsook experimenteel behaalde resultaten, die de geldigheid van het model aantonen, presenteren.

2.2.1 Theoretisch modelleren van het golflengteschakelgedrag

Theoretisch onderzoek van de dynamische eigenschappen van halfgeleiderlasers gebeurt meestal a.h.v. balansvergelijkingen [17]. Voor een afstembare laser wordt de dynamica van het de optische intensiteit beschreven door de optische en elektrische balansvergelijkingen van de actieve sectie alsook door de elektrische balansvergelijkingen van de passieve secties. Dit is zo omdat de absorptie in de passieve sectie verandert met de stroom door deze secties. De golflengtedynamica wordt beschreven door de elektrische en thermische balansvergelijkingen van de passieve secties alsook door de thermische balansvergelijking van de actieve sectie. De thermische effecten kunnen gemodelleerd worden a.h.v. het bekende eenvoudige geconcentreerde–constanten model,

waarbij de laser wordt opgesplitst in verschillende discrete deelcomponenten. Van elke deelcomponent wordt verondersteld dat hij een oneindig grote thermische geleidbaarheid heeft zodat op elk moment de volledige deelcomponent op dezelfde temperatuur staat [34]. De elektrische en thermische effecten beïnvloeden de brekingsindex van elke sectie en deze beïnvloeden op hun beurt de laser golflengte λ via de fase voorwaarde $n_a(t)L_a + n_p(t)L_p + n_d(t)L_{eff} = \frac{m\lambda}{2}$ met L_{eff} met n_x en L_x de brekingsindex en lengte van elke sectie, L_{eff} de effectieve caviteitslengte van de DBR spiegel en m een geheel getal. De vergelijkingen worden besproken in het Engelstalige deel van dit werk en we zullen ze hier niet herhalen. Het model is opgesteld voor een drie–sectie DBR afstembare laser, bestaande uit een actieve, een fase en een reflector sectie. Afstembare lasers met meer dan twee afstemsecties kunnen op een gelijkaardige manier behandeld worden en dezelfde conclusies gelden als deze voor de hier behandelde laser.

2.2.2 Simulatie resultaten

De vergelijkingen van het theoretisch model vormen een stelsel niet–lineair gekoppelde differentiaal vergelijkingen en werden opgelost met het wiskundige programma Maple [42]. Figuur 1 toont de verandering van de temperatuur van de actieve sectie, de reflector sectie, de fase sectie, de laser chip en de laser drager (T_a, T_d, T_p, T_c en T_s) in de tijd nadat de stroom door de reflector sectie I_d geschakeld werd tussen 0 en 30 mA, met I_a=70 mA, I_p=0 mA en T_0=300 K. De tijdschaal is logaritmisch zodat een gedetailleerd overzicht van een grote tijdspanne bekomen wordt. Vlak na het schakelen van de stroom hebben de fase en reflector sectie dezelfde temperatuur als de laser chip. Aangezien I_p=0, blijft $T_p = T_c$. Aangezien de stroom door de reflector sectie wordt veranderd, stijgt T_d eerst. Daarna stijgen T_a en T_p en uiteindelijk ook T_c. Omdat we een geconcentreerde–constanten model gebruikt hebben, kunnen drie discrete tijdsconstanten onderscheiden worden in figuur 1: één op 3.38 ns (dit is van dezelfde grootte orde als de ladingsdrager leeftijd), één rond 1.7 μs en een derde rond 500 μs. Deze tijdsconstanten zijn verbonden met de warmteoverdracht van golfgeleidersectie–naar–chip, chip–naar–drager en van drager–naar–koelelement respectievelijk.

Figuur 2 toont de corresponderende drift van de laser golflengte (λ_l) en de Bragg golflengte (λ_B) na het schakelogenblik. Dezelfde tijdsconstanten als bij het temperatuursverloop kunnen onderscheiden

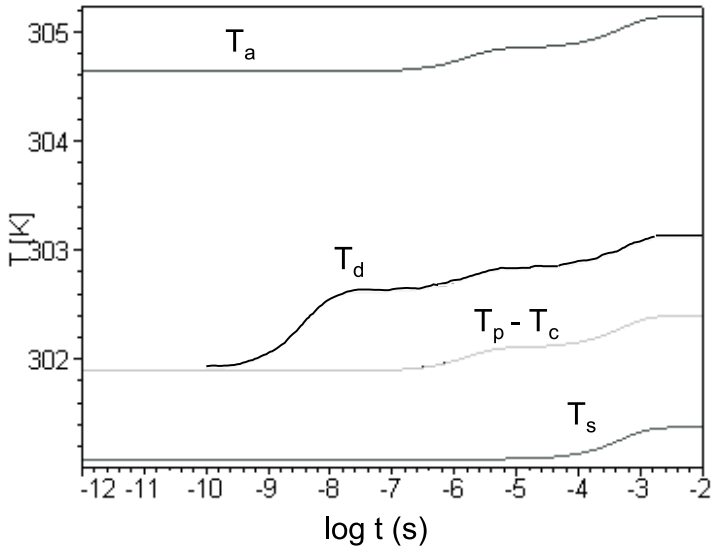

Figuur 1: Verandering van de temperatuur in de tijd nadat I_d geschakeld werd tussen 0 en 30 mA, met I_a=70 mA, I_p=0 mA en T_0=300 K.

worden. De kleinste tijdsconstante wordt echter gemaskeerd door de dynamische effecten van de ladingsdragers. De totale drift is ongeveer 40 pm of 5 GHz. Dit kan klein lijken, maar voor een ITU kanaal spatiëring van 50 GHz is de fout reeds 10 %. En zelfs voor hogere spatiëringen kan een afwijking van de kanaalfrequentie van enkele GHz tot onaanvaardbare verschillen in vermogen leiden door de optische filtering van de kanalen. Bovendien was de grootte van de stroomstap slechts 30 mA en werd slechts één afstemstroom veranderd. In de praktijk zullen bijna altijd (tenminste) twee afstemstromen moeten veranderd worden om een mono-modaal laser spectrum te bekomen na het schakelen. Bovendien is de vereiste (statische) frequentie nauwkeurigheid voor een commercië afstembare laser module typisch al 1 GHz of nog beter.

Figuur 3(a) en 3(b) tonen aan dat de grootte van de golflengte drift afhangt van de grootte van de stroomstap. De drift wordt getoond voor stroomstappen van 10 (laagste curve), 20, 30, 40 en 50 mA (hoogste curve) na een periode van 10 μs en 3 ms respectievelijk. Het blijkt duidelijk dat de grootte van de drift toeneemt met de stroomstap en dat de tijdsconstanten dezelfde zijn voor elke stroomstap. De golflengte is gestabiliseerd na 2.5 ms, wat ongeveer vijf keer de grootste tijdsconstante is.

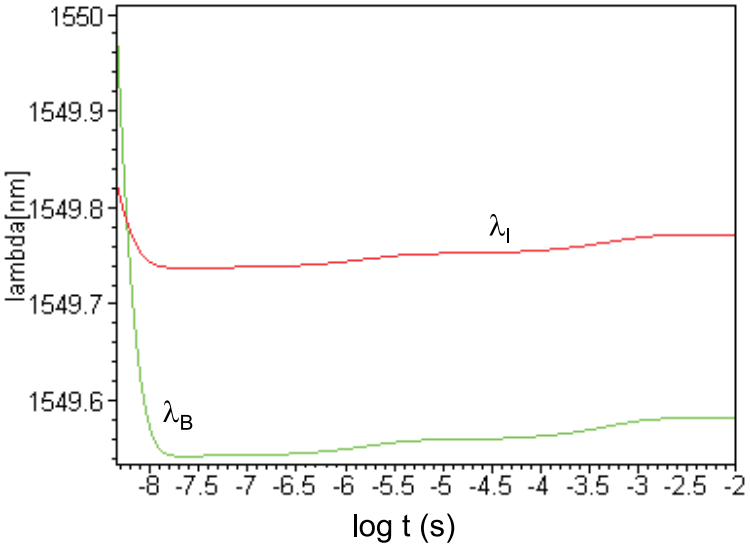

Figuur 2: Drift van de laser golflengte (λ_l) en de Bragg golflengte (λ_B) in de tijd nadat I_d geschakeld werd tussen 0 en 30 mA, met I_a=70 mA, I_p=0 mA en T_0=300 K.

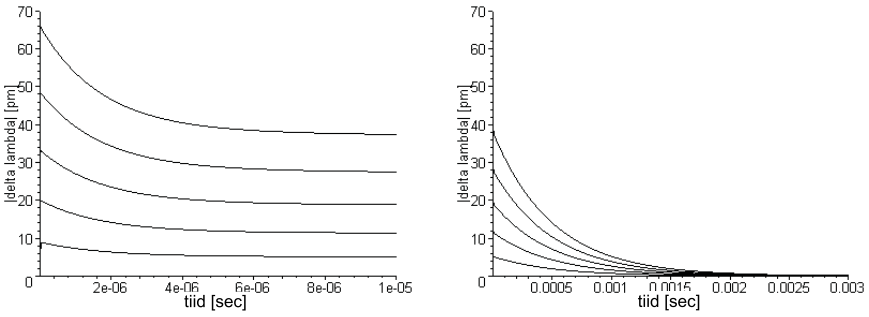

(a) 10 μs (b) 3 ms

Figuur 3: Golflengte drift voor stroomstappen van 10, 20, 30, 40 and 50 mA na een periode van 10 μs en 3 ms respectievelijk(de laagste curve is telkens voor 10 mA, de hoogste voor 50 mA).

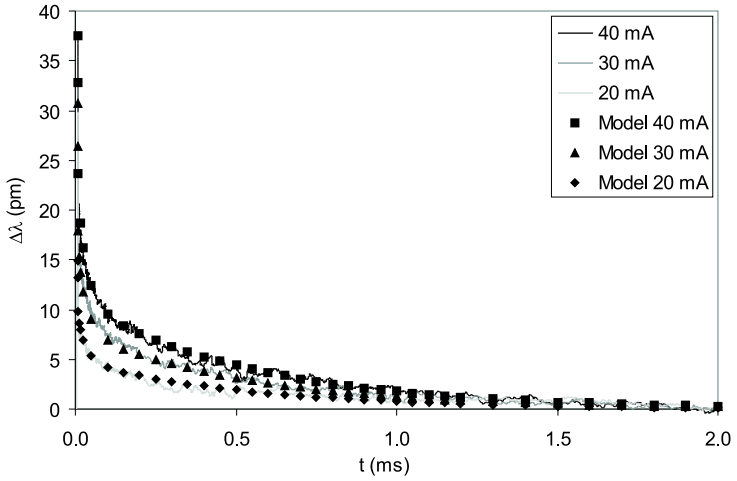

Figuur 4: Gemeten golflengtedrift (volle lijnen) en de drift berekend volgens het model met drie tijdsconstanten (symbolen) voor drie verschillende stroomstappen (20, 30 en 40 mA respectievelijk).

Uit het bovenstaande blijkt duidelijk dat de golflengtedrift kan gemodelleerd worden als een som van exponentiële functies, elk corresponderend met één van de tijdsconstanten.

2.2.3 Experimentele resultaten

We hebben het golflengteschakelgedrag ook experimenteel onderzocht. De gebruikte laser was een verpakte drie–sectie DBR laser van JDS Uniphase. Het laser signaal werd door het afstembaar filter gestuurd om de golflengtevariaties om te zetten in vermogenvariaties en het resulterende signaal werd ingelezen door een digitale oscilloscoop. De meetprocedure is in meer detail beschreven in het Engelstalige deel van dit werk.

Figuur 4 toont de gemeten (absolute waarde van de) golflengtedrift (volle lijnen) en de drift berekend volgens het model met drie tijdsconstanten (symbolen) voor drie verschillende stroomstappen (20, 30 en 40 mA respectievelijk). Er kunnen opnieuw drie tijdsconstanten onderscheiden worden (550 μs, 30 μs en 1.5 μs respectievelijk) en we zien een goede overeenstemming tussen theorie en experiment. Na ongeveer 2 ms is de golflengte gestabiliseerd.

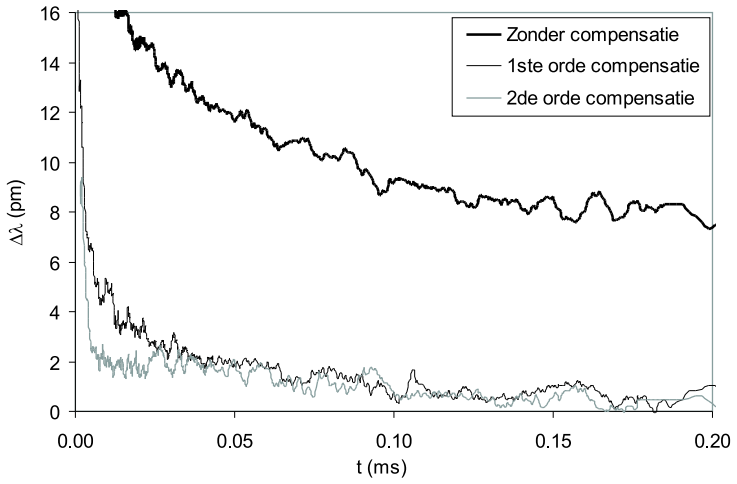

Figuur 5: Onderdrukking van de golflengtedrift door pre–compensatie van de afstemstromen d.m.v. eenvoudige RC–filters. De golflengteverandering na een stroomstap van 40 mA is getoond, zonder compensatie en met compensatie door een eerste en tweede orde filter respectievelijk.

2.3 Pre–compensatie methode

Rekening houdend met de resultaten uit de vorige sectie, zou men er aan kunnen denken de thermisch geïnduceerde golflengtedrift te onderdrukken door het pre–compenseren van de afstemstromen d.m.v. eenvoudige RC–filters [43]. Het bewijs van dit zeer eenvoudige principe is getoond in figuur 5. Het blijkt duidelijk dat de drift reeds sterk onderdrukt wordt door slechts twee tijdsconstanten te onderdrukken. Jammer genoeg is het moeilijk deze techniek te optimaliseren voor verschillende waarden van de stroomstap. Dit komt omdat de temperatuursverandering kwadratisch verandert met de stroom. Dit houdt in dat voor stroomstappen groter of kleiner dan deze waarvoor de pre–compensatie geoptimaliseerd was, onder– respectievelijk overcompensatie zal optreden. Bovendien hangt de golflengtedrift ook af van de schakelgeschiedenis, waardoor het moeilijk is deze techniek te optimaliseren voor alle mogelijke schakelcombinaties.

Wegens de problemen verbonden aan de pre–compensatie methode, hebben we een nieuwe techniek ontwikkeld die is gebaseerd op optische terugkoppeling via een stabiel periodiek referentie filter, waarmee het mogelijk is de thermisch geïnduceerde golflengtedrift te onder-

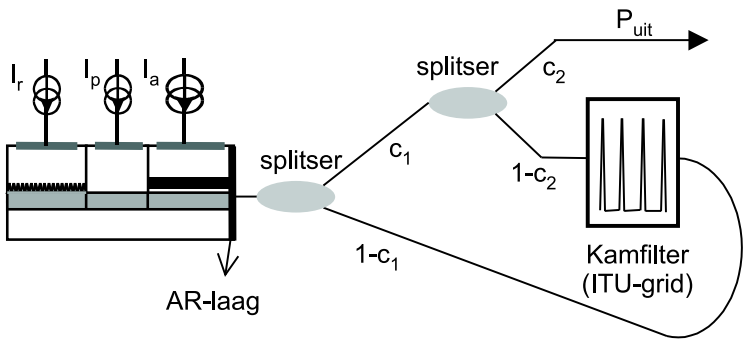

Figuur 6: Nieuw terugkoppelschema om het golflengteschakelgedrag van afstembare halfgeleiderlasers te verbeteren.

drukken onafhankelijk van de stroomstap. Dit betekent dat de compensatie onafhankelijk is van welk kanaal de golflengte naar geschakeld wordt en ook onafhankelijk van de schakelgeschiedenis. Deze techniek wordt beschreven in de volgende sectie.

2.4 Optische terugkoppeling

Opdat het golflengteschakelgedrag van een afstembare laser zou kunnen verbeterd worden door optische terugkoppeling via een periodiek optisch filter, moet dit filter stabiel blijven, onafhankelijk van de temperatuursveranderingen in de lasersecties. Daarom moet dit filter fysisch gescheiden zijn van de laser. Een mogelijke implementatie van het terugkoppelschema is getoond in figuur 6. Het schema bevat slechts twee vermogensplitsers en een kamfilter dat fysisch en dus thermisch is gescheiden van de laser. De sterkte van de terugkoppeling f_{ext} (de verhouding van het vermogen dat terug de laser caviteit binnentreedt tot het uitgestraalde vermogen) wordt bepaald door de koppelfactoren c_1 en c_2.

Het optisch terugkoppelen van het laser licht kan een grote invloed hebben op de performantie van de laser, zowel in de positieve als de negatieve zin. We zullen hier niet verder op ingaan, maar de geïnteresseerde lezer verwijzen we naar de Engelstalige tekst en naar [44, 45, 46, 47, 48, 49, 50, 51, 52, 53, 54, 55]. Wel willen we benadrukken dat, om te vermijden dat de terugkoppeling instabiliteiten veroorzaakt, het zeer belangrijk is dat enerzijds de externe caviteitslengte voldoende kort (niet meer dan enkele centimeters) gehouden wordt en dat anderz-

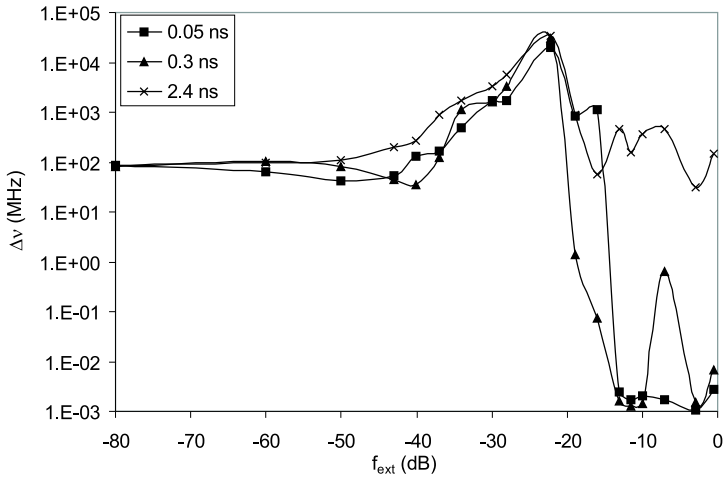

Figuur 7: Lijnbreedte $\Delta\nu$ in functie van de terugkoppelingssterkte f_{ext} voor een laser onderhevig aan optische terugkoppeling.

ijds de terugkoppelingssterkte groot genoeg is (-10 dB of meer) [52, 55]. Zo niet kan de laser in een instabiel regime terechtkomen waarbij zowel de RIN als de lijnbreedte heel sterk toenemen. Dit gebied kan zich uitstrekken over meerdere grootte–ordes van de terugkoppelingssterkte, i.e. van -40 dB tot -10 dB [50, 51, 53, 55]. Dit wordt geïllustreerd in figuur 7, waar de lijnbreedte van een laser onderhevig aan optische terugkoppeling is getoond in functie van de terugkoppelingssterkte f_{ext} en dit voor een rondlooptijd in de externe caviteit τ = 0.05 ns (vierkanten), 0.3 ns (driehoeken) en 2.4 ns (kruisen). Dit correspondeert met een externe caviteitslengte van 7.5 mm, 45 mm en 360 mm respectievelijk. Het blijkt duidelijk dat voor f_{ext} $<$ -16 dB de lijnbreedte onaanvaardbaar groot (tot enkele tientallen GHz) kan worden. Om instabiliteiten te vermijden zal f_{ext} dus zeker groter dan -16 dB moeten zijn. In de praktijk zullen altijd koppelverliezen aanwezig zijn tussen de laser en het filter, daarom kiest men voor de veiligheid best f_{ext} $>$ -10 dB. De resultaten in figuur 7 werden berekend met de commercieel beschikbare software VPI Componentmaker [56].

Uit het voorgaande blijkt dat enerzijds de externe caviteitslengte voldoende kort (niet meer dan enkele centimeters) moet zijn en dat de terugkoppelingssterkte groot genoeg moet zijn (-10 dB of meer) om te vermijden dat de terugkoppeling de laser destabiliseert. Dit is jammer genoeg niet mogelijk voor de praktische implementatie van het

terugkoppelschema in figuur 6 en dit wegens de aanwezigheid van de twee vermogensplitsers die het moeilijk maken de externe caviteitslengte voldoende kort te houden. Er zijn twee vermogensplitsers nodig omdat bestaande kamfilters (zoals het klassieke Fabry Perot etalon) enkel een kamkarakteristiek in transmissie hebben en een tegengestelde karakteristiek in reflectie met dippen op de plaats van de pieken in transmissie [57]. Er bestaan ook filters met een kamkarakteristiek in reflectie, maar deze filters hebben dan weer de tegengestelde karakteristiek in transmissie, waardoor er nog steeds een extra vermogensplitser nodig is in de terugkoppellus om een aanvaardbaar uitgangsvermogen uit de laser te krijgen. Daarom hebben we beslist zelf een filter te ontwikkelen met een kamkarakteristiek in reflectie zowel als in transmissie, zodat er geen extra vermogensplitsers meer nodig zijn om de laser met het filter te koppelen. Om de externe rondlooptijd zo klein mogelijk te houden, moet het filter zo compact mogelijk zijn. Het ontwerp van dit filter wordt beschreven in het volgende deel.

2.5 Besluit

In dit deel hebben we het golflengteschakelgedrag van afstembare lasers besproken. Er werden twee methodes voorgesteld die kunnen gebruikt worden om de thermisch geïnduceerde golflengtedrift te onderdrukken. De eerste methode berust op pre–compensatie van de afstemstromen. Dit is een zeer eenvoudige techniek, maar is jammer genoeg moeilijk te optimaliseren voor alle mogelijke schakelcombinaties. Daarom werd een nieuwe methode ontwikkeld, gebaseerd op optische terugkoppeling via een stabiel referentie filter waarmee de thermisch geïnduceerde golflengtedrift kan onderdrukt worden, onafhankelijk van het kanaal waarnaar de laser golflengte wordt geschakeld en onafhankelijk van de schakelgeschiedenis. Belangrijk hierbij is dat de externe caviteitslengte voldoende kort moet zijn en dat de terugkoppelingssterkte groot genoeg is om te vermijden dat de terugkoppeling de laser destabiliseert. Daartoe moest een nieuw filter ontwikkeld worden, wat wordt beschreven in het volgende deel. Het praktisch bewijs van de verbetering van het golflengteschakelgedrag door de optische terugkoppeling zal worden gegeven in sectie 4.

3. Filter

In dit deel wordt de ontwikkeling van een nieuw filter ontwerp beschreven. De motivatie om een eigen filter te ontwikkelen komt voort uit het onderzoek naar het verbeteren van het golflengteschakelgedrag van afstembare halfgeleiderlasers, zoals beschreven in het vorige hoofdstuk. De golflengte van dergelijke lasers kan in 10 nanoseconden of minder veranderd worden door 1 of meerdere afstemstromen snel te veranderen [22, 23, 24, 25, 26, 27, 28, 29, 30, 31, 32, 33]. De thermische effecten geassocieerd met het schakelen van de afstemstromen veroorzaken echter een trage golflengte drift die de schakeltijd tot enkele milliseconden kan verlengen [34, 35, 36, 37, 38, 39, 40, 41]. Om deze drift te verhinderen, hebben we een nieuw optisch feedback schema ontwikkeld waar een optisch kamfilter gebruikt wordt als een stabiele frequentie referentie die onafhankelijk is van temperatuursvariaties in de laser secties. Met een kamfilter wordt een filter bedoeld met een periodieke karakteristiek waarbij de filterpieken op de standaard ITU-frequenties liggen [58]. Dit schema werd in meer detail beschreven in het vorige deel en in [59]. Simulaties hebben aangetoond dat met dit schema frequentie afwijkingen tot 15 GHz kunnen onderdrukt worden. Om de laser niet te destabiliseren door de terugkoppeling is het belangrijk dat de terugkoppelsterkte (d.i. de verhouding van het gereflecteerde veld tot het uitgezonden veld) groot genoeg is, typisch -10 dB of meer, dit betekent dat het laser facet een anti-reflectie (AR) laag moet krijgen. Bovendien moet de rondlooptijd in de externe caviteit voldoende klein gehouden worden [50, 55]. In het vorige deel werd uitgelegd dat dit niet mogelijk is met bestaande kamfilters zoals b.v. het klassieke Fabry Perot etalon. Daarom hebben we beslist zelf een filter te ontwikkelen met een kamkarakteristiek in reflectie zowel als in transmissie, zodat er geen extra vermogensplitsers meer nodig zijn om de laser met het filter te koppelen. Om de externe rondlooptijd zo klein mogelijk te houden, moet het filter zo compact mogelijk zijn. Het nieuwe filter is gebaseerd op een nieuwe prisma-gebaseerde implementatie van een Fox-Smith resonator [60].

3.1 Filterontwerp

3.1.1 Constructie

Het nieuw filter is gebaseerd op het zelfde principe als een Fabry Perot etalon, namelijk de interferentie van meerdere bundels [57]. Het be-

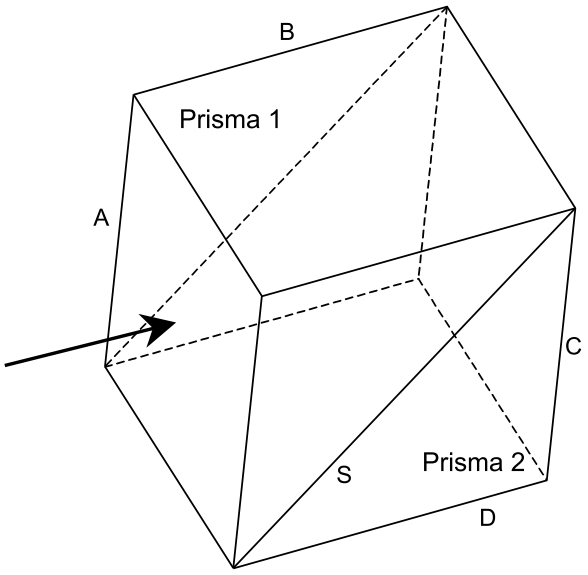

Figuur 8: Schematische voorstelling nieuw filter.

langrijkste verschil is echter dat de eerste bijdrage in reflectie wordt gescheiden van de volgende bijdragen, zodat in reflectie een kamkarakteristiek wordt bekomen, net als in transmissie. Dit geeft aanleiding tot de volgende vorm van het nieuwe filter, zoals te zien in figuur 8.

Het filter bestaat uit twee rechthoekige prisma's met brekingsindex n en basislengte L die op elkaar gekleefd zijn met een UV-uithardende brekingsindex-aangepaste lijm. Het licht zal invallen op facet A van het bovenste prisma (prisma 1) en zal doorgestuurd worden naar facet B, C en D en zal ook terug gereflecteerd worden naar facet A. De invallende lichtbundels zullen meerdere reflecties ondergaan in het onderste prisma (prisma 2) en de verschillende reflecties zullen afhankelijk van de frequentie constructief of destructief interfereren, net zoals in een klassiek Fabry Perot etalon. Het enige verschil is dat er nu drie spiegels zijn i.p.v. twee, namelijk de spiegels op de facetten S, C en D van het onderste prisma. De enige functie van prisma 1 is er voor te zorgen dat het invallend licht horizontaal kan zijn (parallel aan facet B en D) opdat de bundels in prisma 2 loodrecht zouden invallen op facet C en D, zonder rekening te moeten houden met totale interne reflectie op de lucht-glas scheiding aan S (als prisma 1 niet aanwezig zou zijn). Daarom moet facet A van prisma 1 een AR laag krijgen. Aangezien de eerste reflectie (op S) naar B gericht is en niet naar A zoals het geval zou zijn bij een

gewoon Fabry Perot etalon, verwachten we een kamfunctie voor de reflectie karakteristiek in A (en voor de transmissie karakteristiek in C en D). De eerste reflectie mag natuurlijk zo weinig mogelijk interfereren met de overige bijdragen in A, C en D. Daarom moet ook facet B een AR krijgen. In B krijgt men de klassieke Fabry Perot reflectie responsie, met dippen op dezelfde frequenties als de pieken van de responsies in A, C en D. De invloed van de reflectiecoëfficiënten van de facetten S, C en D van prisma 2 is gelijkaardig aan die van de reflectiecoëfficiënten van de spiegels van een gewoon Fabry Perot etalon. Dit betekent dat de extrema breder worden en dat hun amplitude vermindert als de reflectiecoëfficiënten van de spiegels afnemen [57]. Om een voldoende selectief filter te hebben, zullen de spiegels op facetten S, C en D daarom hoog-reflectief moeten zijn. Er wordt in meer detail ingegaan op de reflectiecoëfficiënten in de volgende sectie. Het frequentie verschil tussen de pieken (de FSR: Free Spectral Range), wordt voor dit filter gegeven door $FSR = c/2nL$, met c de lichtsnelheid, n de brekingsindex en L de basis lengte van de prisma's. Voor een brekingsindex van 1.5 en een FSR van 100 GHz (de standaard waarde voor de frequentie scheiding tussen ITU-kanalen), zou de grootte van de prisma's 1 mm zijn. Dit is duidelijk compact genoeg om instabiliteiten veroorzaakt door de terugkoppeling te vermijden. Het praktisch bewijs van dit nieuwe filter principe wordt gegeven in sectie 3.3.

3.1.2 Fabricatie

Zoals uitgelegd in de vorige sectie, moet op facetten A en B een AR-laag komen, en op facetten C, D en S een HR-laag. De AR- en HR-lagen worden gerealiseerd op de klassieke manier. De AR-lagen bestaan uit een kwartgolflengte laag met een brekingsindex die zo goed mogelijk voldoet aan $n_{AR} = \sqrt{n_1 n_2}$, met n_1 en n_2 de brekingsindices van de materialen waartussen de AR-laag wordt aangebracht. In dit geval zijn dit lucht (n_1=1) en BK7 (n_2=1.44402 rond 1550 nm). BK7 is een materiaal dat vaak gebruikt wordt voor prisma's, lenzen en andere glazen optische componenten. Dit leidt tot n_{AR} = 1.202. Een materiaal dat een brekingsindex heeft die deze waarde goed benaderd en dat vaak gebruikt wordt als materiaal voor optische lagen is MgF_2 met een brekingsindex van 1.34 rond 1550 nm. De dikte van de AR-laag is dan $d_{AR} = \lambda/4n_{AR}$ = 294 nm. Dit leidt tot een vermogen reflectiviteit van R_{AR} = 1.27 % voor de AR-lagen en de corresponderende reflectiecoëfficiënt is dan $r_{AR} = -\sqrt{R_{AR}}$.

De HR-lagen worden gerealiseerd als een stapel van kwartgolflengte lagen bestaande uit materialen met afwisselend lage en hoge brekingsindex. Voor de hoge brekingsindex werd amorf Si met n_H = 3.73 genomen, voor de lage brekingsindex Al_2O_3 met n_L = 1.63. De corresponderende dikte is dan 104 nm voor de Si lagen en 238 nm voor de Al_2O_3 lagen. De volgorde van de lagen was steeds BK7–Si–Al_2O_3. Voor de spiegels op facetten C en D werden drie paren genomen, wat leidt tot R_{HR} = 98 %, met corresponderende reflectiecoëfficiënt $r_{HR} = -\sqrt{R_{HR}}$. De corresponderende transmissiecoëfficiënt is $t_{HR} = -n_2 \cdot \sqrt{T_{HR}}$, met de transmitiviteit gegeven door $T_{HR} = 1 - R_{HR}$. Indien de laagvolgorde omgekeerd zou worden, i.e. eerst Al_2O_3 op BK7 en dan een laag Si, zou R_{HR} (nagenoeg) onveranderd blijven, maar r_{HR} zou positief worden i.p.v. negatief. De fase van t_{HR} blijft onveranderd. Reflectiviteiten hoger dan 98 % kunnen gerealiseerd worden met meer dan drie paren, maar voor onze doeleinden volstaat 98 % ruimschoots. Op facet S valt het licht in onder een hoek van 45 graden. Dit betekent dat de laagdiktes moeten aangepast worden. Voor een centrale golflengte van 1550 nm worden de corresponderende diktes 108 nm resp. 376 nm. Voor schuine inval zal de reflectiviteit ook niet meer hetzelfde zijn voor TE- en TM-polarisatie. Maar aangezien het licht van halfgeleiderlasers bijna exclusief TE-gepolariseerd is, beschouwen we enkel de reflectiecoëfficiënten voor TE-polarisatie. Voor de HR-laag op facet S werd slechts 1 paar genomen, wat leidt tot R_s = 70 %, met corresponderende reflectiecoëfficiënt $r_s^- = -\sqrt{R_s}$. De corresponderende transmissiecoëfficiënt is $t_s = -\sqrt{T_s}$. De lichtbundels die vanuit A of B op S invallen, zullen de omgekeerde laagvolgorde zien dan de bundels die van C of D komen. Dit houdt in dat de fase van de reflectiecoëfficiënt verandert (van 180 graden naar 0 graden). Voor reflectie op S in het bovenste prisma wordt de reflectiecoëfficiënt dan $r_s^+ = \sqrt{R_s} = -r_s^-$. De fase van de transmissieiecoëfficiënt blijft onveranderd. De reden waarom slechts 1 paar gebruikt werd voor de spiegel op S, zal duidelijk worden in de volgende sectie. Al de lagen werden aangebracht in onze eigen stofvrije ruimtes d.m.v. e-gun depositie. De gebruikte prisma's waren hoge-precisie rechthoekige prisma's met een basis lengte L = 3.2 mm. Dit komt overeen met een FSR van 32.5 GHz. Dit was de kleinste beschikbare standaard afmeting voor hoge-precisie rechthoekige prisma's. Prisma's met kleinere afmetingen kunnen op aanvraag geproduceerd worden, maar dit is natuurlijk heel wat duurder. En voor het aantonen van het principe van de golflengte stabilisatie d.m.v. optische terugkoppeling van het filter, was een FSR van 32.5 GHz een aanvaardbare waarde.

De prisma's hebben een dimensie tolerantie van ± 0.1 mm, een oppervlakte vlakheid van $\lambda/8$ bij 632.8 nm en een hoektolerantie van ± 30 boogseconden. De prisma's werden manueel aan elkaar gelijmd d.m.v. UV-uithardende brekingsindex-aangepaste lijm met een brekingsindex van 1.445 bij 1550 nm.

3.2 Reflectie- en transmissiekarakteristieken

3.2.1 Theoretische reflectie- en transmissiekarakteristieken

De theoretische karakteristieken kunnen afgeleid worden uit de relaties die bestaan tussen de elektromagnetische velden door de reflecties en de transmissies aan de verschillende facetten. Om interferentie fenomenen te bestuderen moet de fase van de velden in rekening gebracht worden. We zullen daarom dit probleem behandelen in termen van de (complexe) elektrische velden in het filter. Er wordt verondersteld dat we te maken hebben met lineaire, isotrope en homogene materialen, dat de dispersie in het filter medium kan verwaarloosd worden en dat de reflectiecoëfficiënten en transmissiecoëfficiënten van de verschillende facetten onafhankelijk zijn van de polarisatie. Aangezien er geen bronnen van elektromagnetische straling in het filter aanwezig zijn, moet er natuurlijk een externe bron zijn. De toepassing die we voor het filter in gedachten hebben is het verbeteren van het golflengteschakelgedrag van afstembare halfgeleiderlasers door optische terugkoppeling via het filter. Het laser licht zal invallen op facet A en we zijn vooral geïnteresseerd in het licht dat wordt gereflecteerd en het licht dat het filter verlaat via facet C. Men vindt voor de reflectiekarakteristiek R, respectievelijk transmissiekarakteristiek T:

$$R = \left| r_a + \frac{t_a^o t_a e^{-2jkL}\left[r_b R_s + r_c t_s^2 - r_b r_c r_d e^{-2jkL}\right]}{D} \right|^2 \tag{1a}$$

$$T = \left| \frac{t_c t_a t_s e^{-jkL}\left[1 - r_b r_d e^{-2jkL}\right]}{D} \right|^2 \tag{1b}$$

met

$$\begin{aligned} D =& 1 - \left[r_a(r_b R_s + r_c t_s^2) + r_d(r_b t_s^2 + r_c R_s)\right] e^{-2jkL} \\ &+ r_b r_c \left[(r_a R_s + r_d t_s^2)(r_a t_s^2 + r_d R_s) - (r_a - r_d)^2 R_s t_s^2\right] e^{-4jkL} \end{aligned} \tag{2}$$

waarin r_a, r_b, r_c, r_d en r_s (t_a, t_b, t_c, tr_d en t_s) de reflectiecoëfficiënten (transmissiecoëfficiënten) voor reflectie (transmissie) aan facet A, B, C, D en S respectievelijk zijn. t_a^o is de transmissiecoëfficiënt voor transmissie vanuit het prisma door de MgF_2 AR-laag naar lucht. t_a is de transmissiecoëfficiënt voor propagatie in de tegenovergestelde richting. $k = n \cdot 2\pi/\lambda$ is de propagatieconstante van de velden in het (verliesloos) medium met brekingsindex n.

Om de theoretische karakteristieken af te leiden, werden enkele vereenvoudigende veronderstellingen gemaakt zoals loodrechte inval, alsook het verliesloos zijn van materialen en spiegels. Deze veronderstellingen doen echter niets af aan de geldigheid van de gevolgde redenering. Bovendien kunnen niet-loodrechte inval en verlieshebbende materialen en spiegels eenvoudig in rekening gebracht worden als volgt. Niet-loodrechte inval geeft aanleiding tot een fase factor $kL\cos\theta$ met θ de hoek waaronder de velden propageren in het filter. Verlies in de spiegels kan in rekening gebracht worden door complexe veld reflectie en transmissiecoëfficiënten te beschouwen (i.e $r = \sqrt{R}e^{j\psi}$). In dat geval zal $R+T = 1-A$, met A de absorptie in de spiegels. Verliezen in de materialen tenslotte kunnen in rekening gebracht worden door een complexe propagatie constante $k = n \cdot 2\pi/\lambda - j\alpha$ met α het verlies in het materiaal. Een meer uitgebreide behandeling vindt men in [57].

3.2.2 Voorbeelden

Figuur 9 en 10 tonen de reflectie- en transmissiekarakteristiek berekend volgens (1a) resp. (1b). Voor de reflectiecoëfficiënten van de verschillende lagen werden de waarden vermeld in sectie 3.1 genomen: $R_a = R_b = R_{AR}$ = 0.0127, $R_c = R_d = R_{HR}$ = 0.98 and R_s = 0.7. Uit figuur 9 en 10 volgt duidelijk dat zowel in reflectie als in transmissie een kamkarakteristiek bekomen wordt, met de pieken op dezelfde frequenties. De FSR is 32.5 GHz, corresponderend met de basis lengte van 3.2 mm. De 3–dB breedte is 3.3 GHz. Het blijkt ook dat voor de gekozen waarden van de reflectiecoëfficiënten de (piek) reflectie veel sterker is dan de (piek) transmissie. De reden hiervoor is dat we een voldoende grote terugkoppelsterkte willen om de laser niet te destabiliseren. De terugkoppelsterkte moet typisch minstens –10 dB zijn [50, 55]. Ideaal gezien zou 10 % reflectie van het filter dus moeten volstaan. Jammer genoeg zullen er in praktijk steeds koppelverliezen zijn en we moeten ook rekening houden met fabricage toleranties voor de verschillende coatings. Daarom werd voor een voldoende hoge reflectie gekozen. Dit

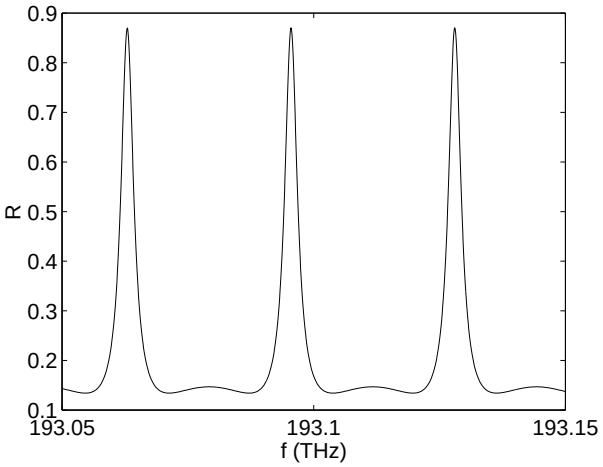

Figuur 9: Reflectie responsie van dubbel-prisma filter ($R_a = R_b$ = 0.0127, $R_c = R_d$ = 0.98 en R_s = 0.7).

is ook de reden waarom slechts 1 Si–Al_2O_3 paar op facet S werd aangebracht: voor meerdere paren was R_s te hoog om nog een voldoende hoge reflectie te krijgen.

We willen nog opmerken dat nog vele andere filterkarakteristieken kunnen bekomen worden door de reflectiecoëfficiënten van de spiegels aan te passen. Zo kan een hogere transmissie bekomen worden (ten koste van een lagere reflectie natuurlijk). Het is zelfs mogelijk om een klassieke Fabry Perot reflectie- en transmissiekarakteristiek te bekomen. Hiervoor moet R_b voldoende groot gekozen worden.

3.3 Experimentele karakterisering

De werking van het nieuwe filter concept werd ook experimenteel geverifieerd. Figuur 11 toont de experimenteel bepaalde reflectie- en transmissiekarakteristiek. We zien een zeer goede overeenkomst met de theoretische karakteristieken in figuur 9 en 10.

We kunnen dus besluiten dat dit nieuwe filter concept wel degelijk werkt. Het kan dus gebruikt worden als een stabiele frequentie referentie om het golflengteschakelgedrag van afstembare halfgeleiderlasers te verbeteren. Dit wordt verder uitgewerkt in het volgende deel.

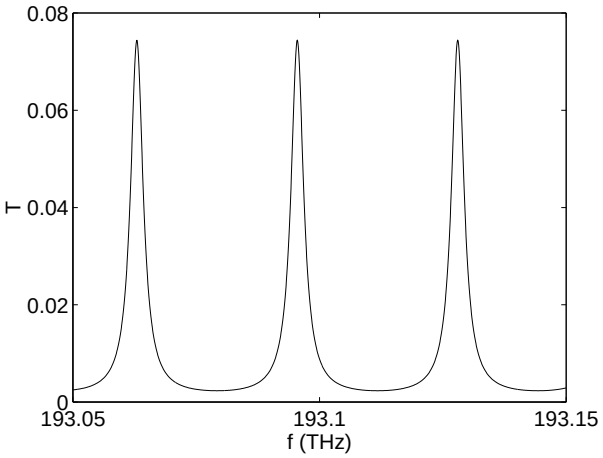

Figuur 10: Transmissie responsie van dubbel-prisma filter ($R_a = R_b$ = 0.0127, $R_c = R_d$ = 0.98 en R_s = 0.7).

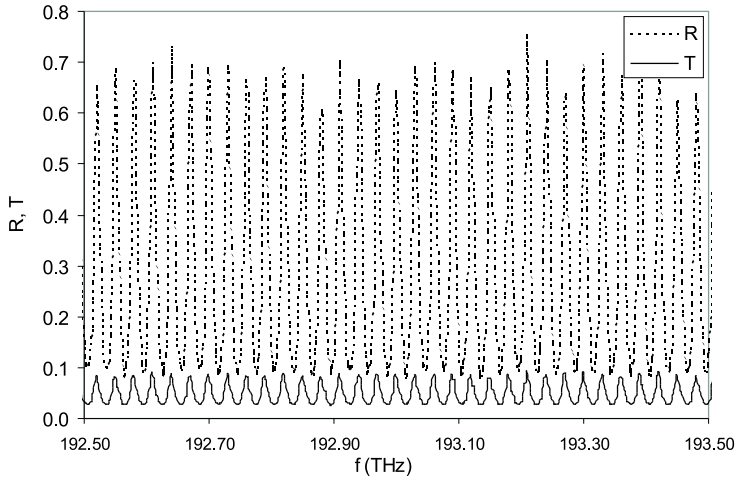

Figuur 11: Experimenteel bepaalde reflectie- en transmissiekarakteristiek van het nieuwe filter type ($R_a = R_b$ = 0.0127, $R_c = R_d$ = 0.98 and R_s = 0.7).

4. Verbeteren van het golflengteschakelgedrag van afstembare lasers door optische terugkoppeling via een periodiek filter

In deze sectie zullen we aantonen dat het golflengteschakelgedrag van een afstembare laser aanzienlijk kan verbeterd worden door optische terugkoppeling via een stabiel periodiek referentie filter. Het filter is gebaseerd op een nieuw ontwerp, beschreven in de vorige sectie, en heeft een zowel in reflectie als in transmissie een karakteristiek die bestaat uit periodiek gespatiëerde pieken. De verbetering van het golflengteschakelgedrag wordt verwezenlijkt door het onderdrukken van de thermisch geïnduceerde golflengtedrift gerelateerd met het schakelen van de afstemstromen. In een eerste deel zullen enkele simulatie resultaten getoond worden die de invloed van de optische terugkoppeling op de afstemtabel en het golflengteschakelgedrag van een afstembare laser aantonen. In het tweede deel wordt de verbetering van het golflengteschakelgedrag experimenteel aangetoond.

4.1 Simulatie resultaten

De simulaties werden uitgevoerd met de laser simulatie software van VPI [56]. Figuur 12 toont (een deel van) de afstemtabel van een driesectie DBR afstembare laser onderhevig aan optische terugkoppeling van een stabiel periodiek filter. De laserfrequentie is getoond als functie van de stroom door de reflector sectie en dit voor enkele waarden van de stroom door de fase sectie (I_p = 0, 1, 2 en 3 mA). Het terugkoppelschema werd reeds besproken in sectie 2.4 en is getoond in figuur 6. Het uitgangsfacet van de laser heeft een anti-reflectie laag met een reflectiviteit van 0.01. Het filter was een Fabry Perot etalon met een FSR van 100 GHz en een spiegel reflectiviteit van 0.9. De terugkoppelingssterkte f_{ext} was -10 dB, de rondlooptijd in de externe caviteit τ_D was 0.3 ns. Uit figuur 7 blijkt dat de laser in een stabiel regime met kleine lijnbreedte werkt.

Uit figuur 12 blijkt duidelijk dat de emissie frequenties nu bepaald worden door de frequentie van de filter pieken. Als de pieken op de ITU–grid gekozen worden, zal de laser automatisch licht uitzenden op ITU-frequenties. Uit de vele verschillende werkingspunten op de ITU-frequenties kan een werkingspunt met optimale karakteristieken gekozen worden.

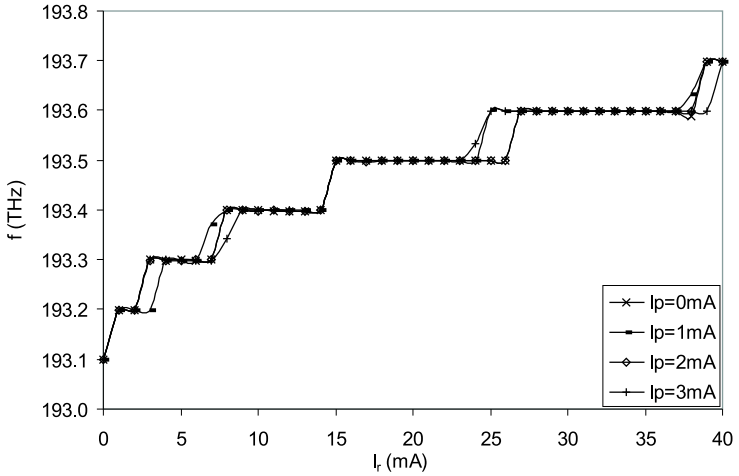

Figuur 12: laserfrequentie als functie van reflector stroom voor een drie-sectie DBR afstembare laser onderhevig aan optische terugkoppeling van een stabiel periodiek filter (I_p = 0, 1, 2 en 3 mA). De terugkoppelingssterkte f_{ext} was -10 dB, de rondlooptijd in de externe caviteit τ_D was 0.3 ns.

Figuur 13 toont het schakelen van de laserfrequentie, met en zonder terugkoppeling van het filter. Aangezien thermische effecten niet gemodelleerd worden in the simulatie software, werd de thermische drift gesimuleerd door een lineair afnemende stroom door de reflector sectie te sturen. Dit zal ook een afwijking van de laserfrequentie veroorzaken, en we zijn vooral geïnteresseerd in de maximale frequentie afwijking die door de optische terugkoppeling kan tegengewerkt worden. De drift werd ook versneld zo dat kortere tijdsintervallen (enkele tientallen nanoseconden i.p.v. enkele milliseconden) konden gesimuleerd worden, aangezien de simulaties anders te veel tijd in beslag zouden nemen. Uit figuur 13 volgt duidelijk dat de frequentie drift (en naderhand ook een modesprong) vlugger optreedt wanneer geen terugkoppeling aanwezig is. Afwijkingen tot 15 GHz konden op deze manier tegengewerkt worden.

4.2 Experimentele resultaten

Figuur 14 toont een schematische voorstelling van het koppelen van een laser met het filter via een ballens (diameter 2 mm en brandpuntsaf-

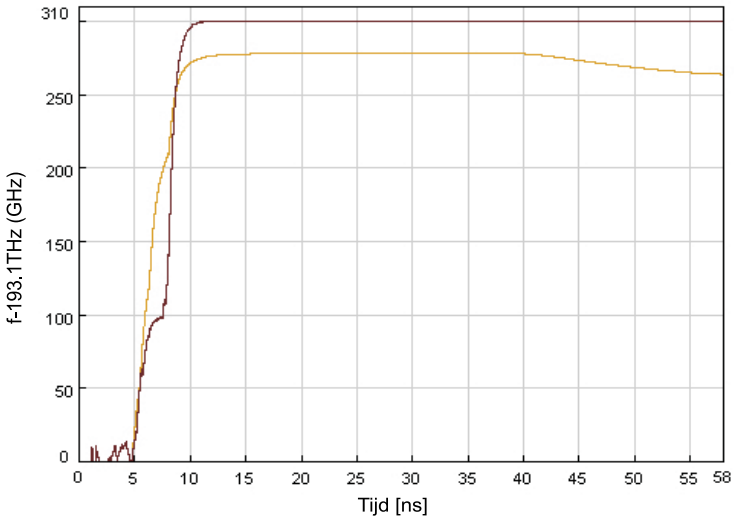

Figuur 13: Schakelen van de laserfrequentie, met en zonder terugkoppeling van het filter. De terugkoppelingssterkte f_{ext} was -10 dB, de rondlooptijd in de externe caviteit τ_D was 0.3 ns.

stand 0.1 mm). De laser is een drie–sectie DBR afstembare laser met een AR–laag.

Figuur 15 toont (een deel van) de experimenteel bepaalde afstemtabel van de externe caviteitslaser uit figuur 14. Naast de laserfrequentie is nu ook de zijmodeonderdrukking (SMSR) getoond in functie van I_r voor I_a = 100 mA en I_p = 2 mA. Het verloop van de frequentie is gelijkaardig aan dat in figuur 12. De intermediaire frequentie sprongen (b.v. rond I_r = 11 mA) en het feit dat de SMSR niet voor elk frequentie plateau boven 40 dB ligt, zijn te wijten aan de kleine FSR van het filter. Deze is slechts 32.5 GHz en aangezien de 3–dB breedte van de Bragg piek typisch 100 GHz of meer is, zullen er steeds tenminste drie filter pieken binnen de Bragg piek gelegen zijn. Dit betekent dat een kleine afwijking reeds een modesprong kan veroorzaken. Dit kan sterk verbeterd worden door enerzijds de FSR van het filter beter af te stemmen op de breedte van de Bragg piek (b.v. een FSR van 50 GHz of 100 GHz) zo dat minder filter piek op hetzelfde moment binnen de Bragg piek liggen. Anderzijds kan men ook de externe caviteitslengte zo kiezen dat de spatiëring tussen de caviteitsmodes groter wordt, waardoor de kans dat twee modes op hetzelfde moment binnen een filterpiek liggen kleiner wordt. Echter, aangezien we hier vooral willen aantonen dat het

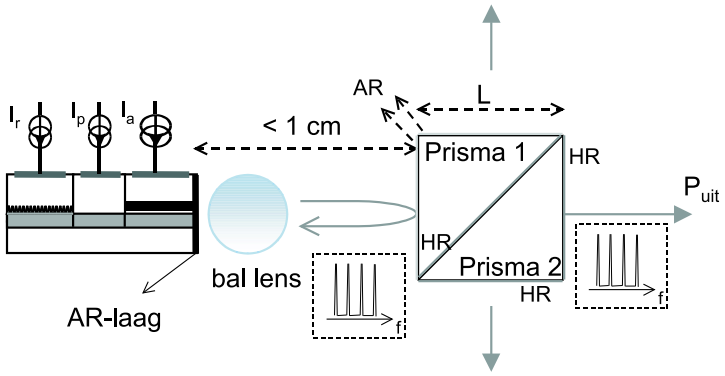

Figuur 14: Schematische voorstelling van het koppelen van een laser met het filter via een ballens.

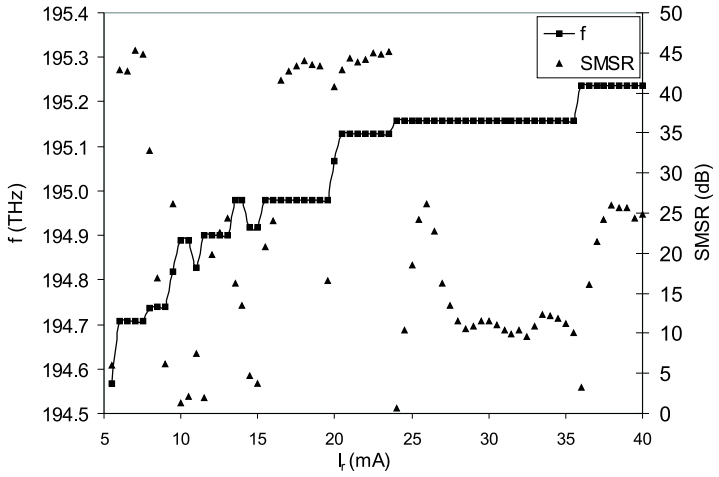

Figuur 15: Experimenteel bepaalde laserfrequentie (vierkanten) en zijmode-onderdrukking (driehoeken) als functie van reflector stroom voor een drie-sectie DBR afstembare laser onderhevig aan optische terugkoppeling van een stabiel periodiek filter (I_a = 100 mA en I_p = 2 mA).

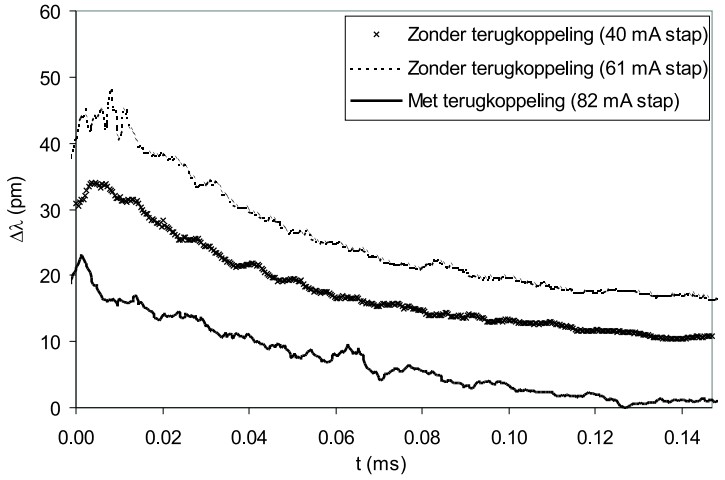

Figuur 16: Experimenteel bepaalde verloop in tijd van de afwijking van de laser golflengte van zijn eindwaarde na het schakelen, met en zonder terugkoppeling van het filter. I_r werd geschakeld tussen 0 mA en 40 mA (kruisjes) en 0 mA en 61 mA (stippellijn) respectievelijk voor het geval zonder terugkoppeling en tussen 0 mA en 82 mA (vette lijn) voor het geval met terugkoppeling (I_a = 100 mA en I_p werd aangepast om een maximale SMSR te bekomen in beide gevallen).

golflengteschakelgedrag kan verbeterd worden, hebben we enkel twee stabiele werkingspunten met hoge SMSR nodig. We willen ook nog benadrukken dat de afstemtabel werd opgemeten zonder dat de laser was opgenomen in een controle lus, zoals normaal gezien het geval is [21]. Mede hierdoor ligt de SMSR niet boven 40 dB voor alle frequentie plateaus.

Figuur 16 toont het experimenteel bepaalde verloop in tijd van de afwijking van de laser golflengte van zijn eindwaarde na het schakelen, opnieuw met en zonder terugkoppeling. De reflector stroom I_r werd geschakeld tussen 0 mA en 40 mA (kruisjes) en 0 mA en 61 mA (stippellijn) respectievelijk voor het geval zonder terugkoppeling en tussen 0 mA en 82 mA (vette lijn) voor het geval met terugkoppeling I_a = 100 mA en I_p werd aangepast om een maximale SMSR te bekomen in beide gevallen. Het blijkt duidelijk dat de golflengtedrift sterk verminderd wordt door de terugkoppeling, ook al is de grootte van de stroomstap 30 % respectievelijk 100 % groter dan in het geval zonder terugkoppeling. De maximale afwijking werd met meer dan 50 % ver-

minderd (van 6 GHz naar minder dan 3 GHz) en de eindwaarde werd veel sneller bereikt (na 0.1 ms i.p.v. na 2 ms). Dit kan nog verder verbeterd worden door de FSR van het filter, de externe caviteitslengte en de breedte van de Bragg piek van de laser nauwkeurig op elkaar af te stemmen.

4.3 Besluit

In dit deel hebben we numeriek en experimenteel aangetoond dat het golflengteschakelgedrag van afstembare halfgeleiderlasers kan worden verbeterd door de laser te stabiliseren op (de pieken) van een periodiek referentie filter. Een verdere verbetering is mogelijk door de FSR van het filter, de externe caviteitslengte en de breedte van de Bragg piek van de laser beter op elkaar af te stemmen. Een bijkomend voordeel van het gebruik van het filter is dat het opstellen van een afstemtabel wordt vereenvoudigd en dat de invloed van component degradatie of onnauwkeurigheden in de afstemtabel verminderd wordt.

5. Degradatie van afstembare lasers – Monitoring en actualisatieprocedure voor de afstemtabel

In dit deel zullen we de uitdagingen en problemen omtrent het degraderen, monitoren en updaten van afstembare halfgeleiderlaser bronnen. We zullen kort uitleggen wat degradatie van halfgeleider materialen inhoudt en ook enkele technieken beschrijven om het uitgangsvermogen, de emissie golflengte en de zijmode onderdrukking te monitoren. Het belangrijkste deel is echter gewijd aan het ontwikkelen van een strategie om de afstemtabel van een verouderde afstembare laser te actualiseren, enkel gebruik makend van de beperkte informatie beschikbaar uit de verandering in de afstemkarakteristieken van één enkel kanaal (nl. het kanaa1 waarop de laser heeft gewerkt).

5.1 Context

Afstembare halfgeleiderlasers zijn zoals reeds vermeld veelbelovende kandidaten voor vele nuttige toepassingen in huidige en toekomstige telecommunicatie netwerken. De betrouwbaarheidscriteria voor zulke netwerken zijn echter zeer streng. Uitgangsvermogen, golflengte en zijmode onderdrukking moeten op de vereiste waarden gehouden worden om signaal degradatie en overspraak te vermijden. Dit houdt o.a.

in dat de relatie tussen deze grootheden enerzijds en de afstemstromen anderzijds altijd correct moet blijven. De waarden van de afstemstromen corresponderend met een bepaald kanaal (en de ermee corresponderende golflengte, uitgangsvermogen en zijmode onderdrukking) zijn opgeslagen in de afstemtabel van de laser. Anders gezegd, wanneer de waarden van de afstemstromen die in de afstemtabel staan, worden toegepast, moet de laser werken op de juiste golflengte, met een voldoend hoog uitgangsvermogen en een hoge zijmode onderdrukking (tenminste 40 dB). Degradatie van de actieve sectie van een (afstembare) halfgeleiderlaser kan een vermindering van het uitgangsvermogen veroorzaken. Dit stelt echter meestal geen probleem, aangezien dit eenvoudig kan gedetecteerd worden en verholpen kan worden door simpelweg de actieve laser stroom te verhogen. Voor afstembare laser stelt zich een ander, meer serieus probleem. Degradatie van de afstemsecties kan een aanzienlijke verandering van de golflengte versus afstemstroom karakteristieken veroorzaken, wat leidt tot een verminderde golflengte (optische frequentie) nauwkeurigheid en een afname van de zijmode onderdrukking. Daarom is een procedure die – liefst op een geautomatiseerde manier– de afstemtabel kan actualiseren een vereiste opdat afstembare lasers in een telecommunicatie netwerk zouden kunnen gebruikt worden.

5.2 Degradatie

Lasers voor (lange–afstand WDM) optische telecommunicatienetwerken worden gemaakt uit (een combinatie) van het III–V halfgeleider materiaal InGaAsP/InP en dit in een begraven hetero–structuur waarbij de twee materialen (met verschillende bandkloof) tezamen worden gestapeld. In een multi-sectie afstembare halfgeleiderlaser hebben de afstemsecties dezelfde structuur als de actieve sectie, maar met een andere samenstelling en een verschillende bandkloof. Een gevolg van het gebruik van halfgeleider materialen is dat deze lasers nadelige degradatie fenomenen vertonen [61, 62, 63, 64, 65] en dit zowel voor de actieve als de passieve secties. In de volgende twee secties zullen we de degradatie van de actieve en passieve secties afzonderlijk behandelen.

5.2.1 Degradatie van actieve laser secties

Degradatie van de actieve sectie veroorzaakt een toenamen van de drempelstroom en een afname van de externe differentiële quantum efficiëntie [61, 66, 67, 68]. Deze veranderingen zijn echter beperkt en ver-

mits een afname van het uitgezonden optisch vermogen zoals reeds vermeld eenvoudig kan verholpen worden, vormt degradatie van de actieve sectie niet echt een probleem voor het gebruik van afstembare halfgeleiderlasers in telecommunicatie netwerken. Levensduren tot 10^6 uur voor een uitgangsvermogen van 5 mW bij een temperatuur van 25 °C zijn haalbaar [62].

5.2.2 Degradatie van passieve laser secties

Daar waar degradatie van de actieve sectie het langdurig gebruik van een halfgeleiderlaser in een netwerk niet verhinderd, vormt het degraderen van de passieve secties wel een belangrijk probleem voor het gebruik van afstembare lasers in een netwerk omgeving. Dit is vooral omdat de degradatie een verandering van de afstemkarakteristieken veroorzaakt [61, 62, 63, 64, 65]. Dit betekent dat bij toepassing van de stroomwaarden in de afstemtabel –die opgesteld is voor het degraderen van de laser– het resulterende werkingspunt hoogst waarschijnlijk de verkeerde golflengte zal hebben en een te lage zijmode onderdrukking. Dit is geïllustreerd in figuur 17 en 18 waar de golflengte en zijmode onderdrukking van een drie–sectie DBR laser zijn getoond als functie van de stroom door de reflector sectie, zowel voor als na degradatie van de reflector sectie. Deze resultaten werden bekomen via simulaties. De actieve stroom was 100 mA (corresponderend met een uitgangsvermogen van 18 mW), er vloeide geen stroom door de fase sectie. De laser werkt meestal in het midden van een golflengte plateau in de afstem karakteristiek, waar de zijmode onderdrukking maximaal is t.o.v. de naburige werkingspunten. Veronderstel dat het originele werkingspunt van de laser punt A was en dit voor een periode waarin de laser is gedegradeerd tot op het punt dat de bovenste afstemkarakteristiek (stippellijn) geldig is. Zolang de laser op het golflengtekanaal corresponderend met A blijft werken, houdt het controlesysteem van de laser hem op de correcte golflengte en zijmodeonderdrukking door de afstemstromen zodanig aan te passen dat de veranderingen veroorzaakt door de degradatie (of andere externe invloeden zoals een veranderende omgevingstemperatuur) tegengewerkt worden [69]. Indien echter op een bepaald moment beslist wordt om het werkingspunt te veranderen naar b.v. punt B, treden er problemen op. Aangezien de originele afstemkarakteristiek (volle lijn) niet langer geldig is, zou de laser naar een punt op de nieuwe karakteristiek schakelen, heel dicht

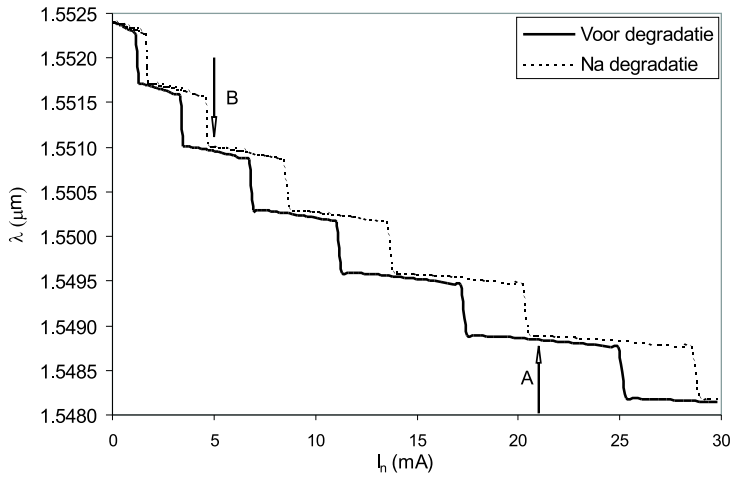

Figuur 17: Laser golflengte vs. afstemstroom voor een drie–sectie DBR laser, voor en na degradatie van de reflector sectie.

bij een mode sprong (figuur 17) en met een onaanvaardbaar lage zijmodeonderdrukking (figuur 18).

Figuur 19 toont ook het uitgangsvermogen voor en na degradatie. Het blijkt duidelijk dat degradatie van de afstemsecties niet veel invloed heeft op het uitgangsvermogen: zelfs in punt B is het verschil in uitgangsvermogen nog geen 5 %. De resultaten getoond in figuur 17, 18 en 19 zijn geen experimenteel bepaalde data, maar zijn bekomen uit simulaties. De reden hiervoor is dat, in tegenstelling tot een commercieel laser bedrijf, wij noch genoeg lasers, noch de infrastructuur hebben om experimentele degradatietesten uit te voeren. Bovendien zijn experimentele degradatie data een heel gevoelig iets wat bedrijven –om voor de hand liggende redenen– niet zomaar willen distribueren. De simulaties zijn uitgevoerd met software die is ontwikkeld op de vakgroep INTEC [21]. Zowel actieve als passieve sectie degradatie wordt veroorzaakt door een toename van de niet-radiatieve recombinatie, te wijten aan het ontstaan van defecten [61, 62, 63]. Bijgevolg, kan het degradatieproces gesimuleerd worden door de waarde van de niet-radiatieve recombinatie parameter A te verhogen van b.v. 10^8 s^{-1} naar $1.5x10^8$ s^{-1}, waarden die overeenkomen met experimentele data [65]. De geldigheid van de simulaties wordt bewezen door het feit dat de resultaten getoond in figuur 17, 18 en 19 zeer goed overeenstemmen met gepubliceerde experimentele resultaten [62, 63, 64, 65].

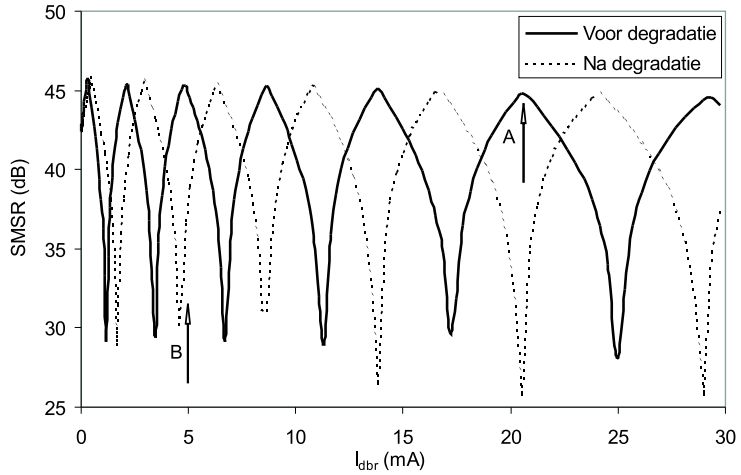

Figuur 18: Zijmodeonderdrukking vs. afstemstroom voor een drie–sectie DBR laser, voor en na degradatie van de reflector sectie.

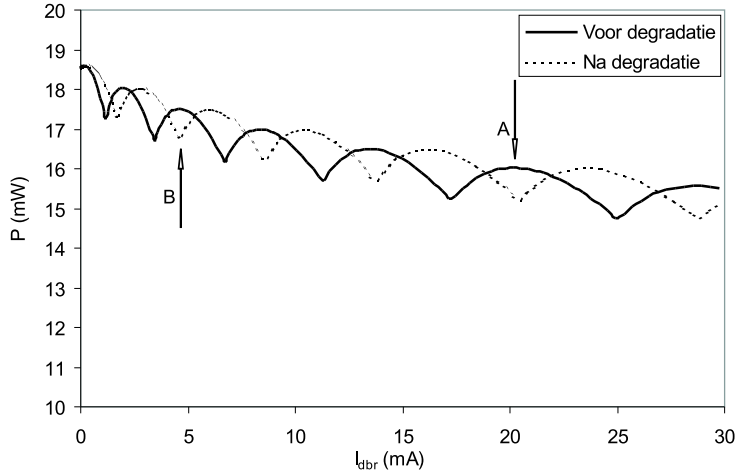

Figuur 19: Uitgangsvermogen vs. afstemstroom voor een drie–sectie DBR laser, voor en na degradatie van de reflector sectie.

Degradatie van de actieve en passieve secties beïnvloeden elkaar niet. Dit betekent dat degradatie van de actieve sectie een verwaarloosbaar effect heeft op de afstemkarakteristieken en dat degradatie van de passieve secties een verwaarloosbaar effect zal hebben op de lichtkarakteristieken (dit is het uitgangsvermogen in functie van de actieve stroom) [62]. De degradatie van de passieve secties hangt af van de stroomdichtheid door die secties: hoe hoger de dichtheid, hoe groter de verandering van de afstemkarakteristieken [62, 63, 64, 65]. Uit talrijke (versnelde) degradatietesten is gebleken dat na een zekere tijd de drift door degradatie vermindert [63, 64, 65, 67]. De nadelige invloed van degradatie kan dus verminderd worden indien de laser eerst onderworpen wordt aan een aangepaste stress test. Er zal echter steeds een zekere drift blijven bestaan. En aangezien in huidige netwerken een frequentie nauwkeurigheid van enkele GHz vereist is, is een actualisatie procedure voor de afstemtabel vereist. Dit zal in meer detail worden besproken in sectie 5.4.

5.3 Monitoren van afstembare transmitters

Wanneer een laser of een andere component in een telecommunicatie netwerk wordt gebruikt, is het heel belangrijk dat zijn karakteristieken (uitgangsvermogen, laser golflengte, zijmodeonderdrukking, ...) binnen bepaalde gespecifiëerde limieten blijven. Degradatie of omgevingsinvloeden kunnen er echter een onaanvaardbare verandering van de karakteristieken veroorzaken. Het is dan ook heel belangrijk de systeem performantie te monitoren om in staat te zijn (beperkte) veranderingen in de karakteristieken te detecteren en op te vangen. Dit laatste gebeurt meestal door één of andere vorm van terugkoppeling. Monitoren is vooral nuttig bij het opvangen van trage, graduele veranderingen in de performantie van een component. Wanneer plotse of grote fouten optreden, duidt dit meestal op een defecte component die vervangen moet worden. In dit geval kan monitoren helpen om de component in kwestie te lokaliseren.

5.3.1 Monitoren van het uitgangsvermogen

Het vermogen kan eenvoudig gemonitored worden m.b.v. een detector. Deze zijn meestal geïntegreerd in de verpakking van een commerciële laser. Een kleine fractie P_m wordt afgetapt en het vermogen wordt dan gestabiliseerd door correcties toe te voegen aan de stroom door

de actieve sectie evenredig met $(P_{ref} - P_m)$ met P_{ref} evenredig met het gewenste uitgangsvermogen.

5.3.2 Monitoren van de golflengte

Hiervoor worden vaak optische filters gebruikt om de golflengtevariaties om te zetten in vermogenvariaties [70, 71, 72]. Hiervoor zijn uiteraard heel stabiele filters vereist die weinig gevoelig zijn aan veranderende omgevingscondities. Aangezien een afstembare laser op meerdere (periodiek gespatiëerde) golflengtes kan werken, is een filter met een hele brede karakteristiek of een periodiek filter nodig. Een Fabry Perot etalon heeft een inherente periodieke transmissiekarakteristiek en wordt vaak gebruikt als periodieke golflengte referentie en zijn commercieel beschikbaar [73]. In dergelijke componenten wordt een kleine fractie ($\approx 5\%$) van het laser licht afgetapt voor het controleren van de laser golflengte. Deze fractie wordt verdeeld in een deel dat direct wordt gedetecteerd (P_1) en een deel dat eerst door een hoog stabiel Fabry Perot etalon wordt gestuurd voor detectie (P_2). De functie $log(\eta P_2/P_1)$, met η een calibratie factor, is dan vrij lineair als functie van de frequentie in de buurt van een ITU frequentie en gaat door nul bij die frequentie voor een correcte waarde van η [69]. Deze functie kan gebruikt worden om de golflengte te monitoren en de golflengte kan gestabiliseerd worden door correcties evenredig met $log(\eta P_2/P_1)$ aan de fase stroom toe te voegen. Het ongefilterde vermogen P_1 kan bovendien gebruikt worden om het uitgangsvermogen van de laser te controleren. In [74] wordt een golflengte monitor voorgesteld die samen met een afstembare laser op één enkele chip kan gefabriceerd worden.

5.3.3 Monitoren van de zijmodeonderdrukking

Een mogelijke methode om de zijmodeonderdrukking te monitoren steunt op het feit dat wanneer een zijmode naast de hoofdmode in het laser spectrum aanwezig is, er een hoog frequente zwevingscomponent in de gedetecteerde intensiteit aanwezig zal zijn. Hoe sterker de zijmode, hoe sterker het zwevingssignaal. Aangezien het frequentie verschil tussen de modes van een afstembare halfgeleiderlaser typisch van de orde van enkele tientallen GHz is, moet de detector een voldoende hoge bandbreedte hebben. En zelfs dan kunnen enkel zijmodes gedetecteerd worden die naast de hoofdmode liggen. Normaal gezien zijn dit echter ook de sterkste zijmodes, en dus ook diegene die

het belangrijkst zijn om te monitoren en te onderdrukken. De zijmodeonderdrukking kan ook afgeleid worden uit het vermogen in de zijmodes die het dichtst bij de hoofdmode gelegen zijn. Immers, als dit vermogen minimaal is, is de zijmodeonderdrukking maximaal. Hiervoor kan opnieuw de component beschreven in [73] gebruikt worden. Als we veronderstellen dat de golflengte van de hoofdmode λ_{MM} op de ITU–grid ligt, zal P_2 maximaal zijn en dus een maat zijn voor het vermogen in de hoofdmode P_{MM}. P_1 is natuurlijk een maat voor het totale uitgangsvermogen P_{tot}. Aangezien $P_{tot} = P_{MM} + P_{SM}$, met P_{SM} het vermogen in de zijmodes en aangezien $P_{tot} = aP_1$ en $P_{MM} = bP_2$, zal $P_{SM} = aP_1 - bP_2$ met a en b calibratie factoren. De zijmodeonderdrukking kan dus maximaal gehouden worden door de afstemstromen zo aan te passen dat $(aP_1 - bP_2)$ minimaal blijft. Deze redenering is natuurlijk maar correct, zolang de zijmodes niet op de ITU-grid liggen, omdat anders P_{SM} ook (gedeeltelijk) door het filter zou gaan. Gelukkig is dit meestal het geval voor de gangbare afstembare lasers.

5.4 Actualisatieprocedure voor de afstemtabel

In deze sectie zullen we een procedure beschrijven om de afstemtabel van een gedegradeerde laser te actualiseren, en dit zonder de laser uit het netwerk te verwijderen. De tabel zal niet volledig opnieuw opgesteld worden zoals wanneer de laser voor de eerste keer werd gekarakteriseerd voor gebruik [69]. De bestaande tabel zal worden geactualiseerd a.h.v. de informatie die beschikbaar is uit de geobserveerde, door degradatie veroorzaakte wijzigingen in de afstemkarakteristieken. Deze wijzigingen kunnen geëxtraheerd worden uit de wijziging van de afstemstromen die ontstaat wanneer het controle systeem van de laser [69] de door de degradatie veroorzaakte golflengte drift probeert tegen te werken. Het verloop van de afstemstromen in de tijd kan eenvoudig worden bijgehouden door de micro–processor waarmee een commerciële transmitter gebaseerd op een afstembare laser steeds mee is uitgerust. In de meeste gevallen is enkel informatie over de degradatie van één enkel kanaal —namelijk het kanaal waarop de laser heeft gewerkt— beschikbaar om de tabel te actualiseren. Maar, zoals reeds vermeld, is het heel belangrijk dat de volledige afstemtabel wordt geactualiseerd. Aangezien de enige informatie waarover we beschikken de door de degradatie veroorzaakte wijziging van de afstemstromen ΔI voor een bepaald golflengtekanaal is, moeten we zoeken naar een relatie tussen de golflengte en de afstemstromen. Het blijkt dat volgende

uitdrukking kan bekomen worden uit de relatie tussen de stroom I door een afstemsectie en de corresponderende ladingsdichtheid N:

$$\Delta I = eV \cdot \Delta A \cdot N' \cdot \delta\lambda \tag{3}$$

Hierin is e de eenheid van elektrische lading, V het volume van de afstemsectie en ΔA de verandering van de niet–radiatieve recombinatie parameter A. Verder is $\delta\lambda = \lambda - \lambda_0$ met λ_0 de golflengte corresponderend met een afstemstroom nul, $N' = (dN/d\lambda)|_{\lambda_0}$ en n_0=I_0=0. Bij de afleiding van (3) werd er rekening mee gehouden dat de verandering van de afstemkarakteristieken veroorzaakt wordt door een toename van de niet-radiatieve recombinatie en dus door een verandering ΔA van A [61, 62, 63, 67]. Voor meer details m.b.t. de afleiding verwijzen we naar de Engelstalige tekst. Uit vergelijking (3) blijkt duidelijk dat de verhouding $\Delta I/\delta\lambda$ constant is. Dit betekent dat als ΔI_i gekend is voor een bepaalde golflengte drift $\delta\lambda_i$ (corresponderend met een bepaald kanaal i), we dan automatisch $\Delta I_j/\delta\lambda_j$ en dus ΔI_j kennen voor alle andere kanalen j. We willen opmerken dat $\delta\lambda$ in vergelijking (3) staat voor de verschuiving van de Bragg golflengte $\delta\lambda_B$ wanneer een DBR sectie beschouwd wordt, of voor de verschuiving van het spectrum van de caviteitsmodes $\delta\lambda_p$ wanneer een fase sectie beschouwd wordt. In een praktische situatie zijn $\delta\lambda_B$ en $\delta\lambda_p$ meestal niet gekend. Maar aangezien the laser golflengte die is van de caviteitsmode die het dichtst bij het centrum van de Bragg piek is gelegen en sinds we toch te maken hebben met vrij kleine golflengte verschuivingen, kan $\delta\lambda_B$ bepaald worden uit de $\lambda - I_{dbr}$ karakteristiek voor een bepaalde waarde van I_p (diegene corresponderend met het werkingspunt van de laser). Analoog kan $\delta\lambda_p$ bepaald worden uit de $\lambda - I_p$ karakteristiek voor een bepaalde waarde van I_{dbr} (diegene corresponderend met het werkingspunt van de laser). De $\lambda - I_{dbr}$ en $\lambda - I_p$ karakteristieken kunnen gemakkelijk afgeleid worden uit de $\lambda - I_{dbr} - I_p$ karakteristiek, die opgeslagen wordt in de afstemtabel tijdens de karakterisatieprocedure van de laser. Het algoritme afgeleid van vergelijking (3), dat zonet beschreven werd, zal hierna geïllustreerd worden a.h.v. enkele simulatie resultaten.

In [65] werd voor een laser met één afstemsectie experimenteel aangetoond dat bovenstaand algoritme werkt. De meeste afstembare lasers hebben echter twee of meer afstemsecties. Het is daarom belangrijk te controleren of het algoritme ook voor dergelijk lasers kan gebruikt worden. In figuur 20 en 21 is een simulatie resultaat getoond voor een drie–sectie DBR laser waarvan zowel de reflector als de fase sectie gedegradeerd zijn (voor beide secties werd A verhoogd van 10^8 s^{-1}

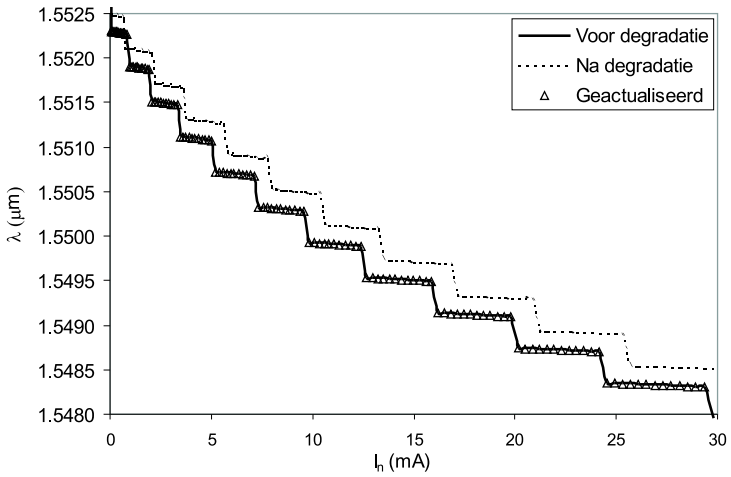

Figuur 20: Laser golflengte vs. afstemstroom voor een drie–sectie DBR laser, voor en na degradatie van de reflector en de fase sectie, en na actualisatie van de afstemtabel.

naar 1.5x10^8 s^{-1}, I_p was 5 mA). Opnieuw wordt een deel van de afstemtabel getoond (laser golflengte en zijmodeonderdrukking versus de stroom door de reflector sectie), voor (volle lijn) en na (stippellijn) degradatie. De driehoekige symbolen stellen hetzelfde deel van de afstemtabel voor, maar nu voor de gedegradeerde laser met geactualiseerde waarden voor de afstemstromen, bekomen via het hierboven beschreven algoritme. Een nagenoeg perfecte overeenkomst tussen de originele en de geactualiseerde afstemtabel wordt bekomen. In praktische gevallen zal de verandering van A zelfs niet zo groot zijn als degene gebruikt in de simulaties, vermits zoals reeds vermeld de laser een stress test heeft ondergaan.

Voor de volledigheid toont figuur 22 dat ook de relatie tussen het uitgangsvermogen en de afstemstromen kan hersteld worden a.h.v. hetzelfde algoritme.

In al deze resultaten was slechts één ΔI (corresponderend met het kanaal waarop de laser werkte) nodig per afstemsectie om de volledige golflengte versus afstemstroom karakteristiek voor die sectie te actualiseren. Uit bovenstaande resultaten volgt duidelijk dat de afstemtabel van een afstembare laser volledig kan geactualiseerd worden a.h.v. het zeer eenvoudige algoritme dat hierboven beschreven is. Ook voor lasers met meer dan twee afstemsecties kan hetzelfde algoritme op een

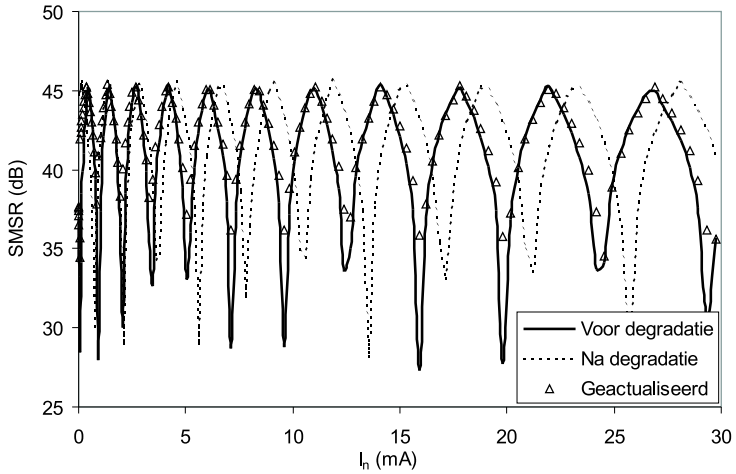

Figuur 21: Zijmodeonderdrukking vs. afstemstroom voor een drie–sectie DBR laser, voor en na degradatie van de reflector en de fase sectie, en na actualisatie van de afstemtabel.

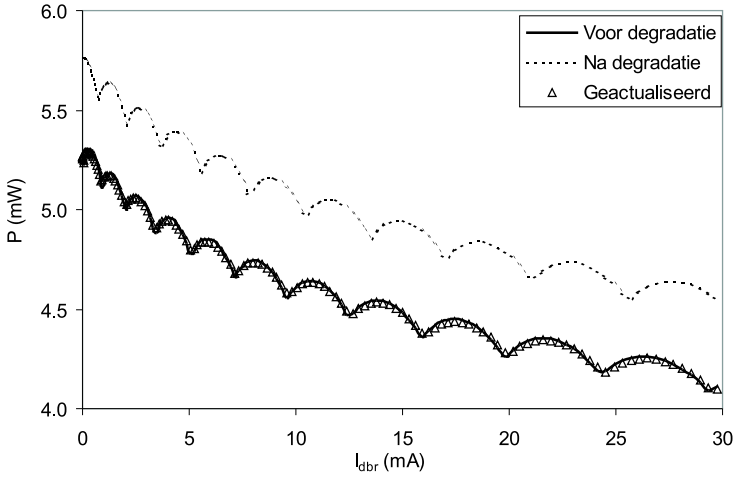

Figuur 22: Uitgangsvermogen vs. afstemstroom voor een drie–sectie DBR laser, voor en na degradatie van de reflector en de fase sectie, en na actualisatie van de afstemtabel.

voor de hand liggende manier toegepast worden aangezien de onderliggende fysische processen steeds dezelfde zijn.

5.5 Besluit

In dit deel hebben we de verschillende degradatie mechanismen die optreden in afstembare lasers uitgelegd. Er werden technieken beschreven om de performantie van afstembare lasers te controleren. Verder werd ook een procedure beschreven die toelaat op een automatische manier de afstemtabel van een afstembare laser te actualiseren. Hierbij wordt een nagenoeg perfecte overeenkomst tussen de originele en de geactualiseerde afstemtabel behaald.

6. Versterker

In dit deel onderzoeken we de invloed van een (geïntegreerde) optische versterker op belangrijke laser karakteristieken zoals de RIN, de lijnbreedte en de SMSR. Er wordt theoretisch, numeriek en experimenteel aangetoond dat de RIN en de lijnbreedte aanzienlijk kunnen toenemen tengevolge van de versterkte spontane emissie (ASE) afkomstig van de versterker die in de laser wordt geïnjecteerd. De SMSR daarentegen zal afnemen en dit door een toename van de spontane emissie die in de zijmode(s) inkoppelt, opnieuw tengevolge van de ASE van de versterker. Zowel de toename van de RIN en de lijnbreedte als de afname van de SMSR worden groter naarmate de versterking toeneemt.

6.1 Context

Veel van de geavanceerde laser diodes die gebruikt worden in de transmitter modules voor (lange-afstand) telecommunicatie netwerken hebben een beperkt uitgangsvermogen. Zo bevatten (breed-) afstembare laser diodes [74, 75, 76, 77, 78, 79, 80] vaak passieve afstemsecties aan één of beide zijden van de actieve sectie die een deel van het licht uitgezonden door de actieve sectie absorberen. Multi-golflengte lasers [81, 82] bestaan vaak uit een laser rij en een koppelaar die het licht van de individuele lasers combineert en die aanzienlijke verliezen introduceert. Omwille van de absorptie en verliezen die in deze lasers optreden, wordt dikwijls een optische versterker met deze componenten geïntegreerd. We zullen echter aantonen dat hierdoor zowel de

ruiskarakteristieken (de RIN en de lijnbreedte [17, 18, 19]) als de spectrale karakteristieken (de SMSR) van de laser aanzienlijk kunnen gedegradeerd worden. Deze degradatie kan natuurlijk ook optreden wanneer de laser verbonden is met een aparte versterker zonder isolator ertussen, net zoals voor een laser die direct verbonden is of geïntegreerd met een op een optische versterker gebaseerde golflengte convertor [83].

6.2 Theoretische modellering

In deze sectie zullen we kort het theoretisch model bespreken dat kan gebruikt worden om een analytische uitdrukking voor de RIN, lijnbreedte en SMSR van een laser verbonden met een optische versterker af te leiden. Voor meer details verwijzen we naar de Engelstalige tekst.

De afleiding vertrekt van een set verbeterde balansvergelijkingen die meer algemeen geldig zijn dan de conventionele balansvergelijkingen die b.v. in [17] kunnen gevonden worden. De afleiding van de meer algemene balansvergelijkingen uit de dynamische gekoppelde-golf vergelijkingen kan gevonden worden in [84]. De invloed van de versterker op de laser bestaat uit (achterwaarts propagerende) ASE die in de laser wordt geïnjecteerd. Dit wordt in rekening gebracht door in de algemene balansvergelijkingen een Langevin-functie op te nemen die de ASE karakteriseert. De RIN en de lijnbreedte kunnen dan bepaald worden uit de frequentieafhankelijke klein-signaal oplossingen van de balansvergelijkingen. De SMSR kan bepaald worden door de toename van het vermogen in een zijmode in aanwezigheid van ASE te bepalen. Voor meer details verwijzen we naar de Engelstalige tekst. Het blijkt dat zowel de toename van de RIN en de lijnbreedte als de afname van de SMSR door een zelfde (vereenvoudigde) factor bepaald wordt:

$$\frac{RIN^{SOA}}{RIN^{noSOA}} = \frac{\Delta\nu^{SOA}}{\Delta\nu^{noSOA}} = \frac{SMSR^{noSOA}}{SMSR^{SOA}} = \left[1 + \frac{\eta}{a}\frac{A-1}{\ln(A)}\right] \qquad (4)$$

waarin A de versterking is van de versterker, η een constante en a een factor die de sterkte van de ASE die in de laser wordt geïnjecteerd beschrijft.

We hebben de invloed van een optische versterker op de laser karakteristieken ook numeriek en experimenteel onderzocht. De behaalde resultaten worden in de volgende secties getoond en bevestigen de theoretische resultaten (en dus ook de geldigheid van de theorie).

6.3 Toename van de RIN en de lijnbreedte

6.3.1 Simulatie resultaten

De simulaties werden opnieuw uitgevoerd met de laser simulatie software van VPI [56]. De RIN en lijnbreedte werden berekend voor een 400 μm $\lambda/4$-verschoven DFB laser met anti-reflectie lagen op de facetten, eens met en zonder een geïntegreerde halfgeleider optische versterker (SOA). De laser heeft een genormaliseerde koppelingscoëfficiënt κL_d = 2. De SOA is 350 μm lang, heeft een versterking A = 16 dB en heeft eveneens anti-reflectie lagen op de facetten. De inversiefactor van zowel de laser als de SOA is 2.

Figuur 23 en 24 tonen de RIN respectievelijk de lijnbreedte voor een toenemend ASE vermogen P_{ase} dat in de laser wordt geïnjecteerd, en dit voor een laser uitgangsvermogen van 2 en 5 mW respectievelijk. Deze waarden corresponderen met het uitgangsvermogen van de afzonderlijke laser, zonder aanwezigheid van de versterker. We willen ook opmerken dat de numerieke waarden van P_{ase} in de figuur overeenstemmen met het totale ASE vermogen dat door de versterker wordt uitgezonden wanneer geen laser aanwezig is en dit is verschillend van het ASE vermogen dat in de laser koppelt. De stroom door de versterker werd constant gehouden en om het ASE vermogen dat in de laser werd geïnjecteerd te veranderden werd het ASE vermogen dat uit de versterker komt door een regelbare attenuator gestuurd.

De degradatie van de RIN en lijnbreedte blijkt duidelijk uit figuur 23 en 24. De RIN neemt 15 respectievelijk 16 dB toe voor een laser uitgangsvermogen van 2 en 5 mW respectievelijk voor een toename van P_{ase} van 21 dB (van –33 tot –9 dBm). De lijnbreedte neemt zowel voor een laser uitgangsvermogen van 2 als 5 mW 8.5 dB toe (van 50 tot 355 MHz en van 18 tot 126 MHz respectievelijk) voor een toename van P_{ase} van 17 dB (van –37 tot –20 dBm).

De simulatie resultaten werden ook vergeleken met de theoretische uitdrukking (4). De theoretische fits bekomen uit deze uitdrukking zijn ook getoond (voorgesteld door -th in de legende) in figuur 23 en 24. We zien een goede kwantitatieve overeenkomst tussen de theoretische en simulatie resultaten en dit voor de verschillende laser uitgangsvermogens.

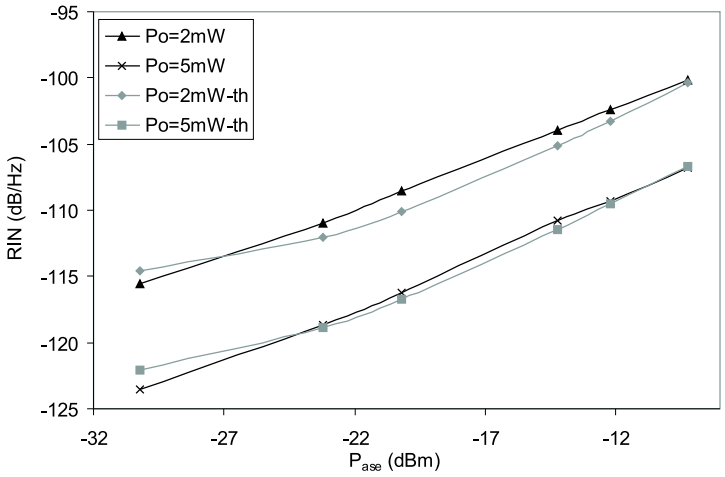

Figuur 23: Numeriek bepaalde RIN en theoretische fits versus P_{ase} van een $\lambda/4$-verschoven DFB met en zonder geïntegreerde SOA voor een laser uitgangsvermogen van 2 en 5 mW respectievelijk (P_o is het uitgangsvermogen van de afzonderlijke laser, -th duidt de gefitte theoretische resultaten bekomen via vgl. (4) aan).

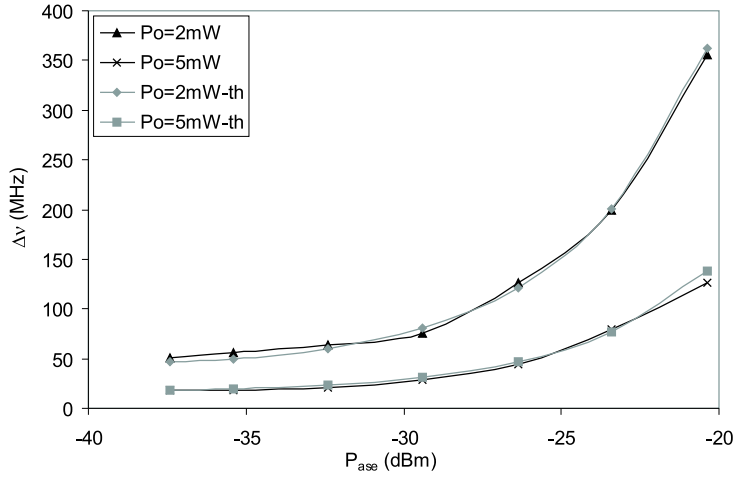

Figuur 24: Numeriek bepaalde lijnbreedte en theoretische fits versus P_{ase}van een $\lambda/4$-verschoven DFB met en zonder geïntegreerde SOA voor een laser uitgangsvermogen van 2 en 5 mW respectievelijk (P_o is het uitgangsvermogen van de afzonderlijke laser, -th duidt de gefitte theoretische resultaten bekomen via vgl. (4) aan).

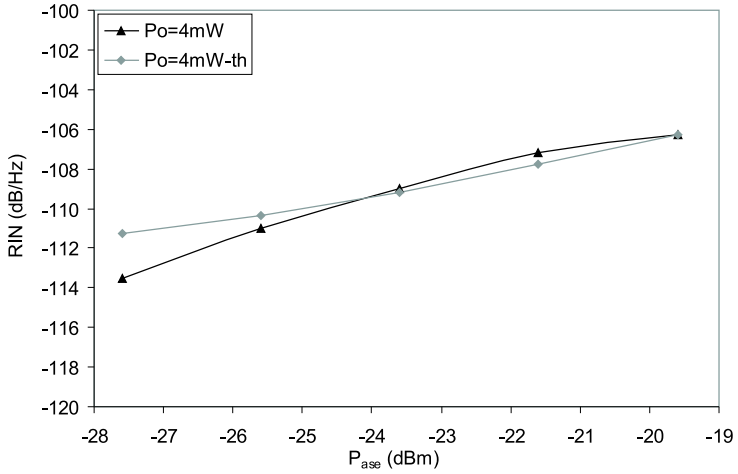

Figuur 25: Experimenteel bepaalde RIN en theoretische fits versus P_{ase} voor een laser uitgangsvermogen van 4 mW (P_o is het uitgangsvermogen van de afzonderlijke laser, -th duidt de gefitte theoretische resultaten bekomen via vgl. (4) aan).

6.3.2 Experimentele resultaten

Figuur 25 toont de experimenteel bepaalde RIN voor een toenemend ASE vermogen P_{ase}, voor een laser uitgangsvermogen van 4 mW. De gebruikte laser was een verpakte afstembare drie-sectie DBR laser met een anti-reflectie laag op het uitgangsfacet. De versterker was een polarisatie onafhankelijke SOA met een centrale golflengte van 1550 nm, een versterking van 16 dB en een ASE vermogen van -7.5 dBm. De ASE werd in de laser geïnjecteerd d.m.v. een circulator en P_{ase} werd gevariëerd d.m.v. een attenuator. Meer uitleg over de meetprocedure is te vinden in de Engelstalige tekst.

We zien opnieuw duidelijk de degradatie van de RIN wanneer P_{ase} toeneemt: voor een toename van P_{ase} van 8 dB (van –27.6 tot –19.6 dBm) is de toename van (de piek van) de RIN 7.2 dB. De theoretische fits bekomen via vergelijking (4) zijn ook getoond (voorgesteld door -th in de legende) en we zien dat er ook een goede overeenkomst is tussen de theoretische en de experimentele resultaten.

In de Engelstalige tekst worden nog verscheidene andere simulatie en experimentele resultaten getoond.

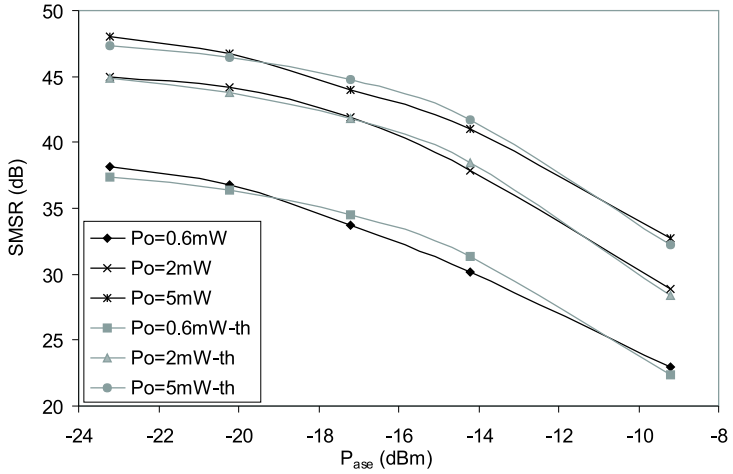

Figuur 26: Numeriek bepaalde SMSR en theoretische fits versus P_{ase} voor een laser uitgangsvermogen van 0.6, 2 en 5 mW respectievelijk (P_o is het uitgangsvermogen van de afzonderlijke laser, -th duidt de gefitte theoretische resultaten bekomen via vgl. (4) aan).

6.4 Afname van de SMSR

6.4.1 Simulatie resultaten

Figuur 26 toont de numeriek bepaalde SMSR voor een toenemend ASE vermogen P_{ase} dat in de laser wordt geïnjecteerd, en dit voor een laser uitgangsvermogen van 0.6, 2 en 5 mW respectievelijk. We zien ook hier duidelijk de degradatie van de SMSR voor toenemende P_{ase}: voor een toename van P_{ase} van 14 dB (van –23 tot –9 dBm) is de afname van de SMSR 15 dB, 16 dB en 15 dB respectievelijk. De theoretische fits bekomen via vergelijking (4) zijn ook getoond (voorgesteld door -th in de legende) en we zien ook hier een goede overeenkomst tussen de theoretische en de numerieke resultaten.

6.4.2 Experimentele resultaten

Figuur 27 toont de experimenteel bepaalde SMSR voor een toenemende P_{ase}, en dit voor een laser uitgangsvermogen van 2.3, 4.9 en 7.9 mW respectievelijk. Opnieuw zien we duidelijk de degradatie van de SMSR wanneer P_{ase} toeneemt: een toename van P_{ase} van 16 dB (van –29.5 tot –13.5 dBm) leidt tot een afname van de SMSR 7 dB, 8 dB and 7.5 dB

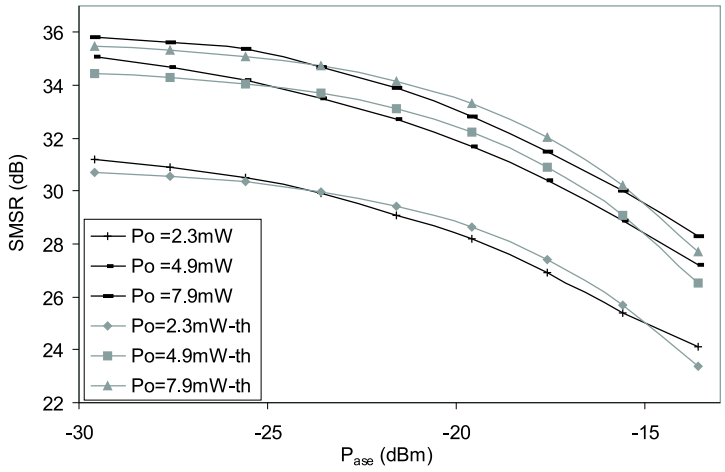

Figuur 27: Experimenteel bepaalde SMSR en theoretische fits versus P_{ase} voor een laser uitgangsvermogen van 2.3, 4.9 en 7.9 mW respectievelijk (P_o is het uitgangsvermogen van de afzonderlijke laser, -th duidt de gefitte theoretische resultaten bekomen via vgl. (4) aan).

respectievelijk. De theoretische fits bekomen via vergelijking (4) zijn ook getoond (voorgesteld door -th in de legende) en we zien ook hier een goede overeenkomst tussen de theoretische en de experimentele resultaten.

Ook voor de SMSR worden in de Engelstalige tekst nog verscheidene andere simulatie en experimentele resultaten getoond.

6.5 Besluit

In dit deel hebben we theoretisch, numeriek en experimenteel aangetoond dat de RIN, lijnbreedte en SMSR van een laser (sterk) kunnen degraderen wanneer de laser verbonden wordt met een optische versterker. Dit is te wijten aan de versterkte spontane emissie van de versterker die in de laser wordt geïnjecteerd. De degradatie wordt erger naarmate de versterking toeneemt. De nadelige invloed van de versterker kan alleen onderdrukt worden door een isolator te voorzien tussen de laser en de versterker.

7. Besluit

In dit werk hebben we enkele dynamische aspecten verbonden met multi-sectie afstembare halfgeleiderlasers grondig onderzocht. Dergelijke lasers dragen veel potentieel in zich als optische signaalbron voor huidige en toekomstige optische communicatie netwerken gebaseerd op de (D)WDM technologie. Om echter aan de strenge eisen van een netwerkomgeving te voldoen, moeten bepaalde aspecten nog onderzocht en/of opgelost worden.

Een eerste aspect betreft het golflengteschakelgedrag van deze componenten. De golflengte kan snel veranderd worden op een elektronische manier, maar jammer genoeg treden hierbij problemen op op een grotere tijdsschaal (orde micro– of zelfs milliseconden) door de thermisch geïnduceerde golflengtedrift. Er werden twee methodes voorgesteld om deze drift tegen te werken. De eerste is gebaseerd op pre–compensatie van de afstemstromen en is een zeer eenvoudige techniek, maar is jammer genoeg moeilijk te optimaliseren voor alle mogelijke schakelcombinaties. Daarom werd een nieuwe methode ontwikkeld, gebaseerd op optische terugkoppeling via een stabiel referentie filter waarmee de thermisch geïnduceerde golflengtedrift kan onderdrukt worden, onafhankelijk van welk kanaal de laser golflengte naar wordt geschakeld en onafhankelijk van de schakelgeschiedenis. Belangrijk hierbij is dat de externe caviteitslengte voldoende kort moet zijn en dat de terugkoppelingssterkte groot genoeg is om te vermijden dat de terugkoppeling de laser destabiliseert. Daartoe moest een nieuw filter ontwikkeld worden met een kamkarakteristiek in reflectie zowel als in transmissie. Het ontwerp en de karakterisatie van dit filter werd beschreven in hoofdstuk 3.

In hoofdstuk 4 werd de invloed van de optische terugkoppeling via een periodiek referentie filter (in een korte externe caviteit) op een afstembare halfgeleiderlaser onderzocht. Simulatie resultaten toonden aan dat afwijkingen tot 15 GHz onderdrukt kunnen worden door de terugkoppeling. De verbetering van het golflengteschakelgedrag werd ook experimenteel aangetoond: de maximale afwijking werd met meer dan 50 % verminderd (van 6 GHz naar minder dan 3 GHz) en de eindwaarde werd veel sneller bereikt (na 0.1 ms i.p.v. na 2 ms). Dit kan nog verder verbeterd worden door de FSR van het filter, de externe caviteitslengte en de breedte van de Bragg piek van de laser nauwkeurig op elkaar af te stemmen. Een bijkomend voordeel van het gebruik van het filter is dat het opstellen van een afstemtabel wordt vereenvoudigd en

dat de invloed van component degradatie of onnauwkeurigheden in de afstemtabel verminderd wordt.

In hoofdstuk 5 werden de verschillende degradatie mechanismen die optreden in afstembare lasers uitgelegd. Er werden technieken beschreven om de performantie van afstembare lasers te controleren. Verder werd ook een eenvoudige procedure beschreven die toelaat op een automatische manier de volledige afstemtabel van een gedegradeerde afstembare laser te actualiseren, en dit enkel op basis van de informatie die kan gehaald worden uit de verandering (door degradatie) in de afstemkarakteristieken van één golflengte kanaal. Hierbij werd een nagenoeg perfecte overeenkomst tussen de originele en de geactualiseerde afstemtabel behaald.

In hoofdstuk 6 tenslotte werd theoretisch, numeriek en experimenteel aangetoond dat de RIN, lijnbreedte en SMSR van een laser (sterk) kunnen degraderen wanneer de laser verbonden wordt met een optische versterker. Het is belangrijk met deze degradatie rekening te houden wanneer de laser in een telecommunicatie netwerk gebruikt wordt, omdat daar de RIN en lijnbreedte bij voorkeur zo klein mogelijk zijn en de SMSR zo groot mogelijk.

English text

Chapter 1

Introduction

1.1 Optical telecommunication

Sending e–mail, surfing the worldwide web, having visual contact with people you know abroad through a webcam, book a flight with a low–cost airline, download your favorite music and movies, etc... We have become so familiar with these (broadband) internet applications, that it is hard to imagine life without them anymore. All those fancy applications generate enormous amounts of data: the worldwide internet traffic is expected to grow to 1.5 million Terabits (!) per day in 2005 and this number will continue to grow exponentially in the coming years [1]. Fortunately, we can count on a worldwide telecommunication network, based on optical fibre technology to transport that huge number of bits all over the world [2]. The transport medium in these optical networks is standard single-mode fibre, which has a potential bandwidth of 25 THz, this is about 1000 times the bandwidth of the RF radio spectrum of our planet. This 25 THz bandwidth corresponds to the region of low propagation loss of optical fibre, situated around a wavelength of 1.55 μm. In this region the propagation loss can be as low as 0.1-0.2 dB/km, enabling propagation of optical signals over hundreds of kilometers (for comparison: a classical coaxial cable has a propagation loss around 30 dB/km).

The most suitable way to fully use the complete bandwidth of (installed) optical fibres is to use WDM (Wavelength Division Multiplexing): signals coming from different light sources —each at a different wavelength— are combined ('multiplexed') to one optical signal and are sent over the same optical fibre [3, 4, 5, 6, 7, 8]. The cost reduction that can be achieved deploying WDM technology is considerable: for a

connection over 500 km installing a new fibre costs $30.000 more than the introduction of 8 new wavelength channels in an already installed fibre [9]. The wavelength (or optical frequency) of WDM wavelength channels has been standardized by the International Telecommunication Union (ITU) [58]. The so–called ITU–grid consists of equally spaced frequencies, centered around 193.1 THz. Currently the frequency spacing is 100 GHz, but an evolution towards 50 GHz and even 25 GHz is expected. Today, the bit–rate per wavelength channel is typically 2.5 or 10 Gbit/s, but an evolution towards 40 Gbit/s is already noticeable [8, 11]. Each wavelength signal itself can consist of many multiplexed signals with bit-rates ranging from (multiples of) 64 kbit/s (i.e. a single digitized phone conversation) up to 10 Gbit/s (e.g. a dedicated 10 Gbit/s leased line). Furthermore, all of the multiplexed signals can have a different modulation and coding format. The data–rate per wavelength channel can be further increased by enhanced Time Division Multiplexing (TDM). Using TDM, bit–rates higher than 300 Gbit/s are expected [85]. Of course a trade-off exists between the bit–rate per channel and the channel spacing, since e.g. a channel bit–rate of 80 Gbit/s can not be combined with a channel spacing of 25 GHz.

Initially optical (WDM) technologies were only used for point–to–point transmission between network nodes in long–haul backbone networks. In each node the data are processed by electronic routers. This means that the data that travel through the optical fibres in the network first has to be converted from the optical to the electrical domain upon arrival at a network node and back to the optical domain after processing. Obviously, a major 'electronic bottleneck' is created this way. Therefore, an evolution is expected towards optical networks where there will be direct optical connections between begin and end point without electronic processing in between [3, 4, 6, 7, 8, 10, 11]. These networks will employ wavelength routing as well as optical packet/burst switching. It is expected that tunable semiconductor lasers will play an important role in these future optical network technologies [12, 13, 14]. In the next section we will discuss some general requirements for transmitters in optical networks, we will also briefly describe single mode laser diodes and more in particular tunable laser diodes.

1.2 Light sources for telecommunication

Like any communication system, optical telecommunication systems basically exist of a transmitter, a transmission medium (optical fibre)

and a receiver. In this work the focus will be on the transmitter side and more in particular on advanced multi-section tunable semiconductor lasers. In the next sections we will first describe some general requirements for lasers diodes in optical telecommunication networks, after which we will briefly describe single mode lasers and tunable lasers.

1.2.1 Requirements and specifications

Important characteristics for a telecommunication (light) source are output power, frequency accuracy, noise properties and spectral properties.

For long–haul optical fibre networks, output powers of 10 to 20 mW are required, for metropolitan area networks (with shorter propagation distances) values between 2 and 10 mW are common [15, 16].

For multi–channel systems like WDM the frequency accuracy is typically required to be better than 10 % of the channel spacing, i.e. an accuracy of 10, 5, or 2.5 GHz for a channel spacing of 100, 50 or 25 GHz respectively.

The noise properties of a laser diode are usually described by the relative intensity noise (RIN) and the linewidth parameters [17, 18, 19]. The RIN is a measure for the relative strength of the intensity fluctuations in the laser output power compared to the average intensity of the laser signal. The linewidth stands for the spectral width of the laser peak and is a measure for the phase noise of the laser signal. Obviously, the RIN and the linewidth of a laser source are preferably as low as possible when that laser is to be used as a transmitter in a telecommunication network. Typically the RIN lies well below –120 dB/Hz. The linewidth typically ranges between 1 and 100 MHz. For systems based on coherent detection the linewidth is preferably not higher than a few MHz [2].

The spectral properties are usually described by the side mode suppression ratio (SMSR). This parameter is a measure for the spectral pureness of the laser. To avoid problems caused by fibre dispersion, laser sources for (long–haul) optical communication preferably are single mode lasers, i.e. the optical power is mainly confined within the narrow frequency range of one spectral line (mode) in the laser spectrum [2]. The SMSR is defined as the ratio of the power in the main mode and that of the strongest side mode. For telecom lasers it is required that the SMSR is at least 40 dB.

It is of course very important that the performance of the laser is not degraded while it is being used, i.e. that the reliability of the laser should be sufficiently high.

1.2.2 Single mode lasers

As mentioned above, telecommunication lasers are preferably single mode lasers. The classical Fabry Perot laser–diode has multiple longitudinal modes in its spectrum. Therefore, techniques have been developed to select one of the longitudinal modes and suppress the others. This is also the case for the distributed feedback (DFB) laser, one of the most widespread optical signal sources, especially in long-haul optical networks [19]. In a DFB laser a periodic structure (a Bragg grating) is integrated on top of the active layer to enhance the wavelength selectivity of the laser cavity. The purpose of the Bragg grating is to filter out the longitudinal mode that lies around the Bragg wavelength. For an elaborated treatment, the reader is referred to [19].

DFB lasers fulfill all requirements mentioned above, they are based on a proven technology with a well established fabrication process, they have excellent wavelength stability and they are highly reliable. Unfortunately, their emission frequency cannot be tuned over a wide range. Limited tuning is possible by changing the temperature of the laser, which translates in a slow tuning speed. Due to the limited tuning range and the slow switching speed, DFB lasers are not able to meet the requirements for future optical network technologies like wavelength routing or optical packet/burst switching. Instead, tunable transmitters are required that have a wide tuning range and that can be rapidly tuned. This is discussed in the next section.

1.2.3 Tunable lasers

Tunable semiconductor lasers typically consist of multiple sections: an active section supplying the optical power and one or more passive sections enabling the tuning of the emission frequency [20, 21]. This is illustrated in figure 1.1, which show the schematic structure of a three-section distributed Bragg reflector (DBR) tunable laser, consisting of an active section, a phase section and a reflector section.

By changing the current through the reflector section, the spectral position of the Bragg peak can be changed and another longitudinal mode can be selected. By changing the current through the phase section, the optical length of the laser cavity can be changed, i.e. that the

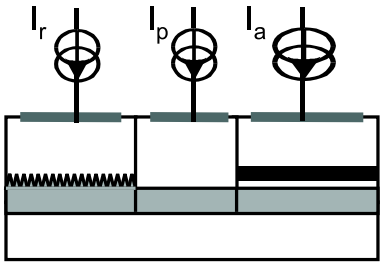

Figure 1.1: Schematic structure of a three-section DBR tunable laser.

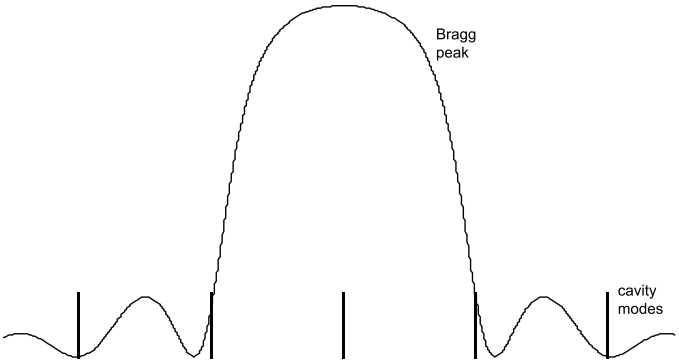

Figure 1.2: Schematic representation of the Bragg peak and the cavity modes for a three-section DBR tunable laser.

position of the entire comb spectrum of the cavity modes can be shifted. In other words, a longitudinal mode can be nicely aligned with the center of the Bragg peak by changing the phase current. This is illustrated in figure 1.2 which shows a schematic representation of the Bragg peak and the cavity modes for a three-section DBR tunable laser.

The tunable laser type shown in figure 1.1 is limited in tuning range to about 2 THz. This is obviously a lot smaller than the available fibre bandwidth. Therefore advanced tunable laser types were developed which have a wider tuning range. These lasers are usually denoted widely tunable lasers. The tuning range of widely tunable lasers is enlarged by using the Vernier effect between two comb reflectors [20, 21]. Examples of widely tunable lasers are the sampled grating DBR (SG–DBR) [86], the super–structure grating DBR (SSG–DBR) [87], the grating–assisted codirectional coupler sampled reflector laser (GCSR) [88] and the modulated grating Y–branch lasers [89]. The SG–DBR and SSG–DBR have a reflector on each side of the active section, the GCSR

uses a grating–assisted codirectional coupler tunable filter to select one of the peaks of a comb reflector (SG or SSG), with the filter and the reflector on the same side of the active section. In a Y–branch laser both reflectors are placed on the same side of the active section using a power splitter. Of course, each of these lasers also contains a phase section. It should be clear that the basic principle is always the same: an active section supplies the optical power and two or more tuning section enable tuning of the wavelength. Therefore, the simple three-section DBR tunable laser will be used as an example throughout this work to investigate some important (dynamical) aspects of multi-section tunable semiconductor lasers. The obtained results and the conclusions drawn from them will usually be equally valid for more complicated tunable lasers.

The tunable lasers discussed so far are all of the monolithic type. Other types of (widely) tunable lasers exist. As already mentioned, the wavelength of a DFB can be tuned over a limited range by changing the temperature of the device. A wider tuning range can be accessed by combining a number of DFB's (each with another output wavelength, spaced about 3 to 4 nm apart) in an array using a multimode interference coupler or a MEMS (micro–electromechanical systems) mirror. The wavelengths between those of the individual components can be accessed by changing the temperature of the whole chip, but this leads to a rather high power dissipation [14]. Another approach is a tunable vertical–cavity surface–emitting laser (VCSEL) using a movable MEMS-based top mirror. VCSELs are traditionally used at wavelengths around 850 nm and 1330 nm, unfortunately at wavelengths around 1550 nm, construction of the VCSELs is difficult [14]. Yet another example of a tunable laser is an external cavity laser incorporating a wavelength–selective filter in the external cavity. Usually, the filter is a diffraction grating and the wavelength is changed by rotating and/or translating the retro–reflecting mirror that completes the external cavity [14]. Just like the DFB array and VCSEL based tunable lasers, the external cavity lasers based on movable mirrors have the disadvantage that they cannot be used for fast wavelength switching applications. The focus of this work will therefore be on monolithic tunable lasers.

For more background on the construction of tunable lasers, tuning mechanisms and the different types of semiconductor tunable lasers etc., we would like to refer to [20, 21] and references therein.

Today, monolithic (widely) tunable lasers can be manufactured that have the same specifications as fixed–frequency DFB lasers over their whole tuning range [14]. This means that every DFB could be replaced by a tunable laser. There are however important advantages related to the use of tunable lasers instead of fixed–frequency lasers. A first one is related to inventory reduction: one tunable laser can be used as a source for different wavelength channels, so that one does not need a large inventory containing a separate DFB laser for each wavelength in the network. Another advantage is that one tunable laser can act as a back–up for several DFB's, reducing the cost for spare transmitters considerably and again simplifying inventory management. Other advantages are related to the increased flexibility that is obtained using tunable lasers: traffic fluctuations can be handled better ('bandwidth on demand') and dynamic provisioning of new services is possible [15, 16]. However, the most important advantage is that future optical network technologies based on wavelength routing and optical packet/burst switching will be feasible using (widely) tunable lasers [12, 13, 14]. This will help create the so-called "all-optical" network. The all-optical network will have an increased capacity, functionality, scalability and flexibility and will be transparent to modulation and coding formats. All these advantages hold a potential for network architecture simplification and cost–effective exploitation of networks.

1.3 Remaining issues – Goals of this work

From the previous sections it is clear that tunable semiconductor lasers are promising candidates for many very useful applications in current and future optical networks. Unfortunately, some issues remain to be solved. The first one —and probably the most important one— concerns the fast wavelength switching of these devices. For optical packet/burst switching applications, wavelength switching times in the order of a few nanoseconds are required. Semiconductor tunable lasers allow such rapid tuning but unfortunately problems occur on a larger time scale (in the order of microseconds or even milliseconds) due to the thermally induced wavelength (or optical frequency) drift. In this work, we will investigate the wavelength switching behaviour of tunable lasers and propose solutions to improve it.

Another issue is related to the degradation of (tunable) semiconductor lasers. In order to be used in a telecommunication network environment, reliability requirements are very stringent. Output power

should obviously be kept at a sufficiently high level. Furthermore the lasing wavelength should remain at its predefined value on the ITU grid throughout the device lifetime. Otherwise the emission wavelength could drift out of its assigned channel band or —in a worst-case scenario— even a mode hop could occur. Even when the wavelength (optical frequency) remains within the assigned channel band, small frequency changes (e.g. 5 GHz) already result in power changes due to the optical filtering of the signals. In both cases this would cause severe signal degradation and crosstalk, obviously to be avoided at all time. To avoid wavelength drift and mode hops, it is important that the relation between a channel wavelength and the corresponding values of the tuning currents always remains correct. I.e., when applying the values of the tuning currents that are stored in the look-up or tuning table of the laser, the laser should emit at the correct wavelength, with sufficient output power and a high SMSR (at least 40 dB). Aging of the tuning sections can cause the wavelength versus tuning current characteristics to change significantly, leading to a reduced wavelength accuracy and a decrease of the SMSR, accompanied by the problems mentioned above. Therefore, a mechanism to update —preferably automatically— the tuning table is a prerequisite for tunable lasers to be used in a telecommunication network environment. Such a mechanism will be presented in this work.

Very often an optical amplifier is integrated with a tunable laser to boost its output power. However, it still has to be investigated how this will influence important laser characteristics like the RIN, linewidth and SMSR and this is also a goal of this work.

1.4 Outline of thesis

In chapter 2 the wavelength switching behaviour of tunable semiconductor lasers will be investigated and two possible methods for improvement of the wavelength switching behaviour will be proposed and discussed. One method is based on the pre–compensation of the tuning currents, the other is based on optical feedback from a periodic reference filter. It is shown that practical implementation of the optical feedback scheme is difficult using existing filters without destabilizing the laser by the feedback. Therefore, a novel filter was developed, the design of which is described in chapter 3. In chapter 4 it is shown that the wavelength switching behaviour of a semiconductor tunable laser can be improved by stabilizing the laser through optical feedback from

the novel filter. It is shown, both numerically and experimentally, that not only the wavelength switching behaviour is considerably improved but also that the tuning characteristics are simplified, which is a nice extra, since tunable —and especially widely tunable— lasers are not that easy to control with their multiple (two to four) tuning currents.

Chapter 5 deals with the issues and problems associated with aging, monitoring and updating of tunable laser sources. Techniques to monitor the performance of a laser that is working in a network environment are described. The development of a strategy to update the complete tuning table of a tunable laser, using only the limited information obtained from the aging–induced changes in characteristics of a single channel is also described.

The influence of an (integrated) optical amplifier on the RIN, linewidth and SMSR of a (tunable) semiconductor laser is investigated in chapter 6.

Finally, in chapter 7 the main conclusions of this work will be presented and an outlook for the deployment of (widely) tunable lasers in future optical networks will be given.

1.5 Publications

The results obtained in the context of this work have been published in a number of journal papers and have been presented at various conferences.
The following papers have been published in international peer reviewed journals or are submitted for publication:

1. B. Moeyersoon, G. Morthier, R. Bockstaele, R. Baets, "Improvement of the Wavelength Switching Behaviour of Semiconductor Tunable Lasers Through Optical Feedback from a Periodic Reference Filter based on a Novel Prism-Based Implementation of a Fox-Smith Resonator," accepted for publication in *IEEE Photonics Technology Letters*, October 2005.

2. B. Moeyersoon, G. Morthier, M. Zhao, "Degradation of the mode suppression in Single Mode Laser Diodes due to integrated optical amplifiers," *IEEE Journal of Quantum Electronics*, vol. 40, pp. 241–244, March 2004.

3. Ronan ODowd, Yonglin Yu , Gavin Mulvihill, Sean ODuill, G. Morthier, B. Moeyersoon, "Transmitters for two-tier optical data-

packet labeling in advanced IP networks," accepted for publication in *IEE Proc. Optoelectronics*, June 2005.

4. G. Morthier, B. Moeyersoon, "Improvement of the direct modulation behaviour of semiconductor lasers by using a holding beam," *IEEE Photonics Technology Letters*, vol. 16, pp. 1616–1618, July 2004.

5. G. Morthier, B. Moeyersoon, "Intensity Noise and Linewidth of Laser Diodes with Integrated Semiconductor Optical Amplifier," *IEEE Photonics Technology Letters*, vol. 14, pp.1644–1646, December 2002.

6. G. Morthier, B. Moeyersoon, R. Baets, "A $\lambda/4$-shifted Sampled or Superstructure Grating Widely Tunable Twin-Guide Laser," *IEEE Photonics Technology Letters*, vol. 13, pp.1052–1054, October 2001.

The following papers have been presented at international conferences and are published in the conference proceedings:

7. B. Moeyersoon, G. Morthier, "Influence of a holding beam on the direct modulation behaviour of semiconductor lasers," Proceedings of SPIE, 5452, France, pp. 546–552 (2004).

8. B. Moeyersoon, M. Zhao, G. Morthier, "Degradation of the mode suppression in single mode laser diodes due to integrated optical amplifiers," Optical Amplifiers and Their Applications – Topical Meeting, Japan, pp. 97–99 (2003).

9. B. Moeyersoon, J. Wittebolle, G. Morthier, R. Baets, "Wavelength Switching of Semiconductor Tunable Lasers – How to Suppress Thermally Induced Wavelength Drift," 2002 IEEE/LEOS Benelux Annual Symposium, Netherlands, pp. 24–27 (2002).

10. B. Moeyersoon, G. Morthier, R. Baets, "Novel Optical Feedback Scheme for Improvement of the Wavelength Switching Behaviour of Tunable Lasers," 2002 IEEE 18th International Semiconductor Laser Conference, Germany, pp. 91–92 (2002).

11. M. Zhao, G. Morthier, J. Dekoster, B. Moeyersoon, R. Baets, "Influence of intensity noise in spectrum-sliced WDM systems," Proceedings of ONDM'01, pp. 253–261 (2001).

12. B. Moeyersoon, G. Morthier, R. Baets, ”On the Influence of Optical Feedback on the Wavelength Switching Behaviour of Tunable Lasers,” European Semiconductor Laser Workshop 2001, Belgium, (2001).

13. G. Morthier, B. Moeyersoon, R. Baets, ”A sampled or Superstructure Grating Tunable Twin-Guide laser for Wide Tunability with 2 tuning Currents”, OFC 2001, United States, p.TuB2–1/TuB2–3 (2001).

Chapter 2

Wavelength switching of tunable semiconductor lasers

In this chapter we will investigate how the wavelength switching behaviour of tunable semiconductor lasers can be improved. First we will explain how wavelength switching can be realized with a tunable laser, what the possible applications are and which problems and issues remain to be solved. We will present a theoretical model that can be used to numerically investigate the wavelength switching. Together with measurement results, this will allow us to quantitatively identify the related problems and their implications. Based on the conclusions drawn from the theoretical and numerical results, two possible methods for improvement of the wavelength switching behaviour will be proposed and discussed: pre-compensation of the tuning currents and optical feedback from a stable reference filter.

2.1 Introduction

In present (D)WDM networks most of the routing of the data packets in the crossconnects and add-drop multiplexers is done in an electronic way. This means that the data that travel through the optical fibres in the network first has to be converted from the optical to the electrical domain upon arrival at a network node. This conversion is not as easy as it sounds. As explained in chapter 1 an optical fibre typically carries several signals at different wavelengths, whereby the data-rate at each

wavelength is 2.5 Gbit/s, 10 Gbit/s or even 40 Gbit/s. Furthermore, each wavelength signal itself can consist of many multiplexed signals with bit-rates ranging from (multiples of) 64 kbit/s (i.e. a single digitized phone conversation) up to 10 Gbit/s (e.g. a dedicated 10 Gbit/s leased line). On top of that, not all the multiplexed signals have the same modulation and coding format. This means that the incoming signal first has to be de-multiplexed at least to the level of individual wavelength signals and most likely even further down to allow the different data packets to be switched. Then, after the switching electronics have determined to which output port of the node each data packet has to be transmitted, the different signals are multiplexed again and converted back to the optical domain. Bearing in mind that the transmission capacity of an optical fibre is typically 25 THz and that the speed of top of the line electronics currently is limited to 40 Gbit/s, it should be clear that a major 'electronic bottleneck' is created this way.

In order to avoid the electronic bottleneck of current network routers, and also to have a more flexible and efficient usage of the very high bandwidth capacities of the WDM technology, it is expected that future network technologies will employ wavelength routing as well as optical packet/burst switching [3, 4, 6, 7, 8, 10, 11]. This will help create the so-called "all-optical" network. The all-optical network will have an increased capacity, functionality, scalability and flexibility and will be transparent to modulation and coding formats. All these advantages hold a potential for network architecture simplification and cost-effective exploitation of networks. Obviously, rapidly (in the order of a few nanoseconds) tunable transmitters will be one of the key components for such a technology [12, 13, 14]. Some semiconductor tunable lasers allow such rapid, electronic tuning [22, 23, 24, 25, 26, 27, 28, 29, 30, 31, 32, 33], but then one encounters problems on a larger time scale (in the order of microseconds or even milliseconds) due to the thermally induced wavelength (or optical frequency) drift. This drift is due to the temperature change caused by the heating associated with the switching of the tuning currents [34, 35, 36, 37, 38, 39, 40, 41]. A consequence of the slow frequency drift is that it limits the residency time (this is the time the frequency remains within a certain band around the center channel frequency). This means that the maximum packet length in packet switching application has to be limited so that the wavelength is already switched to another wavelength before the thermal effects start to work. Still, when two or more packets have to be switched to the same output wavelength, problems due to the thermally induced

wavelength drift might occur. Another negative consequence is that in wavelength routing applications e.g. one has to wait until the steady-state wavelength is reached. Since this can take up to a few milliseconds, this is not really an option in high-speed, high-capacity networks. Furthermore, in communication systems with narrow channel spacing (nowadays the standard is 100 GHz, but an evolution towards 50 GHz or even 25 GHz is expected [58]), a signal might drift into a neighboring channel band and cause crosstalk. This is obviously to be avoided at all time.

It should be clear that it is very important to switch the channel frequency in a fast and stable way. In the following sections of this chapter we will quantify the thermally induced wavelength drift as well as propose two methods that can be used to counteract this wavelength drift.

2.2 Wavelength switching of semiconductor tunable lasers

The wavelength (or optical frequency) of a semiconductor tunable laser can be switched in a rather simple and straightforward manner, i.e. by switching one or more of the tuning currents of the laser [23]. A distinction can be made according to the time scale and the amplitude of the wavelength switching.

According to the time scale of the switching one can make a distinction between fast switching on a nanosecond scale (required for optical packet switching as already mentioned above) and (relatively) slow wavelength switching on a time scale of a few milliseconds. Wavelength switching on a millisecond timescale is for instance required for protection switching [8]. Protection switching is the substitution of a failed light path with a new working one. A light path being a signal at a certain wavelength connecting two network nodes over optical fibre. When this signal is interrupted, it is important to restore the connection as soon as possible. This is handled by the control infrastructure of the network [8], which will try to set up a new light path (at the same wavelength as the failed path). Of course, every wavelength in the network has to be protected this way. And since many wavelengths are travelling through a WDM network, it would be very expensive to supply a back-up laser for each wavelength. A tunable laser with a tuning range spanning (part of) the wavelength range of the network is a

much more cost effective solution, because it can act as a back-up laser for more than one wavelength.

According to the amplitude of the switching a distinction can be made between the switching of the optical frequency over several channel spacings (the frequency is thereby switched from one longitudinal mode to another) and the modulation of the optical frequency called Frequency Shift Keying or FSK (where the laser mode is not changed). FSK can be obtained by simply modulating one of the tuning currents, while for a frequency switch usually all tuning current have to be switched simultaneously. FSK can be used e.g. to attach a label to an optical channel in order to enhance switching of (bursts of) optical packets in DWDM networks [90]. The label information is hereby modulated in FSK format (at a moderate bit rate, e.g. 155 Mbit/s), orthogonally to the payload information (which is encoded using amplitude modulation).

In all cases it is very important to ensure, both for the operation points before and after the switch has taken place, that the wavelength is stable, that the output power has the correct value and that the SMSR is sufficiently high. A prerequisite for this is that the tuning table (containing the relation between the laser wavelength, output power and SMSR on the one hand and the tuning currents on the other hand) of the tunable laser is very accurate. Methods for constructing accurate tuning tables have already been developed [21]. Using the information in the tuning tables, the tuning currents must be switched so that stable laser operation at the desired wavelength is achieved within a few nanoseconds or milliseconds, depending on the application. How this can be achieved and how possible obstacles can be circumvented will be explained in the next sections.

2.2.1 Theoretical modelling of wavelength switching

In this section we will present a theoretical model that can be used to numerically investigate the wavelength switching of semiconductor tunable lasers. Theoretical investigation of the dynamic characteristics of semiconductor lasers is usually done using rate equations [17]. For a tunable laser, the dynamics of the optical intensity are described by the optical and electrical rate equations of the active section as well as by the electrical rate equations of the passive tuning sections. The wavelength dynamics are described by the electrical and thermal rate equations of the passive tuning sections as well as by the thermal rate equation of the active section. The model will be given for a three-section

DBR tunable laser, consisting of an active section, a phase section and a reflector section. Tunable lasers with more than two tuning sections can be treated in a similar manner and the same conclusions hold as for the device treated here.

Rate equation model

The build-up of optical power through the injection of electrical carriers in a (tunable) semiconductor laser can be described by the rate equations for the photon density S and the carrier density N_a in the active section. These equations are given by:

$$\frac{dS}{dt} = \Gamma_a v_g g_N (N_a - N_0) S + \eta B_a N_a^2 - \frac{S}{\tau_p} \tag{2.1a}$$

$$\frac{dN_a}{dt} = \frac{\sigma I_a}{eV_a} - \left(A_a N_a + B_a N_a^2 + C_a N_a^3\right) - \Gamma_a v_g g_N (N_a - N_0) S \tag{2.1b}$$

where Γ_a is the optical confinement factor of the active section, v_g is the group velocity, g_N is the linear gain coefficient, N_0 is the carrier density at transparency, η is a coefficient representing the coupling of the spontaneous emission into the lasing mode and τ_p is the photon lifetime. In the equation for the carrier density σ is the current injection efficiency, e is the unit of electron charge, V_a is the volume of the active layer and A_a, B_a and C_a are the non-radiative, bimolecular and Auger recombination coefficients of the active section respectively. Since we are mainly interested in the change of wavelength with the tuning currents, we have neglected nonlinear gain suppression in the above equations. The photon lifetime τ_p is determined by:

$$\frac{1}{\tau_p} = \frac{c}{L_c}\left\{\zeta - \frac{1}{2} ln\left(\xi^2 R_f R_d(\lambda)\right)\right\} \tag{2.2}$$

where c is the speed of light, L_c is the effective cavity length, ζ is the total absorption within the cavity, ξ is a coupling coefficient and R_f and $R_d(\lambda)$ are the power reflectivities of the facet and the DBR respectively. $1/\tau_p$ represents the total cavity loss. The effective cavity length L_c is determined by $L_c = n_a L_a + n_p L_p + n_d L_{eff}$ where n_a, n_p and n_d are the refractive indices of the active, the phase and the reflector section respectively. L_a and L_p are the lengths of the active and the phase section respectively and L_{eff} is the effective length of the DBR mirror. The total cavity absorption ζ is determined by:

$$\zeta = \Gamma_a \alpha_a L_a + \Gamma_p \alpha_p L_p + \Gamma_d \alpha_d L_{eff} \tag{2.3}$$

with Γ_p and Γ_d the optical confinement factor of the phase and reflector section respectively and α_a, α_p and α_d the internal absorption of the active, phase and reflector section respectively. The internal absorption depends on the carrier density through:

$$\alpha_i = \alpha_{0,i} + \xi \Gamma_i \frac{d\alpha_i}{dN_i} N_i \tag{2.4}$$

From this equation it is clear that the photon density in the active section, and thus the emitted power, will depend on the current through the passive tuning sections. This means that we also have to take into account the rate equations for the carrier density N_d and N_p in the reflector and phase section respectively. These are given by:

$$\frac{dN_d}{dt} = \frac{\sigma I_d}{eV_d} - \left(A_d N_d + B_d N_d^2 + C_d N_d^3\right) \tag{2.5a}$$

$$\frac{dN_p}{dt} = \frac{\sigma I_p}{eV_p} - \left(A_p N_p + B_p N_p^2 + C_p N_p^3\right) \tag{2.5b}$$

with V_d (V_p) the volume of the reflector (phase) section and A_d (A_p), B_d (B_p), and C_d (C_p) the non-radiative, bimolecular and Auger recombination coefficients of the reflector (phase) section respectively.

Equations (2.1) to (2.5) form a set of coupled non-linear differential equations that have to be solved to investigate the dynamics of the laser output intensity.

The wavelength dynamics are determined by the carrier and thermal effects in the tuning sections and by the thermal effects in the active section. The electrical rate equations for the tuning sections are already given by (2.5). For the investigation of the wavelength switching we will use the following simplified form which can be obtained from (2.5) by only taking into account the linear term for the carrier recombination contribution (the second term in the right-hand side of the equations):

$$\frac{dN_d}{dt} = \frac{\sigma I_d}{eV_d} - \frac{N_d}{\tau_n} \tag{2.6a}$$

$$\frac{dN_p}{dt} = \frac{\sigma I_p}{eV_p} - \frac{N_p}{\tau_n} \tag{2.6b}$$

where τ_n represents the carrier lifetime. We have made this simplification because in this form the equations can be solved analytically, which is handy since we want to simulate effects that work over a rather large time span. The only consequence is that the simulated switching shows a small deviation up until a few nanoseconds after the switching moment. This is however not a major problem, since we are mainly interested in the influence of the much slower thermal effects.

The thermal effects can be modelled using the well known simple concentrated-constant thermal model. The laser is split up into several discrete sub-components. Each sub-component is assumed to have an infinite thermal conductivity so that at each moment the whole subcomponent has the same temperature. As a consequence the temperature will not be a continuous varying function, but will have a constant value for each sub-component. Every sub-component can then be represented by a thermal capacity and the heat flow between subcomponents can be modelled by a thermal resistance. Since the contact surface beween the active and phase section waveguides and the phase and reflector section waveguides respectively is very small, it is assumed that there is no thermal flux between the waveguides. This means that we assume that the waveguides only dissipate heat through their bottom contact, this heat flow is represented by R_1. Figure 2.1 shows a schematic representation of the thermal model of a three-section DBR laser consisting of an active, a phase and a Bragg section. The laser chip is mounted on a subcarrier which is mounted on a heat sink. The heat flow between the laser chip and the subcarrier and the subcarrier and the heat sink is represented by R_2 respectively R_3. The heat sink is assumed to have an infinite heat capacity and thus has a constant temperature T_0.

The thermal rate equations can now be written as follows [34]:

$$C_i \frac{dT_i}{dt} = E_i \sigma I_i + \sum_n \frac{\rho_n d_n}{w_i L_i} (\sigma I_i)^2 - \frac{T_i - T_c}{R_1} \tag{2.7a}$$

$$C_c \frac{dT_c}{dt} = \frac{\rho_5 d_0}{w_0 L_0} I_L^2 + \sum_i \frac{T_i - T_c}{R_1} - \frac{T_c - T_s}{R_2} \tag{2.7b}$$

$$C_s \frac{dT_s}{dt} = \frac{T_c - T_s}{R_2} - \frac{T_s - T_0}{R_3} \tag{2.7c}$$

where C_i is the heat capacity of each section and is determined by $C_i = C_{vi}\rho_{vi}V_i$ with C_{vi} the specific heat, ρ_{vi} the density and V_i the volume of each section. C_c and C_s are the heat capacity of the laser chip

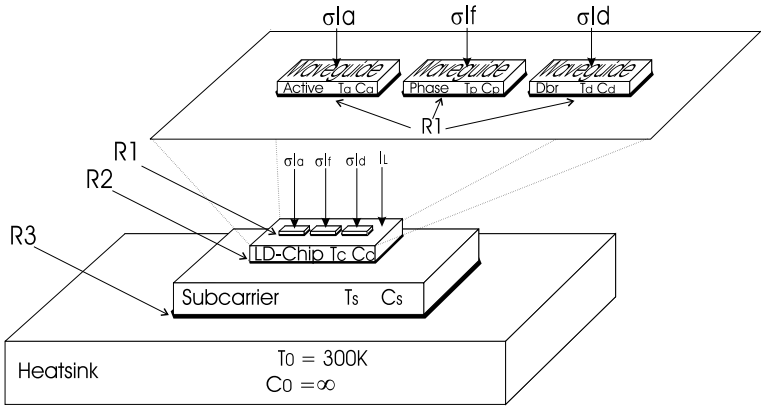

Figure 2.1: Thermal model of a three-section DBR laser.

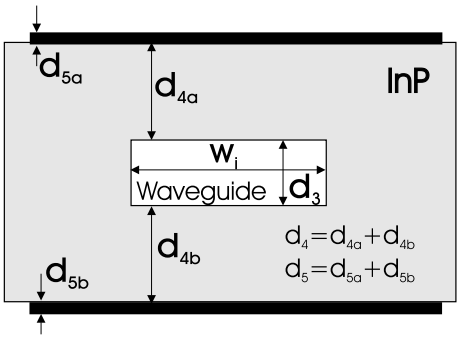

Figure 2.2: Schematic representation of the waveguide structure.

and the subcarrier respectively. E_i is the junction voltage, ρ_n and d_n are the ohmic resistivity and the thickness of the n-th region. With $n = 3$, 4, 5 for each section, corresponding to the thickness of the waveguide, the InP and quaternary contact layers respectively. this is schematically represented in figure 2.2. L_i and w_i are the length and width of each section and L_0 and w_0 are the length and width of the total laser chip.

Equations (2.7) express that the (thermal) power that is dissipated in a subcomponent equals the power that is supplied to that subcomponent minus the power that flows away to other subcomponents. Supply of power can come from subcomponents that have a higher temperature or from thermal sources (e.g. Joule heating). Since not all of the current that is injected into a section effectively flows through that section, a leak current $I_L = (1 - \sigma) \sum_i I_i$ has to be taken into account. Fur-

thermore, the current flowing through the active section is partly converted to optical power. However, since this is typically a very small fraction (10 to 20 %), we will neglect this fraction. Equation (2.7a) determines the temperature of each laser section T_i ($i = a, p, d$). The first term on the right-hand side of (2.7a) represents the heat generated by the electrical power dissipation in each section. The second term represents the heat generated by the Joule effect, i.e. the power dissipated by the current through a section in the Ohmic resistor with length d_i, surface $w_i L_i$ and resistivity ρ_n. The third term on the right-hand side of (2.7a) represents the heat flux between each section and the laser chip. Equation (2.7b) determines the temperature of the laser chip. The first term on the right-hand side represents the Joule heat generated by the leak current in the laser chip, while the second and third term represent the heat flux between the laser chip and the waveguide sections and the subcarrier respectively. Equation (2.7c) determines the temperature of the subcarrier and takes into account the heat flux between the subcarrier and the laser chip and the heat sink respectively.

The carrier density and temperature effects that are described above both influence the refractive index n_i of each section. This can be expressed as follows [20]:

$$\frac{dn_i}{dt} = \Gamma_i \frac{e^2 \lambda_0^2}{8\pi^2 c^2 n_i \epsilon_0 m_c} \frac{dN_i}{dt} + \frac{dn_i}{dT} \frac{dT_i}{dt} \tag{2.8}$$

with λ_0 the laser wavelength, ϵ_0 the permitivity and m_c the carrier weight.

Once the refractive index of each laser section is known, the laser wavelength can be determined from the phase condition:

$$n_a(t) L_a + n_p(t) L_p + n_d(t) L_{eff} = \frac{m\lambda}{2} \tag{2.9}$$

with L_{eff} the effective cavity length of the DBR mirror and m an integer. It is assumed that the laser wavelength is the wavelength fulfilling (2.9) that lies closest to the Bragg wavelength. Mode competition [26] has not been taken into account in this model.

2.2.2 Simulation results

The system of non-linear coupled rate equations described above was solved using the math tool Maple [42]. The differential equations can be solved symbolically by transforming them to the Laplace domain.

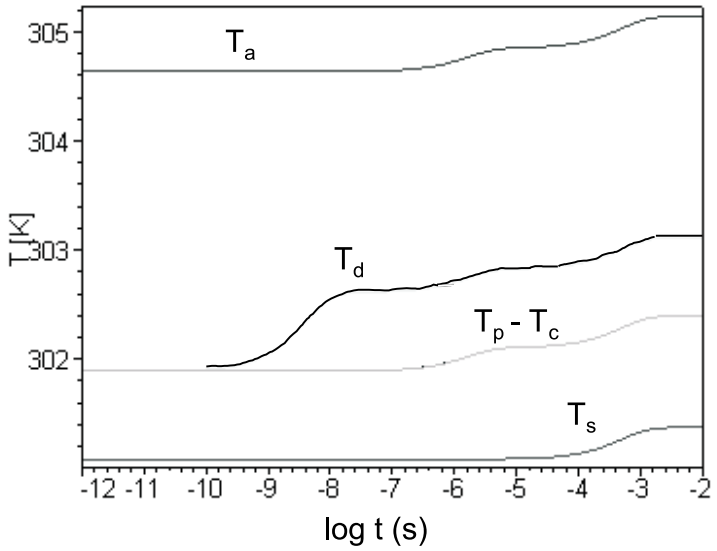

Figure 2.3: Change of temperature in time after I_d was switched between 0 and 30 mA, with I_a=70 mA, I_p=0 mA and T_0=300 K.

This yields a set of closed expressions for the temperature, carrier density and refractive index in the different sections which can be used to determine the laser wavelength. Table 2.1 summarizes the parameter values [34] that will be used in the numerical calculations.

Figure 2.3 shows the change of temperature (T_a, T_d, T_p, T_c and T_s) in time after the current through the reflector section I_d was switched between 0 and 30 mA, with I_a=70 mA, I_p=0 mA and T_0=300 K. The graph has a logarithmic time-scale, so that a detailed view can be given for a large time span. Right after the current switch the phase and reflector section have the same temperature as the laser chip. And since there is no current flowing through the phase section it remains on the same temperature as the laser chip. Since the current through the reflector section is switched (to a higher value) the temperature of this section starts to rise first. Then the active and phase section and laser chip temperature rises and finally also the temperature of the subcarrier rises.

Since we have used a concentrated-constant thermal model, three discrete time constants can be distinguished in figure 2.3: one at 3.38 ns, which is of the same order of magnitude as the carrier lifetime. The second time constant lies around 1.7 μs and the third one lies around 500 μs. These time constants are associated with the heat transfer from

Table 2.1: Laser parameters used for the thermal modelling of a three-section DBR laser [34]

Parameters	Symbol	Active	Phase	DBR	Unit
Length	L_i	300	250	300	μm
Effective Length	L_{eff}			135	μm
Width	w_i	1.0	1.5	1.5	μm
Thickness	d_i	0.15	0.25	0.25	μm
Refractive index	n_i	3.20	3.18	3.19	–
Confinement factor	Γ_i	0.325	0.488	0.488	–
Coupling coefficient	ξ	0.8			–
Current injection coeff.	σ	0.75			–
Reflectivity of facet	R_f	0.35			–
Reflectivity of DBR	$R_d(\lambda_B)$	0.35			–
Internal absorption	α_i	$2.0{\cdot}10^{3}$	$1.5{\cdot}10^{3}$	$1.5{\cdot}10^{3}$	m^{-1}
Shift of absorption	$d\alpha_i/dN_i$	$1.8{\cdot}10^{-21}$			m^2
Non-radiative rec. coeff.	A_i	$1.4{\cdot}10^{8}$	$0.5{\cdot}10^{8}$	$0.5{\cdot}10^{8}$	s^{-1}
Bimolecular rec. coeff.	B_i	100	100	100	$\mathrm{s}^{-1}\mu\mathrm{m}^3$
Auger rec. coeff.	C_i	$7.5{\cdot}10^{-5}$	$2.5{\cdot}10^{-5}$	$2.5{\cdot}10^{-5}$	$\mathrm{s}^{-1}\mu\mathrm{m}^6$
Spont. emission coupling coeff.	η	$1.0{\cdot}10^{-4}$			–
Gain coefficient	g_N	$4.83{\cdot}10^{-21}$			m^2
Transp. carrier dens.	N_0	$1.37{\cdot}10^{24}$			m^{-3}
Shift of refractive index	dn_i/dT	$1.1{\cdot}10^{-4}$	$1.6{\cdot}10^{-4}$	$1.6{\cdot}10^{-4}$	K^{-1}
Junction voltage	E_i	0.83	0.95	0.95	V
Specific heat	C_{vi}	$3.125{\cdot}10^{2}$	$3.123{\cdot}10^{2}$	$3.123{\cdot}10^{2}$	$\mathrm{m}^2\mathrm{s}^{-2}\mathrm{K}^{-1}$
Density	ρ_{vi}	$4.83{\cdot}10^{3}$	$4.82{\cdot}10^{3}$	$4.82{\cdot}10^{3}$	$\mathrm{kg/m}^3$
Laser chip heat capacity	C_c	$2.46{\cdot}10^{-7}$			J/K
Submount heat capacity	C_s	$5.32{\cdot}10^{-6}$			J/K
Thermal resistance	R_1	24.0			K/W
	R_2	7.0			K/W
	R_3	9.4			K/W
Heat sink temperature	T_0	300			K
Ohmic resistivity	ρ_3	$9.24{\cdot}10^{-5}$			Ωm
	ρ_4	$2.19{\cdot}10^{-3}$			Ωm
	ρ_5	$2.23{\cdot}10^{-3}$			Ωm
Thickness	d_4	3			μm
	d_5	50			μm
Laser chip dimensions	w_0	300			μm
	L_0	1000			μm
	d_0	100			μm

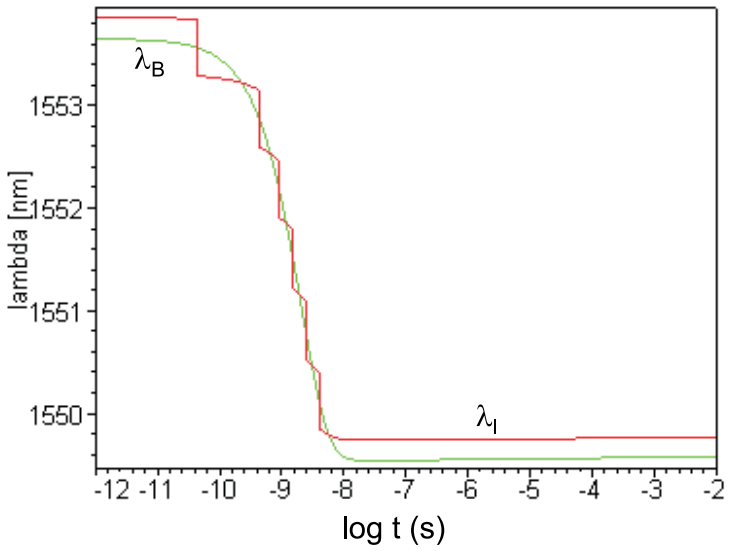

Figure 2.4: Change of the lasing wavelength (λ_l) and the Bragg wavelength (λ_B) in time after I_d was switched between 0 and 30 mA, with I_a=70 mA, I_p=0 mA and T_0=300 K.

waveguide-to-chip, chip-to-subcarrier and subcarrier-to-heat sink respectively.

Figure 2.4 shows the change of the lasing wavelength (λ_l) and the Bragg wavelength (λ_B) in time after the current through the reflector section I_d was switched between 0 and 30 mA, with I_a=70 mA, I_p=0 mA and T_0=300 K. Since the lasing wavelength fulfills the phase condition (2.9), it changes stepwise during the switching of the reflector current. The different steps correspond with the different cavity modes that lie in the center of the Bragg peak during the switch. It can be seen that after the switch (strong decrease of the wavelength) the wavelength drifts (slight increase of the wavelength) towards its steady state value.

Since the wavelength drift is so small compared to the wavelength switch, figure 2.5 shows a detail of figure 2.4 after the switch. The same time constants that appeared in the change of the temperature can also be distinguished in the wavelength drift. The smallest time constant is however masked by the carrier density dynamic effects.

The total drift is around 40 pm or 5 GHz. This might seem small. However, for an ITU-channel spacing of 50 GHz the error is already 10 %. And even for higher spacings, a deviation of a few GHz of the

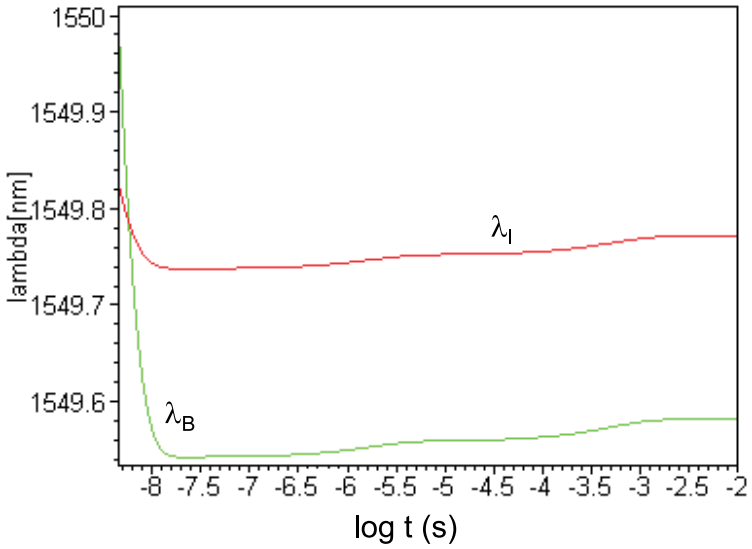

Figure 2.5: Drift of the lasing wavelength (λ_l) and the Bragg wavelength (λ_B) in time after I_d was switched between 0 and 30 mA, with I_a=70 mA, I_p=0 mA and T_0=300 K.

channel frequency can lead to intolerable power differences between channels due to the optical filtering of the signals. Furthermore, the current step was only 30 mA and only one tuning current was switched. In practice nearly always at least 2 tuning currents will have to be switched to ensure single-mode operation before and after the switch. Also, the (static) frequency accuracy of a commercial tunable laser module is typically required to be 1 GHz or better.

The dependence of the wavelength drift on the size of the switching current step can be seen in figure 2.6(a) and 2.6(b) which show the (absolute value of the) wavelength drift for switching current steps of 10, 20, 30, 40 and 50 mA after a period of 10 μs and 3 ms respectively. In each graph the lowest curve corresponds with a switching current step of 10 mA, the next corresponds to 20 mA, up to the upper curve which corresponds to 50 mA. The time scale of these graphs is now linear. From figure 2.6 it clearly follows that the wavelength drift increases as the switching current step increases and that the time constants are the same for every switching current step. The wavelength is stabilized after 2.5 ms, which is about 5 times the biggest time constant.

From the above it is clear that the wavelength drift can be modelled by a sum of two exponential functions: one corresponding to the

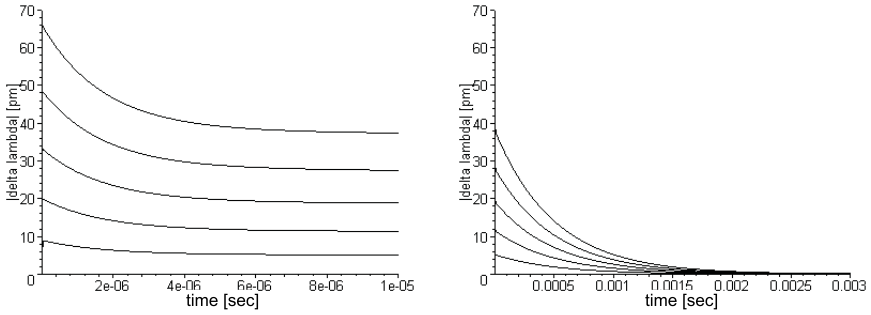

(a) 10 μs (b) 3 ms

Figure 2.6: Wavelength drift (absolute value) for switching current steps of 10, 20, 30, 40 and 50 mA after a period of 10 μs and 3 ms respectively (each time the lowest curve is for 10 mA, while the highest is for 50 mA).

time constant of 1.7 μs, the other one corresponding to the time constant of 500 μs. Since we are interested in the thermally induced (i.e. slow) wavelength drift, the smallest time constant can be omitted. Figure 2.7 shows the dependence of the amplitude of each of the exponential contributions on the switching current step. For increasing current steps, the (wavelength) deviation also increases. The increase is slightly quadratic, which is obviously due to the quadratical dependence of the Joule heating on the current.

2.2.3 Experimental results

The wavelength switching behaviour of semiconductor tunable lasers also was investigated experimentally. The measurement setup is shown in figure 2.8. The laser is a three-section DBR packaged tunable laser from JDS Uniphase. There are no RF-connections to the tuning sections, but since we are investigating the influence of slow thermal effects, this is not a major problem. The laser currents and temperature are controlled by the laser diode controller. The reflector current is switched using a pulsed current source with a pulse width of 3.225 ms and a duty cycle of 50 %. The laser output is sent through the tunable filter of the spectrum analyzer to convert the wavelength variations to power variations. The resulting signal is monitored on a digital sampling oscilloscope which is triggered from the pulsed current source. The data on the scope are read out using a Labview program and are further treated using Excel.

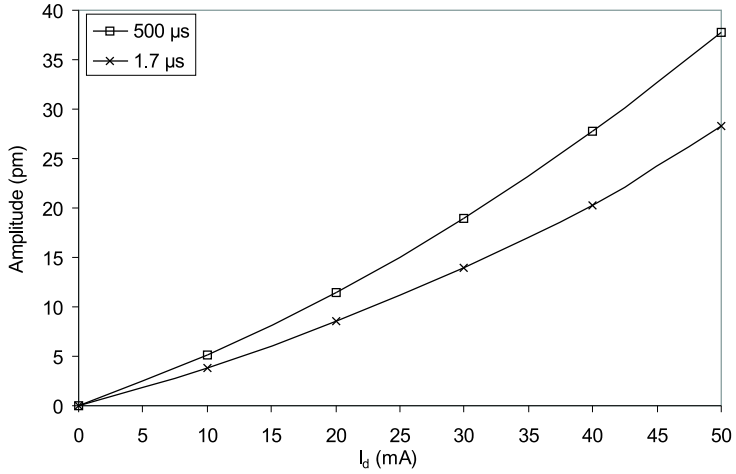

Figure 2.7: Amplitude of the exponential contributions (with time constant 1.7 μs and 500 μs resp.) in the thermally induced wavelength drift versus increasing switching current step.

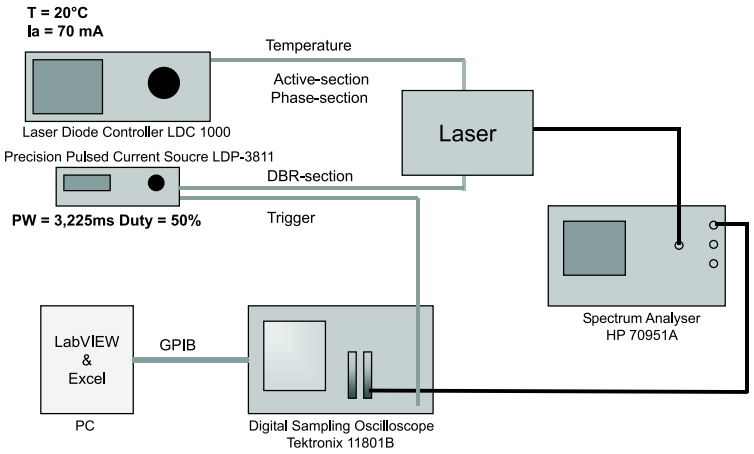

Figure 2.8: Measurement setup to characterize the wavelength switching behaviour of semiconductor tunable lasers.

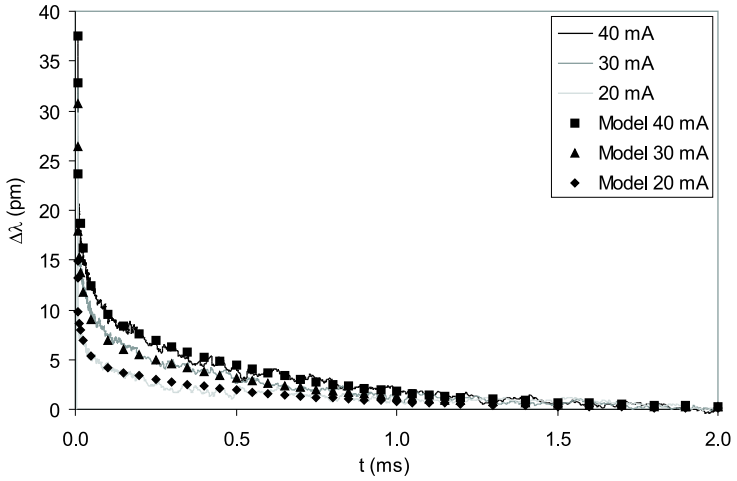

Figure 2.9: Measured (full lines) wavelength drift (absolute value) versus the drift calculated using a three time constant model (symbols) for three different step amplitudes (20, 30 an 40 mA respectively).

By carefully tuning the filter in the spectrum analyzer, the drift can be determined quantitatively. The filter is tuned to a wavelength that is slightly smaller then the destination wavelength. The power of the signal after the filter will then decrease due to the drift after a switch to a higher current (i.e. a switch to a lower wavelength followed by a drift towards higher wavelengths). Using the measured filter characteristic, the wavelength versus time response can now be determined from the power versus time response of the filtered signal [42].

Figure 2.9 shows the measured (full lines) wavelength drift and the drift calculated using a three time constant model (symbols) for three different step amplitudes (20, 30 an 40 mA respectively). The graph shows the absolute value of the wavelength drift. Again, three time constants, independent of the step amplitude can be observed and there is good agreement between theory and experiment. The time constants are 550 μs, 30 μs and 1.5 μs (these are the same for each step amplitude). After 2 ms the steady–state wavelength has been reached.

Figure 2.10 shows the measured amplitude of the exponential contribution with a 550 μs time constant in the thermally induced wavelength drift for increasing switching current steps. Again, we see a slightly quadratic increase when the switching current step increases.

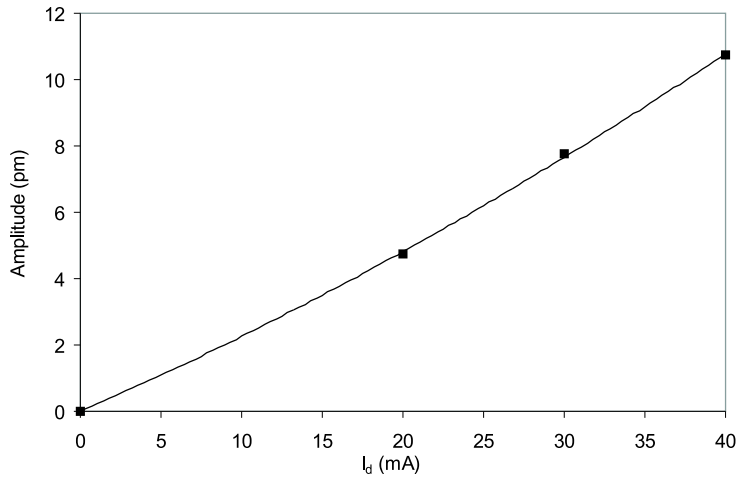

Figure 2.10: Measured amplitude of the 550 μs time constant contribution in the thermally induced wavelength drift versus increasing switching current step.

2.3 Pre-compensation method

Taking into account the results presented in section 2.2, one could think of counteracting the thermally induced wavelength drift by pre–compensating the tuning currents using simple first order RC–filters [43]. Proof of this very simple principle is shown in figure 2.11. It can be seen that the drift is already strongly suppressed by only compensating two time constants. Unfortunately, due to the quadratical dependence of the heating on current, compensation for different current step values is difficult to obtain using only linear elements. For current steps bigger or smaller than the one the pre-compensation was optimized for, under- respectively over compensation occurs, as is shown in figure 2.12. Furthermore, the wavelength drift depends on the switching history, making it difficult to optimize this technique for all possible switching combinations.

Due to the problems associated with the RC pre-compensation technique, we developed a novel method, based on optical feedback from a stable reference filter, that can be used to suppress the thermally induced wavelength drift independent of the size of the current step. I.e. the compensation is independent from which channel the wavelength is being switched to and also independent from the switching history.

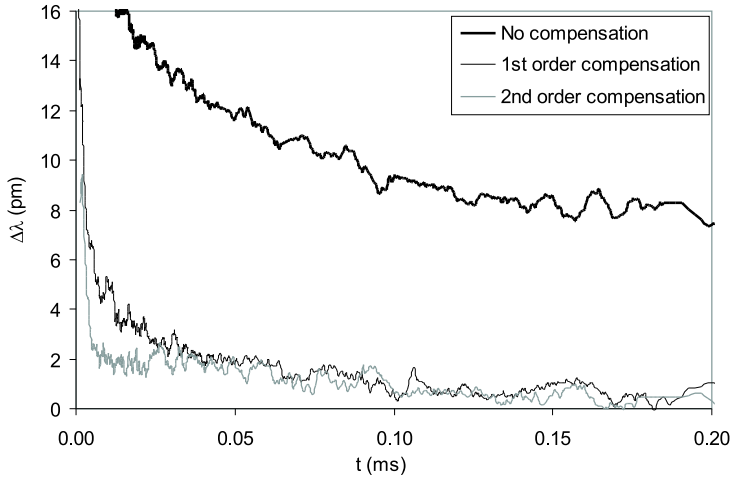

Figure 2.11: Suppression of wavelength drift using simple RC-filters to pre-compensate the tuning currents. The wavelength change after a current step of 40 mA is shown, without compensation and with compensation of a first and second order filter respectively.

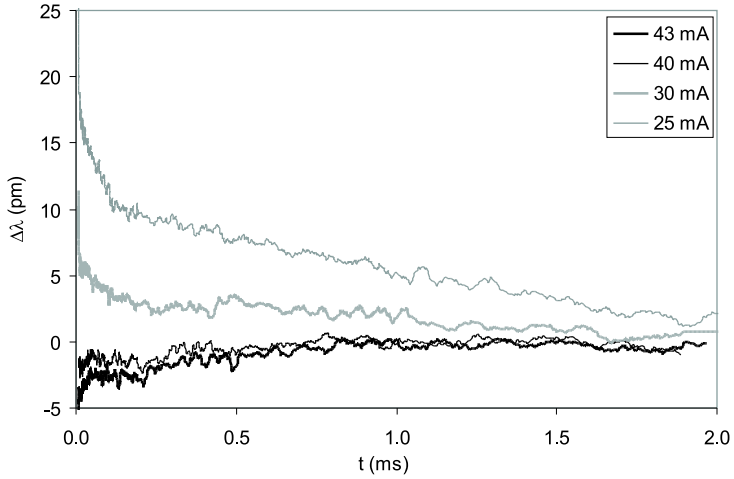

Figure 2.12: Over- and under compensation for current steps smaller (25 mA and 30 mA) resp. bigger (43 mA) then the one the pre-compensation was optimized for (40 mA).

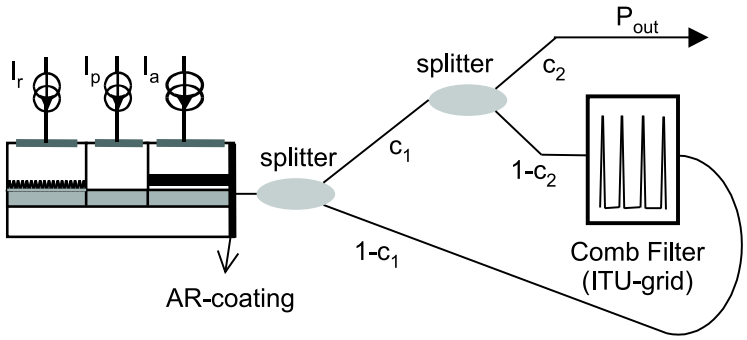

Figure 2.13: Novel feedback scheme to improve the wavelength switching behaviour of semiconductor tunable lasers.

In the next section we will describe the principle of the stabilization. A short theoretical background on the influence of optical feedback on a semiconductor laser will be given together with some numerical results.

2.4 Optical feedback

In this section we will investigate how the wavelength switching behaviour of semiconductor tunable lasers can be improved through optical feedback from a periodic optical filter. The filter should be physically separated from the laser so that it is not influenced by temperature variations in the laser and can thus act as a stable reference for the laser wavelength, independent from the time evolution of the tuning currents. A possible implementation of the feedback scheme is shown in figure 2.13. The scheme only contains two power splitters and a comb filter that is physically –and thus thermally– separated from the laser, thus providing a stable frequency reference, independent of temperature changes in the laser sections. The feedback strength is determined by the splitting ratios c_1 and c_2. The reason why the right facet of the laser is anti-reflection coated will become clear below. If the feedback is correctly applied, the laser will then operate on wavelengths (optical frequencies) determined by the filter peaks. What "correctly" means, will be explained in the following sections.

For a laser that is to be used in a telecommunications network, the filter peaks should obviously be situated at the ITU-frequencies. In that case the peak separation will typically be 100 GHz or 50 GHz [58]. In

order not to have too much interference between adjacent peaks, the 3–dB width (or the FWHM: Full Width Half Maximum) of the filter peaks should be smaller than 10 GHz. On the other hand, the peaks cannot be too narrow (e.g. smaller than 1 GHz), because then the feedback will become too weak to obtain stable external cavity operation. This will be explained in the following sections. More details about the filter specifications will be given in chapter 3.

2.4.1 Theoretical background

Optical feedback can have a large influence on the performance of a semiconductor laser. Already for very low feedback levels (-40 dB or less) the static, dynamic and spectral behaviour can be strongly affected. Such low feedback levels can for instance be caused by a reflection at the end of a fibre pigtail. Hence, an isolator is often integrated in the package of a laser that is coupled to fibre to ensure error-free operation of the laser.

Optical feedback has some practical applications like the enhancement of single longitudinal mode operation, linewidth narrowing and wavelength tuning [44, 45]. But unfortunately, as we will see, optical feedback can also cause instabilities and laser performance can be severely degraded. In this section we will give an overview of the different phenomena that can occur when a semiconductor laser is subject to optical feedback.

During the past decades and up until today, a lot of research has been conducted towards the influence of optical feedback on laser performance. It is certainly not our aim to fully explain the theory behind optical feedback –this alone could be (has been) the subject of several doctoral theses. Nor will we try to give a complete overview of the literature concerning this subject. We simply want to provide some basic knowledge to be able to understand the problems that (can) occur when one tries to improve the (wavelength switching) behaviour of a semiconductor (tunable) laser through optical feedback. References to key publications in the field of semiconductor lasers subject to optical feedback will also be given.

Rate equation model

The analysis of a laser subject to optical feedback (or a laser in an external cavity configuration), usually starts from the rate equation for the

electric field $E(t)$ in its complex form. Neglecting spontaneous emission and assuming that the solitary laser (i.e. the laser without feedback) is mono modal one gets [46]:

$$\frac{dE(t)}{dt} = \left\{ j\omega(N) + \frac{1}{2}\left[G(N,|E|^2) - \frac{1}{\tau_p} \right] \right\} E(t) + \frac{\kappa}{\tau_D} E(t-\tau) \quad (2.10)$$

In this equation $\omega(N)$ stands for the angular optical frequencies of the longitudinal modes of the laser diode cavity. These are determined by the Fabry Perot resonance condition (i.e. the phase difference after one round trip in the cavity should be a multiple of 2π):

$$\omega(N) = \frac{p\pi c}{n(\omega, N) L_D} \quad (2.11)$$

for the p–th longitudinal mode, where p is an integer, N is the carrier density in the laser diode cavity, c is the speed of light, $n(\omega, N)$ is the effective refractive index of the laser medium and L_D is the length of the laser diode.

As mentioned earlier, it is assumed that the solitary laser oscillates in a (single) longitudinal mode with angular frequency

$$\omega_0 = \omega(N_{th}) \quad (2.12)$$

with N_{th} the threshold carrier density of the solitary laser.

$G(N,|E|^2)$ is the modal gain per second and τ_p is the photon lifetime. The gain can be expressed as

$$G(N,|E|^2) = G_N(N - N_0)(1 - \varepsilon\Gamma\,|E|^2) \quad (2.13)$$

with G_N the differential gain, N_0 the transparency carrier density, ε the nonlinear gain suppression coefficient and Γ the confinement factor, which are all constants. When no feedback is present N_{th} can be determined from $G(N_{th}, 0) = \tau_p^{-1}$.

The last term on the right hand side of (2.10) represents the external feedback contribution. τ_D and τ are the round-trip times in the laser and external cavity respectively. κ represents the coupling of the reflected field back into the laser mode. For a Fabry Perot laser or for a tunable laser where the reflected field enters the laser through the facet of the active section (e.g. two- or three section DBR lasers), an expression for κ can easily be derived. Considering figure 2.14 and neglecting multiple reflections in the external cavity (i.e. we assume that $\kappa \ll 1$),

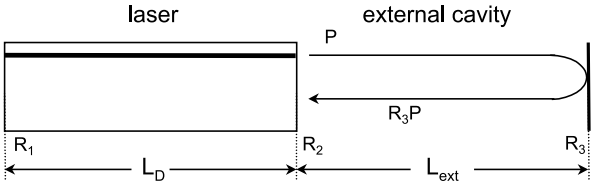

Figure 2.14: Schematic representation of an external cavity laser diode

the ratio of the field component that enters back into the laser cavity after one round trip in the external cavity and the field component that is directly reflected at the right laser facet is given by

$$\eta t_2^2 \frac{r_3}{r_2} e^{-j\omega_0 \tau} \tag{2.14}$$

with t_2, r_2, r_3 the field transmission and reflection coefficients of the right laser facet and the external reflective surface respectively, η the (power) coupling efficiency between the two cavities and ω_0 the laser frequency. Since $r = \sqrt{R}$ and (for normal incidence) $t^2 = T = 1 - R$, we get for κ

$$\kappa = (1 - R_2)\sqrt{\frac{f_{ext}}{R_2}} \tag{2.15}$$

where we have introduced the feedback fraction

$$f_{ext} = \eta^2 R_3 \tag{2.16}$$

which is the ratio of the power entering back into the laser cavity to the power emitted from it. For DFB lasers, the expression for κ becomes slightly more complicated and κ may become complex [91], but for the rest the analysis of (2.10) remains unchanged.

Now that we have explained all variables and parameters in equation (2.10), we will split it up in an equation for the amplitude and the phase of the (complex) electrical field $E(t)$. Using the plane wave and the slowly varying envelope approximation, $E(t)$ can be written as

$$E(t) = E_0(t) e^{j(\omega_0 t + \phi(t))} \tag{2.17}$$

where $E_0(t)$ and $\phi(t)$ are both real and slowly varying functions of t.

Inserting (2.17) into (2.10), one obtains:

$$\frac{dE_0(t)}{dt} = \frac{1}{2}\left[G(N, E_0^2) - \frac{1}{\tau_p}\right] E_0(t) + \frac{\kappa}{\tau_D} E_0(t-\tau)\cos(\omega_0\tau + \Delta(t)) \tag{2.18a}$$

$$\frac{d\phi(t)}{dt} = \omega(N) - \omega_0 - \frac{\kappa}{\tau_D}\frac{E_0(t-\tau)}{E_0(t)}\sin(\omega_0\tau + \Delta(t)) \tag{2.18b}$$

where $\Delta(t) = \phi(t) - \phi(t-\tau)$ is the phase delay over an external cavity round-trip time τ. Since the instantaneous optical angular frequency is given by $\omega = \omega_0 + d\phi/dt$ it follows that

$$\frac{1}{\tau}\int_{t-\tau}^{t} \omega(t')dt' = \omega_0 + \frac{\Delta}{\tau} \tag{2.19}$$

which shows that Δ/τ can be regarded as an average frequency deviation from the oscillation frequency of the solitary laser.

For a semiconductor laser amplitude and phase variations are coupled through the carrier density dependence of the refractive index. This coupling is described by the linewidth enhancement factor α [92]

$$\alpha = -2\frac{\omega_0}{n_g}\frac{\partial n/\partial N}{\partial G/\partial N} \tag{2.20}$$

where $n_g = n + \omega_0(\partial n/\partial\omega)$ is the group effective index. The minus sign in this definition is chosen so that α is positive at semiconductor laser wavelengths. Typically α lies between 3 and 6 for GaAs/AlGaAs and InP/InGaAsP semiconductor lasers [92].

We will now introduce α into the rate equations by expanding ω around $\omega_0 = \omega(N_{th})$. We will assume that the carrier density N for the external cavity laser lies around N_{th} as is the case for a laser without feedback, so that we can limit the expansion of $\omega(N)$ to the first order term:

$$\omega(N) = \omega_0 + \left.\frac{d\omega}{dN}\right|_{N=N_{th}} \Delta N \tag{2.21}$$

With $d\omega/dN$ from (2.11) and using (2.20) it follows that

$$\omega(N) = \omega_0 - \frac{\omega_0}{n_g}\frac{\partial n}{\partial N}\Delta N = \omega_0 + \frac{\alpha}{2}\frac{\partial G}{\partial N}\Delta N. \tag{2.22}$$

Equation (2.18b) then becomes

$$\frac{d\phi(t)}{dt} = \frac{1}{2}\frac{\partial G}{\partial N}\alpha\Delta N - \frac{\kappa}{\tau_D}\frac{E_0(t-\tau)}{E_0(t)}\sin(\omega_0\tau + \Delta(t)) \tag{2.23}$$

To complete our laser model, the rate equation for the (average) carrier density in the laser section is also considered:

$$\frac{dN}{dt} = J - \frac{N}{\tau_c} - G(N, E_0^2)E_0^2(t) \tag{2.24}$$

with J the injection current density and τ_c the carrier lifetime.

Steady-state solutions

First we will consider the steady-state or stationary solutions of the rate equations. From these solutions the feedback-induced change of the (steady-state) gain ΔG and that of the oscillation frequency $\Delta\omega$ can be obtained. ΔG and $\Delta\omega$ are solutions of equations (2.18a) and (2.23) (in their stationary form) and thus determine the possible modes of the external cavity system consisting of the laser and the external cavity. Hence, these modes are called external cavity modes.

A steady-state solution satisfies $E_0(t) = \tilde{E}_0$, $\phi(t) = \Delta\omega t$ (or $\omega = \omega_0 + \Delta\omega$) and $N(t) = \tilde{N}$ where $\tilde{E}_0$, $\Delta\omega$ and $\tilde{N}$ are time-independent. Substitution in (2.18a) renders:

$$\frac{1}{2}\left[G(\tilde{N}, \tilde{E}_0^2) - \frac{1}{\tau_p}\right] + \frac{\kappa}{\tau_D}\cos(\omega_0\tau + \Delta\omega\tau) = 0 \tag{2.25}$$

Using $G(N_{th}, 0) = \tau_p^{-1}$, this leads to:

$$\Delta G = -2\frac{\kappa}{\tau_D}\cos(\omega\tau) \tag{2.26}$$

From (2.23) it follows that

$$\frac{d\phi}{dt} = \Delta\omega = \frac{1}{2}\frac{\partial G}{\partial N}\alpha\Delta N - \frac{\kappa}{\tau_D}\sin(\omega\tau) \tag{2.27}$$

So that using $\Delta N(\partial G/\partial N) \approx \Delta G$ leads to:

$$\Delta\omega = -\frac{\kappa}{\tau_D}\left[\alpha\cos(\omega\tau) + \sin(\omega\tau)\right] \tag{2.28}$$

or

$$\Delta\omega\tau = -C\sin(\omega\tau + \arctan(\alpha)) \tag{2.29}$$

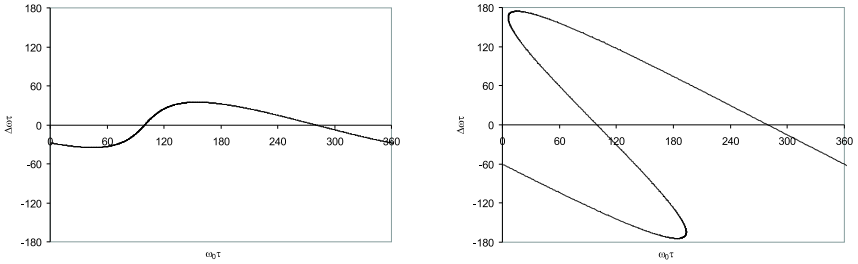

(a) C = 0.6 (b) C = 3

Figure 2.15: Optical feedback induced shift of the laser frequency versus the external phase shift for the solitary laser frequency, for a feedback coefficient C of 0.6 and 3 respectively and with α = 6.

with $C = \frac{\kappa}{\tau_D}\tau\sqrt{1+\alpha^2}$. Equation (2.29) is the phase condition for the external cavity modes.

The linewidth of an external cavity laser can also be calculated from the above rate equations. We will not resume the calculation here, but refer to [45] instead.

$$\Delta\nu = \frac{\Delta\nu_0}{\left[1 + C\cos(\omega\tau + \arctan\alpha)\right]^2} \tag{2.30}$$

with $\Delta\nu_0$ the linewidth of the solitary laser. The above expression only holds when the external cavity round-trip time τ is smaller than the coherence time of the laser [45].

The parameter C in the above equations is the feedback coefficient and is often used to describe the stability of lasers under weak to moderate external optical feedback [55]. The feedback coefficient is proportional to the coupling coefficient and thus is a measure for the feedback strength.

To illustrate the influence of (increasing) external optical feedback, $\Delta\omega\tau$, $\Delta G\tau$ and $\Delta\nu/\Delta\nu_0$ (determined by (2.29), (2.26) and (2.30) respectively) are shown in figure 2.15, 2.16 and 2.17 respectively versus the phase change in the external cavity for the solitary laser frequency $\omega_0\tau$. The results are shown for two different values of the feedback coefficient $C < 1$ (C = 0.6) and for $C > 1$ (C = 3).

From figure 2.15(a) it can be seen that as long as C is smaller than unity, there is only one steady-state solution. This means that the external cavity laser will emit light in a single (external cavity) mode, the linewidth of which is narrowed or broadened depending on the phase

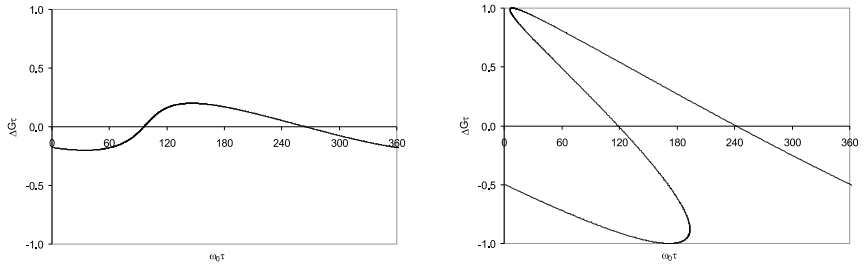

(a) C = 0.6 (b) C = 3

Figure 2.16: Optical feedback induced shift of the threshold gain versus the external phase shift for the solitary laser frequency, for a feedback coefficient C of 0.6 and 3 respectively and with α = 6.

of the feedback, cfr. figure 2.17(a). This can already be noticed for feedback levels as low as -80 dB [50]. As soon as C becomes larger than unity, the system becomes much more complex and can have multiple solutions. This is illustrated in figures 2.15(b), 2.16(b) and 2.17(b). The laser emits in multiple external cavity modes and shows noise-induced frequency hopping between the different modes [50, 51, 53]. Since C depends on the external cavity round-trip time, the transition to this second regime not only depends on the the feedback strength, but also on the distance to the reflector. In [50, 51, 53] it is also shown that the preferred external cavity modes are those with minimum linewidth, that the magnitude of the splitting depends on the strength of the feedback and on the external cavity length and that the rate of the mode hopping decreases for increasing feedback. When the feedback strength is increased further, a third regime is entered where the laser locks to the (external) cavity mode with minimum linewidth. This is explained in [93] using a potential model. The laser is now operating in a single, relatively stable narrow linewidth mode. The corresponding feedback levels lie between -50 and -40 dB. This stable condition is unfortunately not maintained for increasing feedback levels. Already for feedback levels as low as -40 dB, the laser can enter an unstable state, denoted as "coherence collapse" [48, 49, 50, 51, 52, 53, 55]. This is accompanied by a drastic increase in linewidth and RIN, rendering the external cavity laser totaly useless for application in a telecommunication network. This unstable state can be maintained for feedback levels spanning several decades, i.e. from -40 dB up to -10 dB [50, 51, 53, 55]. Since in the

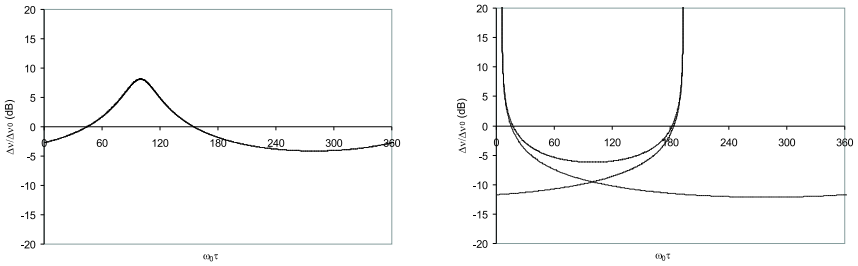

(a) C = 0.6 (b) C = 3

Figure 2.17: Optical feedback induced change of the linewidth versus the external phase shift for the solitary laser frequency, for a feedback coefficient C of 0.6 and 3 respectively and with α = 6.

coherence collapse state laser performance is seriously degraded, it is obviously to be avoided at all time. Therefore, an isolator is mostly integrated in the package of laser to be used as a transmitter in a network.

For very high feedback levels the laser can enter a fifth feedback regime [50, 52, 53, 55]. In this regime the laser operates in a stable narrow linewidth mode for all phases of feedback. The linewidth is still influenced by the feedback phase but the laser always stays stable, independent of the phase. The linewidth stays within the same order of magnitude for all phase shifts and does not exceed the linewidth of the solitary laser. When a very narrow linewidth is required, the linewidth can be minimized by adjusting the phase (mechanically) by changing the distance between the laser and the filter. This is not always possible and furthermore very difficult to control in a stable manner. For a tunable laser however, the phase can always be adjusted electronically by changing the current through the phase section. The fifth regime can only be reached for feedback levels above -10 dB, this means that the laser has to be anti-reflection coated.

From the above it is clear that five regimes of feedback effects can be distinguished for a semiconductor laser experiencing optical feedback. In the first regime for very low feedback levels (below -70 dB) the laser operates on a single external cavity mode and linewidth narrowing or broadening occurs depending on the phase of the feedback. In the second regime the laser is no longer mono-modal and shows noise-induced frequency hopping between the different external cavity modes. The corresponding feedback strength lies between -70 and

-50 dB, depending on the distance to the external reflection. The third regime is reached for feedback levels between -50 and -40 dB for which the laser operates in a stable single narrow mode. Unfortunately, this stable regime is rather narrow and if the feedback strength is increased further the laser enters the fourth regime: the unstable coherence collapse regime, characterized by a drastic increase in linewidth and RIN. The corresponding feedback levels range from -40 dB up to -10 dB. The fifth regime finally, can only be reached for feedback levels above -10 dB. In this regime, the laser operates in a stable narrow linewidth mode for all phases of feedback. It is in this regime that we want the tunable laser with optical feedback from a periodic reference filter to operate. Therefore –as mentioned before– the laser facet will have to be anti-reflection coated in order to obtain a sufficiently high feedback level. Furthermore, it is extremely important to avoid the laser from entering the coherence collapse regime (regime IV). To this end it is recommended to keep the external cavity length as short as possible. For lasers with a very short external cavity (shorter than 5 mm) it has been found that the laser remains stable for any feedback level, without the occurrence of coherence collapse [52].

It could be remarked that in the fifth regime one could consider the system as a laser with an extended cavity, rather than a laser with optical feedback. As is common practice in the literature on this subject, we will use the terms 'feedback' and 'external cavity laser'.

The existence of the five feedback regimes and the distinct separation between them has been experimentally verified rather early on in the work on optical feedback [50]. Theoretical verification of the observed effects and their dependence on laser parameters was achieved in a number of preceding and following papers [46, 45, 47, 49, 51, 52, 93, 53, 54, 55] and references therein. All five regimes can be described by equations (2.18a) and (2.23). For low to moderate feedback levels (regime I to IV) the equations can be solved analytically [46, 45, 47, 49] but for higher feedback levels numerical calculations are necessary [51, 52, 53, 54].

2.4.2 Simulation results

In this section we will numerically investigate the influence of the feedback strength (f_{ext}) and the external cavity length on some general semiconductor laser characteristics like the RIN and the linewidth, with the focus on the fifth feedback regime. For this we will use the commer-

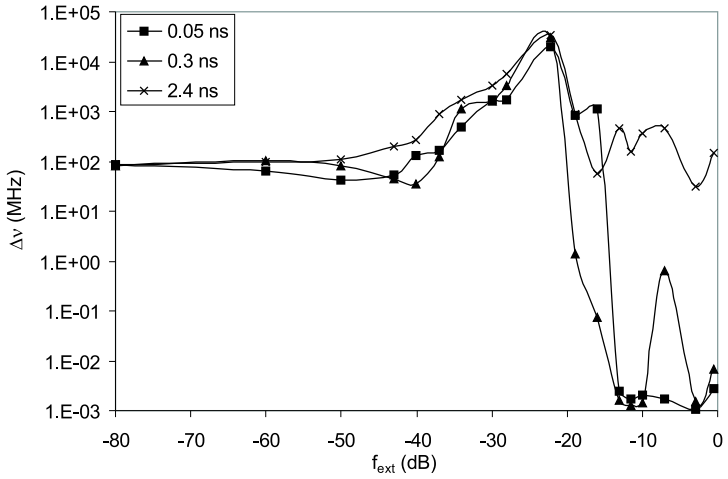

Figure 2.18: Linewidth for an external cavity laser subject to optical feedback from a periodic filter. Results are shown for an external cavity round-trip time τ = 0.05 ns (squares), 0.3 ns (triangles) and 2.4 ns (crosses).

cially available software VPI Componentmaker [56]. In chapter 4, the influence of the feedback parameters on characteristics more specific to semiconductor tunable lasers (like the tuning table and the wavelength switching behaviour) will be investigated.

Figure 2.18 and 2.19 show the calculated linewidth and the RIN versus the feedback strength for an external cavity laser subject to optical feedback from a periodic filter, and this for an external cavity round-trip time τ = 0.05 ns (squares), 0.3 ns (triangles) and 2.4 ns (crosses) respectively. These round-trip times correspond to an external cavity length of 7.5 mm, 45 mm and 360 mm respectively. The laser had an AR–coating with a reflectivity of 0.01 and the output power of the solitary laser was 4 mW. It is obvious that both the linewidth and RIN can reach intolerable high values if f_{ext} becomes smaller than –16 dB. The linewidth can reach values up to a few ten GHz, the RIN values up to –100 dB. As mentioned in chapter 1, these values are much too high to be used in a telecommunication network. On the other hand, for high feedback levels (corresponding to the fifth feedback regime, mentioned above) the linewidth can be reduced up to a few kHz. It can also be noticed that for longer external cavities it is more difficult to reach the fifth feedback regime or that it is not even reached. The reason that the

linewidth and RIN are rather high for feedback levels below –50 dB is that the laser facet is AR–coated.

In the previous section it was mentioned that for very short external cavity lengths (smaller than 5 mm) it has been found that the laser remains stable for any feedback level, without the occurrence of coherence collapse [52]. For our feedback scheme we have not simulated external cavity lengths smaller than 7.5 mm. This is because for practical coupling of the laser with the filter, a spacing of at least 5 mm is required, this will become clear in chapter 3 and 4. However, from figure 2.18 and 2.19 it is clear that even for an external cavity length of 45 mm, stable external cavity operation can be obtained, provided that the feedback level is sufficiently high. For completeness, figure 2.20 shows the RIN of a Fabry Perot laser subject to optical feedback from a mirror, and this for an external cavity round-trip time τ = 0.0133 ns (squares) and 0.3 ns (triangles) respectively. These round-trip times correspond to an external cavity length of 2 mm and 45 mm respectively. The laser had an AR–coating with a reflectivity of 0.01 and the output power of the solitary laser was 7 mW. For an external cavity length of 45 mm we see the same behaviour as in figure 2.19, but for an external cavity length of 2 mm it can clearly be seen that the coherence collapse regime does not occur.

Another advantage of the external cavity configuration is that the high-frequency modulation behaviour is improved and that the chirp is decreased, making direct modulation at speeds above 10 GHz possible [94, 95]. This falls outside the scope of this work however, so we will not go into further detail on it.

2.4.3 Practical implementation

Practical implementation of the feedback scheme shown in figure 2.13 is hindered by the fact that two power splitters are required, making it difficult to keep the external cavity round-trip time sufficiently small. The scheme requires two power splitters because existing comb filters like Fabry Perot etalons only have a comb-like response in transmission, the response in reflection has a complementary form with dips in stead of peaks on the ITU-frequencies [57]. There are filter types (for instance based on fibre Bragg gratings [96]) that have a comb-like response in reflection, but since these filters have the complementary response with dips in transmission, one still needs one extra power splitter to obtain a reasonable output power from the laser. Furthermore,

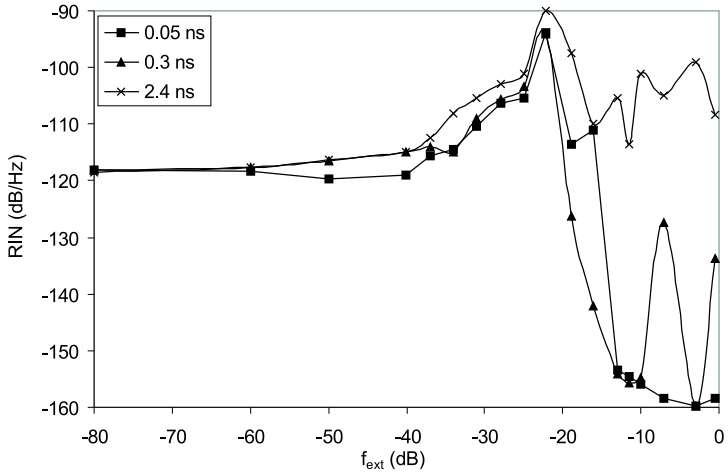

Figure 2.19: RIN for an external cavity laser subject to optical feedback from a periodic filter. Results are shown for an external cavity round-trip time τ = 0.05 ns (squares), 0.3 ns (triangles) and 2.4 ns (crosses).

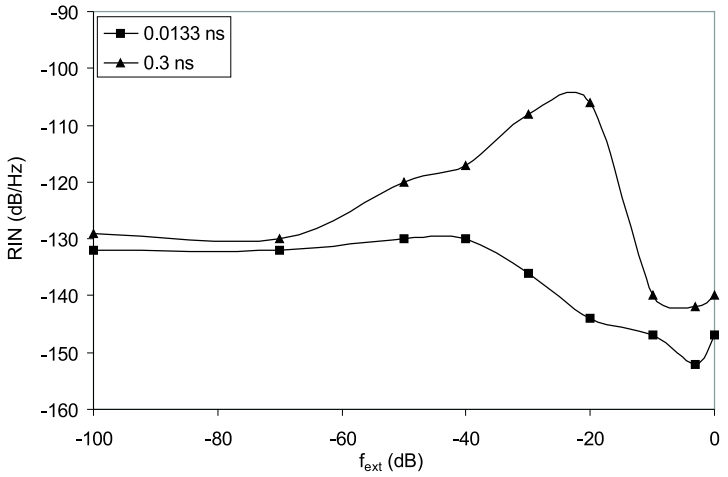

Figure 2.20: RIN for an external cavity laser subject to optical feedback from a mirror. Results are shown for an external cavity round-trip time τ = 0.0133 ns (squares) and 0.3 ns (triangles).

fibre Bragg grating based filters are usually quite long (a few centimeters or more), making it more difficult to avoid feedback induced instabilities. Therefore we decided to develop a filter that has a comb-like response in reflection as well as in transmission and that is as small as possible. The construction of the filter will be described in the next chapter.

2.5 Conclusion

In this chapter we have investigated the wavelength switching behaviour of semiconductor tunable lasers. Using a theoretical model we have shown that the wavelength of these devices can rapidly (in the order of a few nanoseconds) be changed electronically by switching the tuning currents. Unfortunately the thermally induced wavelength drift related to the switching of the tuning currents causes an increase of the switching time up to a few milliseconds. This was evidenced both by numerical and experimental results.

Based on the conclusions drawn from the theoretical and numerical results, two possible methods to counteract the thermally induced wavelength drift were presented. Pre-compensation of the tuning currents is a very simple technique, but it is difficult to optimize for all possible switching combinations. Therefore, a novel method based on optical feedback from a periodic reference filter was developed. This method can be used to suppress the thermally induced wavelength drift independent from which channel the wavelength is being switched to and also independent from the switching history. The effect of optical feedback on laser characteristics was described using a theoretical model and simulation results. The important conclusion is that the feedback level must be high enough and the external cavity length short enough to avoid feedback induced instabilities. To obtain this, a novel filter has to be developed, the design of which is described in the next chapter. Practical evidence of the improvement of the wavelength switching behaviour will be given in chapter 4.

Chapter 3

Filter

In this chapter we will describe a novel filter design that we developed to enhance the wavelength switching behaviour of semiconductor tunable lasers. After indicating what was the rationale for developing our own filter we will explain the design of the filter and describe how it is fabricated. Then we will study the reflection and transmission characteristics and the influence of different design parameters on them. Finally, the results of the experimental characterization of the filter will be presented.

3.1 Rationale

The development of this novel filter design was inspired by our work on wavelength switching of semiconductor tunable lasers. The wavelength of these devices can be changed in 10 ns or less [22, 23, 24, 25, 26, 27, 28, 29, 30, 31, 32, 33], as required for applications like optical packet/burst switching. The wavelength switching is obtained by rapidly changing one or more of the tuning currents. Unfortunately thermal effects associated with the switching of the tuning currents cause the wavelength to drift, increasing the switching time up to the order of a few milliseconds [34, 35, 36, 37, 38, 39, 40, 41]. To counteract this drift, we developed an optical feedback scheme where an optical comb filter is used as a stable frequency reference that is independent of temperature changes in the laser sections, as is explained in more detail in chapter 2. The schematic representation of the feedback scheme is shown in figure 2.13. The comb filter is a filter with a periodic response with its peaks on the ITU-frequencies [58]. An example of a

comb filter is the well know Fabry Perot etalon [57]. Apart from the filter, the feedback scheme only contains two power splitters.

In [59] it was shown numerically that frequency deviations up to 15 GHz from the channel frequency can be suppressed using this scheme. It was also shown that it is very important that the feedback ratio (i.e. the fraction of the power emitted by the laser that is coupled back into the laser) is sufficiently large (-10 dB or more, hence the facet of the laser facing the filter must be AR-coated) and that the external cavity round-trip time is kept sufficiently small (preferably the external cavity length is less than 10 cm). This is required to avoid instabilities caused by the feedback (e.g. coherence collapse) [50, 52, 55].

The feedback scheme requires two power splitters because existing comb filters like Fabry Perot etalons only have a comb-like response in transmission, the response in reflection has a complementary form with dips in stead of peaks on the ITU-frequencies [57]. The fact that two splitters are required makes it difficult to keep the external cavity round-trip time sufficiently small. There are filter types (for instance based on fibre Bragg gratings [96]) that have a comb-like response in reflection, but since these filters have the complementary response with dips in transmission, one still needs one extra power splitter to obtain a reasonable output power from the laser. Furthermore, fibre Bragg grating based filters are usually quite long (a few centimeters or more), making it more difficult to avoid feedback induced instabilities. Therefore we decided to develop a filter that has a comb-like response in reflection as well as in transmission and that is as small as possible. The construction of the filter will be described in the next section.

3.2 Design

3.2.1 Construction

Our filter is based on the same principle as a Fabry Perot etalon, namely the interference of multiple beams [57]. A Fabry Perot etalon consists of a plane parallel plate with refractive index n and thickness d, placed in a surrounding medium with refractive index n_0. Another way of looking at it is that it consists of two parallel mirrors, separated by a medium with refractive index n and thickness d. A schematic representation of a Fabry Perot etalon is shown in figure 3.1, where we have assumed that the surrounding medium on both sides is air (with a refractive index of 1).

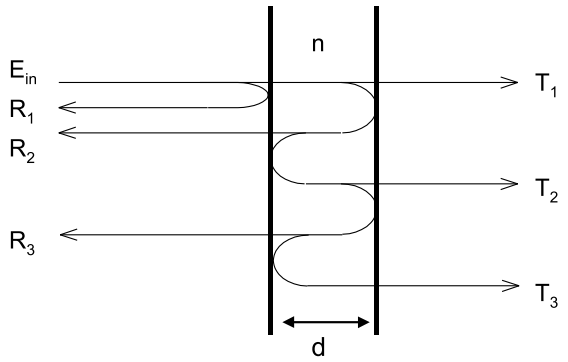

Figure 3.1: Schematic representation of a Fabry Perot etalon.

To study interference effects, the phase relation between the interfering fields has to be taken into account. Therefore we will treat this problem in terms of the (complex) electrical fields travelling through the etalon. We will assume that we are dealing with linear, isotropic and homogeneous media. If, for simplicity, we also assume that the incident field E_{in} is normal to the mirrors, we can write an electrical field travelling along the optical axis Z (which we assume perpendicular to the mirrors) in the form of a monochromatic plane wave [97]:

$$E(z) = E_0 e^{-jkz} \tag{3.1}$$

where $k = n \cdot 2\pi/\lambda$ is the propagation constant of the plane wave in a lossless medium with refractive index n, E_0 is the constant complex amplitude of the electrical field.

When a beam E_{in} is incident on the front mirror, it will be split into two parts: one that is reflected back and one that is transmitted through the front mirror towards the back mirror where it will also will be split into two parts etc. The overall reflection and transmission of an etalon can easily be obtained by simply adding the different contributions in reflection and transmission respectively. For the total reflected field it follows:

$$E_r = E_{in}\left\{r + tt'r'e^{-j2kd}\left[1 + r'^2 e^{-j2kd} + r'^4 e^{-j4kd} + \ldots\right]\right\} \tag{3.2}$$

where r and r' (t and t') are the field reflection (transmission) coefficients for reflection (transmission) from the surrounding medium (air in this case) into the medium between the mirrors and vice versa. r,

r', t and t' are determined by the Fresnel formulas and for normal incidence $r = -r'$ and $t = t'$ so that the power reflectivity R and power transmissivity T are given by $R = r^2 = r'^2$ and $T = tt' = t^2$ respectively [97]. When the mirrors are lossless $R + T = 1$. The term in (3.2) between straight brackets is a power series and can be reduced to $1/(1 - r'^2 e^{-2jkd})$. The total reflected field can thus be written as:

$$E_r = E_{in} \frac{\sqrt{R}(1 - e^{-2jkd})}{(1 - Re^{-2jkd})} \tag{3.3}$$

The reflection response of a Fabry Perot etalon is then given by:

$$R_{FP} = \left| \frac{E_r}{E_{in}} \right|^2 = \frac{4R \sin^2 kd}{(1 - R)^2 + 4R \sin^2 kd} \tag{3.4}$$

The transmission response can be derived in an identical way and is given by:

$$T_{FP} = \frac{(1 - R)^2}{(1 - R)^2 + 4R \sin^2 kd} \tag{3.5}$$

Equation (3.4) and (3.5) are often written in the following form:

$$R_{FP} = \frac{F \sin^2 kd}{1 + F \sin^2 kd} \tag{3.6}$$

and

$$T_{FP} = \frac{1}{1 + F \sin^2 kd} \tag{3.7}$$

with the parameter F determined by $F = 4R/(1 - R)^2$.

To obtain (3.4) and (3.5) we made some simplifying assumptions, i.e. normal incidence, lossless mirrors and lossless media. These assumptions do not change the validity of the above reasoning, however. Furthermore, non-normal incidence, lossy mirrors and lossless media can easily be taken into account. Non-normal incidence will lead to a phase factor $kd \cos\theta$ instead of kd, with θ the angle under which the fields propagate in the etalon. Mirror loss can be taken into account by considering complex field reflection and transmission coefficients (i.e. $r = \sqrt{R}e^{j\psi}$). Obviously, then $R + T = 1 - A$, with A the absorption in the mirrors. Losses in the media finally, can be taken into account by using a complex propagation constant $k = n \cdot 2\pi/\lambda - j\alpha$ with α the loss of the medium. For a more elaborated treatment, the reader is referred to [97].

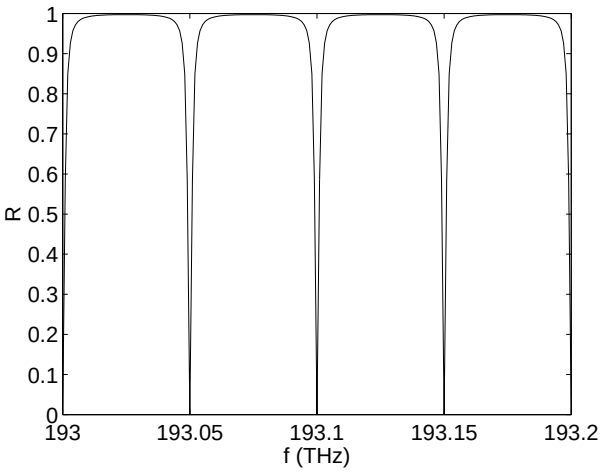

Figure 3.2: Reflection response of a Fabry Perot etalon.

Typical reflection and transmission responses are shown in figure 3.2 and 3.3 respectively. The (power) reflection coefficient of each of the mirrors was 0.9, n was 1.5, the mirrors and the medium in between them were assumed to be lossless. The peaks (dips) occur for frequencies that fulfill the condition $d = m.\lambda/2$, with λ the wavelength of the incident beam and m an integer. The separation between the peaks (dips) is called the free spectral range (FSR) and fulfills $FSR = c/2nd$, with c the speed of light. In this example the FSR was 50 GHz, corresponding with a thickness of 2 mm. As the reflection coefficients of (one of) the mirrors decrease, the extrema will become less pronounced (i.e. they will become wider and their amplitude will decrease) [57].

For a Fabry Perot etalon, it is the interference of the first reflection of the incident beam on the front mirror with the multiple (delayed) reflected beams from the second mirror that gives rise to the form of the reflection response as can be seen in figure 3.2. This is actually the opposite of the comb-like form we want to obtain. But if we could somehow separate the first reflection from the others, the resulting reflection response would resemble the form of the transmission response shown in figure 3.3, thus we would have a filter which has a comb-like response, both in reflection and transmission.

The above reasoning gave rise to the form of our filter, shown in figure 3.4. The filter consists of two right-angle prims with refractive index n and base length L, cemented together with UV-curable index-matching glue. The light will be incident from the left, on facet A of

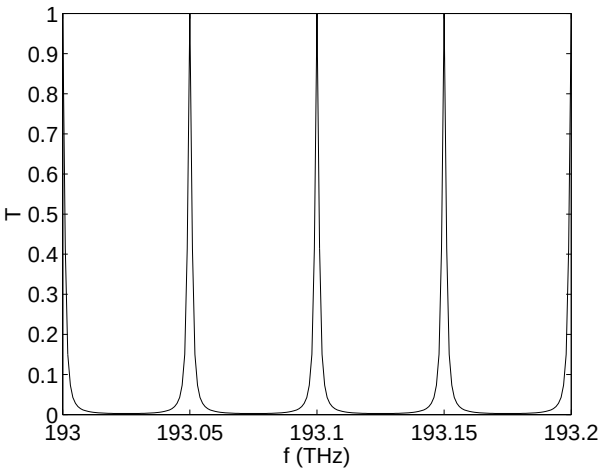

Figure 3.3: Transmission response of a Fabry Perot etalon.

prism 1 and will be transmitted to facet B, C and D and also reflected back to facet A. The beams will undergo multiple reflections in prism 2 and the different reflections will interfere constructively or destructively depending on the frequency of the light, just like in a normal Fabry Perot etalon. Only now there are three mirrors instead of two, namely the three facets S, C and D of the lower prism. The only function of prism 1 is that the incident light can be horizontal (parallel to B and D) for the beams reflecting in prism 2 to be perpendicular to C and D and this without having to worry about total internal reflection on the air-glass interface S (when prism 1 would not be present). For this reason, facet A of prism 1 should be anti-reflection coated.

Since the first reflection (on S) of the incident light is directed towards B and not towards A as would be the case for a normal Fabry Perot etalon, one expects a comb-like reflection response in A (and a comb-like transmission response in C and D). It is of course very important that this first reflection interferes as little as possible with the outputs in A, C and D. That is why facet B also has to be anti-reflection coated. In B one gets the classical Fabry Perot reflection response shown in figure 3.2. The influence of the reflection coefficients of facet S, C and D of prism 2 is analogous to that of the reflection coefficients of the mirrors of a normal Fabry Perot etalon, i.e. that the extrema become wider and their amplitude decreases when the reflection coefficients of the mirrors decrease [57]. Like in a classical Fabry Perot etalon, the mirrors on facet S, C and D will be highly reflective in order to have a

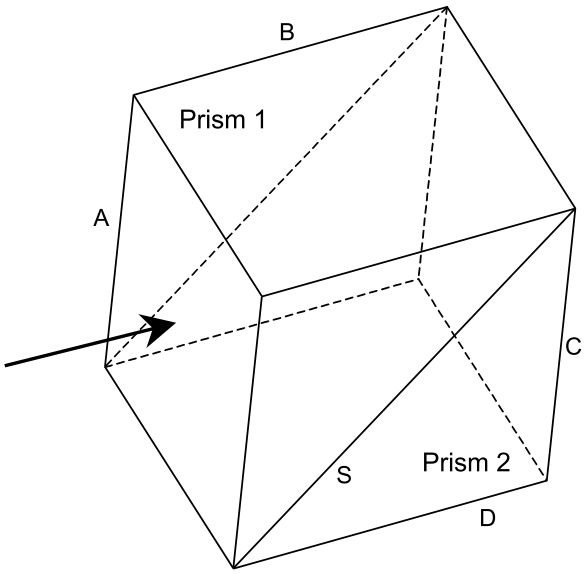

Figure 3.4: Schematic representation of new filter.

sufficiently selective filter. We will go into more detail on the reflection coefficients of these facets in section 3.2.2.

The FSR of this filter is given by $FSR = c/2nL$, with L the base length of the prisms. Thus for a refractive index of 1.5 and a FSR of 100 GHz respectively 50 GHz (standard values for the frequency separation between ITU-channels [58]), the size of the prisms would be 1 mm respectively 2 mm. This is more than small enough to avoid feedback induced instabilities. Practical evidence of this principle will be given in section 3.4.

It should also be noted that the filter basically acts as a 4-port device. The transmission to the (unused) output port at the top facet has periodic dips, while the transmission to the (unused) bottom facet port is similar in behaviour to the transmission to the right facet. These output ports can be used for monitoring purposes.

It was only after we had 'invented' this filter and wanted to patent it, that we found that it was in fact a novel prism-based implementation of a Fox-Smith resonator [60]. This resonator consists of three mirrors in a triangular configuration, which can be compared with the bottom prism of our filter.

3.2.2 Fabrication

As was explained in the previous section, facets A and B should be anti-reflection coated, while the facets S, C and D should receive a highly reflective coating.

A classical way of realizing an anti-reflection coating between two materials with different refractive indices n_1 and n_2 is to apply a layer of a quarter wavelength thickness and with a refractive index of $n_{AR} = \sqrt{n_1 n_2}$ between the two materials. The prisms we used were made of BK7 material (a material often used for lenses and other glass optical components) which has a refractive index n_2 = 1.44402 for wavelengths around 1550 nm. The surrounding medium is air, thus n_1 = 1. This leads to n_{AR} = 1.202. A material that has a refractive index that approximates this value and that is often used as an optical coating material is MgF_2. It has a refractive index of 1.34 around 1550 nm. The corresponding layer thickness of the anti-reflection coating is then $d_{AR} = \lambda/4n_{AR}$ = 294 nm. The calculated (power) reflectivity over the wavelength range between 1450 nm and 1650 nm for normal incidence on a $\lambda/4$ layer of MgF_2 between air and BK7 is shown in figure 3.5. The corresponding phase of the (field) reflection coefficient is constant ($\pm\pi$). Around 1550 nm the reflectivity is R_{AR} = 1.27 % and the corresponding reflection coefficient is $r_{AR} = -\sqrt{R_{AR}}$. When loss in the MgF_2 layer is neglected, the transmissivity is $T_{AR} = 1 - R_{AR}$ = 98.73 % and the corresponding transmission coefficient is $t^i_{AR} = -i \cdot \sqrt{T_{AR}}/n_2$ [97], with n_2 = 1.44402 the refractive index of the prism material BK7. For transmission from the prisms through the anti-reflection coating into air, the corresponding transmission coefficient would be $t^o_{AR} = -i \cdot \sqrt{T_{AR}} \cdot n_2$.

It should be mentioned that an even lower reflectivity can be obtained with more complex multiple layer coatings from selected materials. But since for our purpose, a remaining reflectivity of around 1 % could be tolerated, we opted for the fastest and cheapest solution.

The highly reflective mirrors were realized by depositing a stack of alternating high and low refractive index $\lambda/4$ layers on top of the BK7 material. This is also a classical way of realizing highly reflective coatings. For the high refractive index material we used amorphous Si with n_H = 3.73, for the low refractive index material we used Al_2O_3 with n_L = 1.63. The corresponding thickness (again for a central wavelength of 1550 nm) of the Si layers is then 104 nm, that of the Al_2O_3 layers 238 nm. Figure 3.6 shows a schematic representation of a highly reflective mirror consisting of three Si–Al_2O_3 pairs.

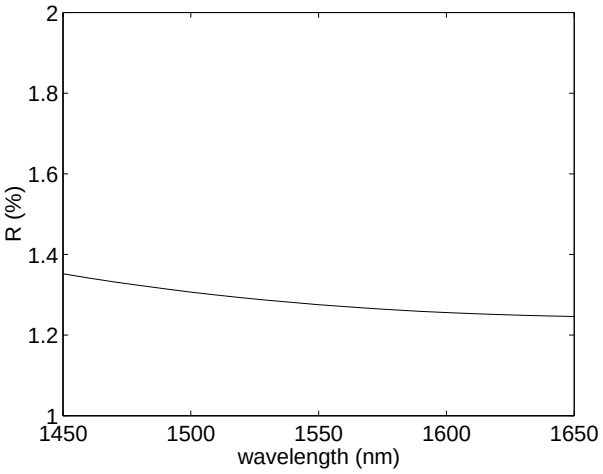

Figure 3.5: Calculated reflectivity for a $\lambda/4$ MgF_2 AR-coating on top of BK7 material, for normal incidence from air into BK7.

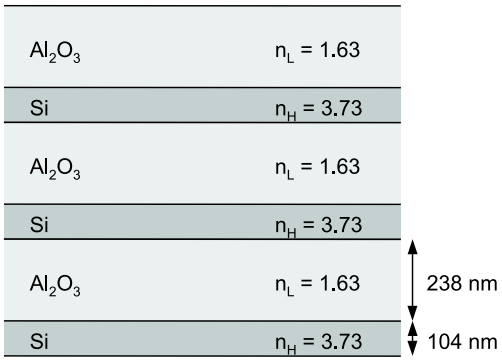

Figure 3.6: Schematic representation of a highly reflective mirror consisting of three Si–Al_2O_3 pairs.

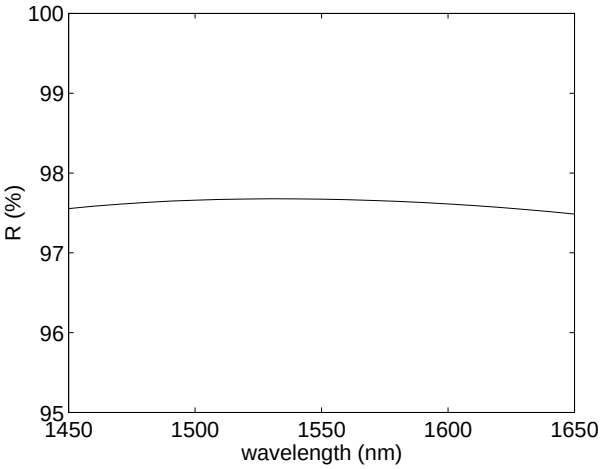

Figure 3.7: Calculated reflectivity for an HR-coating consisting of three Si–Al_2O_3 pairs on top of BK7, for normal incidence from BK7 into air.

For the coatings on facet C and D three pairs were applied, on facet S only one pair was applied. In all cases the order of the layers was BK7–Si–Al_2O_3. The calculated reflectivity for normal incidence out of the lower prism through a stack of three Si–Al_2O_3 pairs on top of BK7 is shown in figure 3.7. Around 1550 nm the reflectivity is R_{HR} = 98 % and the corresponding reflection coefficient is $r_{HR} = -\sqrt{R_{HR}}$. The phase of the field reflection coefficient is constant ($\pm\pi$). The transmissivity is $T_{HR} = 1 - R_{HR}$ = 2 % and the corresponding transmission coefficient is $t_{HR} = -n_2 \cdot \sqrt{T_{HR}}$. If the layer order would be reversed, i.e. first a layer of Al_2O_3 on top of the BK7 and then a layer of Si, R_{HR} would remain (nearly) unchanged, but r_{HR} would become positive instead of negative. The phase of t_{HR} remains unchanged.

Higher reflectivities can be obtained by using more pairs, but for our purposes 98 % suffices.

On facet S the light will be incident under an angle of 45 degrees. This means that the layer thickness will have to be adapted. For a central wavelength of 1550 nm the thickness of the Si layers becomes 108 nm, that of the Al_2O_3 layers becomes 376 nm. For non-normal incidence the reflectivity for TE– and TM–polarization will no longer be the same. However, since light from semiconductor lasers is almost exclusively TE–polarized, we will only consider the reflection coefficients for TE–polarization. Figure 3.8 shows the calculated reflectivity for TE-polarization, for incidence under 45 degrees from the lower

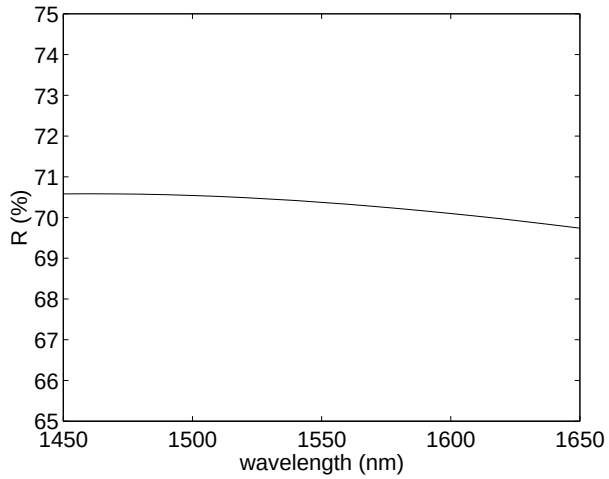

Figure 3.8: Calculated reflectivity for TE-polarization for an HR-coating consisting of a Si–Al_2O_3 pair on top of BK7, for incidence under 45 degrees in BK7.

prism through the Si–Al_2O_3 pair into the upper prism. The phase of the field reflection coefficient is constant ($\pm\pi$). Around 1550 nm the reflectivity is R_s = 70 % and the corresponding reflection coefficient is $r_s^- = -\sqrt{R_s}$. The transmissivity is $T_s = 1 - R_s$ = 30 % and the corresponding transmission coefficient is $t_s = -\sqrt{T_s}$. The rays that are coming from facet A or B and that are transmitted through facet S, will see a different layer order than the rays that are reflected at facet C or D. The layer order for rays coming from facet A or B is BK7–Al_2O_3–Si instead of BK7–Si–Al_2O_3. The angle of incidence is also 45 degrees for rays coming from facet A or B and the reflectivity also stays the same. The corresponding phase however does change: for reflection in the upper prism on facet S the phase of the reflection coefficient is 0 degrees instead of –180 degrees, so that $r_s^+ = \sqrt{R_s} = -r_s^-$. The phase of the transmission coefficient remains unchanged at 180 degrees. The reason that only one pair was used for the mirror on facet S will be explained in section 3.3.

All the coatings were applied in our own clean-room facilities by e-gun deposition. The prisms that we used were high-precision right-angle prisms with a base length L of 3.2 mm, giving rise to a FSR of around 32.5 GHz. This was the smallest available standard size for these high-precision right-angle prisms. In a network environment, a prism base length that corresponds with a FSR of 100 GHz (or 50 GHz)

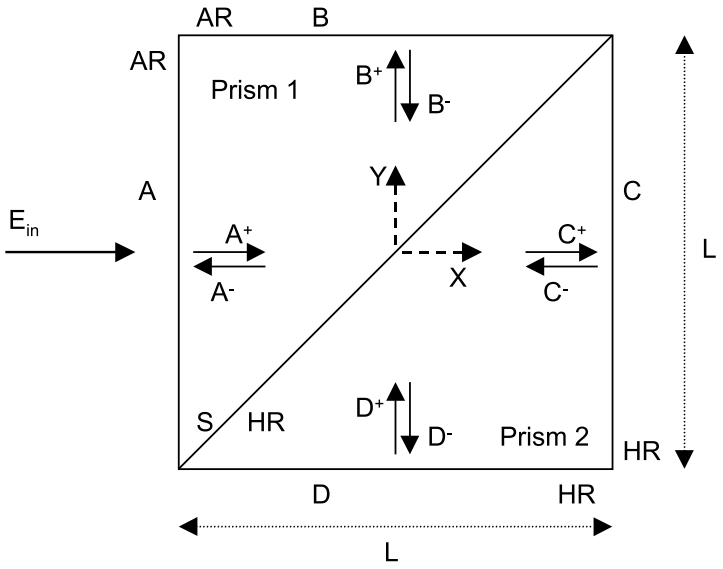

Figure 3.9: Nomenclature of the electrical fields in the filter.

would be more desirable. In that case the base length would be around 1 mm and 2 mm respectively and one would require custom-made prisms. For a proof of principle however, a FSR of 32.5 GHz is an acceptable value. If necessary, any prism size and thus any FSR can be custom made. The prisms have a dimension tolerance of ± 0.1 mm, a surface flatness of $\lambda/8$ at 632.8 nm and an angle tolerance of ± 30 arcseconds. The two prisms were manually cemented together with UV-curable index-matching paste with a refractive index of 1.445 at 1550 nm.

3.3 Reflection and transmission characteristics

3.3.1 Theoretical derivation

In this section we will determine the reflection and transmission characteristics of our filter. As we explained when deriving the reflection and transmission characteristics of a Fabry Perot etalon, the phase relation between the interfering fields has to be taken into account. Therefore we will also treat this problem in terms of the (complex) electrical fields inside the filter. Assuming that we are dealing with linear, isotropic and homogeneous media and with the coordinate axes chosen as in

figure 3.9 we can write an electrical field travelling along the X-axis in the form of a (monochromatic) plane wave [97]:

$$E^{\pm}(x) = E_0^{\pm} e^{\mp jkx} \tag{3.8}$$

where $k = \beta - j\alpha$, with $\beta = n \cdot 2\pi/\lambda$ the propagation constant of the filter medium (with refractive index n) and α the loss of the medium, E_0 is the constant complex amplitude of the electrical field. $E^+(x)$ is the field propagating along the direction of the X-axis and $E^-(x)$ the field propagating in the opposite direction. Similar observations hold for fields travelling along the Y-axis.

We will also assume that dispersion in the medium can be neglected and that the reflection and transmission coefficients of the different facets are independent of wavelength and polarization. The fields will be denoted as represented in figure 3.9

The reflection and transmission characteristics of the filter can now be deduced from the relations that exist between the fields due to the reflections and transmissions at the different facets. In the center of the filter ($x = y = 0$) the following relations hold:

$$A^-(0) = r_s^+ B^-(0) + t_s C^-(0) \tag{3.9a}$$
$$B^+(0) = r_s^+ A^+(0) + t_s D^+(0) \tag{3.9b}$$
$$C^+(0) = t_s A^+(0) + r_s^- D^+(0) \tag{3.9c}$$
$$D^-(0) = t_s B^-(0) + r_s^- C^-(0) \tag{3.9d}$$

or

$$a^- = r_s^+ b^- + t_s c^- \tag{3.10a}$$
$$b^+ = r_s^+ a^+ + t_s d^+ \tag{3.10b}$$
$$c^+ = t_s a^+ + r_s^- d^+ \tag{3.10c}$$
$$d^- = t_s b^- + r_s^- c^- \tag{3.10d}$$

where r_s^+ and r_s^- are the reflection coefficients for reflection at facet S in the upper and lower prism respectively. As was explained in section 3.2.2 $r_s^+ = -r_s^- = \sqrt{R_s}$. t_s is the transmission coefficient for transmission at facet S (as also explained in section 3.2.2 this is the same for transmission from the upper into the lower prism as for transmission in the opposite direction).

The fields will also reflect (and refract) at the different facets. In this way, $A^+(-\frac{L}{2})$, $B^-(\frac{L}{2})$, $C^-(\frac{L}{2})$ and $D^+(-\frac{L}{2})$ will be coupled with

$A^-(-\frac{L}{2})$, $B^+(\frac{L}{2})$, $C^+(\frac{L}{2})$ and $D^-(-\frac{L}{2})$ respectively through the reflection coefficients of the corresponding facets.

Since there are no sources of fields inside the filter, there obviously has to be an (external) input field E_{in} incident on the filter. The application we have in mind for this filter is the stabilization of the wavelength switching behaviour of tunable lasers through optical feedback from the filter. As already mentioned above, the laser light will be incident on the filter at facet A and we are interested in the light leaving the filter through facet C. In that case we have a comb-like reflection characteristic, the peaks of which will provide a stable frequency reference to the laser. But we will also have a comb-like transmission characteristic with its peaks on the same frequencies as the peaks of reflection characteristic. This means that on the frequencies the laser is stabilized on, the output power will not be suppressed by dips in the filter transmission characteristic.

Thus, we will calculate the reflection and transmission characteristics of the filter for an input field E_{in} incident on facet A. The reflection of $A^-(-\frac{L}{2})$, $B^+(\frac{L}{2})$, $C^+(\frac{L}{2})$ and $D^-(-\frac{L}{2})$ at facet A, B, C and D respectively, leads to the following relations:

$$a^+ = r_a a^- e^{-jkL} + t_a E_{in} e^{-jk\frac{L}{2}} \tag{3.11a}$$

$$b^- = r_b b^+ e^{-jkL} \tag{3.11b}$$

$$c^- = r_c c^+ e^{-jkL} \tag{3.11c}$$

$$d^+ = r_d d^- e^{-jkL} \tag{3.11d}$$

where r_a, r_b, r_c and r_d are the reflection coefficients for reflection at facet A, B, C and D respectively and where we have taken the incidence of the input field E_{in} on facet A into account.

If we now substitute (3.10d) into (3.11d), it follows that:

$$d^+ = r_d(t_s b^- + r_s^- c^-)e^{-jkL} \tag{3.12}$$

So that, substituting (3.11a) and
(3.12) into (3.10b) respectively (3.10c) yields:

$$b^+ = r_s^+(t_a e^{-jk\frac{L}{2}} E_{in} + r_a a^- e^{-jkL}) + t_s r_d(t_s b^- + r_s^- c^-)e^{-jkL} \tag{3.13}$$

and

$$c^+ = t_s(t_a e^{-jk\frac{L}{2}} E_{in} + r_a a^- e^{-jkL}) + r_s^- r_d(t_s b^- + r_s^- c^-)e^{-jkL} \tag{3.14}$$

Substituting (3.10a) into (3.13) respectively (3.14) and using (3.11b) and (3.11c) yields for b^+ and c^+:

$$b^+ = \frac{r_s^+ t_a e^{-jk\frac{L}{2}} E_{in} + r_s^+ t_s (r_a - r_d) r_c e^{-2jkL} c^+}{1 - r_b(r_a R_s + r_d t_s^2) e^{-2jkL}} \tag{3.15}$$

and

$$c^+ = \frac{t_a t_s e^{-jk\frac{L}{2}} E_{in} + r_s^+ t_s (r_a - r_d) r_b e^{-2jkL} b^+}{1 - r_c(r_a t_s^2 + r_d R_s) e^{-2jkL}} \tag{3.16}$$

where we have used $r_s^+ = -r_s^-$ and $r_s^{+2} = r_s^{-2} = R_s$.

So that substituting (3.15) into (3.16) finally yields for $C^+(\frac{L}{2}) = c^+ e^{-jk\frac{L}{2}}$:

$$C^+(\frac{L}{2}) = \frac{t_a t_s e^{-jkL}\left[1 - r_b r_d e^{-2jkL}\right]}{D} E_{in} \tag{3.17}$$

where we have used $t_s^2 + R_s = 1$. In the above equation the denominator D is determined by:

$$\begin{aligned} D =& 1 - \left[r_a(r_b R_s + r_c t_s^2) + r_d(r_b t_s^2 + r_c R_s)\right] e^{-2jkL} \\ &+ r_b r_c \left[(r_a R_s + r_d t_s^2)(r_a t_s^2 + r_d R_s) - (r_a - r_d)^2 R_s t_s^2\right] e^{-4jkL} \end{aligned} \tag{3.18}$$

Now, $B^+(\frac{L}{2}) = b^+ e^{-jk\frac{L}{2}}$ can be obtained from (3.15):

$$B^+(\frac{L}{2}) = \frac{t_a r_s^+ e^{-jkL}\left[1 - r_c r_d e^{-2jkL}\right]}{D} E_{in} \tag{3.19}$$

Finally, $A^-(-\frac{L}{2}) = a^- e^{-jk\frac{L}{2}}$ and $D^-(-\frac{L}{2}) = d^- e^{-jk\frac{L}{2}}$ can be obtained from (3.10a) and (3.10d) using (3.11b), (3.11c), (3.17) and (3.19):

$$A^-(-\frac{L}{2}) = \frac{t_a e^{-2jkL}\left[r_b R_s + r_c t_s^2 - r_b r_c r_d e^{-2jkL}\right]}{D} E_{in} \tag{3.20}$$

and

$$D^-(-\frac{L}{2}) = \frac{t_a e^{-2jkL} r_s^+ t_s (r_b - r_c)}{D} E_{in} \tag{3.21}$$

The (power) reflection and transmission characteristics of the filter can now be obtained from $A^-(-\frac{L}{2})$, $B^+(\frac{L}{2})$, $C^+(\frac{L}{2})$ and $D^-(-\frac{L}{2})$ as follows:

$$R = \left| \frac{r_a + t_a^o A^-(-\frac{L}{2})}{E_{in}} \right|^2 \tag{3.22a}$$

$$T_B = \left| \frac{t_b B^+(\frac{L}{2})}{E_{in}} \right|^2 \tag{3.22b}$$

$$T = \left| \frac{t_c C^+(\frac{L}{2})}{E_{in}} \right|^2 \tag{3.22c}$$

$$T_D = \left| \frac{t_d D^-(-\frac{L}{2})}{E_{in}} \right|^2 \tag{3.22d}$$

t_a^o is the transmission coefficient for transmission out of the prism through the MgF_2 anti-reflection coating into air. The t_a used in the other equations is the transmission coefficient for the opposite direction of propagation.

3.3.2 Examples

We will now show some reflection and transmission characteristics of our filter, calculated using the expressions we have just derived. As values for the reflection coefficients of the different coatings we will use the values mentioned in section 3.2.2: $R_a = R_b = R_{AR}$ = 0.0127 for the anti-reflection coatings on facet A and B, $R_c = R_d = R_{HR}$ = 0.98 for the highly reflective coatings on facet C and D and R_s = 0.7 for the highly reflective coatings on facet S. As explained in section 3.2.2, care has to be taken to determine the phase of the corresponding field reflection and transmission coefficients. For the AR coatings we have applied, the field reflection and transmission coefficients are given by $r_a = -\sqrt{R_a}$, $r_b = -\sqrt{R_b}$, $t_a^i = -i \cdot \sqrt{T_a}/n_{BK7}$, $t_a^o = -i \cdot \sqrt{T_a} \cdot n_{BK7}$ and $t_b^o = -i \cdot \sqrt{T_b} \cdot n_{BK7}$, where t_a^i is the field coefficient for transmission from air into BK7 and t_a^o and t_b^o are the field coefficient for transmission from BK7 into air. For the HR coatings we have applied, the field reflection and transmission coefficients are given by $r_c = -\sqrt{R_c}$, $r_d = -\sqrt{R_d}$, $t_c^o = -n_{BK7} \cdot \sqrt{T_c}$, $t_d^o = -n_{BK7} \cdot \sqrt{T_d}$ for the HR coating consisting of three Si–Al_2O_3 pairs on facets C and D. As mentioned in section 3.2.2, the phase of r_c and r_d can be changed from -180° to 0°. For the coating consisting of one Si–Al_2O_3 pair on facet S we have $r_s^+ = \sqrt{R_s} = -r_s^-$ and $t_s = -\sqrt{T_s}$.

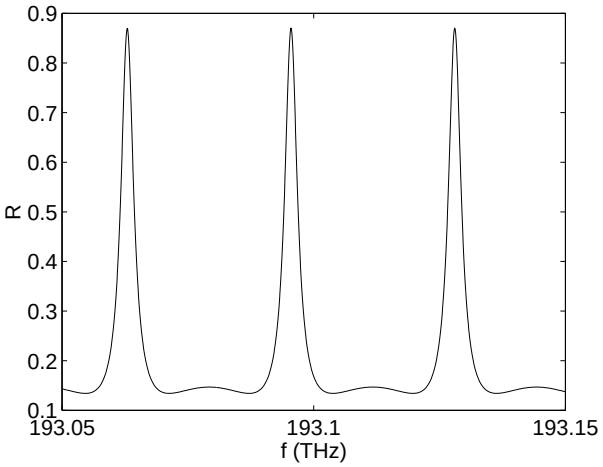

Figure 3.10: Reflection response of double-prism filter. The reflection coefficients of the HR coatings are chosen so that the reflection at the peaks is at least 80 % ($R_a = R_b$ = 0.0127, $R_c = R_d$ = 0.98 and R_s = 0.7).

As already mentioned, we are especially interested in the reflection back to the laser R and the transmission through the filter T. Figure 3.10 shows the reflection calculated from (3.22a) and figure 3.11 shows the transmission calculated from (3.22c).

From figure 3.10 and 3.11 it is clear that we have a comb-like response in reflection as well as in transmission, with the peaks on the same frequencies. The FSR of the filter lies around 32.5 GHz, which corresponds with a base length of the prisms L = 3.2 mm. The FWHM of the filter peaks is about 3.3 GHz. As mentioned in section 3.2.1, the FWHM will increase (decrease) when the reflectivity of (one of) the coatings decreases (increases). It can also be seen that for these values of the reflection coefficients of the different coatings, the (peak) reflection back to the laser is a lot stronger (more than 80 %) than the (peak) transmission through the filter (which is less than 10 %). The reason that we designed the filter like this is that we want to stabilize the wavelength switching behaviour of a semiconductor tunable laser through optical feedback from the filter. In chapter 2 it was explained that not only should the external cavity round-trip time be kept sufficiently small, but that it is also very important that the feedback ratio (i.e. the fraction of the power emitted by the laser that is coupled back into the laser) is sufficiently large to avoid instabilities caused by the feedback (e.g. coherence collapse) [50, 55]. Typically, the feedback ratio

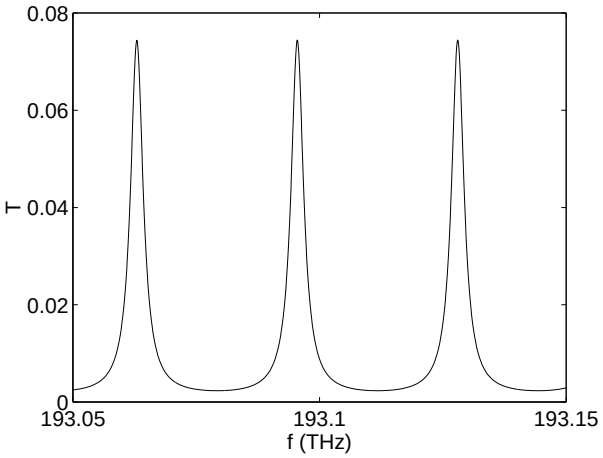

Figure 3.11: Transmission response of double-prism filter. The reflection coefficients of the HR coatings are chosen so that the reflection at the peaks is at least 80 % ($R_a = R_b$ = 0.0127, $R_c = R_d$ = 0.98 and R_s = 0.7).

should be at least –10 dB. In an ideal situation 10 % reflection from the filter should thus suffice. Unfortunately, in practice one has to deal with coupling losses between the laser and the filter. Furthermore, one has to take into account manufacturing tolerances for the different coatings. For these reasons and since our main goal was to prove the stabilization of the wavelength switching behaviour of a tunable laser through optical feedback from the filter, we opted for a reflection of a least 80 %.

This is also the reason why only one Si–Al_2O_3 pair was applied on facet S. For two Si–Al_2O_3 pairs R_s would already be 97 % and with this value for R_s it is not possible to obtain a high reflection back to the laser. This is illustrated in figure 3.12 where R is shown for $R_a = R_b$ = 0.0127, $R_c = R_d$ = 0.98 and R_s = 0.97. Comparing figure 3.10 and figure 3.12, it can be clearly seen that the FWHM of the filter peaks decreases when the reflectivity of (one of) the coatings increases.

For completeness figure 3.13 shows the upward and downward transmission through facet B and D, calculated from (3.22b) and (3.22d) respectively for $R_a = R_b$ = 0.0127, $R_c = R_d$ = 0.98 and R_s = 0.7. As explained in section 3.2.1 the transmission through facet B resembles a classical Fabry Perot reflection response, while in facet D one gets a classical Fabry Perot transmission response. As a verification of the theoretical expressions for R, T_B, T and T_D, the sum $R + T_B + T + T_D$, which must equal unity, is also shown on figure 3.13.

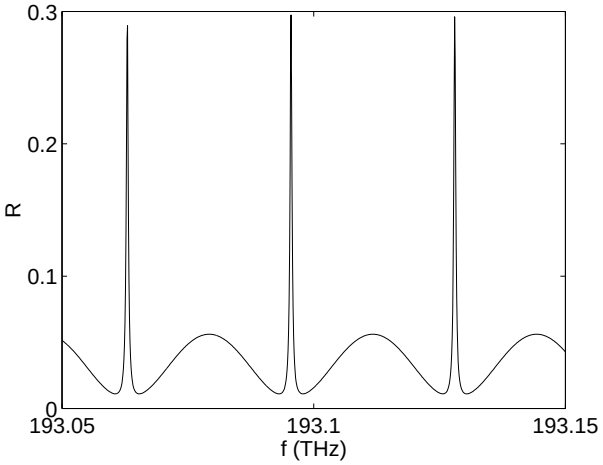

Figure 3.12: Reflection response of double-prism filter for a HR coating on facet S consisting of two Si–Al_2O_3 pairs ($R_a = R_b$ = 0.0127, $R_c = R_d$ = 0.98 and R_s = 0.97).

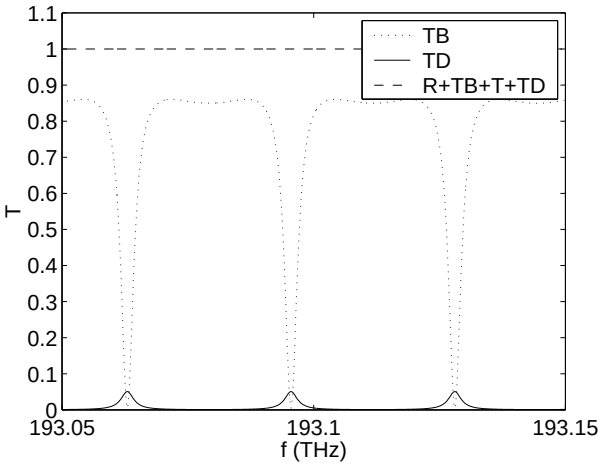

Figure 3.13: Upward and downward transmission response of double-prism filter. The sum $R+T_B+T+T_D$ is also shown ($R_a = R_b$ = 0.0127, $R_c = R_d$ = 0.98 and R_s = 0.7).

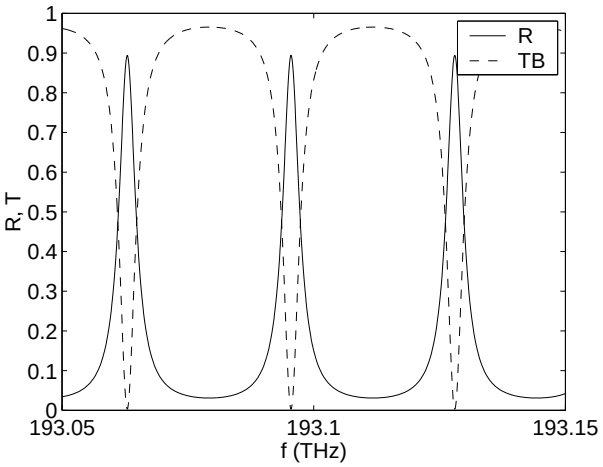

Figure 3.14: Reflection and upward transmission response of double-prism filter for perfect AR coatings on facet A and B ($R_a = R_b$ = 0, $R_c = R_d$ = 0.98 and R_s = 0.7).

The small ripple that is visible between the filter peaks in figure 3.10 and figure 3.12 and between the filter dips in figure 3.13 is due to the imperfect AR coatings on facet A and B. This is illustrated in figure 3.14 where the reflection back to the laser R and the upward transmission T_B are shown for $R_a = R_b$ = 0, $R_c = R_d$ = 0.98 and R_s = 0.7.

For application in a telecommunication network, an as high as possible laser output power is desirable. Therefore a higher transmission through the filter would be necessary. It is possible to have more transmission (at the cost of a lower reflection of course) by adapting the reflection coefficients of the different coatings. However, the reflection back to the laser should remain high enough to avoid feedback induced instabilities. Since at least 10 % reflection is required and since the coupling loss of the light from the laser to the filter and back into the laser will be a least 3 dB [98], a design aimed at 30 to 40 % reflection would be preferable. This can be obtained by appropriately choosing the reflection coefficients of the different HR coatings. Basically we want to divide the input power between the reflection through facet A and the transmission through facet C. Therefore, to avoid loss of power through facet D, the reflectivity of this facet should be as high as possible. The maximum obtainable reflectivity is of course R_d = 1. From equation (3.22c) it can be found that appropriate values for R_c and R_s would be 0.9. The values of the reflection coefficients of the AR coat-

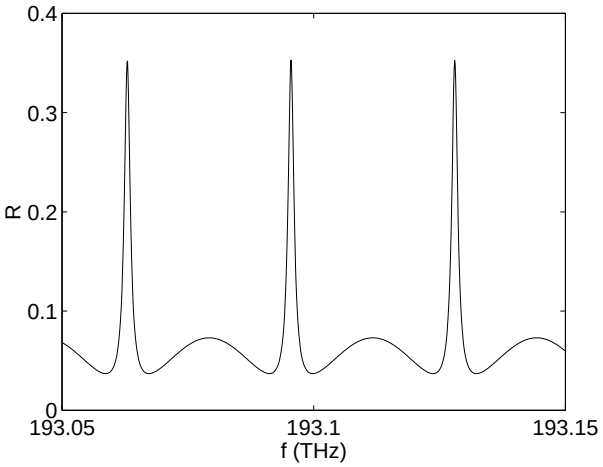

Figure 3.15: Reflection response of double-prism filter. The reflection coefficients of the HR coatings are chosen so that the reflection at the peaks is between 30 and 40 % ($R_a = R_b$ = 0.0127, $R_c = R_s$ = 0.9 and R_d = 1).

ings remain $R_a = R_b$ = 0.0127. Figure 3.15 and 3.16 show the reflection and transmission response of the filter with the reflection coefficients of the HR coatings chosen in such a way that the reflection at the peaks is between 30 and 40 %.

It can be remarked that even in the case where there is only about 40 % reflection back to the laser, there still is an additional loss of about 50 % or –3 dB compared to the case without filter. This does not pose a major problem however, since this additional loss can be compensated by increasing the laser gain, which can be achieved e.g. by making the gain section of the laser (slightly) longer.

So far we only have discussed very few of the obtainable reflection and transmission responses of this filter. There are many more combinations of reflection coefficients (amplitude and phase) possible, however not all with equal practical usefulness. It is not the goal of this thesis to investigate all possible combinations of reflection coefficients. One thing we would like to show however, is that our filter can also behave as a classical Fabry Perot etalon. I.e. that the reflection from facet A R will resemble a classical Fabry Perot reflection and the transmission through facet C T will resemble a classical Fabry Perot transmission. To obtain this, it is clear from section 3.2.1 that R_b should be increased. This is illustrated in figure 3.17 where R and T are shown for R_a = 0.0127, $R_b = R_c$ = 0.9 and $R_d = R_s$ = 0.98. The phase of r_c

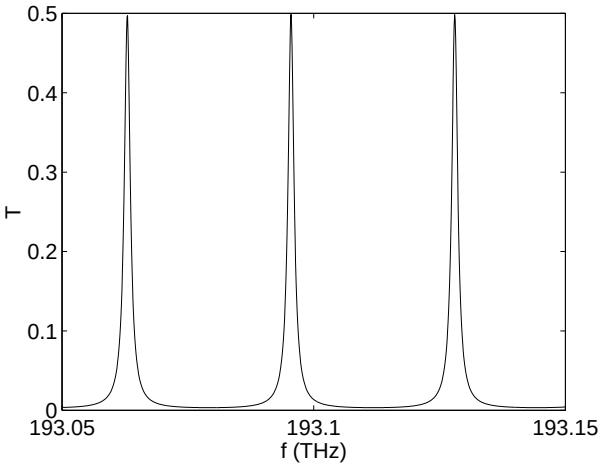

Figure 3.16: Transmission response of double-prism filter. The reflection coefficients of the HR coatings are chosen so that the reflection at the peaks is between 30 and 40 % ($R_a = R_b$ = 0.0127, $R_c = R_s$ = 0.9 and R_d = 1).

and r_d was changed from -180° to 0°. In practice this can be achieved by reversing the layer order of the HR coatings from BK7–Si–Al_2O_3 to BK7–Al_2O_3–Si.

So far we have always assumed that the light was incident normal to facet A (i.e. parallel to the X-axis in figure 3.9). This is also the way the filter will be used in practice. Because for non-normal incidence (either because the laser plus lens or the filter or both are not positioned perfectly horizontally) a few complications arise. First of all, the reflected rays will not leave the filter at the same vertical position. This is illustrated in figure 3.18: the first three rays leave the filter at different vertical positions. As a consequence, part of the beams will not be captured by the lens . Furthermore, even a part of the rays that are captured by the lens will not be able to re-enter in the (very small) active layer of the laser. Other beams will even be reflected under opposite angles. This is also illustrated in figure 3.18: the fourth contribution (ray 4 on the figure) to the overall reflection has first reflected on facet D before leaving the filter through facet A and it will leave the filter under a different angle than the first three contributions. Another consequence of non-normal incidence is that the frequency of the peaks in the filter response will shift [57].

It should be clear that for non–normal incidence less beams will be able to re-enter the active layer of the laser than for normal incidence.

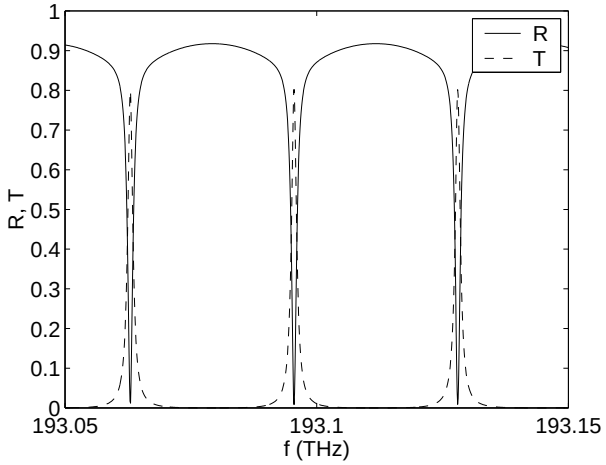

Figure 3.17: Reflection and transmission response of double-prism filter behaving like a Fabry Perot etalon (R_a = 0.0127, $R_b = R_c$ = 0.9 and $R_d = R_s$ = 0.98).

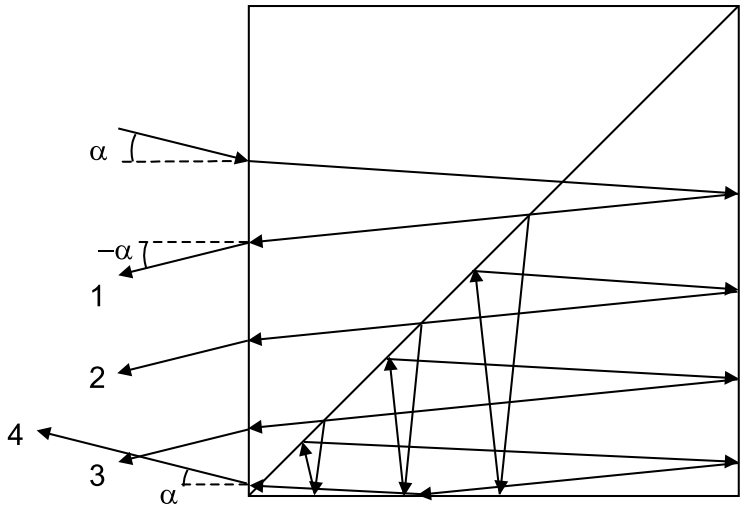

Figure 3.18: Schematic representation of the rays for non-normal incidence.

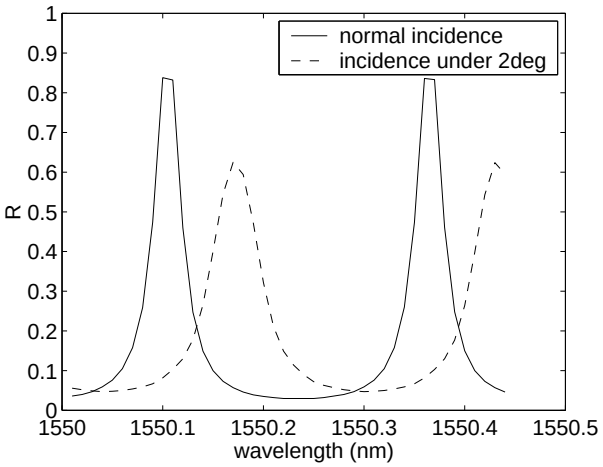

Figure 3.19: Reflection response for normal incidence and for incidence under an angle of 2° with the X-axis ($R_a = R_b$ = 0, $R_c = R_d$ = 1 and R_s = 0.7).

This means that the resulting interference will be less strong. This is illustrated in figure 3.19 which shows the reflection of the filter for normal incidence and for incidence under an angle of 2° with the X-axis (i.e. the axis perpendicular to the page). These results were calculated with the ray-tracing tool ASAP. In ASAP, a laser beam is represented by a Gaussian beam, which gives a more accurate result than a simple ray representation. To speed up the calculations, we assumed that the AR-coatings on facet A and B were perfect (i.e. $R_a = R_b$ = 0) and that the HR-coatings on facet C and D were perfect mirrors (i.e. $R_c = R_d$ = 1), the reflectivity of the coating on facet S was as before (i.e. R_s = 0.7). It can be seen that the response for normal incidence agrees very well with that shown in figure 3.14. As was expected, for non-normal incidence the response has shifted and is less pronounced. Figure 3.19 even gives an over-estimation for the reflection that will re-enter in the laser for the case of non-normal incidence, since the lens was assumed to be ideal and the detector was bigger than the typical dimensions of the active layer of a semiconductor laser.

We did also take into account the influence of the glue layer between the prisms. This layer has a slightly different refractive index (1.445 versus 1.44402 for the prism material at 1550 nm) and was assumed to be around 1 μm thick. As can be seen from figure 3.19, the glue layer does not have a noticeable effect on the filter response.

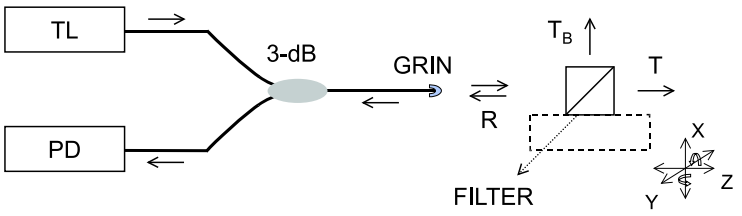

Figure 3.20: Measurement setup for determining the filter responses. The filter is mounted on a 3D-translation/2D-rotation stage (TL = tunable laser source, PD = photo detector, 3-dB = 3-dB fibre coupler, GRIN = GRIN-lens).

3.4 Experimental Characterization

A prototype of the filter design described in section 3.2 has been experimentally characterized to determine the viability of the novel filter concept. The responses were obtained by collimating the light of a tunable laser through a GRIN-lens and making it incident on the filter. Then the output power at the respective output ports was measured while the wavelength of the laser was swept. The reflection response was measured by coupling the reflected light through the GRIN lens back into the fibre coming from the tunable laser source. The backward propagating light in the fibre was sent to a photo detector using a 3–dB fibre coupler. Figure 3.20 shows a schematic representation of the measurement setup with the filter mounted on a 3D-translation/2D-rotation stage (TL is the tunable laser source, PD is a photo detector, 3–dB represents the 3–dB fibre coupler, GRIN is the GRIN-lens).

The experimentally determined outputs at facet A (the reflection response R – broken line) and C (the transmission response T – full line) are shown in figure 3.21. For completeness the output at B (the upward transmission T_B) is shown in figure 3.22. It is clear that the experimentally determined responses R, T and T_B agree very well with the corresponding theoretical responses shown in figure 3.10, 3.11 and 3.13 respectively. Small differences (e.g. the fact that T_B does not completely drop to zero in figure 3.22) are due to losses in the mirrors, the filter material and in the glue layer, and due to fabrication tolerances on the different coatings. For the same reasons, the measured FWHM of the filter peaks is higher than expected: 4.2 GHz instead of 3.3 GHz.

It is clear that we have succeeded in our main goal, which was to develop a compact filter with a comb-like response in reflection as well as in transmission. Using this filter it will be possible to improve

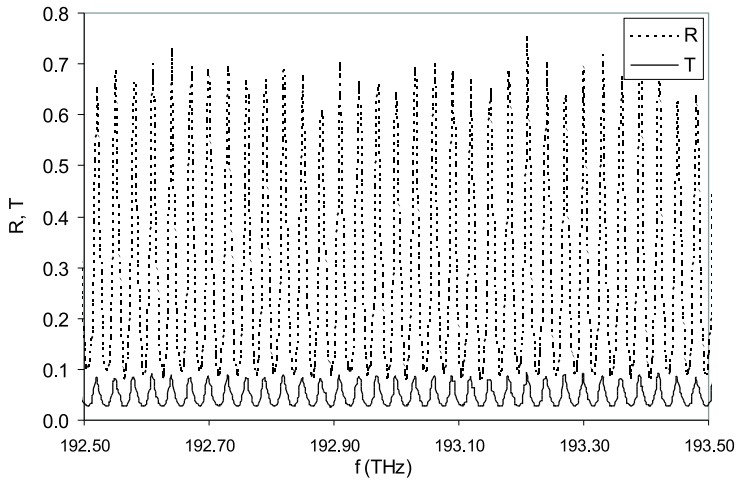

Figure 3.21: Experimentally determined reflection (broken line) and transmission (full line) response of the novel filter type ($R_a = R_b$ = 0.0127, $R_c = R_d$ = 0.98 and R_s = 0.7).

the wavelength switching behaviour of a semiconductor tunable laser through optical feedback. The strong reflection of more than 70 % will ensure a feedback ratio (i.e. the fraction of the power emitted by the laser that is coupled back into the laser after reflection on the filter) that is sufficiently large to avoid instabilities caused by the optical feedback.

3.5 Conclusion

In this chapter, we have described the design of a filter that has a comb-like response in transmission as well as in reflection. The filter was based on a novel prism-based implementation of a Fox-Smith resonator. The reason we developed this filter is that we needed such a filter to enhance the wavelength switching behaviour of semiconductor tunable laser through optical feedback from a reference filter. And since existing comb filters only have a comb-like response in transmission, it was difficult to implement the feedback scheme without destabilizing the laser by the feedback.

We have described the design of the filter, derived theoretical expressions for its reflection and transmission characteristics and showed numerical examples of possible filter characteristics. The processing

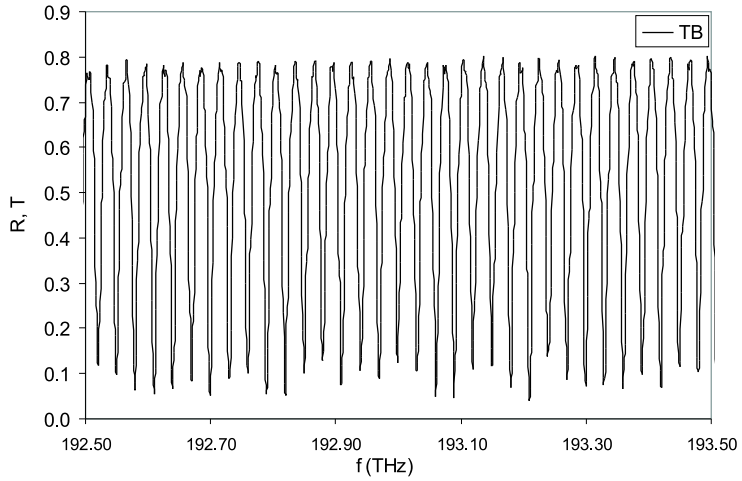

Figure 3.22: Experimentally determined upward transmission response of the novel filter type ($R_a = R_b$ = 0.0127, $R_c = R_d$ = 0.98 and R_s = 0.7).

of a prototype device was described and experimentally determined reflection and transmission responses where shown, proving that the novel filter concept indeed works. The filter can thus be used as a reference filter where the wavelength of a semiconductor (tunable) laser can be stabilized at through optical feedback. The improvement of the wavelength switching behaviour of a tunable laser through optical feedback from the filter will be described in the next chapter.

Chapter 4

Improvement of the wavelength switching behaviour of tunable lasers through optical feedback from a periodic filter

In this chapter we will show that the wavelength switching behaviour of semiconductor tunable lasers can be considerably improved through optical feedback from a stable periodic reference filter. The filter is based on the novel design described in the previous chapter and has a response consisting of periodically spaced peaks, both in reflection and transmission. The improvement of the wavelength switching behaviour stems from the suppression of the thermally induced wavelength drift associated with the switching of the tuning currents. In a first section some numerical results will be presented that show the influence of the optical feedback on the tuning table and the wavelength switching behaviour of a tunable laser. In the second section experimental characteristics of a tunable laser optically coupled with the filter will be shown.

4.1 Simulation results

In this section we will numerically investigate the influence of the optical feedback on the tuning table and the wavelength switching be-

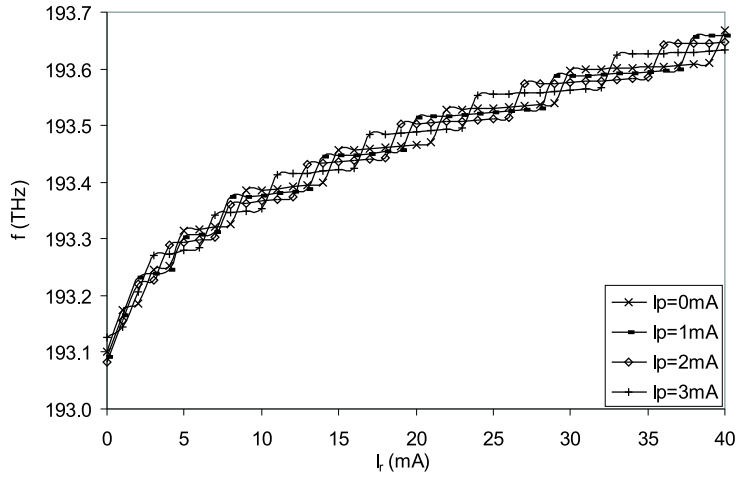

Figure 4.1: Laser frequency of a solitary three-section DBR tunable laser as a function of reflector tuning current for I_p = 0, 1, 2 and 3 mA.

haviour of a tunable laser. More in particular we will investigate the influence of the external cavity length and the feedback strength. The simulations were again performed using the commercially available software VPI Componentmaker [56]. First we will briefly review the tuning characteristics of a tunable laser without feedback.

4.1.1 Tunable laser without feedback

Figure 4.1 shows (part of) the calculated tuning table of a three-section DBR tunable laser without any form of feedback. The laser frequency is shown as a function of the tuning current through the reflector section I_r and this for a couple of different values of the tuning current through the phase section (I_p = 0, 1, 2 and 3 mA). The current through the active section was 60 mA, the output facet was not anti-reflection coated and had a reflectivity of 0.32.

The frequency–tuning current relation shown in figure 4.1 is well known and typical for tunable lasers. For fixed I_p the frequency increases discontinuously with I_r: tilted plateaus are separated by frequency jumps which correspond to (longitudinal) cavity mode jumps [20]. The lasing mode is the mode with the highest netto round-trip gain (for a fixed gain this corresponds to the mode with the lowest cavity loss). For a tunable laser the gain (or loss) is not only determined

by the material gain of the active section, but also by the filtering effect of the Bragg grating in the reflector section. This means that the lasing mode is the cavity mode (fulfilling the phase condition of the laser cavity) that lies closest to the center of the Bragg peak. As already mentioned in chapter 1, the position of the Bragg peak can be shifted by changing the current through the reflector section. After a certain shift of the Bragg peak (approximately equal to half of the cavity mode spacing) one of the neighbouring modes of the lasing mode will experience a lower loss and will become the lasing mode. This is accompanied by a jump of the laser frequency from one mode to another. Between mode jumps, the laser frequency increases slightly because the refractive index of the reflector section decreases when I_r increases. This causes a spectral shift of the entire cavity mode spectrum. It can also be noticed from figure 4.1 that the frequency plateaus become wider when the tuning current increases. This is due to the non-linear relationship between current and carrier density in a tuning section (as expressed e.g. by equation (2.5)).

The spectral position of the cavity modes can also be changed by changing the current through the phase section of the laser. This leads to a shift of the laser frequency versus reflector current characteristic when the phase current is changed. For a fixed reflector current the laser frequency (i.e. the frequency of the cavity mode with minimum loss) can be tuned continuously over a certain range by changing the phase current. This corresponds to a shift of the lasing mode through the Bragg peak. After a certain shift, a neighbouring cavity mode will experience a lower loss and will become the lasing mode. Hereby the laser frequency jumps back to the value corresponding to the starting value of the phase current. This is illustrated in figure 4.2 which shows the laser frequency as a function of phase tuning current for I_r = 10 mA. It can again be noticed that the tuning becomes less efficient due to the non-linear relationship between current and carrier density.

The mode spacing of a three-section DBR laser is determined by the total (optical) cavity length and is given by [20]:

$$\Delta\lambda_m = \frac{\lambda^2}{2(n_{g,a}L_a + n_{g,p}L_p + n_{g,r}L_{eff})} \tag{4.1}$$

with $n_{g,a}$, $n_{g,p}$ and $n_{g,r}$ the effective group indices of the active, phase and reflector section respectively and L_a and L_p the length of the active and phase section and L_{eff} the effective length of the reflec-

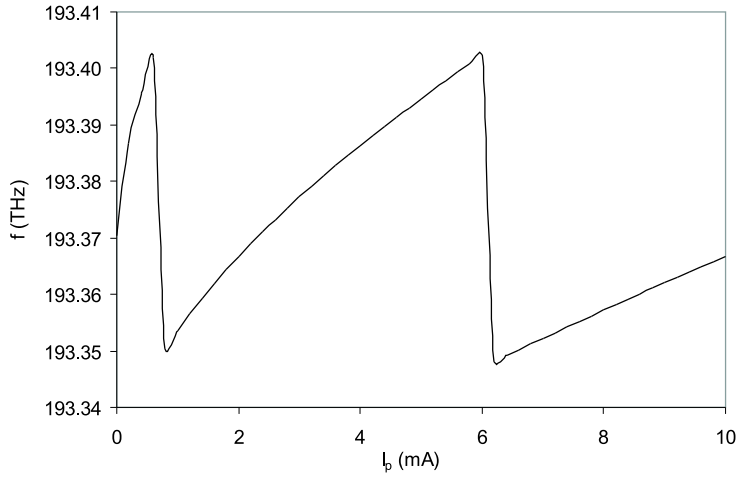

Figure 4.2: Laser frequency of a solitary three-section DBR tunable laser as a function of phase tuning current for I_r = 10 mA.

tor section. In this case, the mode spacing lies around 60 GHz. This value of course (slightly) depends on the value of the tuning currents.

A more detailed explanation of the different tuning mechanisms discussed above can be found in [20] and [21]. Here, we will not go into more detail on the tuning characteristics, we are mainly interested in how they are influenced by optical feedback from a periodic reference filter. Apart from the laser frequency, the output power and especially the SMSR are other important laser parameters. We will just briefly mention them here, for a detailed treatment of the influence of the different tuning parameters on the output power and the SMSR we again refer to [20] and [21]. The output power of the solitary laser varied between 11.5 and 12.3 mW. The SMSR varied between 20 and 48 dB. An operating point at a certain wavelength and a SMSR higher than 40 dB can be obtained by carefully selecting the tuning currents. A procedure to construct the tuning table so that the laser emits at ITU-frequencies with sufficiently high output power and a SMSR higher than 40 dB is described in [21].

4.1.2 Tunable laser with feedback from a periodic reference filter

Tuning table

Figure 4.3 shows (part of) the calculated tuning table of a three-section DBR tunable laser subject to optical feedback from a stable periodic reference filter. The feedback scheme has already been discussed in chapter 2 and it is shown in figure 2.13. The output facet of the laser in now anti-reflection coated and has a reflectivity of 0.01. The laser frequency is again shown as a function of the tuning current through the reflector section I_r and this for a couple of different values of the tuning current through the phase section (I_p = 0, 1, 2 and 3 mA). The filter was a Fabry Perot etalon with a FSR of 100 GHz and a mirror reflectivity of 0.9, corresponding to a 3–dB width or FWHM of the filter peaks of 3.3 GHz (this corresponds to the FWHM that is expected for our filter, as described in chapter 3). The central frequency of the filter was chosen so that the peak frequencies lie on the ITU–grid. The feedback ratio f_{ext} (i.e. the ratio of the reflected power to the power emitted by the laser) was -10 dB (for frequencies around the filter peaks), the external cavity round-trip time τ_D was 0.3 ns (corresponding to an external cavity length of 4.5 cm and an external cavity mode spacing of around 3.2 GHz). According to the results shown in section 2.4.2, the laser should work in feedback regime V for these values of the feedback parameters, i.e. it operates in a stable narrow linewidth mode for all phases of feedback.

From figure 4.3 it is clear that the emission frequencies are now determined by the frequency of the filter peaks. It can be seen that the frequency plateaus are horizontal contrary to the (slightly) tilted plateaus of a free-running DBR laser. As already explained, the tilt of the plateaus for a free-running DBR laser is caused by the spectral shift of the entire cavity mode spectrum due to the decrease of the refractive index of the reflector section for increasing I_r. For an external cavity laser, this shift is reduced due to the increased cavity length of the laser. This can be understood as follows. The phase condition of the (external) laser cavity can be expressed as:

$$n_{g,a}L_a + n_{g,p}L_p + n_{g,r}L_{eff} + n_{g,ext}L_{ext} = m\frac{\lambda}{2} \tag{4.2}$$

with $n_{g,ext}L_{ext}$ the total external optical cavity length and m an integer. For typical tunable semiconductor laser dimensions (e.g. to be

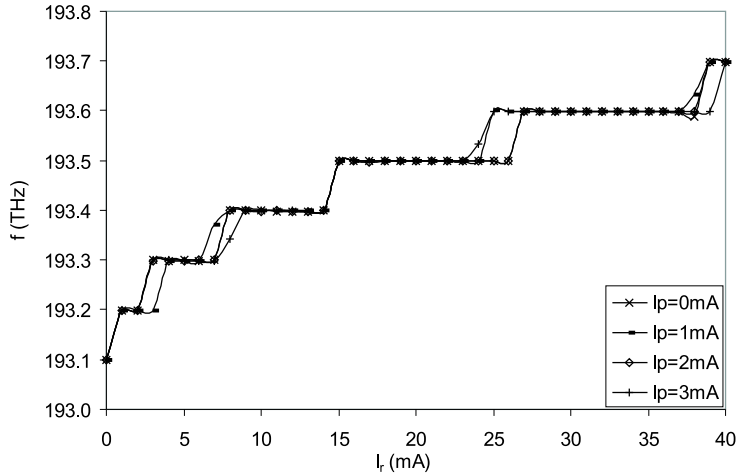

Figure 4.3: Laser frequency as a function of reflector tuning current for a three-section DBR tunable laser subject to optical feedback from a stable periodic filter (I_p = 0, 1, 2 and 3 mA). The feedback ratio f_{ext} was -10 dB, the external cavity round-trip time τ_D was 0.3 ns.

found in table 2.1 in chapter 2) and L_{ext} = 10 mm it follows from expression (4.2) that for wavelengths around 1550 nm m is already more than five times larger than for the solitary laser (corresponding with L_{ext} = 0). This means that a certain refractive index change (caused by a change in tuning current or by a temperature change) will lead to a spectral shift of the cavity modes that is five times smaller for the external cavity laser.

As for the solitary laser, the lasing mode will be the (external) cavity mode (fulfilling the phase condition) that experiences the lowest loss. In this case the modes with lowest loss are those lying within a peak of the filter that lies within the Bragg peak. This is schematically represented in figure 4.4 which shows the Bragg peak, the filter peaks and the external cavity modes for the laser used in the simulations. The width of the Bragg peak of this laser was 100 GHz.

It is obvious that the tuning table becomes simpler due to the feedback, since the emission frequencies are now determined by the filter peaks. If the frequency of the filter peaks are chosen on the ITU–grid, the laser automatically emits at ITU frequencies. From the many different operating points on the ITU–frequencies an optimum point can then be chosen. On a coarse scale (e.g. corresponding to the ITU chan-

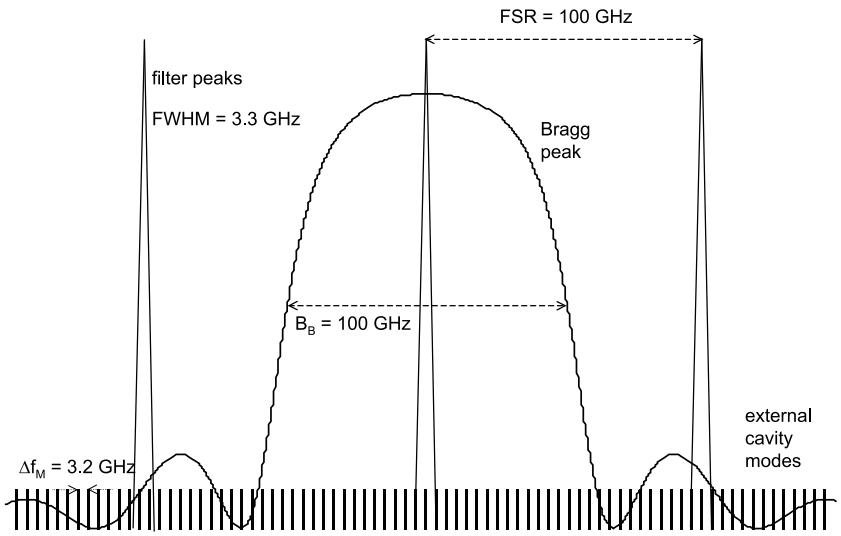

Figure 4.4: Schematic representation of the Bragg peak, the filter peaks and the external cavity modes for a three-section DBR tunable laser subject to optical feedback from a stable periodic filter.

nel spacing of 100 GHz or 50 GHz), the frequency can be changed by changing the current through the reflector section of the laser so that another peak of the filter is 'selected' by the Bragg peak. Fine tuning of the frequency can be achieved by changing the current through the phase section so that an (external) cavity mode is aligned with the center of the filter peak that is selected by the Bragg peak. If the FSR of the filter is not too small compared to the width of the Bragg peak and if the phase current of the laser is carefully adapted so that an (external cavity) mode is aligned with the filter peak lying within the Bragg peak, stable operation can be obtained, with high SMSR.

The effect of the relation between the FSR and the width of the Bragg peak on the SMSR of the external cavity laser is illustrated in figure 4.5. The SMSR is shown as a function of I_r for I_p = 0 mA and for a FSR of 100 and 50 GHz respectively. For a FSR of 50 GHz the reflectivity of the filter mirrors was changed to 0.8 so that the FWHM was again 3.3 GHz. The width of the Bragg peak was 100 GHz in both cases, the other parameters were the same as in figure 4.3. For completeness the SMSR of the solitary laser is also shown. It can be clearly seen from figure 4.5 that for a FSR of 50 GHz it is more difficult to obtain a high SMSR.

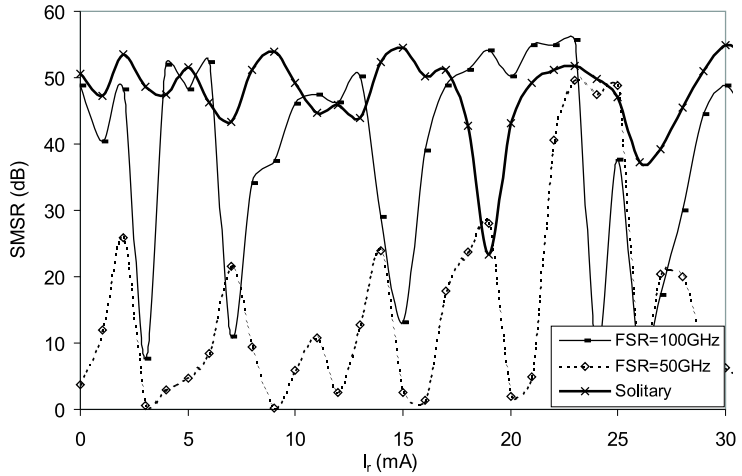

Figure 4.5: SMSR as a function of I_r for I_p = 0 mA and for a FSR of 100 and 50 GHz respectively.

Increasing the feedback strength will not help to increase the SMSR. Some improvement might be obtained by decreasing the external cavity length so that the cavity mode spacing is increased, but this might not be feasible in practice. The influence of the feedback strength and the external cavity length on the SMSR is illustrated in figure 4.6 which again shows the SMSR as a function of I_r for I_p = 0 mA and for a FSR of 50 GHz, once for τ_D = 0.3 ns and f_{ext} = -10 dB, once for τ_D = 0.3 ns and f_{ext} = -7 dB and once for τ_D = 0.1 ns and f_{ext} = -10 dB.

The width of the filter peaks also has to be chosen properly. It can not be too small, because then the risk exist that the feedback level becomes too low (e.g. when there is a small deviation of the tuning currents) so that the laser will become unstable. On the other hand, the filter peaks should not be too wide, because if too many cavity modes lie within a filter peak, it becomes difficult to obtain a high SMSR. One could of course increase the cavity mode spacing by decreasing the external cavity length, but as already mentioned, this is not always possible in practice. Furthermore, it should be realized that for wide filter peaks the risk of interference between adjacent filter peaks increases. An appropriate value for the 3–dB width of the filter peaks would lie between 2 and 5 GHz.

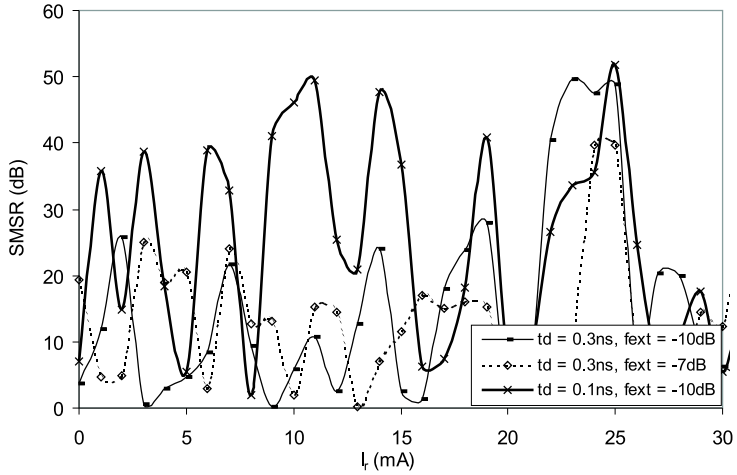

Figure 4.6: SMSR as a function of I_r for I_p = 0 mA, once for τ_D = 0.3 ns and f_{ext} = -10 dB, once for τ_D = 0.3 ns and f_{ext} = -7 dB and once for τ_D = 0.1 ns and f_{ext} = -10 dB.

Wavelength switching behaviour

Figure 4.7 shows a simulated frequency switch, with and without feedback. The frequency is shown relative to a center frequency of 193.1 THz. In both cases I_r was switched between 0 and 12 mA and I_p was kept constant (at 0 mA). This corresponds to operation points lying in the center of a frequency plateau in the tuning table, i.e. they have a high SMSR. The end frequency is of course different in both cases, as could also be expected from figure 4.1 and figure 4.3 respectively. The feedback parameters were the same as before. Since thermal effects are not included in the simulation software, the thermal drift was simulated by applying a linearly decreasing current to the Bragg section. This will also cause a deviation of the laser frequency and what we are mostly interested in, is the maximum frequency (or wavelength) deviation that can be counteracted by the optical feedback. The drift was also sped up so that shorter time spans (a few tens of nanoseconds in stead of a few milliseconds) could be simulated, since the simulations would otherwise take too much time. The drift was initiated at t = 40 ns. From figure 4.7 it can be seen that the frequency drift (and eventually the mode hop) occur earlier when there is no feedback applied. As explained before, this is because on one hand the frequencies of minimum loss cor-

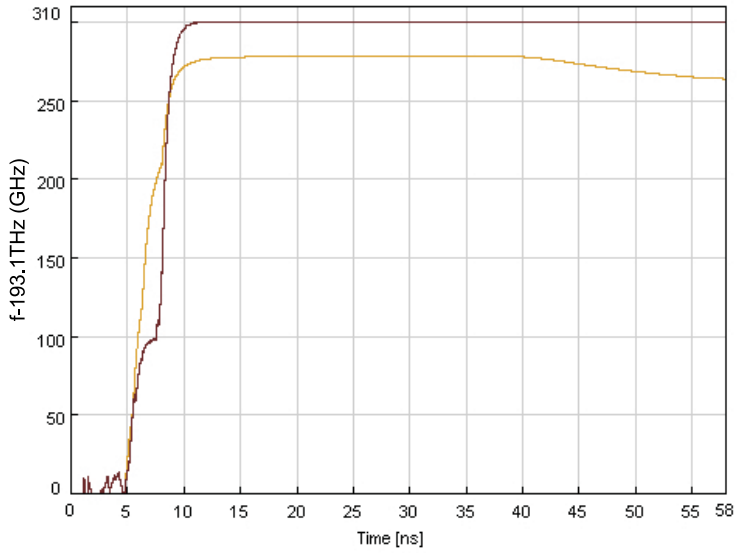

Figure 4.7: Simulated frequency switch, with (upper trace) and without (lower trace) feedback. I_r was switched between 0 and 12 mA, I_p = 0 mA.

respond to the filter peaks whose spectral position is not affected by the thermal effects in the laser cavity. On the other hand, the spectral position of the cavity modes is less sensitive to refractive index changes in the laser sections for the external cavity laser. Deviations up to 15 GHz can be counteracted this way.

Figure 4.8 shows the output power during the frequency switch, with feedback. It can be seen that the output power decreases due to the imposed drift. This is caused by the shift of the Bragg peak (due to the temperature change in the Bragg section) which leads to a decrease of the round–trip gain of the lasing mode and thus to a decrease of the output power. This does not pose a major problem however, since one has to take into account that in reality this drift takes place over several tens of microseconds (or even milliseconds) so that the power decrease can easily be counteracted by increasing the active section current using an electronic feedback loop.

To prove that the improvement of the wavelength switching behaviour is independent of the value of the current step (and also of the switching history), figure 4.9 shows a frequency switch for a switch of I_r from 0 to 32 mA.

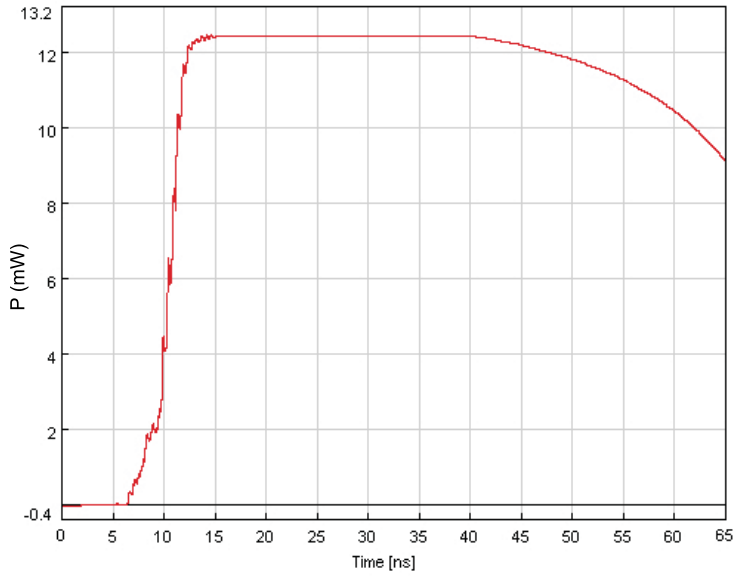

Figure 4.8: Output power during the frequency switch, with feedback. I_r was switched between 0 and 12 mA, I_p = 0 mA.

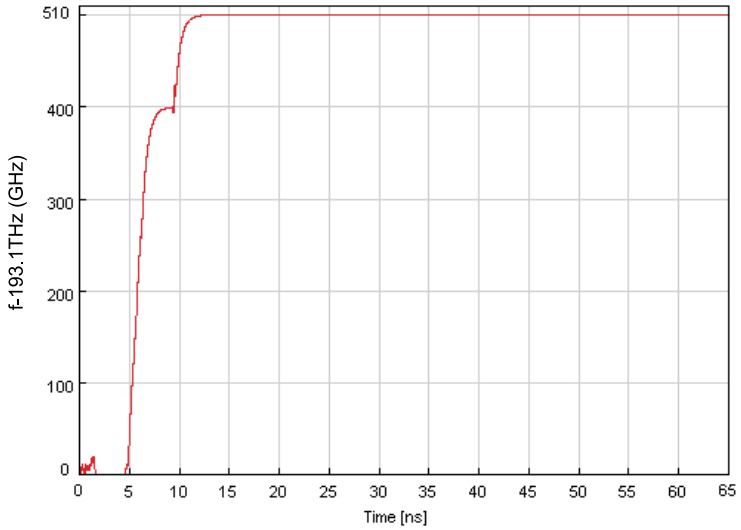

Figure 4.9: Simulated frequency switch, with feedback. I_r was switched between 0 and 32 mA, I_p = 0 mA.

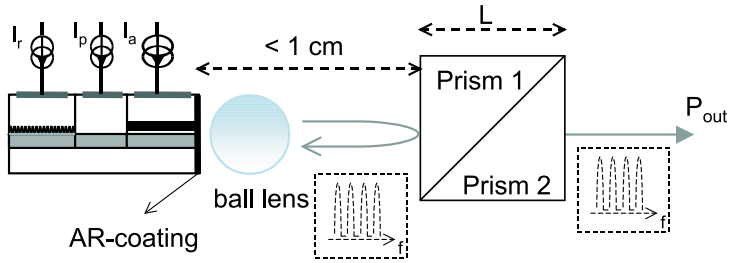

Figure 4.10: Schematic representation of the coupling of a semiconductor (tunable) laser with the filter through a ball lens (diameter = 2 mm, focal distance = 0.1 mm).

4.2 Experimental results

Figure 4.10 shows a schematic representation of the coupling of the laser with the filter through a ball lens. The laser is a three section DBR tunable laser with an AR-coated facet and an output power of 5 mW for an active current I_a of 100 mA. The ball lens has a diameter of 2 mm and a focal distance of 0.1 mm. Both the ball lens and the prisms of the filter are low-cost standard components that are readily available. By developing this novel filter type, we were able to keep the external cavity length below 10 cm. Even with a short external cavity it is still required to ensure a sufficiently high feedback level. Therefore, good coupling of the laser with the filter is very important.

Figure 4.10 shows a picture of the top view of the laser coupled with the filter through the ball lens on the measurement setup. The laser is contacted using four probe needles: one for the active, phase and reflector section and one for the ground connection.

Figure 4.12 and 4.13 show a part of the experimentally obtained tuning table of the external cavity laser shown in figure 4.10. The lasing frequency respectively the SMSR are shown versus the current I_r through the reflector section for I_a = 100 mA and this for a couple of different values of the tuning current through the phase section (I_p = 2, 3 and 5 mA). It can be seen that the frequency plateaus are horizontal contrary to the (slightly) tilted plateaus of a free-running DBR laser. As explained above this is because the frequency of each plateau is now determined by a fixed peak of the filter, while for a free-running DBR laser it is determined by the (quasi-)continuously shifting Bragg peak. The difference between the plateaus is (a multiple of) the FSR of the fil-

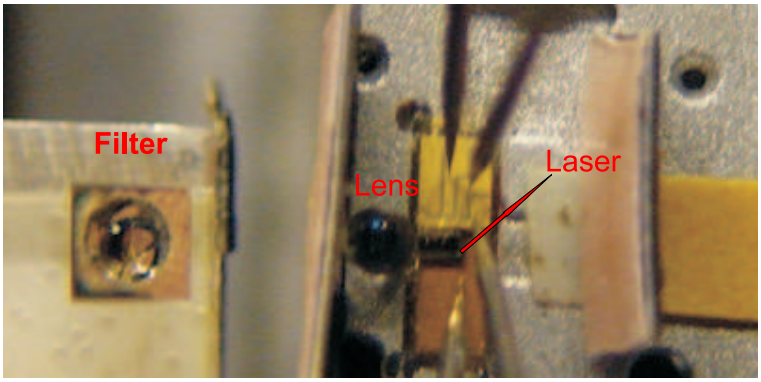

Figure 4.11: Picture (top view) of (tunable) laser coupled with the filter through a ball lens on the measurement setup.

ter, whereas for a free-running DBR laser this is the cavity-mode spacing. The intermediate frequency jumps (e.g. around I_r = 11 mA for I_p = 2 mA) and the fact that the SMSR is not above 40 dB for every frequency plateau can both be attributed to the small FSR of the filter. The FSR is only 32.5 GHz and since the 3–dB width of the Bragg peak is typically 100 GHz or more, there are always at least three filter peaks lying within the Bragg peak. The round-trip gain is thus nearly the same for these filter peaks, so that minor deviations (e.g. a small parasitic change of the external cavity length or noisy tuning currents) can already cause a mode hop to an adjacent filter peak. This can be greatly improved on one hand using a filter with a FSR that is better adapted to the width of the Bragg peak (e.g. a FSR 50 GHz or 100 GHz) so that less filter peaks lie within the Bragg peak at the same time. On the other hand one could also adapt the external cavity length to change the external cavity mode spacing so that the probability that two cavity modes lie within a filter peak at the same moment decreases. However, since our goal is to prove that the wavelength switching behaviour can be improved using this principle, we only need two stable operating points with high SMSR to switch between. We also want to stress that the tuning table was recorded without any control loop applied to the laser as is normally the case [21]. This is also a reason why the SMSR is not above 40 dB for all frequency plateaus. By properly adjusting the tuning currents it is possible to obtain a SMSR above 40 dB for every filter peak within the tuning range of the laser. An extra advantage is that it is easier to build a tuning table for a tunable laser that is stabilized to an (external) frequency reference, since one no longer has to search

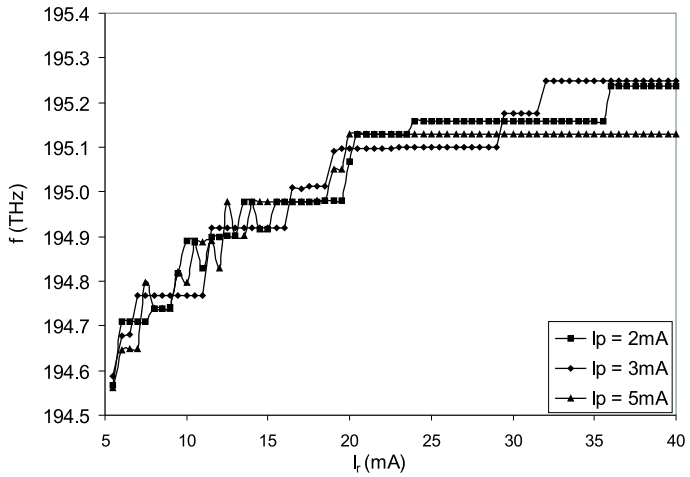

Figure 4.12: Excerpt from the experimentally obtained tuning table. The lasing frequency is shown versus I_r for I_a = 100 mA and I_p = 2, 3 and 5 mA.

for the desired frequencies in the frequency vs. tuning currents plane. Furthermore, aging of the tuning sections or tuning table inaccuracies will have a reduced influence. The maximum output power after the filter for each frequency plateau lies around 1.4 mW. This value critically depends on the beam quality within the Fox-Smith resonator and therefore on the lens quality. Replacement of the simple ball lens by a high quality lens is expected to increase the output power considerably.

Figure 4.14 shows experimentally obtained traces of the (absolute value of the) deviation of the laser wavelength from it's steady-state value after switching, both with and without feedback from the filter. These traces were obtained with the same measurement setup as the one in figure 2.8. The reflector current was switched at t = 0 ms between 0 mA and 40 mA (crosses) and 0 mA and 61 mA (broken line) respectively for the case without feedback and between 0 mA and 82 mA (thick line) for the case with feedback. The active current was 100 mA in both cases and the phase current was adjusted for maximum SMSR each time. It can be clearly seen that the drift is considerably reduced by the feedback, even though the switching current is 30 % respectively 100 % higher compared to the situation when no feedback is present. The maximum deviation is reduced and the steady-state value is reached much faster. Without feedback the steady-state is not reached before 2 ms after the switch, with feedback it is reached already

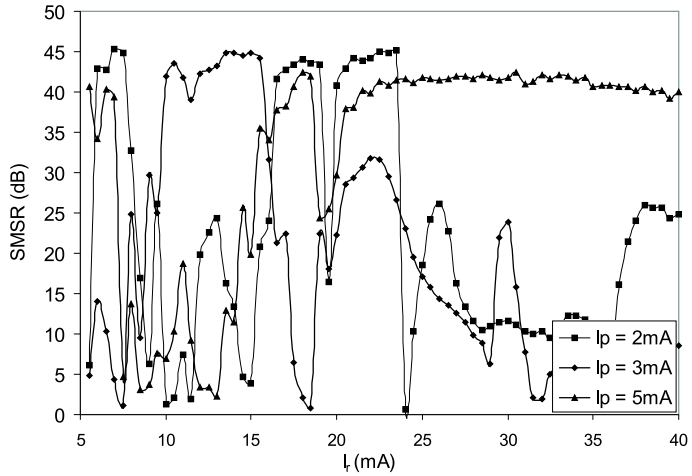

Figure 4.13: Excerpt from the experimentally obtained tuning table. The SMSR is shown versus I_r for I_a = 100 mA and I_p = 2, 3 and 5 mA.

after 0.1 ms. The fact that no complete suppression of the thermal drift is obtained is again (partly) due to the low FSR of the filter. On top of that, the current source that was used to switch I_r only had a limited resolution (0.1 mA), which –taking into account the low FSR of the filter– makes it even more difficult to obtain stable switching between channels with high SMSR.

One could remark that even without feedback the maximum deviation is only 50 pm or 6 GHz. However, for an ITU-channel spacing of 50 GHz the error is already above 10 %. And even for higher spacings, a deviation of a few GHz of the channel frequency can lead to intolerable power differences between channels due to the optical filtering of the signals.

4.3 Conclusion

In this chapter we have shown that the wavelength switching behaviour of a semiconductor tunable laser can be improved by stabilizing the laser at (the peaks of) a periodic reference filter. It was shown, both numerically and experimentally, that the tuning characteristics are simplified and that the wavelength switching behaviour is considerably improved. Simulation results showed that drifts up to 15 GHz could

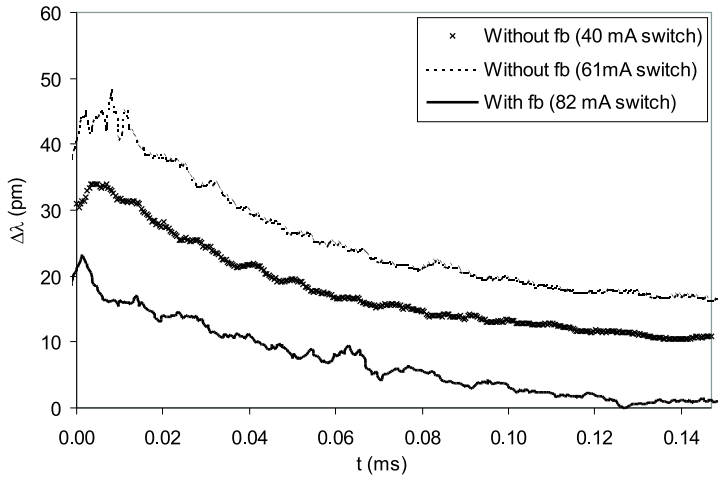

Figure 4.14: Experimentally obtained traces of the deviation of the laser wavelength from it's steady-state value after switching, both with and without feedback from the filter. I_r was switched between 0 mA and 40 mA (crosses) and 0 mA and 61 mA (broken line) respectively for the case without feedback and between 0 mA and 82 mA (thick line) for the case with feedback (I_a = 100 mA in both cases and I_p was adjusted for maximum SMSR each time).

be suppressed through the optical feedback. Experimental results also showed that the wavelength switching was considerably improved: the maximal deviation was reduced by more than 50 % (from 6 GHz to less than 3 GHz) and the steady-state value was reached much faster (after 0.1 ms in stead of 2 ms). This can be further improved by better adapting the FSR of the filter, the external cavity length (and thus the cavity mode spacing) and the width of the Bragg peak of the laser to each other. The use of the filter will furthermore facilitate the generation of tuning tables and will reduce the influence of component aging and tuning table inaccuracies. Another advantage of this external cavity laser is that the small external cavity length allows integration in a standard butterfly package.

Chapter 5

Degradation of tunable lasers - Monitoring and tuning table updating procedure

In this chapter, we will describe the issues and problems associated with aging, monitoring and updating of tunable laser sources. After situating the problem, we will explain the different aging mechanisms that occur in tunable lasers, without going into much detail on the underlying physical mechanisms causing the degradation. We will also briefly describe some techniques that can be used to monitor the output power, emission wavelength and SMSR of tunable lasers. The main part of this chapter however, will be dedicated to the development of a strategy to update the complete tuning table of a tunable laser, using only the limited information obtained from the aging-induced changes in tuning characteristics of a single channel (i.e. the operating laser channel).

5.1 Context

As was mentioned in chapter 1, tunable and widely tunable lasers are promising candidates for many very useful applications in current and future optical networks.

However, in order to be used in a telecommunication network environment, reliability requirements are very stringent. Output power

should obviously be kept at a sufficiently high level. Furthermore the lasing wavelength should remain at its predefined value on the ITU grid throughout the device lifetime. Otherwise the emission wavelength could drift out of its assigned channel band or - in a worst-case scenario - even a mode hop could occur. Even when the wavelength (optical frequency) remains within the assigned channel band, small frequency changes (e.g. 5 GHz) already result in power changes due to the optical filtering of the signals. In both cases this would cause severe signal degradation and crosstalk, obviously to be avoided at all time. To avoid wavelength drift and mode hops, it is important that the relation between a channel wavelength and the corresponding values of the tuning currents always remains correct. I.e., when applying the values of the tuning currents that are stored in the look-up or tuning table of the laser, the laser should emit at the correct wavelength, with sufficient output power and a high SMSR (at least 40 dB).

Aging of the active section of a semiconductor (tunable) laser can cause a decrease of the output power. This usually does not pose a big problem as it can be easily detected and overcome by simply increasing the active laser current.

For tunable lasers however, there is another and more serious problem. Aging of the tuning sections can cause the wavelength versus tuning current characteristics to change significantly, leading to a reduced wavelength (frequency) accuracy and a decrease of the SMSR, accompanied by the problems mentioned above. Therefore, a mechanism to update —preferably automatically— the tuning table is a prerequisite for tunable lasers to be used in a telecommunication network environment.

5.2 Degradation

Since the wavelength of minimum propagation loss lies around 1.55 μm for Silica optical fibres, lasers for (long-haul WDM) optical telecommunication networks are usually made of (a combination of) III-V semiconductor material. The reason for this is that the bandgap of these semiconductors corresponds with wavelengths in the 1.55 μm region. For telecommunication lasers InGaAsP/InP is almost exclusively used, and this usually in a buried heterostructure (BH) construction where two semiconductor materials (InGaAsP and InP) with different bandgaps are stacked together. The reason such a structure is used, is that it a.o. provides better carrier and light confinement. In a multi-section

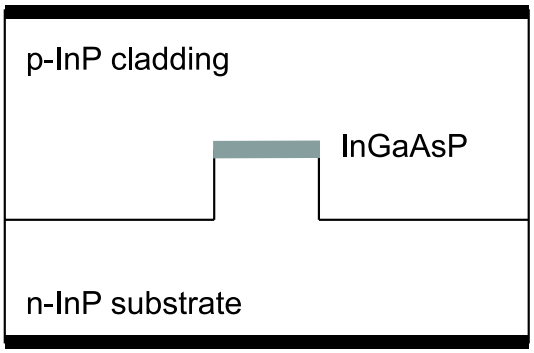

Figure 5.1: Schematic representation of the layer stack of an InGaAsP/InP BH laser.

semiconductor tunable laser, the tuning sections have the same BH structure as the active section, but with a different InGaAsP composition and a different band-gap wavelength. A rudimentary representation of the layer stack of an InGaAsP/InP BH laser is shown in figure 5.1.

A consequence of using semiconductor material is that tunable lasers for telecommunication suffer from degradation phenomena when they age [61, 62, 63, 64, 65]. Furthermore, unlike conventional Fabry Perot or DFB lasers, multi-section tunable lasers not only suffer from degradation of the active section, the passive tuning sections also suffer from degradation. In the next two sections we will treat degradation of the active and passive sections separately.

5.2.1 Degradation of active laser sections

Degradation of the active section may cause an increase of the threshold current and a decrease of the external differential quantum efficiency [61, 66, 67, 68]. These changes are however limited. And since furthermore the decrease of the emitted optical power can easily be counteracted by increasing the current through the active section, degradation of the active section does not pose a major limit on using semiconductor tunable lasers in a (WDM) telecommunication network. The device lifetime can be defined as the time needed for the operating (active) current under a constant optical output power to increase with 50 %. In that case, estimated lifetimes of 10^6 hours for 5 mW of output power at a temperature of 25 °C are feasible [62]. A lifetime of 10^6 hours corresponds to 42667 days or a period of 114 years, which should be more

than sufficient for a component to be used in a telecommunication network.

For completeness, we want to mention briefly the physical mechanisms underlying the degradation of the active section of BH semiconductor tunable lasers (or the degradation of BH semiconductor Fabry Perot lasers). The increase of the threshold current is caused by a decrease of the carrier lifetime through an increase of the non-radiative recombination rate due to the formation of point defects in the active layer. The decrease of the external differential quantum efficiency on the other hand is caused by the increase of the absorption coefficient due to degradation. The formation of the defects is related to the fabrication process of the BH structure [61, 66, 67, 68]. However, as mentioned before, the influence of these effects is minimal, especially for lasers which are made with current state-of-the-art production techniques from high quality semiconductor wafers.

5.2.2 Degradation of passive laser sections

While degradation of the active section usually does not prohibit long term use of a semiconductor laser, degradation of the tuning sections does pose a major problem for the use of tunable lasers in a network environment. This is mainly because it causes a change in the tuning characteristics of the laser [61, 62, 63, 64, 65]. This means that when applying the tuning currents stored in the look-up table of the laser —which was obtained before the laser aged— the resulting operation point will most likely have the wrong wavelength and probably with a low SMSR. This is illustrated in figure 5.2 and in figure 5.3 where the wavelength respectively the SMSR of a three-section DBR laser are shown versus the reflector current, both before and after aging of the reflector section. These results were obtained from simulations. As will be explained below, aging of a semiconductor laser can be simulated by increasing the value of the non–radiative recombination parameter. The active section was biased at 100 mA corresponding to an output power around 18 mW, no current was flowing through the phase section and the current through the reflector section was changed from 0 to 30 mA. The laser is usually operated in the center of one of the wavelength plateaus in the tuning characteristic, where the corresponding SMSR is maximal compared to neighbouring operation points. Suppose that the laser has been operating at the wavelength channel corresponding with a reflector current of 21 mA (point A on the graph), and

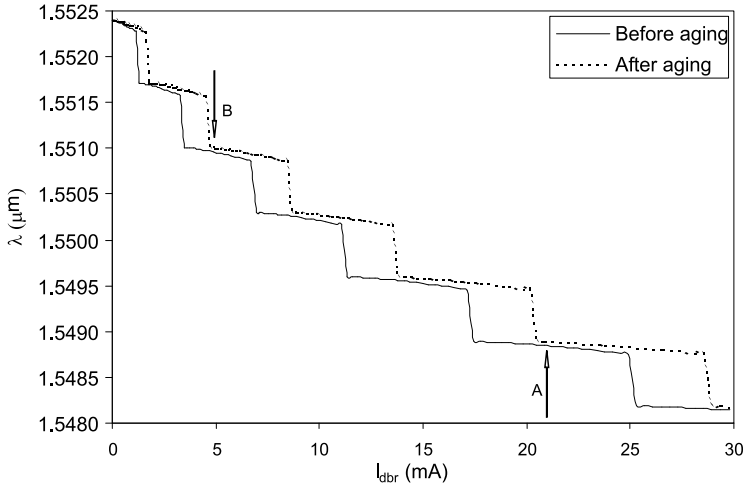

Figure 5.2: Laser wavelength vs. tuning current of a three section DBR laser, before and after aging of the reflector section.

this for a period long enough for the laser to age up to the point where the upper (dashed line) tuning characteristic is valid. As long as the laser is operated at the same wavelength channel, the control system of the laser will keep it at the correct wavelength and SMSR by adapting the tuning currents to counteract the changes caused by aging (or other external influences like a change in the environmental temperature) [69]. However, suppose that at a certain moment the decision would come to operate the laser at a different wavelength channel, say the one around a reflector current of 5 mA (point B on the graph). In that case, since the original tuning characteristic (full line) is no longer up-to-date, the laser would switch to a point on the new tuning characteristic (dashed line) very close to a mode hop (figure 5.2) and with an unacceptable low value for the SMSR (figure 5.3).

Figure 5.4 shows the output power of the same three-section DBR laser as above, again before and after aging of the reflector section. From figure 5.4 it is clear that the output power does not suffer a lot from the aging of (one of) the tuning sections. The difference in power between the original tuning characteristic and the new tuning characteristic is not even 5 % near point B. Furthermore a slight decrease (or increase) of power is not nearly as bad as a shift in wavelength or a decrease of the SMSR and it can be easily counteracted by increasing (or decreasing) the current through the active section.

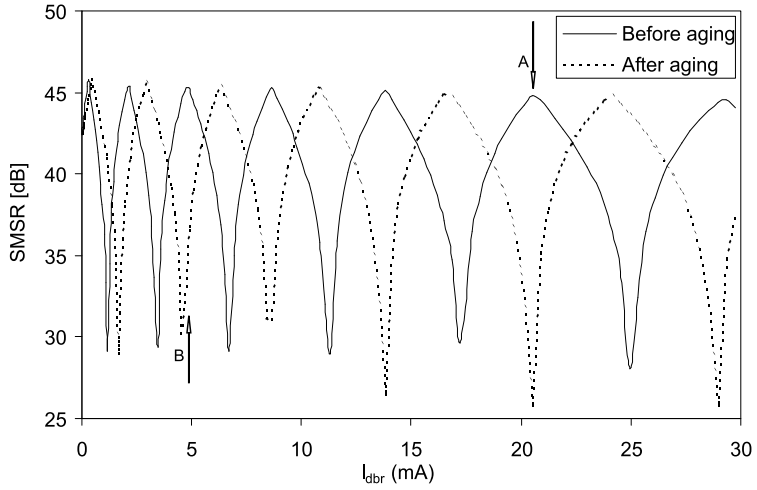

Figure 5.3: SMSR vs. tuning current of a three section DBR laser, before and after aging of the reflector section.

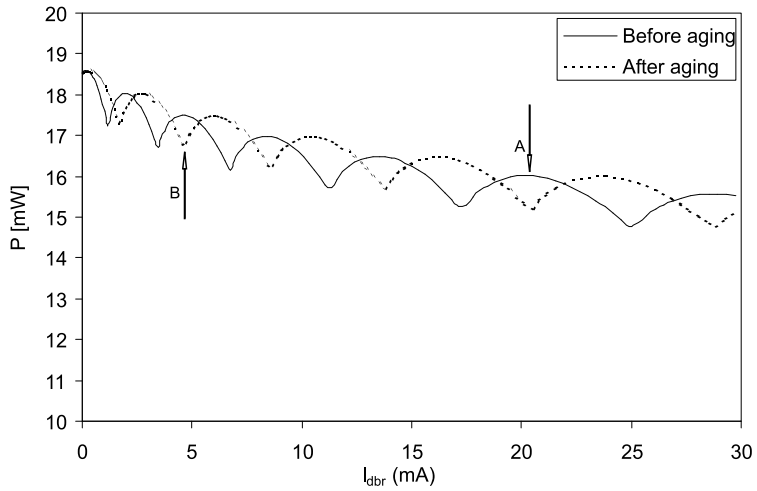

Figure 5.4: Output power vs. tuning current of a three section DBR laser, before and after aging of the reflector section.

The data shown in figures 5.2, 5.3 and 5.4 are not experimental aging data, but are obtained from simulations. The reason for this is that, unlike a commercial laser company, we do not have enough lasers nor the infrastructure to perform real-life aging tests. Furthermore, experimental aging data is very sensitive matter which —for obvious reasons— companies are not eager to distribute or share with the research community. Therefore, we had to perform simulations to study the influence of passive section degradation on the tuning characteristics of tunable lasers. The simulations were performed with software developed at INTEC [21]. As was the case for the active section, the degradation of the passive sections is caused by an increase of the non-radiative recombination due to the development of defects when the laser ages [61, 62, 63]. Hence aging of a tunable laser can be simulated by increasing the value of the non–radiative recombination parameter A, e.g. from 10^8 s^{-1} to $1.5x10^8$ s^{-1}, values corresponding to experimental pre- and post-aging data [65]. The validity of the simulations is proven by the fact that the results shown in figures 5.2 and 5.3 agree very well with published experimental results [62, 63, 64, 65].

Active and passive section degradation do not interfere with each other. This means that degradation of the active section will only have a negligible effect on the tuning characteristics. This is illustrated in figures 5.5 and 5.6 which show the wavelength and SMSR of a three-section DBR laser versus the reflector current, once before and after the active section has aged. For the wavelength as well as for the SMSR there is no noticeable difference before and after aging, proving that active section degradation has a negligible influence on the tuning characteristics.

Vice-versa degradation of the passive sections will only have a negligible effect on the light characteristics (i.e. output power versus active section current) [62]. This is illustrated in figure 5.7 which shows the light characteristic of a three-section DBR laser, once before the laser suffered from any aging, once after only the active section aged and once after only the reflector section aged. It is clear that the light characteristic is practically the same in all three cases, proving that passive section degradation has a negligible influence on the light characteristic and also that the effects of active section degradation are limited, as mentioned in section 5.2.1.

The reason for the limited change of the light characteristic is that the active section carrier density is clamped once the laser is above threshold. Unfortunately this is not the case for the passive sections,

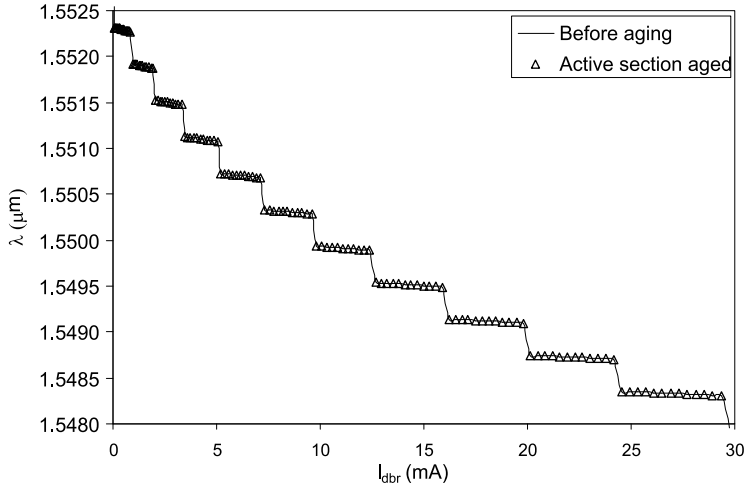

Figure 5.5: Laser wavelength vs. tuning current of a three section DBR laser, before and after aging of the active section.

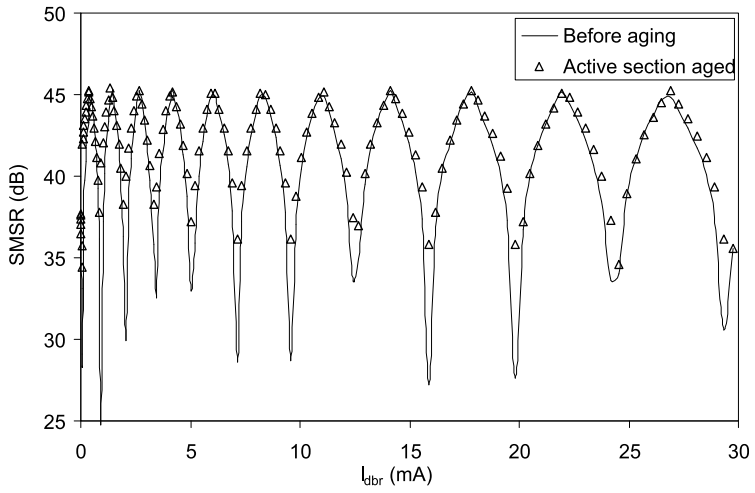

Figure 5.6: SMSR vs. tuning current of a three section DBR laser, before and after aging of the active section.

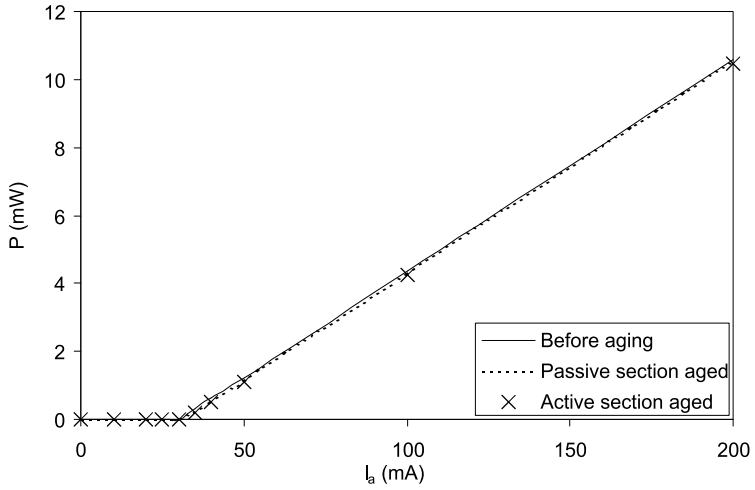

Figure 5.7: Light characteristic of a three section DBR laser, before and after aging of the reflector and active section respectively.

hence passive sections suffer more from degradation than active sections [61, 65]. The degradation of the passive sections also depends on the tuning current density: the higher the tuning current density, the bigger the change in tuning characteristics will be [62, 63, 64, 65].

From numerous (accelerated) aging tests it has appeared that after an initial period with rather large drifts, the wavelength drift saturates [63, 64, 65, 67]. Hence, the detrimental influence of aging on the tuning characteristics can be reduced if a proper burn-in is applied to the laser. A residual drift remains however, and often a frequency drift of no more than a few GHz can be tolerated in current optical networks. This is because typically a frequency accuracy of 10 % of the channel spacing is required and nowadays this spacing is 100 GHz and an evolution towards 50 GHz or even 25 GHz is expected [58]. Therefore, in order to be used in a real-life network environment, a mechanism is required to update the tuning currents so that the aging-induced wavelength drift is compensated for. This will be discussed in more detail in section 5.4.

5.3 Monitoring of tunable transmitters

When using a laser or any other component in a telecommunication network, it is mandatory that its characteristics (output power, emission wavelength, SMSR...) remain within certain specified limits. However, component degradation or environmental influences can lead to an unacceptable change of the characteristics. It is therefore crucial to monitor system performance to be able to detect and counteract — mostly by some sort of feedback— (limited) changes in device characteristics. Monitoring is especially useful in counteracting slow, gradual changes in device performance. When sudden or large errors occur, this mostly indicates component failure and in that case the defective device needs to be replaced anyway. Here too, monitoring can be helpful to locate the device in question.

For a tunable laser, important characteristics that need to be monitored are the optical output power, the emission wavelength and of course the modal stability (expressed by the SMSR).

5.3.1 Power monitoring

The output power can easily be monitored using photodiodes. A monitor diode is usually integrated in the package of commercial lasers. A small fraction P_m of the output power is tapped off and measured by the monitor diode. The power can then be stabilized by correcting the current through the active section by an amount proportional to $(P_{ref} - P_m)$, with P_{ref} proportional to the desired output power.

5.3.2 Wavelength monitoring

Optical filters are often used to monitor and stabilize the emission wavelength by translating wavelength values (variations) into power values (variations). Several types of filters can be used: a fiber Bragg grating [70], an arrayed waveguide grating (AWG) [71] or a Fabry Perot etalon [72]. In order to be used as a wavelength reference, filters that remain very stable over time and show low sensitivity to environmental changes have to be used. Since a tunable laser can be used to emit at multiple ITU wavelengths, periodically spaced by 50 GHz or 100 GHz, a filter with a very broad characteristic or a periodic wavelength reference is required. If a broad filter is chosen so that the different wavelength channels lie on the slope of the filter characteristic, each channel will correspond to a different value of the transmission of the filter.

If the wavelength of a certain channel starts to drift, the transmission through the filter will obviously change for that channel and the wavelength can be stabilized by adding corrections proportional to the deviation from the original value of the transmission to the phase current. For a periodic wavelength reference, a Fabry Perot etalon with its inherently periodic transmission characteristic seems to be a very suitable candidate for wavelength stabilization of tunable lasers. Fabry Perot wavelength lockers (FPWL) are commercially available [73]. In such a component, a small fraction ($\approx 5\%$) of the laser light is tapped off for wavelength monitoring. This light is again divided in a fraction that is directly detected (power P_1) and a fraction that is first sent through a highly stable Fabry Perot etalon with a free spectral range of 100 GHz (or 50 GHz) before detection (power P_2). The function $log(\eta P_2/P_1)$, with η a calibration factor, is then fairly linear in function of frequency around an ITU frequency and crosses zero at that frequency for the correct value of η [69]. This function can thus be used to monitor the wavelength and by adding corrections proportional to $log(\eta P_2/P_1)$ to the phase current, the wavelength can be stabilized. The unfiltered power P_1 can furthermore be used to control the output power of the laser.

The techniques discussed so far all require external devices to monitor the wavelength. In [74] an interference based wavelength monitor is presented that can be fabricated on a single chip with a tunable laser. The sensitivity of the presented device is still rather low (50 GHz), but can be improved by better design of the component [74].

5.3.3 SMSR monitoring

Apart from keeping the emission wavelength constant, it is also very important that the laser spectrum is kept monomodal. This translates in keeping the SMSR sufficiently high. In [69] a scheme is presented where the active section voltage is kept at a minimum to ensure high SMSR. Unfortunately, this scheme can only be used for SG-DBR and SSG-DBR widely tunable lasers and not for GCSR lasers due to the absence of clear local minima in the active section voltage versus tuning currents characteristic for this type of laser. In general, the scheme works for lasers with sharp reflection peaks or sharp peaks in the round-trip gain and does not work for laser with less sharp peaks.

A possible method for monitoring the SMSR —independent of the type of tunable laser— could be the following. When a side mode is present, an RF beat component will appear in the intensity when

it is detected with a photodetector. The stronger the side mode, the stronger the beat signal will be. Since the frequency separation between the modes of a semiconductor tunable laser is typically of the order of several tens of GHz, the photodetector needs to have a sufficiently high bandwidth. Even then, only beat signals caused by the modes lying next to the main mode can be detected. Normally however, these modes are also the strongest side modes, and thus the ones that are most important to monitor and suppress. This method is illustrated in figure 5.8(a) and figure 5.8(b) which show simulation results obtained with the VPI Componentmaker software [56]. Figure 5.8(a) and figure 5.8(b) show the power versus time for a tunable laser, tuned so that the SMSR is 40 dB and 17 dB respectively. In figure 5.8(b) we can clearly see the beat signal with an oscillation frequency of 60 GHz, corresponding to the frequency separation of the main and the nearest side mode. Obviously, a very high bandwidth detector is required for this.

The SMSR can also be derived from the power in the side mode(s) closest to the main mode. Because if the power in the side modes is minimal, the SMSR will be maximal. To measure this power, one can use a FPWL. If we assume that the tuning currents are adjusted so that the wavelength of the main mode λ_{MM} lies on the ITU-grid, the power transmitted through the Fabry Perot filter (P_2) will be maximal and will be a measure for the power in the main mode P_{MM}, the directly detected power P_1 is of course a measure for the total output power P_{tot}. Since $P_{tot} = P_{MM} + P_{SM}$, with P_{SM} the power in the side modes and since $P_{tot} = aP_1$ and $P_{MM} = bP_2$, $P_{SM} = aP_1 - bP_2$ with a and b calibration factors. The SMSR can thus be kept maximal by adjusting the tuning currents so that $(aP_1 - bP_2)$ stays minimal. The above reasoning is of course only correct if none of the side modes lies on the ITU-grid, because then P_{SM} would also pass (partly) through the filter. However the strongest side modes are nearly always the cavity modes closest to the main mode, and most tunable lasers are constructed so that their cavity mode spacing is different from 50 GHz.

5.4 Tuning table updating procedure

In this section we will describe a procedure to update the tuning table of a tunable laser that has been affected by aging. When the laser is being used as a working component in a network environment, it would not be efficient to remove it from the network to completely construct

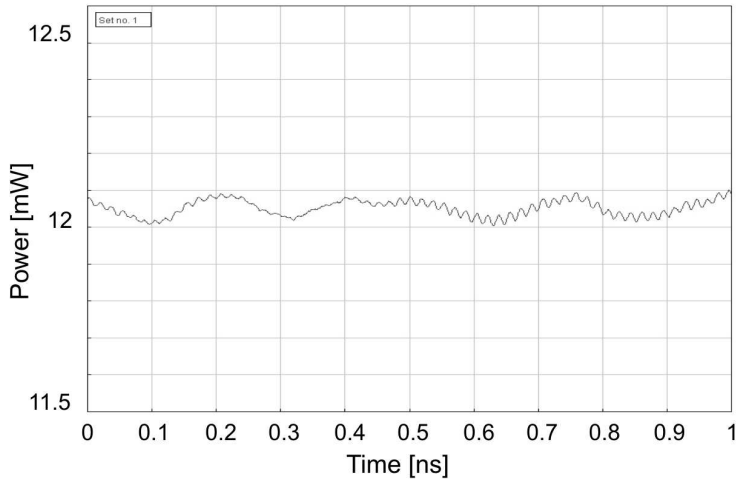

(a) SMSR = 40 dB

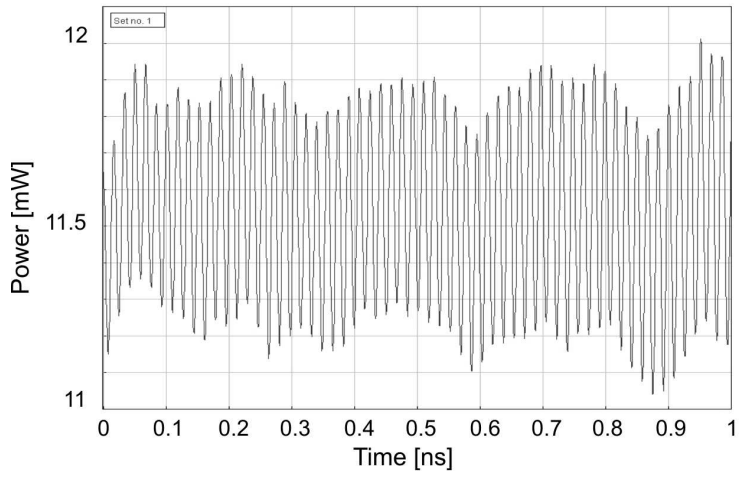

(b) SMSR = 17 dB

Figure 5.8: Power versus time for a SMSR of 40 dB respectively 17 dB

the tuning table again as has been done when the laser was characterized [69] before it was used for the first time. Instead, we want to update the existing tuning table using the information that is available from the observed aging-induced changes in tuning characteristics. These changes can be observed from the changes in tuning currents —that can easily be logged by the micro-controller a commercial transmitter based on a tunable laser is always equipped with— that occur when the control system of the laser [69] tries to counteract the aging-induced wavelength drift. Mostly, only information about the aging of one channel —the working channel— is available to update the laser. Nonetheless, as was explained in 5.2.2, it is very important to update the whole tuning table. To determine when an update is required, e.g. a 10 % deviation of the tuning currents from their initial values could be chosen as a limit.

Since the only information we have is the value of an aging-induced shift in tuning current for a certain wavelength, we should look for a relation between tuning current and wavelength. We start from the relation between the current I through a passive section and the corresponding carrier density N:

$$I = eV \cdot (AN + BN^2 + CN^3) \tag{5.1}$$

In this equation e is the electron charge, V is the volume of the tuning section, A, B and C are the non-radiative, the bimolecular and the Auger recombination parameter respectively. Since the wavelength λ depends on the carrier density, a mathematical relation $\lambda(N)$ exists between N and λ and since this is a non-singular relation the function $N(\lambda)$ can be determined. If we now substitute the Taylor expansion of $N(\lambda)$ in that of $I(N)$ we get, after neglecting higher order terms:

$$I = eV \cdot [AN' \cdot \delta\lambda + B(N')^2(1 + \frac{A}{2B}\frac{N''}{(N')^2}) \cdot \delta\lambda^2 + C(N')^3(1 + \frac{B}{C}\frac{N''}{(N')^2}) \cdot \delta\lambda^3] \tag{5.2}$$

In this equation $\delta\lambda = \lambda - \lambda_0$ with λ_0 the wavelength corresponding to zero tuning current, $N^{(i)} = (d^{(i)}N/d\lambda^{(i)})\big|_{\lambda_0}$ and n_0=I_0=0. If we now take into account that the change in the tuning characteristics is caused by an increase in non-radiative recombination and thus a change ΔA

of A [61, 62, 63, 67], and if we neglect the second derivative N'', we get for the shift of tuning current caused by aging:

$$\Delta I = eV \cdot \Delta A \cdot N' \cdot \delta\lambda \tag{5.3}$$

From equation (5.3) it is clear that the ratio $\Delta I/\delta\lambda$ is constant. This means that if we know ΔI_i for a certain wavelength shift $\delta\lambda_i$ (corresponding to a certain channel i), then we automatically know $\Delta I_j/\delta\lambda_j$ and thus ΔI_j for all other channels j. We want to point out that $\delta\lambda$ in equation (5.3) stands for the shift in Bragg wavelength $\delta\lambda_B$ when dealing with a DBR section, or for the shift of the comb spectrum of the cavity modes $\delta\lambda_p$ when dealing with a phase section. In a practical situation $\delta\lambda_B$ and $\delta\lambda_p$ are usually not know, but since the lasing wavelength will be the one of the cavity mode lying closest to the center of the Bragg peak and since we are dealing with rather small wavelength shifts anyway, $\delta\lambda_B$ can be derived from the $\lambda - I_{dbr}$ characteristic for a certain value of I_p (the one corresponding with the operation point of the laser). Likewise $\delta\lambda_p$ can be derived from the $\lambda - I_p$ characteristic for a certain value of I_{dbr} (the one corresponding with the operation point of the laser). The $\lambda - I_{dbr}$ and $\lambda - I_p$ characteristics can easily be obtained from the whole $\lambda - I_{dbr} - I_p$ characteristic, which is stored in the tuning table of the laser during the characterization procedure of the laser. The algorithm derived from equation (5.3), described above, is illustrated in the following simulation results. Figures 5.9 and 5.10 again show part of the tuning table (the laser wavelength versus the current through the reflector section I_{dbr} for a phase current of 0 mA) of a three-section DBR laser before aging (solid line) and after aging (broken line). The triangles represent the same part of the tuning table, but now for the aged laser and with updated values for the tuning current, obtained through the algorithm described above. We see a nearly perfect match between the original and updated tuning table. Only the DBR section suffered from aging in this case, the current through the phase section was kept zero. To simulate the aging, we again increased the value of the non-radiative recombination parameter A from 10^8 s^{-1} to $1.5x10^8$ s^{-1}. In most cases, when the laser has been through a period of burn-in, the changes in A will not even be as big as the ones we used in our simulations.

In [65] experimental proof of the above algorithm is given for a laser with only one tuning (DBR) section. Most tunable lasers have more than one tuning section however, so it is important to check if our algorithm also works if more than one tuning section has suffered from ag-

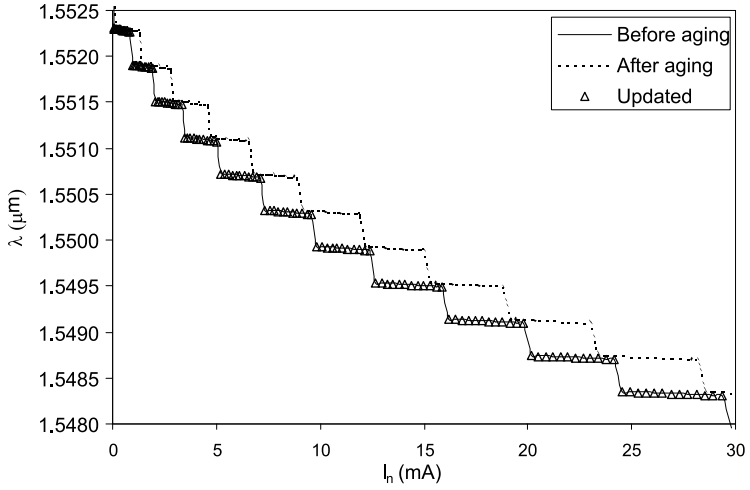

Figure 5.9: Laser wavelength vs. tuning current of a three section DBR laser, before and after aging of the reflector section, and after updating.

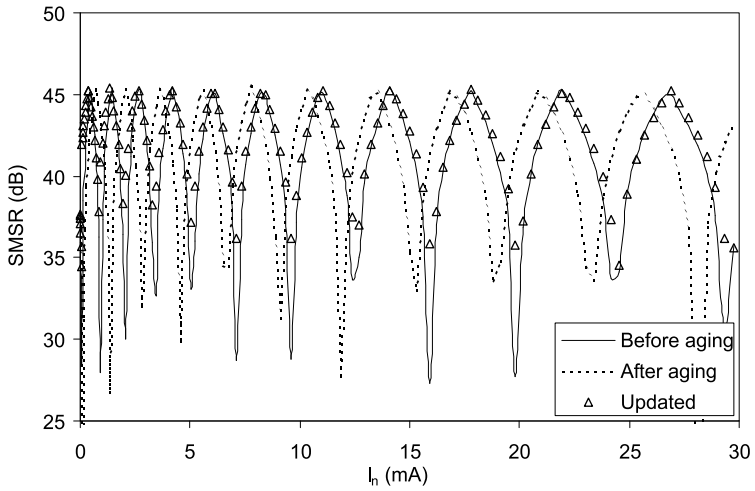

Figure 5.10: SMSR vs. tuning current of a three section DBR laser, before and after aging of the reflector section, and after updating.

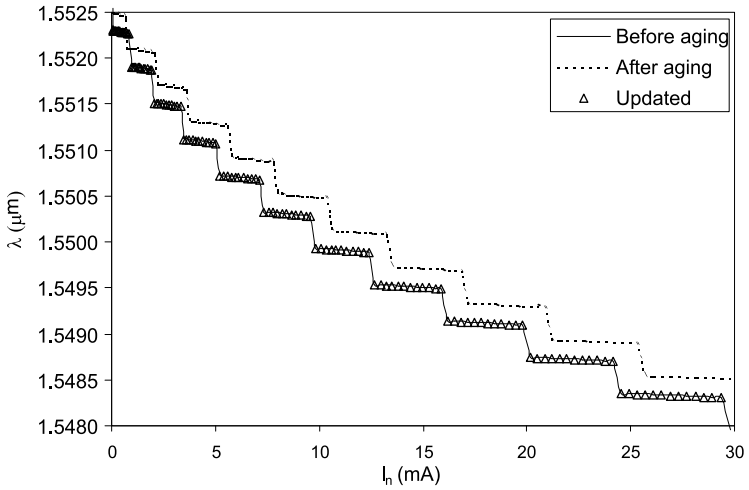

Figure 5.11: Laser wavelength vs. tuning current of a three section DBR laser, before and after aging of the reflector and phase section, and after updating.

ing. Figures 5.11 and 5.12 shows a simulation result for the same laser used above, but now both the phase and DBR section have suffered from aging (for both sections we changed A from 10^8 s^{-1} to $1.5x10^8$ s^{-1}, I_p was 5 mA). Again we see a nearly perfect match between the original and updated tuning table.

For completeness figures 5.13 and 5.14 show that the $\lambda - I_p$ and $SMSR - I_p$ characteristics can also be completely updated, even if both the phase and DBR section have suffered from aging. In this case, care has to be taken to determine $\delta\lambda$, because of the periodic nature of the $\lambda - I_p$ characteristic. If we would simply calculate $\delta\lambda$ as $\delta\lambda = \lambda - \lambda_0$, with λ and λ_0 the laser wavelength for $I_p \neq 0$ and $I_p = 0$ respectively, $\delta\lambda$ would be zero for those phase current for which $\lambda = \lambda_0$, suggesting that for those currents there is no aging-induced drift, which is obviously not correct, as can also be seen from figure 5.13. Instead we have to calculate $\delta\lambda$ as $\delta\lambda = \lambda_p - \lambda_0$, with λ_p the wavelength of the cavity mode that was the lasing mode for $I_p = 0$. This can easily be done by compensating the discontinuous $\lambda - I_p$ characteristic from figure 5.13 with the wavelength period —corresponding to a cavity mode hop— each time a mode hop occurs, yielding the continuous and monotonous $\lambda_p - I_p$ characteristic.

Finally, figure 5.15 shows that also the power-tuning current relation can be restored using the same algorithm.

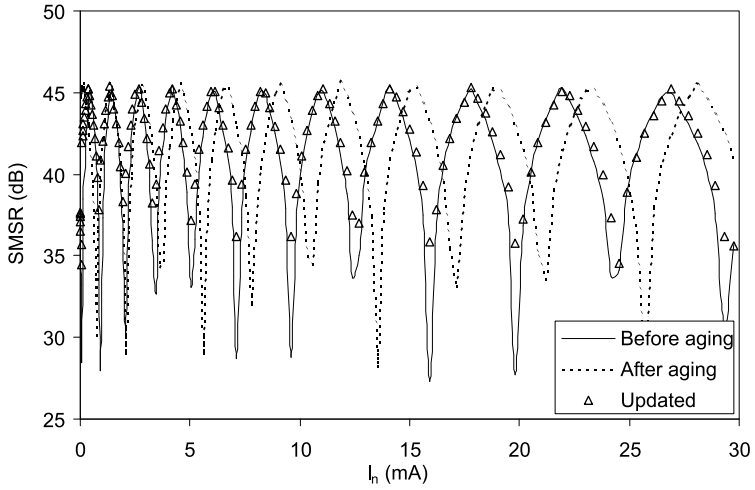

Figure 5.12: SMSR vs. tuning current of a three section DBR laser, before and after aging of the reflector and phase section, and after updating.

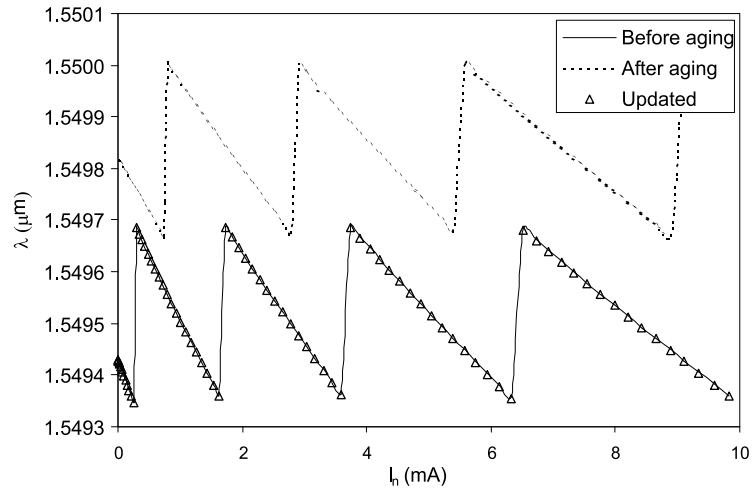

Figure 5.13: Wavelength vs. tuning current of a three section DBR laser, before and after aging of the reflector and phase section, and after updating.

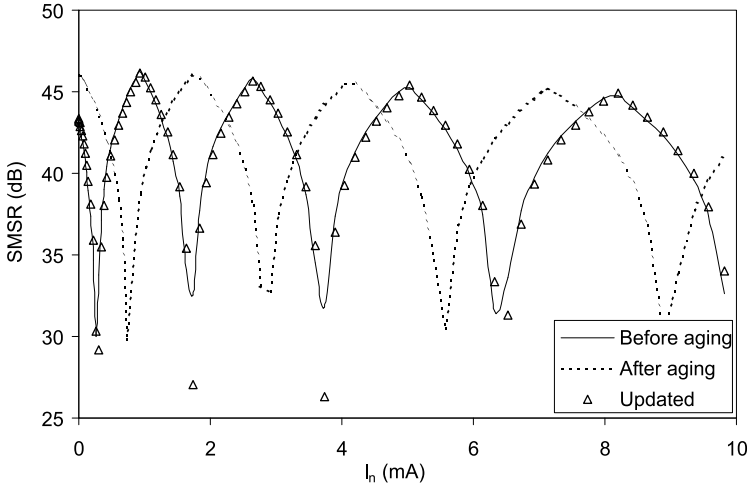

Figure 5.14: SMSR vs. tuning current of a three section DBR laser, before and after aging of the reflector and phase section, and after updating.

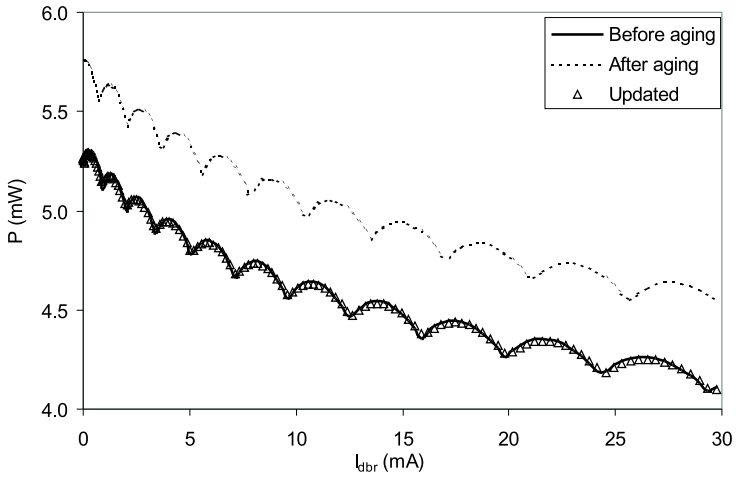

Figure 5.15: Output power vs. tuning current of a three section DBR laser, before and after aging of the reflector and phase section, and after updating.

In all these results, only one ΔI (corresponding to the channel the laser would be operating at) needed to be known per tuning section, to update the complete wavelength versus tuning current characteristic for that section. From the above results it is clear that the tuning table of a tunable laser can completely be updated using the very simple algorithm we described above. For lasers with more than two tuning sections, or for lasers with complex reflector sections like SG–DBRs or SSG–DBRs, the same algorithm can be applied in a straightforward manner since the underlying physical processes are always the same.

5.5 Conclusion

In this chapter we explained the different aging mechanisms that can occur in tunable lasers and the problems they can cause. We stressed the importance of reliability and described techniques to monitor the performance of tunable transmitters. We also described a strategy to update the complete tuning table of a tunable laser that has suffered from aging, using only the value of the aging-induced shift in tuning current(s) corresponding to the operating channel of the laser. Our results show that a nearly perfect match between the original and updated tuning tables can be obtained using the described strategy.

Chapter 6

Lasers with integrated optical amplifier

In this chapter we will investigate the influence of an (integrated) optical amplifier on important laser characteristics such as the relative intensity noise (RIN), the linewidth and the side mode suppression ratio (SMSR).

It is shown that the RIN and the linewidth of a laser diode can increase significantly if an optical amplifier is integrated with the laser diode. This increase is due to the amplified spontaneous emission from the optical amplifier that is injected into the laser. The increase of the RIN and the linewidth depends on the amplification factor of the amplifier and is more severe when the amplification factor increases.

It is also shown that the SMSR in single mode laser diodes, such as DFB or DBR laser diodes, can be reduced by 10 dB or more if an optical amplifier is integrated with the laser diode. The reduction of the side mode rejection is due to an increase of spontaneous emission that couples into the side mode, an increase which in turn is due to ASE originating in the optical amplifier. Like the RIN and the linewidth increase, the SMSR reduction also depends on the amplification factor of the amplifier and is more severe when the amplification factor increases.

6.1 Context

As already explained in chapter 1, core optical networks require transmitter modules capable of delivering high optical power levels. How-

ever, many of the more advanced laser diodes used in such transmitter modules are limited in optical power. In order to boost the power levels, a semiconductor optical amplifier (SOA) is sometimes integrated with the laser diodes. This is e.g. the case for several types of tunable or widely tunable laser diodes [74, 75, 76, 77, 78, 79, 80] as well as for many types of multi-wavelength lasers [81, 82]. Widely tunable laser diodes often have passive tuning sections incorporated on one or both sides of the active section. These passive sections absorb part of the light that is emitted by the active section. This absorption furthermore changes when the current through the tuning sections is changed to tune the laser frequency. The added absorption obviously limits the maximum output power and necessitates the use of an integrated semiconductor optical amplifier for (widely) tunable lasers. Multi-wavelength lasers often consist of laser arrays and a combiner in which the light of the individual lasers is combined. The combiner introduces significant losses, which are preferably compensated by an integrated amplifier.

We will show however that by integrating an optical amplifier with a laser diode, the noise characteristics of the laser diode can be seriously degraded. The noise properties of a laser diode are usually described by the RIN and the linewidth parameters [17, 18, 19]. The RIN is a measure for the relative strength of the intensity fluctuations in the laser output power compared to the average intensity of the laser signal. The linewidth stands for the spectral width of the laser peak and is a measure for the phase noise of the laser signal. Obviously, the RIN and the linewidth of a laser source are preferably as low as possible for a laser that is to be used as a transmitter in a telecommunication network. Unfortunately, as will be shown in this chapter, both the RIN and the laser linewidth can increase with one or more orders of magnitude due to the amplified spontaneous emission noise from the amplifier.

The side mode suppression ratio or SMSR is another important laser diode characteristic. Transmitters for high-end optical communication systems typically need to have side mode rejection over 40 dB. Lower SMSR values may indeed lead to intolerable intensity noise through mode partition noise or to large levels of crosstalk in WDM systems. The power in a side mode typically consists of amplified spontaneous emission and its level is determined by the spontaneous emission rate and by the difference between the threshold gain and the mode loss of the side mode (i.e. the mode discrimination). In this chapter it will be shown that the ASE from the amplifier also seriously degrades the

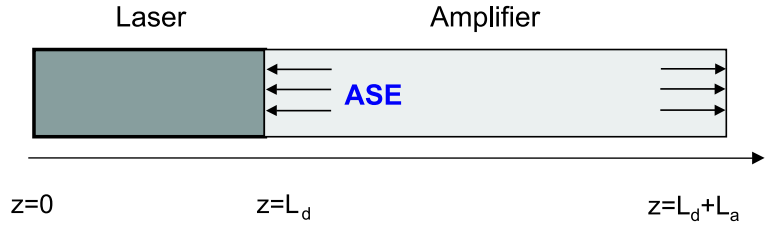

Figure 6.1: Schematic structure of a laser diode integrated with a semiconductor optical amplifier.

SMSR of single mode laser diodes. A degradation of the SMSR of 10 dB or more is possible due to the presence of an integrated SOA.

The degradation of the RIN, linewidth and SMSR can obviously also occur when a laser diode is connected to a separate booster amplifier without an isolator in-between. A related configuration, a laser diode directly connected to or integrated with an SOA-based wavelength converter, will suffer from a similar noise degradation [83].

6.2 Theoretical modelling

In this section we will derive analytical expressions for the RIN, the linewidth and the SMSR of a semiconductor laser connected to an optical amplifier. These expressions will be derived from a set of alternative rate equations that are more generally valid than the conventional rate equations.

Figure 6.1 shows the schematic structure of a laser diode integrated with a semiconductor optical amplifier. The laser part in this structure can represent a general multi-section DFB or DBR laser diode. The influence of the SOA on the laser diode consists of (backward propagating) amplified spontaneous emission noise that is injected in the laser diode at $z = L_d$. This spontaneous emission noise is characterized by a Langevin function $F_i(t)$, which has the following second order moment:

$$\left\langle F_i(L,t)F_i^*(L,t')\right\rangle = h\nu(\Gamma g)_a n_{sp,a}\frac{exp\left[(\Gamma g-\alpha)_a L_a\right]-1}{(\Gamma g-\alpha)_a}\delta(t-t') \quad (6.1)$$

with $h\nu$ the photon energy, L_a the amplifier length and $(\Gamma g)_a$, $n_{sp,a}$, α_a the modal gain, inversion factor and internal loss of the amplifier

respectively. It is assumed that the fields are normalized such that their squared amplitude represents the power.

6.2.1 Rate Equations for a laser connected to an optical amplifier

To model the influence of an integrated optical amplifier on laser performance, we will use a set of improved rate equations that are more generally valid than the conventional rate equations which for instance can be found in [17]. The more general rate equations can be derived from the dynamic coupled-wave equations [84]. We will not go into much detail on the derivation, the interested reader is referred to [84] for a more elaborate treatment.

The dynamic coupled-wave equations are given by:

$$\frac{\partial R^+}{\partial z} + \frac{1}{v_g}\frac{\partial R^+}{\partial t} + j\Delta\beta R^+ = (\kappa_g + j\kappa_i)R^- + F^+(z,t) \tag{6.2a}$$

$$-\frac{\partial R^-}{\partial z} + \frac{1}{v_g}\frac{\partial R^-}{\partial t} + j\Delta\beta R^- = (\kappa_g^* + j\kappa_i^*)R^+ + F^-(z,t) \tag{6.2b}$$

In these equations R^+ and R^- are the amplitudes of the forward and backward propagating fields respectively, v_g is the group velocity, $\Delta\beta$ is the complex Bragg deviation [84], κ_i represents the index coupling and κ_g the gain coupling. F^+ and F^- are uncorrelated Langevin functions with the following second-order moments:

$$\begin{aligned}\left\langle F^+(z,t)F^{+*}(z',t')\right\rangle &= \left\langle F^-(z,t)F^{-*}(z',t')\right\rangle \\ &= h\nu(\Gamma g)_l n_{sp,l} v_g \delta(z-z')\delta(t-t')\end{aligned} \tag{6.3}$$

with $(\Gamma g)_l$ and $n_{sp,l}$ the modal gain and the inversion factor of the laser respectively. The field amplitudes and the complex Bragg deviation can be expanded as follows:

$$R^\pm(z,t) = R_0^\pm(z) + \delta R^\pm(z,t) \tag{6.4a}$$

$$\Delta\beta(z,t) = \Delta\beta_0(z) + \delta(\Delta\beta(z,t)) \tag{6.4b}$$

With $R_0^\pm(z)$ the field amplitudes obtained under static operation and $\Delta\beta_0(z)$ the Bragg deviation under static operation. $R_0^+(z)$ and $R_0^-(z)$ obey the static coupled-wave equations which are given by:

$$\frac{\partial R_0^+}{\partial z} + j\Delta\beta_0 R_0^+ = (\kappa_g + j\kappa_i) R_0^- \tag{6.5a}$$

$$-\frac{\partial R_0^-}{\partial z} + j\Delta\beta_0 R_0^- = (\kappa_g^* + j\kappa_i^*) R_0^+ \tag{6.5b}$$

After substitution of the expansions given by (6.4) into (6.2), a few terms can be removed if (6.5) is taken into account. Next we multiply the resulting equations with R_0^- respectively R_0^+ and likewise multiply (6.5) with δR^- respectively δR^+. If we then subtract the resulting equations for δR^+ and R_0^- and those for δR^- and R_0^+, we obtain:

$$\frac{\partial\left(R_0^-\delta R^+\right)}{\partial z} + \frac{1}{v_g}\frac{\partial\left(R_0^-\delta R^+\right)}{\partial t} + j\delta(\Delta\beta)R^+R_0^- = (\kappa_g + j\kappa_i)R_0^-\delta R^+ - (\kappa_g^* + j\kappa_i^*)R_0^+\delta R^+ + R_0^- F^+ \tag{6.6a}$$

$$-\frac{\partial\left(R_0^+\delta R^-\right)}{\partial z} + \frac{1}{v_g}\frac{\partial\left(R_0^+\delta R^-\right)}{\partial t} + j\delta(\Delta\beta)R^-R_0^+ = -(\kappa_g + j\kappa_i)R_0^-\delta R^+ + (\kappa_g^* + j\kappa_i^*)R_0^+\delta R^+ + R_0^+ F^- \tag{6.6b}$$

Adding (6.6a) and (6.6b) and integrating from the laser facet on the left-hand side ($z = 0$) to the laser facet on the right-hand side ($z = L_d$) yields:

$$\int_0^{L_d} \delta(\Delta\beta)\left[R_0^- R^+ + R_0^+ R^-\right] dz = \frac{j}{v_g}\frac{\partial}{\partial t}\left(\int_0^{L_d}\left[R_0^-\delta R^+ + R_0^+\delta R^-\right] dz\right) - j\int_0^{L_d}\left[R_0^- F^+ + R_0^+ F^-\right] dz - jt_2 R_0^+(L_d)F_i(t) \tag{6.7}$$

For the integration leading to (6.7) we have taken into account the boundary conditions at $z = 0$ (i.e. $R_0^+ = r_1 R_0^-$ and $\delta R^+ = r_1\delta R^-$) and $z = L_d$ (i.e. $R_0^- = r_2 R_0^+$ and $\delta R^- = r_2\delta R^+ + t_2 F_i$), with r_1 the reflection coefficient of the left-hand side laser facet and r_2 and t_2 the reflection and transmission coefficient of the right-hand side laser facet. For the rest of the derivation the fields are normalized such that the

photon density $S(z,t) = |R^+|^2 + |R^-|^2$. It is also assumed that the spatial profiles of δR^+ and δR^- are the same as the spatial profiles of the static fields. This can be expressed as:

$$\begin{aligned} \delta R^{\pm}(z,t) &= R_0^{\pm}(z)\left[\sqrt{1+f(t)}-1\right] \\ \delta S(z,t) &= S_0(z)f(t) \end{aligned} \tag{6.8}$$

with f a real and z-independent function of time and $S_0(z)$ the static optical power profile. Using (6.8) equation (6.7) can now be written as:

$$\begin{aligned} v_g\sqrt{1+f}\int_0^{L_d}\delta(\Delta\beta)\Gamma_z(z)dz = \\ j\frac{\partial(\sqrt{1+f})}{\partial t} + v_gF_c(t) - jt_2v_g\frac{R_0^+(L_d)F_i(t)}{2\int_0^{L_d}R_0^+R_0^-dz} \end{aligned} \tag{6.9}$$

with the longitudinal confinement factor $\Gamma_z(z)$:

$$\Gamma_z(z) = \frac{R_0^+R_0^-}{\int_0^{L_d}R_0^+R_0^-dz} \tag{6.10}$$

and $v_gF_c(t)$ determined by its second-order moment:

$$\begin{aligned} \left\langle v_gF_c(t)F_c^*(t')v_g\right\rangle &= \frac{(\Gamma g)_l n_{sp,l}v_g}{4S_{av}V_{act}}\delta(t-t')\left[\frac{\int_0^{L_d}\left[\left|R_0^+\right|^2+\left|R_0^-\right|^2\right]dz}{\left|\int_0^{L_d}R_0^+R_0^-dz\right|}\right]^2 \\ &= (\Gamma g)_l n_{sp,l}v_g\frac{K_z}{S_{av}V_{act}}\delta(t-t') \end{aligned} \tag{6.11}$$

with K_z the longitudinal Petermann factor [84], S_{av} the spatial average of the photon density and V_{act} the active layer volume. We will denote the third term on the right-hand side of equation (6.9) as $-jv_gF_{inj}(t)$, with the second-order moment of $v_gF_{inj}(t)$ given by:

$$\begin{aligned} &\left\langle v_gF_{inj}(t)F_{inj}^*(t')v_g\right\rangle = \\ &(\Gamma g)_a n_{sp,a}v_g\frac{K_z}{S_{av}V_{act}}\frac{L_a}{L_d}\frac{A-1}{\ln(A)}\left\{\frac{|t_2|^2\left|R_0^+(L_d)\right|^2}{\frac{1}{L_d}\int_0^{L_d}\left[\left|R_0^+\right|^2+\left|R_0^-\right|^2\right]dz}\right\}\delta(t-t') \end{aligned} \tag{6.12}$$

with A the total (net) amplification of the optical amplifier. The factor between the curly brackets is a factor that depends on the laser structure only; it is the extraction efficiency from the right-hand side facet and will be denoted further as $\alpha_r L_d$. For AR-coated lasers this factor is generally very close to unity.

In equation (6.9) $\delta(\Delta\beta)$ still has to be expressed as a function of laser parameters. If for the sake of simplicity we neglect the non-linear gain, $\delta(\Delta\beta)$ can be expressed as follows:

$$\delta(\Delta\beta) = \frac{\Delta\omega}{v_g} + j\frac{1+j\alpha_H}{2}G_d\delta N(z) \tag{6.13}$$

with $\Delta\omega$ the small-signal variation of the optical frequency of the mode, α_H the linewidth enhancement factor, defined by (2.20) and G_d the modal differential gain of the laser waveguide. To determine $\delta N(z)$ we can decompose $N(z,t)$ in a uniform part and a part with the same axial variation as $(S_0(z) - S_{av})$ [84]:

$$N(z,t) = N_0(t) + N_1(t)\frac{S_0(z) - S_{av}}{S_{av}} \tag{6.14}$$

Equation (6.9) can then finally be written as:

$$\begin{aligned}\sqrt{1+f}\left\{\Delta\omega + j\frac{1+j\alpha_H}{2}G'_d\left[\delta N_0 + \delta N_1(\chi - 1)\right]\right\} = \\ j\frac{\partial(\sqrt{1+f})}{\partial t} + v_g F_c(t) - jv_g F_{inj}(t)\end{aligned} \tag{6.15}$$

with $G'_d = v_g G_d$ and where χ is a complex factor that describes the influence of spatial hole burning and is a function of the field distributions in the laser cavity only [84].

6.2.2 Derivation of relative intensity noise and linewidth

For the derivation of laser characteristics rate equation (6.15) has to be combined with the carrier density rate equations. The derivation of the rate equations for N_0 and N_1 can be found in [84]. To simplify the derivation further, we neglect spatial hole burning from now on and assume that the carrier density in the laser cavity is uniform. We also ignore the noise terms in the carrier density rate equations. This implies a.o. that our derivation of the RIN will only be valid at low or moderate power levels. The rate equation for N_0 then is:

$$\frac{dN_0}{dt} = \frac{J}{ed} - \frac{N_0}{\tau(N_0)} - G_l(N_0)S_{av} + S_{av}\Im(2v_gF_c) \tag{6.16}$$

with J the injection current density, e the unit of elektron charge, d the thickness of the active layer, $\tau(N_0)$ the carrier lifetime, $G_l(N_0)$ the modal gain and $\Im(2v_gF_c)$ the imaginary part of $2v_gF_c$. The RIN can be derived from the small signal, frequency-dependent solutions. For this we take the Fourier transform of (6.16) and of the real and imaginary part of (6.15). Then one obtains for the Fourier transform $F(\Omega)$ of $f(t)$:

$$\begin{aligned} F(\Omega)\left\{j\Omega\left[j\Omega + \frac{1}{\tau_d} + G'_dS_{av}\right] + G'_dG_l(N_0)S_{av}\right\} = \\ \left[j\Omega + \frac{1}{\tau_d} + G'_dS_{av}\right]\Re(2v_gF_{inj}) - \left(j\Omega + \frac{1}{\tau_d}\right)\Im(2v_gF_c) \end{aligned} \tag{6.17}$$

So that we obtain for the RIN, which is determined by RIN=$\langle|F|^2\rangle$:

$$\begin{aligned} \langle|F(\Omega)|^2\rangle = \frac{4\left|j\Omega + \frac{1}{\tau_d}\right|^2 G_l(N_0)n_{sp,l}}{\left|j\Omega\left[j\Omega + \frac{1}{\tau_d} + G'_dS_{av}\right] + G'_dG_l(N_0)S_{av}\right|^2}\frac{K_z}{S_{av}V_{act}} \\ \times\left[1 + \frac{A-1}{\ln(A)}\frac{L_a}{L_d}\frac{(\Gamma g)_a n_{sp,a}}{(\Gamma g)_l n_{sp,l}}\alpha_r L_d \frac{\left|j\Omega + \frac{1}{\tau_d} + G'_dS_{av}\right|^2}{\left|j\Omega + \frac{1}{\tau_d}\right|^2}\right] \end{aligned} \tag{6.18}$$

We want to remark that equation (6.18) gives the RIN as would be measured just outside the laser, e.g. at the left-hand side facet of the chip (z=0). At the right-hand side facet of the chip ($z = L_d + L_a$), i.e. after the amplifier, the RIN that is measured is modified further by the beat noise between the laser signal and the forward propagating ASE of the amplifier. This extra RIN has been described before and is usually negligible [99]. If furthermore the amplifier is saturated, then the intensity noise from the right-hand side laser facet will be suppressed in the amplifier.

From a similar derivation, but assuming only low frequencies Ω, one finds for the linewidth:

$$\begin{aligned} \Delta\nu = \frac{G_l(N_0)n_{sp,l}}{4\pi}\frac{K_z}{S_{av}V_{act}}\left(1+\alpha_H^2\right) \\ \times\left[1 + \frac{A-1}{\ln(A)}\frac{L_a}{L_d}\frac{(\Gamma g)_a n_{sp,a}}{(\Gamma g)_l n_{sp,l}}\alpha_r L_d\right] \end{aligned} \tag{6.19}$$

From equations (6.18) and (6.19) it can easily be seen that both the RIN spectrum and the linewidth of the solitary laser are increased by the presence of the optical amplifier with the factor between square brackets. The linewidth and RIN increase due to the ASE noise from the optical amplifier can easily be estimated. We consider a $\lambda/4$-shifted DFB laser, for which $\alpha_r L_d$=1 (i.e. $\kappa L \approx 1.25$). We also assume that laser diode and semiconductor optical amplifier have equal length, equal gain and equal inversion factors. In that case, both the RIN and the linewidth are increased by a factor $1 + (A-1)/\ln(A)$. This factor is around 5 (7 dB) for an amplification of 10 (10 dB), but increases to 22.5 (13 dB) for an amplification of 20 dB. In section 6.3 elaborated numerical and experimental examples will be given.

Almost at the same time as we published the results described above in [100], other researchers have published a paper about the linewidth broadening of a DFB laser with an integrated SOA [101]. Their theoretical model is based on a two-dimensional transverse carrier transport model coupled to a longitudinal model based on the Green's function method. For the case of a perfectly anti-reflection coated SOA facet (R_a = 0) they find an analytical expression (expr. (54) in [101]) similar to (6.19), also indicating that the linewidth broadening is caused by the ASE coming from the SOA that is coupled into the lasing mode. Their model also neglects non-linear gain compression, but it does take into account the effect of spatial hole burning in the laser. From their results it appears however that spatial hole burning only has a considerable influence for lasers with a high normalized coupling coefficient κL and even then the broadening factor (i.e. the factor between square brackets in (6.19)) remains very well within the same order of magnitude as the values we have found (for an amplifier gain of 10 they find a broadening factor of 5 resp. 7 for a κL of 2.6 resp. 3.6). The biggest difference is that the material linewidth enhancement factor α_H in (6.19) is replaced by the effective linewidth enhancement factor α_{eff}. This is because we have neglected spatial hole burning (i.e. the contribution of δN_1 in (6.15)) and therefor we obtain a result with α_H instead of α_{eff}.

The influence of a finite reflectivity of the SOA facet was also investigated in [101]. When the SOA facet has a non-zero reflectivity, the laser will be influenced by the optical feedback from this facet, on top of the amplifier ASE that is injected into the laser. As was already explained in chapter 2, the linewidth can either be increased or decreased by the feedback, depending on the phase of the feedback. These oscil-

lations can lead to a linewidth broadening that is even higher than the one predicted by (6.19).

In our model we also have not taken into account the saturation of the amplifier by the laser light. This would lead to a reduction of the gain and the ASE emitted by the SOA. However, in [101] it is also shown that the broadening is not much influenced by the reduction of the ASE caused by the saturation of the optical amplifier by the laser output power.

6.2.3 Derivation of side mode suppression ratio

To derive an expression for the decrease of the SMSR of a laser-amplifier cascade, we will again start from equation (6.15). For the derivation of equation (6.15) $R_0^{\pm}$ and N_0 have to be chosen such that they fulfill the static coupled wave equations (i.e. also without spontaneous emission). For a side mode, this means that N_0 is the threshold carrier density of that side mode. If a main mode is lasing at lower threshold and spontaneous emission is present, then the power in the side mode will be amplified spontaneous emission and δN can be regarded as the deviation from N_0 due to this amplified spontaneous emission.

Equation (6.15) can be rewritten as

$$\frac{\partial f}{\partial t} = 2j\sqrt{1+f}\left[v_g F_c - j v_g F_{inj}\right] - 2j(1+f)\left\{\Delta\omega + j\frac{1+j\alpha_H}{2}G'_d\delta N\right\} \tag{6.20}$$

where we have again neglected the influence of spatial hole burning. The first term on the right-hand side gives rise to the DC–contribution of the noise and this term can easily be calculated using a perturbation approach. Taking the real part of (6.20) and taking into account that f, $\Delta\omega$ and δN are much smaller then unity, gives the following solution for f:

$$f(t) = \Re \int_{-\infty}^{t} \left[2j v_g F_c(t') + 2 v_g F_{inj}(t')\right] dt' \tag{6.21}$$

where $\Re$ represents the real part of the integral. If we then substitute this expression in (6.20), linearize in f and take the statistical (or time) average, we obtain:

$$\begin{aligned}
&\langle \Re\left[2jv_gF_c(t') + 2v_gF_{inj}(t')\right] f(t)\rangle \\
&= 4v_g^2 \left\langle \Re\left[jF_c(t) + F_{inj}(t)\right] \times \Re \int_{-\infty}^{t} \left[jF_c(t') + F_{inj}(t')\right] dt' \right\rangle \\
&= \frac{v_g(\Gamma g)_l n_{sp,l} K_z}{S_{av}V_{act}} + \frac{v_g(\Gamma g)_a n_{sp,a} K_z}{S_{av}V_{act}} \frac{A-1}{\ln(A)} \frac{L_a}{L_d} \alpha_r L_d
\end{aligned} \tag{6.22}$$

So that when linearizing equation (6.20) and separating it into real and imaginary parts, the equation for f should be written as:

$$\begin{aligned}
\frac{\partial f}{\partial t} = 2v_g \left[\Re(F_{inj}) - \Im(F_c)\right] + G'_d \delta N \\
+ \frac{R_{sp,l} + R_{sp,a} \frac{A-1}{\ln(A)} \frac{L_a}{L_d} \alpha_r L_d}{S_{av}V_{act}}
\end{aligned} \tag{6.23}$$

With $R_{sp,l}$ and $R_{sp,a}$ the spontaneous emission rate per time unit for laser and amplifier respectively. From now on, we ignore the noise and concentrate on the spontaneous emission that couples into the laser mode. And if we replace $S_{av}V_{act}$ by the (static) number of photons in the laser cavity S_0^n, equation (6.23) can then be expressed as:

$$\frac{\partial S^n}{\partial t} = G'_d \delta N S_0^n + R_{sp,l} + R_{sp,a} \frac{A-1}{\ln(A)} \frac{L_a}{L_d} \alpha_r L_d \tag{6.24}$$

As already mentioned above, for a side mode δN is the difference between the actual carrier density in the presence of amplified spontaneous emission and the threshold carrier density for that mode and hence $G_l^d \delta N = G_{th} - 1/\tau_p$ with τ_p the photon lifetime for the side mode and G_{th} the threshold gain of the main mode. The static solution of (6.24) can therefore be written as:

$$S_0 = \frac{R_{sp,l} + R_{sp,a} \frac{A-1}{\ln(A)} \frac{L_a}{L_d} \alpha_r L_d}{1/\tau_p - G_{th}} \tag{6.25}$$

With S_0 representing the power in the side mode. This power is obviously increased due to the presence of the optical amplifier and the increase is with a factor:

$$\frac{S_0^{SOA}}{S_0^{noSOA}} = \left[1 + \frac{A-1}{\ln(A)} \frac{L_a}{L_d} \frac{(\Gamma g)_a n_{sp,a}}{(\Gamma g)_l n_{sp,l}} \alpha_r L_d\right] \tag{6.26}$$

As can be seen from equation (6.19), this is exactly the same factor that was found for the linewidth increase due to the ASE of an integrated optical amplifier. This can be attributed to the fact that both SMSR and linewidth depend on the total spontaneous emission that couples into a laser mode. This factor is of course the factor by which the SMSR, measured at the left-hand side facet (at z=0), decreases.

Shortly after we published our results on the decrease of the SMSR of a laser-amplifier cascade in [102, 103], the same researchers who already published the paper about the linewidth broadening of a DFB laser with an integrated SOA [101], also published a paper on the degradation of the SMSR in a DFB laser with an integrated SOA [104]. Their results are based on the same theoretical model as the one used in [101] and are again in good agreement with our results. As they did for the increase of the linewidth, they also investigated the influence of a finite reflectivity of the SOA facet on the decrease of the SMSR. The same oscillations that appear in the linewidth also occur in the SMSR. These oscillations can make the SMSR decrease even more severe than the one predicted by (6.26).

6.3 Increase of relative intensity noise and linewidth

6.3.1 Simulation results

Relative intensity noise increase

We have verified the above theory using the laser simulation software Componentmaker from VPI [56]. To this end, we calculated the RIN and linewidth of a 400 μm long quarter–wave shifted, AR-coated DFB laser with and without additional SOA at the right-hand side facet. The laser has a normalized coupling coefficient κL_d = 2. The SOA is 350 μm long and gives an amplification of 16 dB and has anti-reflection coated facets. The inversion factor of both laser and SOA is 2.

Figure 6.2 shows the RIN for increasing levels of ASE power P_{ase} injected into the laser and this for two different laser output powers of 2 and 5 mW respectively. These values correspond to the output power of the solitary laser, without the presence of an amplifier. For clarity we would also like to note that the numerical values of P_{ase} in this graph correspond to the total ASE power emitted by the SOA when no laser would be present, this is different from the ASE coupling into the laser mode. The total emitted ASE power from the SOA is proportional with

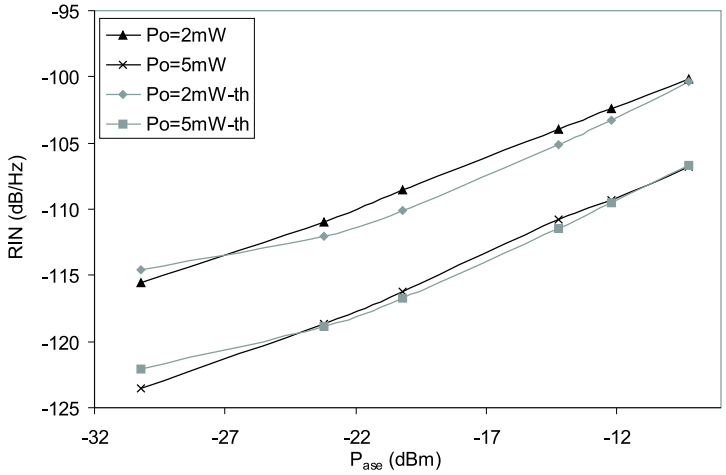

Figure 6.2: Calculated RIN and theoretical fits versus P_{ase} of a $\lambda/4$-shifted DFB with and without integrated SOA for a laser facet output power of 2 and 5 mW respectively (P_o is the output power of the solitary laser, -th indicates the fitted results obtained from eq. (6.27)).

$R_{sp,a}(A-1)/\ln(A)$. However, instead of varying the amplification to vary the ASE injected into the laser, we have applied various levels of attenuation on the ASE emitted from the SOA, while keeping the current through the SOA constant.

From figure 6.2 one can clearly see the degradation of the RIN for increasing P_{ase}. For an increase of P_{ase} of 21 dB (from –30 to –9 dBm) the increase of the RIN is 15 dB and 16 dB for laser output powers of 2 and 5 mW respectively. The numerically obtained results were fitted to the following expression for the RIN increase, which was derived from equation (6.18) by taking the attenuation a, by which the ASE emitted by the amplifier is attenuated (the ASE is proportional to $(\Gamma g)_a n_{sp,a}(A-1)/lnA$), into account and by grouping the remaining parameters into a proportionality factor η:

$$\frac{RIN^{SOA}}{RIN^{noSOA}} = \left[1 + \frac{\eta}{a}\frac{A-1}{\ln(A)}\right] \tag{6.27}$$

To fit this expression to the numerical results, an appropriate value for RIN^{noSOA} and A were chosen and η was varied to obtain a good fit. The theoretical fits obtained from (6.27) are also shown (using -th in the legend) on figure 6.2 and we see good quantitative agreement

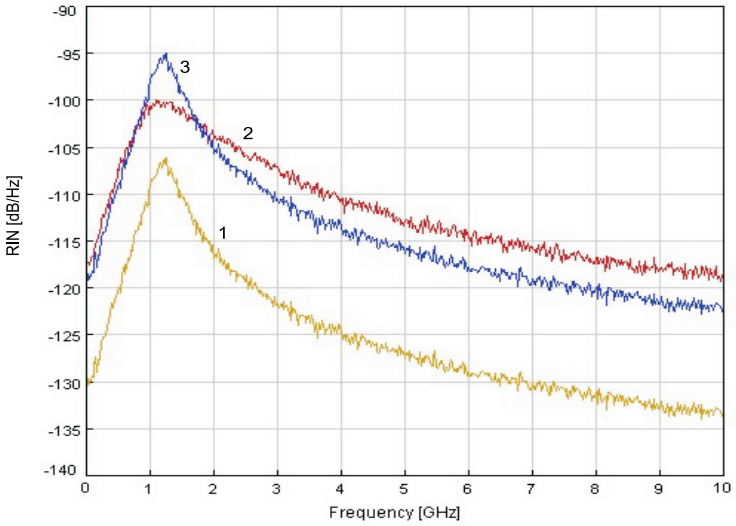

Figure 6.3: Calculated RIN spectrum of a $\lambda/4$-shifted DFB with and without integrated SOA for a laser facet output power of 0.6 mW. (1) is the RIN spectrum of the solitary laser, (2) is the RIN spectrum of the laser with the SOA calculated with the simulation software, (3) is the RIN spectrum of the laser with the SOA and is obtained from (1) using expression (6.18).

between the theoretical and simulated results, and this for the different laser output powers.

The RIN spectrum as would be measured on the left-hand side facet facet is shown in figure 6.3 for the solitary laser (curve (1)) as well as for the laser with integrated SOA (curve (2)). The laser was biased such that the output power from the laser (e.g. from the left-hand side facet) was 0.6 mW without amplification. From expression (6.27), one finds that the RIN of the laser increases by 12.5 dB due to the ASE from the SOA. This is very similar to what is obtained from the numerical simulations, especially at low frequencies. At very high frequencies, the simulations predict a RIN increase with 15 dB, ie. 3 dB more than expression (6.18). This discrepancy could be due to e.g. our simplification of the carrier density dynamics and the neglect of the carrier density shot noise.

Linewidth increase

Figure 6.4 shows the linewidth for increasing levels of ASE power P_{ase} injected into the laser and this for two different laser output powers of

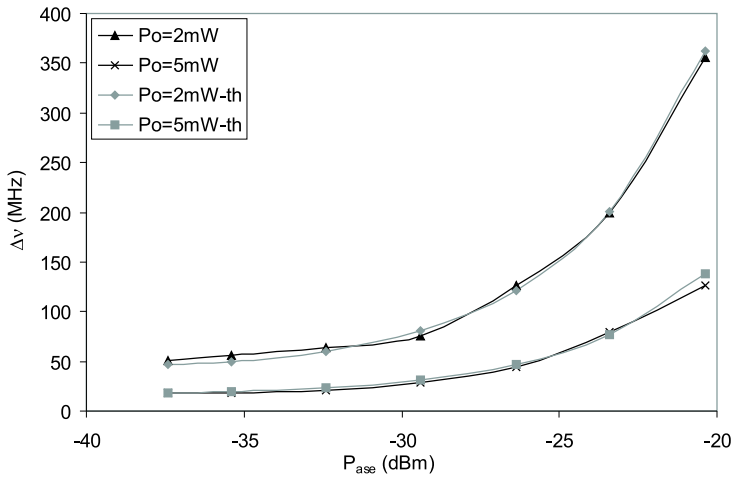

Figure 6.4: Calculated linewidth and theoretical fits versus P_{ase} of a $\lambda/4$-shifted DFB with and without integrated SOA for a laser facet output power of 2 and 5 mW respectively (P_o is the output power of the solitary laser, -th indicates the fitted results obtained from eq. (6.27)).

2 and 5 mW respectively. These values correspond to the output power of the solitary laser, without the presence of an amplifier.

From figure 6.4 one can clearly see the degradation of the linewidth for increasing P_{ase}. For an increase of P_{ase} of 17 dB (from –37 to –20 dBm) the increase of the linewidth is 8.5 dB (from 50 to 355 MHz and from 18 to 126 MHz respectively) for both laser output powers of 2 and 5 mW respectively. The numerically obtained results for the linewidth increase were also fitted to expression (6.27). The theoretical fits that are obtained this way are also shown (using -th in the legend) on figure 6.4 and we again see good qualitative agreement between the theoretical and simulated results, and this for the different laser output powers.

Figure 6.5 shows the optical spectrum for a laser output power of 2 mW and for an ASE power P_{ase} of -37 dBm and -20 dBm respectively (this corresponds to a linewidth increase of 8.5 dB, cfr. figure 6.4). The broadening of the spectrum can clearly be seen.

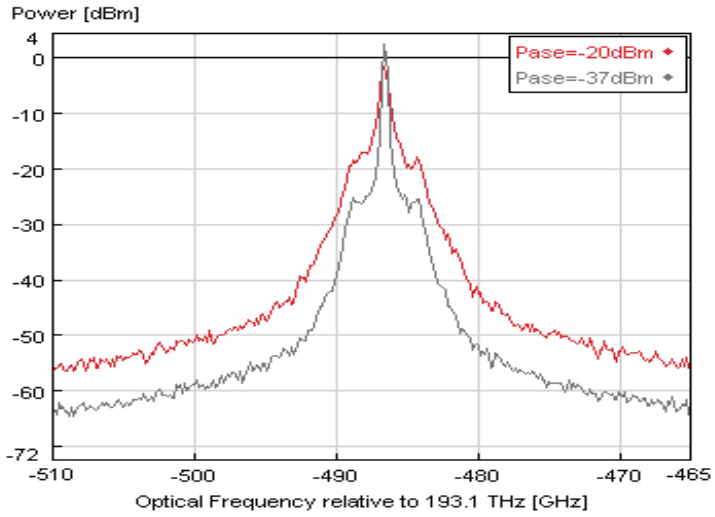

Figure 6.5: Calculated optical spectrum of a $\lambda/4$-shifted DFB with and without integrated SOA for a laser facet output power of 2 mW and for an ASE power P_{ase} of -37 dBm and -20 dBm respectively.

6.3.2 Experimental results

Relative intensity noise increase

Further verification of our theory was again obtained by performing measurements on the RIN of a semiconductor laser coupled with an optical amplifier. The measurement setup is shown in figure 6.6.

The laser was a packaged tunable three section DBR laser with an AR-coated facet and without isolator in the package. We used different optical amplifiers (OA on the figure) as ASE source. The ASE was injected into the laser using a circulator and the injected P_{ase} could be varied using an attenuator (Att. on the figure). The actual amount of (attenuated) ASE that is injected into the laser could be monitored with the integrated photo detector (PD on the figure) of the attenuator. The output of the aggregate system was monitored using a computer-controlled electrical spectrum analyzer (ESA on the figure). In this configuration the amplifier will not be saturated by the laser light, which would be the case for an integrated amplifier. Nevertheless, we will be able to investigate the influence of (different levels of) ASE coupled into a laser diode on the laser performance, more in particular on the RIN and the linewidth.

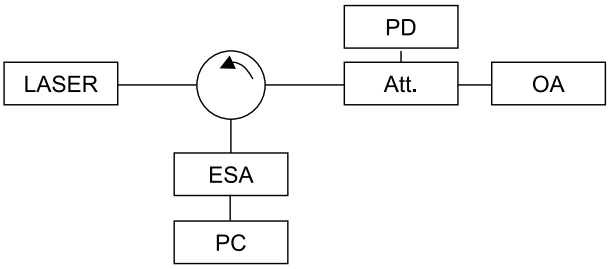

Figure 6.6: Schematic of the measurement setup to measure the RIN of a cascade of a laser and an optical amplifier (ESA = Electrical Spectrum Analyzer, Att. = attenuator, PD = Photo Detector).

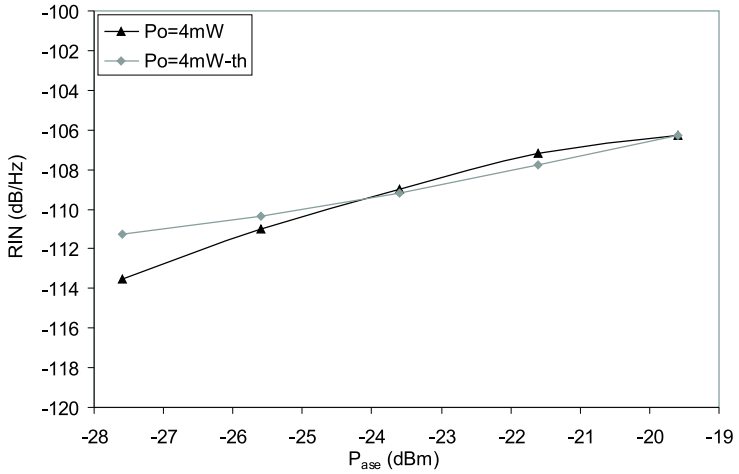

Figure 6.7: Measured RIN values and theoretical fits versus P_{ase} for a laser output power of 4 mW (P_o is the output power of the solitary laser, -th indicates the fitted results obtained from eq. (6.27)).

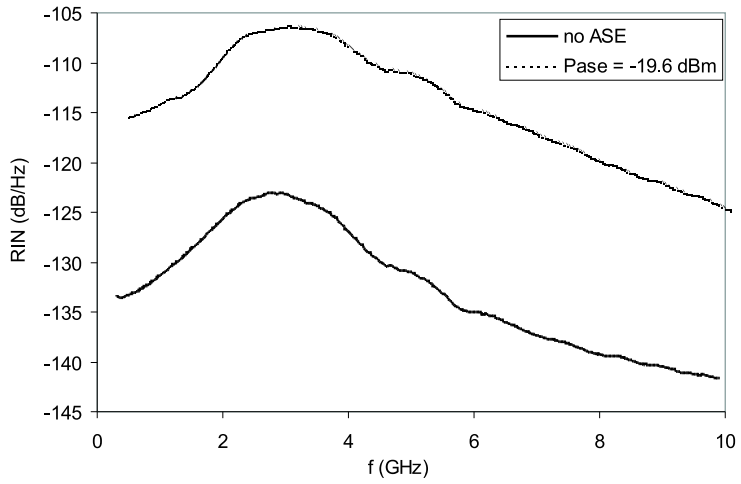

Figure 6.8: Measured RIN spectrum of a laser-SOA cascade. The RIN spectrum is shown for the solitary laser (thick line) and for the cascade with the SOA injecting -19.6 dBm of ASE into the laser (broken line).

Figure 6.7 shows the RIN for increasing levels of ASE power P_{ase} injected into the laser. The bias current through the active section of the laser was 80 mA, corresponding to an output power of 4 mW for the solitary laser (i.e. without the presence of an amplifier). The amplifier was a polarization independent SOA with a center wavelength of 1550 nm, an amplification of 16 dB and an ASE power of -7.5 dBm.

From figure 6.7 one can clearly see the degradation of the RIN for increasing P_{ase}. For an increase of P_{ase} of 8 dB (from -27.6 to -19.6 dBm) the increase of (the peak of) the RIN spectrum is 7.2 dB. The theoretical fits obtained from (6.27) are also shown (using -th in the legend) in figure 6.7 and we see good agreement between the experimental and theoretical results.

Figure 6.8 shows the measured RIN spectrum for the solitary laser and for the cascade with the SOA injecting -19.6 dBm of ASE into the laser. For the solitary laser, the peak value of the RIN spectrum was -123 dB/Hz. For an injected P_{ase} of -19.6 dBm the increase of the RIN, compared to the RIN without amplification, is then 17 dB. This is even more than the increase predicted by (6.27). This is possibly due to the fact that we neglected the shot noise in the rate equation for the carrier density. This shot noise becomes more and more dominant when the laser output power increases.

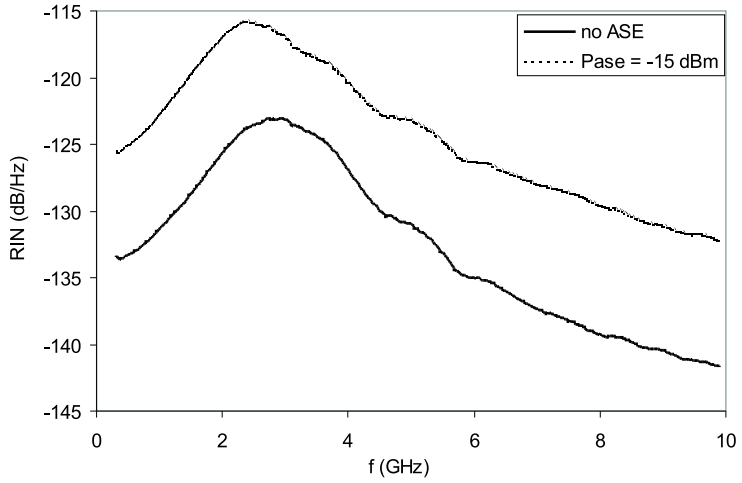

Figure 6.9: Measured RIN spectrum of a laser-EDFA cascade. The RIN spectrum is shown for the solitary laser (thick line) and for the cascade with the EDFA injecting -15 dBm of ASE into the laser (broken line).

We performed the same measurement with an EDFA as ASE source. The EDFA had a gain of around 30 dB. Figure 6.9 shows the measured RIN spectrum for the solitary laser and for the cascade with the EDFA injecting -15 dBm of ASE into the laser. For low frequencies, the increase of the RIN is only 7 dB, for higher frequencies the increase is around 10 dB. This is lower than one would expect from (6.27). A possible explanation lies in the fact that the ASE spectrum of the EDFA is different from that of a SOA. The values of the injected P_{ase} are measured with a power meter and represent the total amount of ASE power in the ASE spectrum of the amplifier. Hence, these values do not give any information about the spectral content of the amplifier ASE. This means that in the spectral band of the laser gain, the ASE emitted by the EDFA could be lower than the ASE emitted by the SOA. The important fact remains that the RIN of the laser is increased when it is connected to an optical amplifier.

Figure 6.11 shows the increase of the RIN (spectrum) for a laser-amplifier cascade with a direct connection between the laser and the amplifier. The measurement setup is shown in figure 6.10. The amplifier will now be saturated by the laser light, causing a decrease of the ASE emitted by the amplifier. The output power of the solitary laser was 4 mW and the total ASE power the amplifier injected into the laser

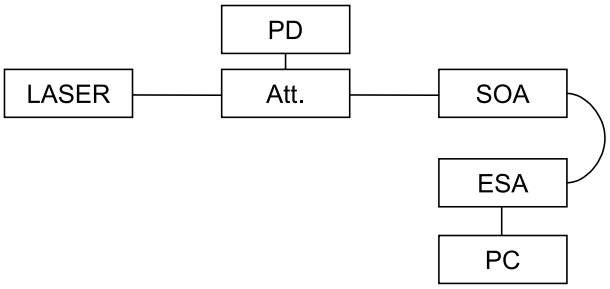

Figure 6.10: Schematic of the measurement setup to measure the RIN of a laser-SOA cascade with a direct connection between the laser and the SOA (ESA = Electrical Spectrum Analyzer, Att. = attenuator, PD = Photo Detector).

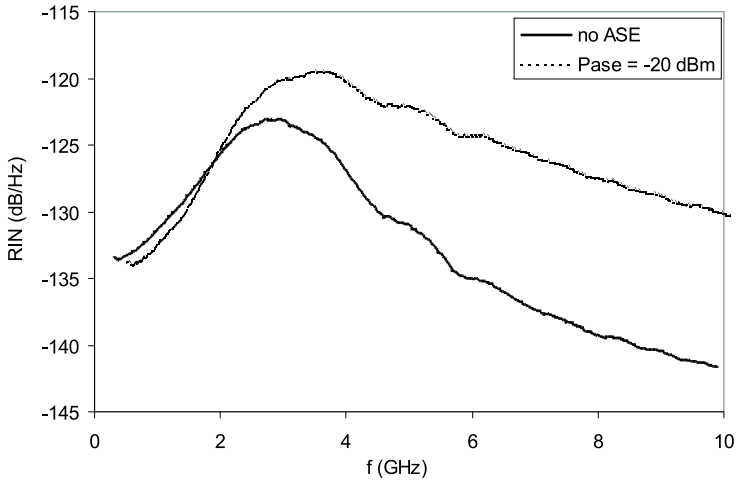

Figure 6.11: Measured RIN spectrum of a laser-SOA cascade with a direct connection between the laser and the SOA. The RIN spectrum is shown for the solitary laser (thick line) and for the cascade with the SOA injecting -20 dBm of ASE into the laser (broken line).

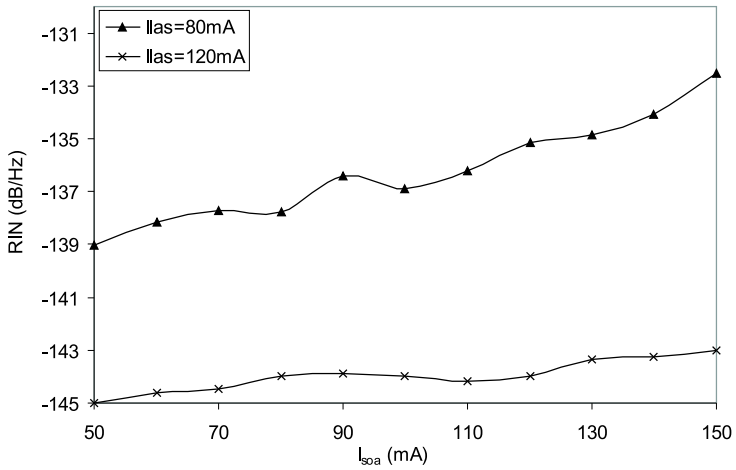

Figure 6.12: Measured RIN versus amplifier current for a DFB laser integrated with an optical amplifier with a non–perfect AR–coating. The laser bias current was 80 mA and 120 mA respectively.

was -20 dBm. The amplifier was a regular SOA with a non-saturated gain of 13 dB. Again we see that, even though the amplifier is saturated by the laser light, there is an increase of the RIN. The peak RIN increases about 4 dB (from -123 dB/Hz to -119 dB/Hz). For higher frequencies the increase is even 11 dB (from -141 dB/Hz to -130 dB/Hz at 10 GHz). It has to be remarked that in this setup the RIN is measured at the SOA facet. This means that the measured RIN will be influenced by the beat noise between the laser signal and the (forward propagating) ASE of the SOA. But as was mentioned before, this contribution is usually negligible [99].

All the measurements that we have shown so far were obtained using stand-alone components. I.e. that the laser and the amplifier were not integrated on one chip, but were connected by optical fibers via a circulator. The reason for this is that measurements on an integrated device were not necessary to proof the validity of our theory. But also, we did not have such a device when we performed our first measurements. However, nearly a year after our first experiments, we obtained an integrated device consisting of four fixed wavelength DFB lasers that were coupled to an SOA through a 4x1-coupler. This means that there is a (fixed) attenuation of 6 dB between a laser and the amplifier.

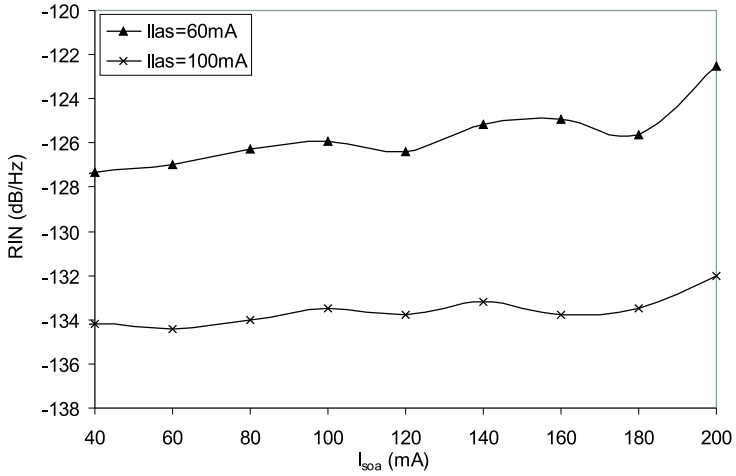

Figure 6.13: Calculated RIN values versus amplifier current for a DFB laser integrated with an optical amplifier with a non-perfect AR-coating. The laser bias current was 60 mA and 100 mA respectively.

Figure 6.12 shows the RIN versus increasing current through the amplifier, for a current of 80 mA and 120 mA through the laser. Again we see an increase of the RIN when the current through the amplifier and thus the emitted ASE increases. We can also clearly see that the amplifier is now saturated by the laser light: for a laser current of 80 mA the increase of the RIN is 6.5 dB, while for a laser current of 120 mA the increase of the RIN is only 2 dB. The slight oscillation in the RIN-increase is of course due to the non-perfect AR-coating on the amplifier facet [101]. For completeness figure 6.13 shows the RIN increase for a DFB laser integrated with an optical amplifier with a non-perfect AR-coating, calculated with Componentmaker from VPI [56]. The laser bias current was 60 mA and 100 mA respectively. The reflectivity of the AR-coating was assumed to be 10^{-5}. The oscillations are also visible in the simulation results and we see again the saturation of the amplifier by the laser: for a laser current of 60 mA the increase of the RIN is around 5 dB, while for a laser current of 100 mA the increase of the RIN is only about 2 dB.

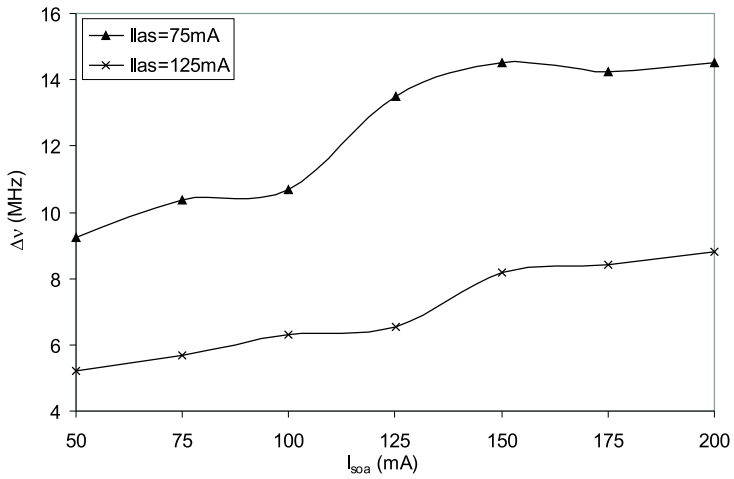

Figure 6.14: Measured linewidth versus amplifier current for a DFB laser integrated with an optical amplifier with a non-perfect AR-coating. The laser bias current was 75 mA and 125 mA respectively.

Linewidth increase

To measure the increase of the linewidth, we used the integrated component, since the linewidth of the tunable DBR laser that was used in the other experiments was already broadened due to the noisy current source that was used for the tuning currents of that laser. Figure 6.14 shows the linewidth versus increasing current through the amplifier, for a current of 75 mA and 125 mA through the laser. Again we see an increase of the linewidth when the current through the amplifier and thus the emitted ASE increases. Both for a laser current of 75 mA and 125 mA the increase of the linewidth is only 2 dB for an increase of amplifier current from 50 mA to 150 mA. This is partly due to the saturation of the amplifier and partly due to the oscillations caused by the non-perfect AR-coating on the amplifier facet [101].

To conclude figure 6.15 shows the linewidth increase (calculated with VPI) for a DFB laser integrated with an optical amplifier with a non-perfect AR-coating. The laser bias current was 60 mA and 100 mA respectively. The reflectivity of the AR-coating was assumed to be 10^{-5}. The oscillations are also visible in the simulation results. The increase of the linewidth is around 2 dB, both for a laser current of 60 mA and 100 mA.

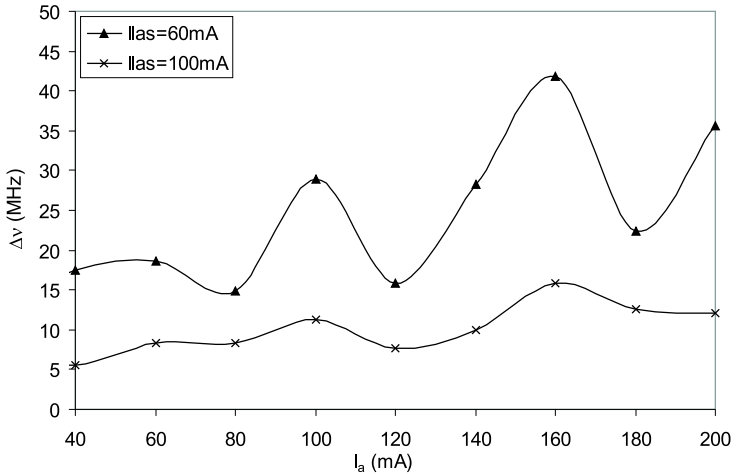

Figure 6.15: Calculated linewidth versus amplifier current for a DFB laser integrated with an optical amplifier with a non-perfect AR-coating. The laser bias current was 60 mA and 100 mA respectively.

6.4 Decrease of side mode suppression ratio

6.4.1 Simulation results

As a first verification of the theoretical results obtained above and more precisely of expression (6.26) we again performed some numerical simulations using the commercially available VPI software. The following parameters are applicable for the structure from figure 6.1: the laser was a quarter wave shifted DFB laser with a length of L_d = 400 μm and a normalized coupling coefficient κL_d = 2. The integrated optical amplifier was a semiconductor optical amplifier (SOA) with a length L_a = 350 μm and an amplification A = 16 dB, the facets are anti-reflection coated. Both laser and SOA had an inversion factor of 2.

Figure 6.16 shows the obtained variation of the side mode suppression for increasing levels of ASE power P_{ase} injected into the laser and this for three different laser output powers of 0.6, 2 and 5 mW respectively. Again these power levels correspond to the output power of the solitary laser, without the presence of an amplifier. The numerical values of P_{ase} in this graph again correspond to the total ASE power emitted by the SOA when no laser would be present, this is different from the ASE coupling into the side mode.

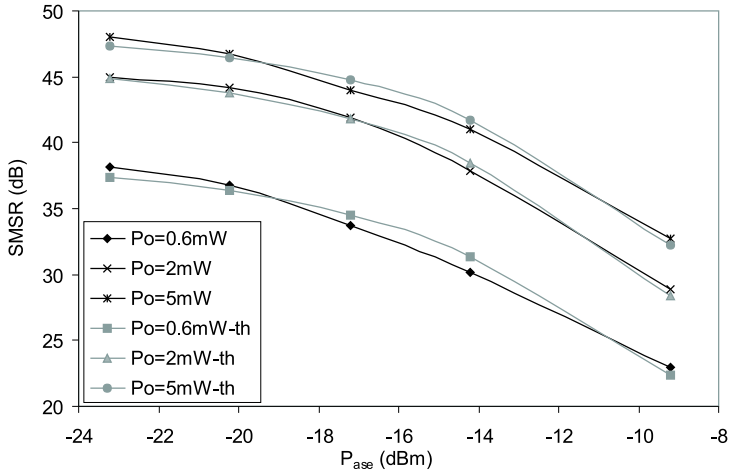

Figure 6.16: Calculated SMSR values and theoretical fits versus P_{ase} for three different laser output powers of 0.6, 2 and 5 mW respectively (P_o is the output power of the solitary laser, -th indicates the fitted results obtained from eq. (6.28)).

From figure 6.16 one can clearly see the degradation of the SMSR for increasing P_{ase}. For an increase of P_{ase} of 14 dB (from -23 to -9 dBm) the decrease of the SMSR is 15 dB, 16 dB and 15 dB for laser output powers of 0.6, 2 and 5 mW respectively. The numerically obtained results were again fitted to a theoretical expression for the SMSR. This expression can be derived from equation (6.26) by taking the attenuation a, by which the ASE emitted by the amplifier is attenuated into account, in the same way as was done to obtain the (reduced) theoretical expression (6.27) for the RIN and linewidth increase:

$$\frac{SMSR^{SOA}}{SMSR^{noSOA}} = \left[1 + \frac{\eta}{a}\frac{A-1}{\ln(A)}\right]^{-1} \tag{6.28}$$

The theoretical fits obtained from (6.28) are also shown (using -th in the legend) on figure 6.16 and we see good qualitative agreement between the theoretical and simulated results, and this for the different laser output powers.

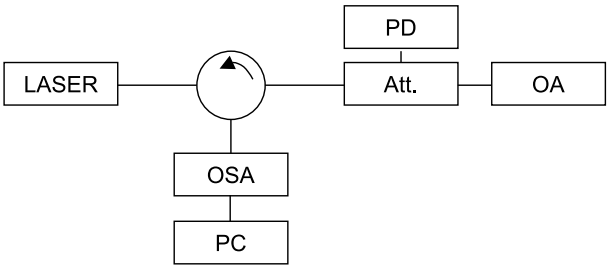

Figure 6.17: Schematic of the measurement setup to measure the SMSR of a cascade of a laser and an optical amplifier (OSA = Optical Spectrum Analyzer, Att. = attenuator, PD = Photo Detector).

6.4.2 Experimental results

Experimental verification of our theory was obtained by performing measurements on the SMSR of a semiconductor laser coupled with an optical amplifier. The measurement setup was the same as the one shown in figure 6.6. The only difference is that now we used a (computer–controlled) optical spectrum analyzer (OSA) to measure the SMSR of the aggregate system instead of the electrical spectrum analyzer that was used for the RIN and the linewidth.

The laser was the same packaged tunable three section DBR laser with an AR-coated facet and without isolator in the package. The SMSR of this laser is rather low (only 35 dB), but this does not pose a problem, since we are mainly interested in the decrease of the SMSR when ASE is injected into the laser. We used a polarization independent SOA with a center wavelength of 1550 nm and an ASE power of -7.5 dBm as ASE source.

Figure 6.18 shows the measured variation of the SMSR for increasing levels of emitted ASE power P_{ase} and again the theoretical fits obtained from (6.28) are also shown (using –th in the legend), and this for 3 different laser output powers of 2.3, 4.9 and 7.9 mW respectively (again, these values indicate the output power of the laser when no amplifier would be present). The amplification of the SOA was 16 dB. Again we see the degradation of the SMSR. When the emitted ASE power increases 16 dB (from -29.5 to -13.5 dBm), the SMSR decreases 7 dB, 8 dB and 7.5 dB for laser output powers of 2.3, 4.9 and 7.9 mW respectively. We also see good agreement between the theoretical and measured results.

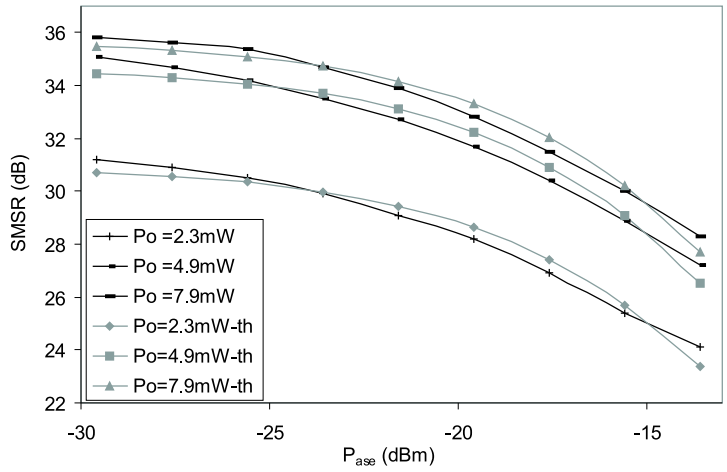

Figure 6.18: Measured SMSR values and theoretical fits versus P_{ase} for 3 different laser output powers of 2.3, 4.9 and 7.9 mW respectively (P_o is the output power of the solitary laser, -th indicates the fitted results obtained from eq. (6.28)).

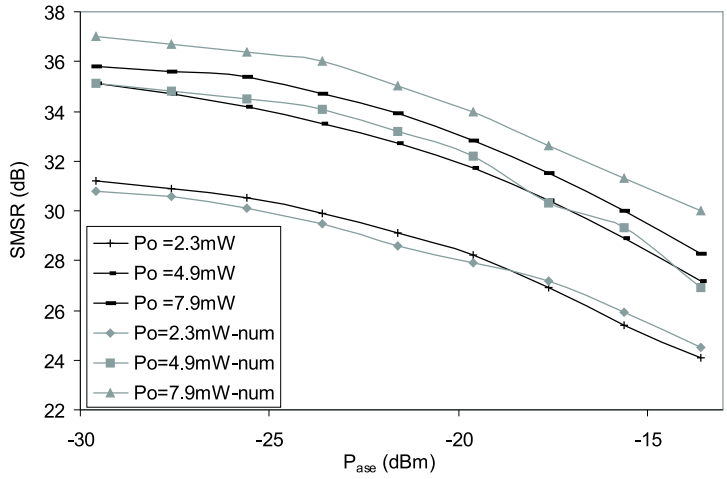

Figure 6.19: Measured SMSR values and numerically calculated values versus P_{ase} for 3 different laser output powers of 2.3, 4.9 and 7.9 mW respectively (P_o is the output power of the solitary laser, -num indicates the numerically calculated results).

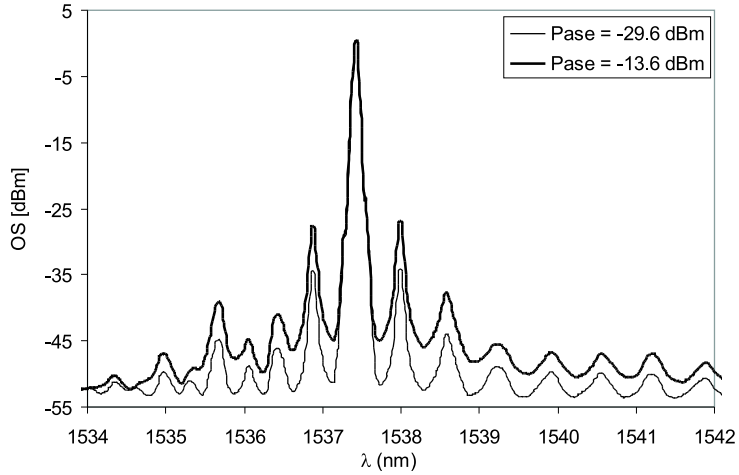

Figure 6.20: Measured optical spectrum (OS) for two different levels of P_{ase} (-29.6 (thin line) and -13.6 dBm (thick line) respectively).

Figure 6.19 again shows the experimental results, now compared with the numerical values calculated using VPI. For this calculation the parameters of the laser model were adapted to match as good as possible with those of the laser used in the experiments. Since we do not know all the parameters of our laser that are required for the numerical model [56] and furthermore also do not know the parameter values related to the coupling of the laser and the amplifier, it is difficult to get good agreement between numerical and experimental values for all laser output powers. On the contrary, expression (6.28) yields an easy and reliable means to correctly describe the experimental results, without having to know all parameters involved (only A and η need to be known).

Figure 6.20 shows the optical spectrum for two different levels of P_{ase} (-29.6 (thin line) and -13.6 dBm (thick line) respectively). The peaks of the spectra are overlapping and the decrease of the SMSR can clearly be seen.

We also investigated the SMSR decrease of the integrated device already described in section 6.3.2. Figure 6.21 shows the SMSR versus increasing current through the amplifier, for a current of 80 mA and 120 mA through the laser. Again we see a decrease of the SMSR when the current through the amplifier and thus the emitted ASE increases. The amplifier is clearly saturated by the laser light: for a laser current

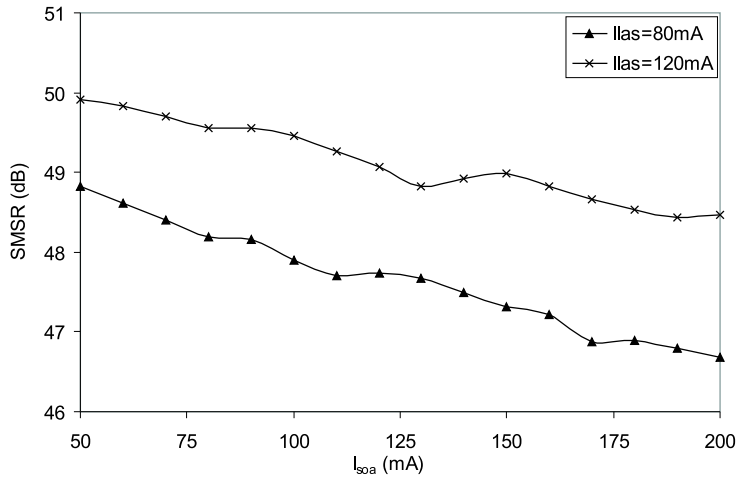

Figure 6.21: Measured SMSR versus amplifier current for a DFB laser integrated with an optical amplifier with a non-perfect AR-coating. The laser bias current was 80 mA and 120 mA respectively.

of 80 mA the decrease of the SMSR is only 2 dB, and for a laser current of 120 mA it is only 1.5 dB. The slight oscillation in the SMSR-decrease is again due to the non-perfect AR-coating on the amplifier facet [104].

For completeness figure 6.22 shows the SMSR increase for a DFB laser integrated with an optical amplifier with a non-perfect AR-coating, calculated with the Componentmaker software. The laser bias current was 60 mA and 100 mA respectively. The reflectivity of the AR–coating was assumed to be 10^{-5}. The oscillations are again visible in the simulation results. For a laser current of 60 mA the decrease of the SMSR is around 9 dB, for 100 mA the decrease of the RIN is around 6 dB. The (slight) difference in decrease between the experimental and numerical results can be explained by the non-perfect AR-coating and by the different level of saturation of the amplifier in experiments and simulations. Also, we only had a few parameters of the laser and the SOA at our disposal, so we had to estimate them to do the simulations.

6.5 Conclusion

In this chapter we have derived theoretical expressions for the RIN, the linewidth and the SMSR of a laser diode integrated with an optical

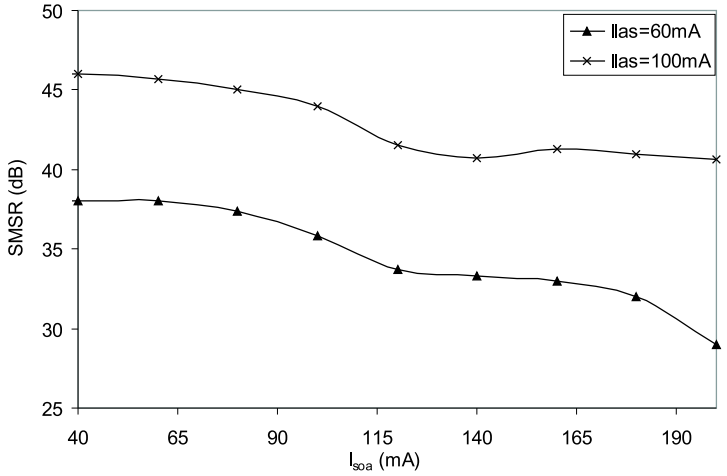

Figure 6.22: Calculated SMSR versus amplifier current for a DFB laser integrated with an optical amplifier with a non-perfect AR-coating. The laser bias current was 60 mA and 100 mA respectively.

amplifier. The expressions have been derived from previously derived alternative and more generally valid rate equations and are therefore valid under very general conditions.

From the theoretical derivation as well as from the numerical and experimental results, it follows that both the RIN and the linewidth can increase significantly due to the amplified spontaneous emission from the amplifier that is injected into the laser diode. This is especially the case for large amplification factors. The increase of RIN and phase noise is found both for low and high frequencies. The detrimental influence of the amplifier noise can only be suppressed by inserting an attenuating or isolating element between laser and amplifier. The large influence of the ASE-noise from the amplifier on the RIN of the laser diode only exists at low to moderate power levels. At high power levels, the laser RIN is completely dominated by the shot noise in the carrier density. The entire contribution given by (6.18) decreases with the third power of the output power and can be neglected at high output powers.

For the SMSR we have also shown theoretically, numerically and experimentally that an SOA integrated with a laser diode degrades the SMSR of that laser diode significantly. This is due to an increase of the amplified spontaneous emission coupled in the side mode and not

due to any change in the mode discrimination. As a result the increased side mode power will not result in a deterioration of the dynamic single mode stability or to increased mode partition noise. It may however lead to increased crosstalk in WDM systems.

Chapter 7

Conclusions and outlook

7.1 Conclusions

In this work we have thoroughly investigated some of the dynamical aspects related to multi-section (widely) tunable semiconductor lasers. These lasers are very promising components for application as transmitters in current and future optical communication networks based on (D)WDM technology. However, in order to be used in a network environment with stringent requirements, some issues still need to be investigated and/or resolved.

A first one concerns the wavelength switching behaviour of these components. In chapter 2 it was shown that the wavelength of semiconductor tunable laser can be changed within a few nanoseconds by changing the tuning currents of the device. Unfortunately, one encounters problems on a larger time scale (in the order of microseconds or even milliseconds) due to the thermally induced wavelength drift. This drift is due to the temperature change caused by the heating associated with the switching of the tuning currents. The wavelength switching behaviour was investigated using a theoretical model based on optical, electrical and thermal rate equations and also through simulations and experimental characterization. It was shown that the thermally induced wavelength drift was determined by three time constants (corresponding to the heat transfer from waveguide–to–chip, chip–to–subcarrier and subcarrier–to–heat sink respectively). Two methods were proposed to counteract the thermal drift. The first one is pre-compensation of the tuning currents. This is a very simple technique, but it was shown that it is difficult to optimize for all possible switching combinations. Therefore, a novel method based on optical feedback from a periodic

reference filter was developed. This method can be used to suppress the thermally induced wavelength drift independent from which channel the wavelength is being switched to and also independent from the switching history. It was also shown that, in order to avoid instabilities caused by the optical feedback, the feedback level must be sufficiently high and that the external cavity length must be short enough. To obtain this, a novel filter had to be developed.

The design and fabrication of the novel filter was described in chapter 3. The filter is based on the interference of multiple beams (like a classical Fabry Perot etalon). Particular to our filter is that it has a comb–like response, both in reflection and transmission, while a Fabry Perot etalon only has a comb–like response in transmission. The resulting filter design was a novel prism-based implementation of a Fox-Smith resonator and consisted of two right-angled prisms, cemented together with UV–curable index–matching paste. Theoretical expressions for the reflection and transmission responses were derived and the influence of the reflectivity of the different facets was investigated. The processing of the filter was described and a prototype was manufactured in our own clean–room facilities. Experimentally determined reflection and transmission responses where shown, proving that the novel filter concept indeed works. The filter can thus be used as a reference filter with which the wavelength of a semiconductor (tunable) laser can be stabilized through optical feedback.

In chapter 4 the influence of optical feedback from a periodic reference filter (in a short external cavity) on the tuning and switching characteristics of a tunable three-section DBR laser was investigated. It was shown, both numerically and experimentally, that the tuning characteristics were simplified and that the wavelength switching behaviour was considerably improved. Simulation results showed that drifts up to 15 GHz could be suppressed through the optical feedback. Experimental results also showed that the wavelength switching was considerably improved: the maximal deviation was reduced by more than 50 % (from 6 GHz to less than 3 GHz) and the steady-state value was reached much faster (after 0.1 ms instead of 2 ms). This can be further improved by better adapting the FSR of the filter, the external cavity length (and thus the cavity mode spacing) and the width of the Bragg peak of the laser to each other. The use of the filter will furthermore facilitate the generation of tuning tables and will reduce the influence of component aging and tuning table inaccuracies.

The issues and problems associated with aging, monitoring and updating of tunable laser sources were discussed in chapter 5. The different aging mechanisms that occur in tunable lasers were briefly explained and some techniques that can be used to monitor the output power, emission wavelength and SMSR of tunable lasers were described. The most important result of this chapter was however that a procedure was developed to update the complete tuning table of a tunable laser that has suffered from aging. This procedure only uses the value of the aging–induced shift in tuning current(s) corresponding to the operating channel of the laser to update the complete tuning table.

Finally, in chapter 6 the influence of an (integrated) optical amplifier on important laser characteristics such as the relative intensity noise (RIN), the linewidth and the side mode suppression (SMSR) ratio was investigated. It was shown theoretically, numerically and experimentally that these characteristics can be seriously degraded in the presence of an optical amplifier. The degradation is due to the amplified spontaneous emission from the amplifier that is injected into the laser diode and becomes worse when the amplifier gain increases. The RIN and linewidth can easily increase by 3 to 15 dB, while the SMSR can easily decrease by the same amount. The detrimental influence of the amplifier noise can be suppressed by inserting an attenuating or isolating element between laser and amplifier, provided this is possible. The degradation of the laser characteristics is important to take into account when the laser is to be used as a transmitter in a telecommunication network, where RIN and linewidth are preferably as low as possible and SMSR as high as possible.

7.2 Outlook

The introduction of (widely) tunable lasers into optical telecommunication networks has been considerably delayed by the downturn in the telecommunications industry at the beginning of the 21th century. Nevertheless, since (monolithic) tunable lasers can be manufactured with the same specifications as fixed–frequency DFB lasers (which currently form the majority of the optical telecommunication transmitters) over their whole tuning range, it seems inevitable that tunable lasers will become the preferred choice for transmitters in future optical networks. Already today they offer the significant advantage of inventory reduction (read: price reduction), both in the manufacturing and operation of WDM systems [14]. Their greatest potential however, lies is the intro-

duction of novel, more efficient, flexible network technologies based on wavelength routing and optical packet/burst switching. These novel optical network technologies will have an increased capacity, functionality, scalability and flexibility and will be transparent to modulation and coding formats.

Telecom transmitters are (nearly) always supplied on a line card and this will be no different for transmitters based on tunable lasers. On the card, the tunable laser will be surrounded by a complete electronic control system and the tuning table of the laser will have been constructed in the factory before it was shipped to the customer. This allows the user to select a certain wavelength channel by a simple channel–setting command, without having to worry about the exact values of the tuning currents etc. The control electronics will ensure that the output power, the laser wavelength and the SMSR of the laser are kept at their required values. It will monitor laser performance and if necessary the tuning table can automatically be updated, and the user will not have to worry about a thing (at least what the tunable transmitter is concerned).

List of figures

List of tables

Bibliography

[1] "Report: Internet traffic boom redux, http://www.lightreading.com/."

[2] P. S. Henry, "Lightwave primer," *IEEE J. Quant. Electron.*, vol. 21, pp. 1862–1879, December 1985.

[3] C. A. Brackett, "Dense wavelength division multiplexing networks: principles and applications," *IEEE J. Sel. Areas in Communications*, vol. 6, pp. 948–964, August 1990.

[4] A. E. Willner, "Mining the optical bandwidth for a terabit per second," *IEEE Spectrum*, pp. 32–41, April 1997.

[5] H. Yoshimura, K. Sato, and N. Takachio, "Future photonic transport networks based on wdm technologies," *IEEE Communications Magazine*, vol. 37, pp. 74–81, February 1999.

[6] K. Sato and S. Okamoto, "Photonic transport technologies to create robust backbone networks," *IEEE Communications Magazine*, vol. 37, pp. 78–87, August 1999.

[7] A. Manzalini, "Milestones for the evolution towards an integrated optical transport network," *Optical Networks Magazine*, vol. 1, pp. 29–34, January 2000.

[8] P. Green, "Progress in optical networking," *IEEE Communications Magazine*, vol. 39, pp. 54–61, January 2001.

[9] T. Hausken, "WDM spells robust market for telecommunications lasers," *Compound Semiconductor*, vol. 5, July/August 1999.

[10] W. Sitter and M. Sauter, "Transparent networks: operators see the light," *FibreSystems Europe*, pp. 31–34, August 2002.

[11] K. Sato, "Key enabling technologies for future neworks," *Optics & Photonics News - OSA*, pp. 34–39, May 2004.

[12] F. Delorme, "Widely tunable 1.55-μm lasers for wavelength-divison-multiplexed optical fiber communications," *IEEE J. Quant. Electron.*, vol. 34, pp. 1706–1716, September 1998.

[13] L. Coldren, "Monolithic tunable diode lasers," *IEEE J. Sel. Top. Quant. Electron*, vol. 6, pp. 988–999, November/December 2000.

[14] L. A. Coldren, G. Fish, Y. Akulova, J. S. Barton, L. Johansson, and C. Coldren, "Tunable semiconductor lasers: a tutorial," *IEEE J. Lightw. Technol.*, vol. 39, pp. 193–202, January 2004.

[15] A. Lindstrom, "Tunable lasers strive to meet industry's demands," *FibreSystems Europe*, pp. 34–37, December 2001.

[16] M. Telford, "Widely tunable lasers power up for narrow–spaced DWDM," *Lightwave Europe*, pp. 24–25, May 2002.

[17] G. P. Agrawal and N. K. Dutta, *Long-wavelength semiconductor lasers*. New York: Van Nostrand Reinhold, 1986.

[18] K. Petermann, *Laser Diode Modulation and Noise*. Dordrecht: Kluwer Academic Publishers, 1988.

[19] G. Morthier and P. Vankwikelberge, *Handbook of distributed feedback laser diodes*. Artech House, Norwood, MA, 1997.

[20] M. C. Amann and J. Buus, *Tunable Laser Diodes*, vol. ISBN 3-540-10193-4. Artech House optoelectronics library, 1998.

[21] G. Sarlet, *Tunable Laser Diodes for WDM communication - Methods for Control and Characterisation*. Ghent University, Phd. thesis, 2000.

[22] B. Glance, U. Koren, R. W. Wilson, D. Chen, and A. Jourdan, "Fast optical packet switching based on WDM," *IEEE Photon. Technol. Lett.*, vol. 4, pp. 1186–1188, October 1992.

[23] F. Delorme, P. Gambini, M. Puleo, and S. Slempkes, "Fast tunable 1.5 μm distributed Bragg reflector laser for optical switching applications," *Electron. Lett.*, vol. 29, pp. 41–43, January 1993.

[24] Y. Tada, O. Ishida, N. Shibata, and K. Nosu, "Design consideration on a DBR-laser transmitter for fast frequency-switching in an optical FDM cross-connect system," *IEEE J. Lightw. Technol.*, vol. 11, pp. 813–818, May/June 1993.

[25] F. Kano, H. Ishii, Y. Tohmori, M. Yamamoto, and Y. Yoshikuni, "Broad range wavelength switching in superstructure grating distributed Bragg reflector lasers," *Electron. Lett.*, vol. 29, pp. 1091–1092, June 1993.

[26] L. Zhang and J. C. Cartledge, "Influence on the mode competition on the fast wavelength switching of three-section DBR lasers," *IEEE Photon. Technol. Lett.*, vol. 5, pp. 1143–1145, October 1993.

[27] P. Ottolenghi, S. Benedetto, and I. Montrosset, "Switching and optical modulation of three-section DBR lasers," *IEEE J. Quant. Electron.*, vol. 30, pp. 1381–1388, June 1994.

[28] L. Zhang and J. C. Cartledge, "Fast wavelength switching of three-section DBR lasers," *IEEE J. Quant. Electron.*, vol. 31, pp. 75–81, January 1995.

[29] F. Delorme, J. Hourany, H. Nakajima, N. Kalonji, J. Semo, M. Bollard, and R. Lefevre, "12 wavelength channel fast switching operation of compact DBR laser modules including IC-drivers," *Electron. Lett.*, vol. 32, pp. 1670–1671, August 1996.

[30] R. O'Dowd, S. O'Duill, G. Mulvihill, N. O'Gorman, and Y. Yu, "Frequency plan and wavelength switching limits for widely tunable semiconductor transmitters," *IEEE J. Sel. Top. Quant. Electron*, vol. 7, pp. 259–269, March/April 2001.

[31] O. A. Lavrova, L. Rau, and D. J. Blumenthal, "10-Gb/s agile wavelength conversion with nanosecond tuning times using a multisection widely tunable laser," *IEEE J. Lightw. Technol.*, vol. 20, pp. 712–717, April 2002.

[32] E. Buimovich and D. Sadot, "Physical limitation of tuning time and system considerations in implementing fast tuning of GCSR lasers," *IEEE J. Lightw. Technol.*, vol. 22, pp. 582–588, February 2004.

[33] Y. Su, J. E. Simsarian, and L. Zhang, "Improving the switching performance of a wavelength-tunable laser transmitter using a

simple and effective driver circuit," *IEEE Photon. Technol. Lett.*, vol. 16, pp. 2132–2134, September 2004.

[34] M. Teshima, "Dynamic wavelength tuning characteristics of the 1.5 μm three-section DBR lasers: Analysis and experiment," *IEEE J. Quant. Electron.*, vol. 31, pp. 1389–1400, August 1995.

[35] H. Kobrinski, M. P. Vecchi, M. S. Goodman, E. L. Goldstein, T. Chapuran, J. M. Cooper, M. Tur, C. E. Zah, and S. G. Menocal, "Fast wavelength-switching of laser transmitters and amplifiers," *IEEE J. Sel. Areas in Communications*, vol. 8, pp. 1190–1201, August 1990.

[36] H. Kobrinski, M. P. Vecchi, T. Chapuran, J. B. Georges, C. E. Zah, C. Caneau, S. G. Menocal, P. S. D. Lin, A. S. Gozdz, and F. J. Favire, "Simultaneous fast wavelength switching and intensity modulation using a tunable DBR laser," *IEEE Photon. Technol. Lett.*, vol. 2, pp. 139–142, February 1990.

[37] E. G. Vicente De Vera and B. Glance, "Switching-time limitations in tunable multisection lasers," *IEEE Photon. Technol. Lett.*, vol. 2, pp. 781–783, November 1990.

[38] C. Braagaard, B. Mikkelsen, T. Durhuus, and K. E. Stubkjaer, "Modelling the dynamics of wavelength tuning in DBR lasers," *IEEE Photon. Technol. Lett.*, vol. 6, pp. 694–696, June 1994.

[39] A. A. Saavedra, R. Passy, and J. P. von der Weid, "Thermal drift in wavelength-switching DFB and DBR lasers," *Electron. Lett.*, vol. 33, pp. 780–781, April 1997.

[40] E. Buimovich and D. Sadot, "Measurements of thermal frequency chirp in directly modulated DFB lasers and thermal transient induced frequency drift during fast tuning in GCSR lasers using frequency discrimination technique," in *Proc. IEEE-LEOS Annual Meeting 2003*, Paper TuD7, pp. 208–209, October 2003.

[41] G. Mulvihill, Y. Yonglin, S. O'Duill, and R. O'Dowd, "Thermal contribution to wavelength switching characteristics of widely tunable lasers," in *Proc. IEEE-LEOS Annual Meeting 2003*, Paper WT4, pp. 640–641, October 2003.

[42] J. Wittebolle, *Golflengteschakeldynamica van afstembare laserdiodes*. Ghent University, Graduate thesis, 2002.

[43] E. G. Vicente De Vera and B. Glance, "Suppression of laser frequency drifts caused by thermal transients in optical WDM packet switching systems," *Electron. Lett.*, vol. 8, pp. 1930–1932, November 1990.

[44] M. W. Fleming and A. Mooradian, "Spectral characteristics of external-cavity controlled semiconductor lasers," *IEEE J. Quant. Electron.*, vol. 17, pp. 44–59, January 1981.

[45] G. P. Agrawal, "Line narrowing in a single-mode injection laser due to external optical feedback," *IEEE J. Quant. Electron.*, vol. 20, pp. 468–471, May 1984.

[46] R. Lang and K. K., "External optical feedback effects on semiconductor injection laser properties," *IEEE J. Quant. Electron.*, vol. 16, pp. 347–355, March 1980.

[47] B. Tromborg, J. H. Osmundsen, and H. Olesen, "Stability analysis for a semiconductor laser in an external cavity," *IEEE J. Quant. Electron.*, vol. 20, pp. 1023–1032, September 1984.

[48] D. Lenstra, B. H. Verbeek, and A. J. den Boef, "Coherence collapse in single-mode semiconductor lasers due to optical feedback," *IEEE J. Quant. Electron.*, vol. 21, pp. 674–679, June 1985.

[49] C. H. Henry and R. F. Kazarinov, "Instability of semiconductor lasers due to optical feedback from distant reflectors," *IEEE J. Quant. Electron.*, vol. 22, pp. 294–301, February 1986.

[50] R. W. Tkach and A. R. Chraplyvy, "Regimes of feedback effects in 1.5 μm distributed feedback lasers," *IEEE J. Lightw. Technol.*, vol. 4, pp. 1655–1661, November 1986.

[51] N. Schunk and K. Petermann, "Numerical analysis of the feedback regimes for a single-mode semiconductor laser with external feedback," *IEEE J. Quant. Electron.*, vol. 24, pp. 1242–1247, July 1988.

[52] N. Schunk and K. Petermann, "Stability analysis for laser diodes with short external cavities," *IEEE Photon. Technol. Lett.*, vol. 1, pp. 49–51, March 1989.

[53] J. Mørk, B. Tromborg, and M. J., "Chaos in semiconductor lasers with optical feedback: theory and experiment," *IEEE J. Quant. Electron.*, vol. 28, pp. 93–108, January 1992.

[54] A. A. Tager and B. Elenkrig, "Stability regimes and high-frequency modulation of laser diodes with short external cavity," *IEEE J. Quant. Electron.*, vol. 29, pp. 2886–2889, December 1993.

[55] K. Petermann, "External optical feedback phenomena in semiconductor lasers," *IEEE J. Sel. Top. Quant. Electron*, vol. 1, pp. 480–489, June 1995.

[56] "Vpi (Virtual Photonics Inc.) componentmaker, http://www.virtualphotonics.com."

[57] M. Born and E. Wolf, *Principles of Optics*, pp. 323–367. Pergamon Press, Oxford, England, 6 ed., 1980.

[58] "Recommendation g.692: "optical interfaces for multichannel systems with optical amplifiers", series g: Transmission systems and media, digital systems and networks (transmission media characteristics - characteristics of optical components and subsystems)," tech. rep., International Telecommunication Union - Telecommunication Standardization Sector (ITU-T), 1998.

[59] B. Moeyersoon, G. Morthier, and R. Baets, "Novel optical feedback scheme for improvement of the wavelength switching behaviour of tunable lasers," in *2002 IEEE 18th International Semiconductor Laser Conference*, Paper TuP12, pp. 91–92, September 2002.

[60] P. W. Smith, "Stabilized, single-frequency output from a long laser cavity," *IEEE J. Quant. Electron.*, vol. 1, pp. 343–348, November 1965.

[61] S. L. Woodward, P. Parayanthal, and U. Koren, "The effects of aging on the Bragg section of a DBR laser," *IEEE Photon. Technol. Lett.*, vol. 5, pp. 750–752, July 1993.

[62] H. Mawatari, M. Fukuda, F. Kano, Y. Tohmori, Y. Yoshikuni, and H. Toba, "Lasing wavelength changes due to degradation in buried heterostructure distributed Bragg reflector lasers," *IEEE J. Lightw. Technol.*, vol. 17, pp. 918–923, May 1999.

[63] F. Delorme, G. Terol, H. de Bailliencourt, S. Grosmaire, and P. Devoldere, "Long-term wavelength stability of 1.55-μm tunable distributed Bragg reflector lasers," *IEEE J. Sel. Top. Quant. Electron*, vol. 17, pp. 480–486, May/June 1999.

[64] O. A. Lavrova and D. J. Blumenthal, "Accelerated aging studies of multi-section tunable GCSR lasers for dense WDM applications," *IEEE J. Lightw. Technol.*, vol. 18, pp. 2196–2199, December 2000.

[65] D. A. Ackerman, J. E. Johnson, S. N. G. Chu, L. Zhang, E. J. Dean, and L. J.-P. Ketelsen, "Assessment and modeling of aging in electro-absorption distributed Bragg reflector lasers," *IEEE J. Quant. Electron.*, vol. 37, pp. 1382–1387, November 2001.

[66] M. Fukuda and G. Iwane, "Degradation of active region in InGaAsP/InP buried heterostructure lasers," *J. Appl. Phys*, vol. 58, no. 8, pp. 2932–2936, 1985.

[67] M. Fukuda, *Reliability and Degradation of Semiconductor Lasers and LEDs*, vol. ISBN 0-89006-465-2. Artech House optoelectronics library, 1991.

[68] T. Kallstenius, J. Bäckström, U. Smith, and B. Stoltz, "On the degradation of InGaAsP/InP-based bulk lasers," *IEEE J. Lightw. Technol.*, vol. 17, pp. 2584–2594, December 1999.

[69] G. Sarlet, G. Morthier, and R. Baets, "Control of widely tunable SSG-DBR lasers for dense wavelength division multiplexing," *IEEE J. Lightw. Technol.*, vol. 18, pp. 1128–1138, August 2000.

[70] S. L. Woodward, V. Mizrahi, T. L. Koch, U. Koren, and P. J. Lemaire, "Wavelength stabilisation of a DBR laser using an in-fiber Bragg filter," *IEEE Photon. Technol. Lett.*, vol. 5, pp. 628–630, June 1993.

[71] H. Ishii, F. Kano, Y. Yoshikuni, and H. Yasaka, "Mode stabilisation method for superstructure-grating DBR lasers," *IEEE J. Lightw. Technol.*, vol. 13, pp. 433–442, March 1998.

[72] B. Villeneuve, M. Cyr, and H. B. Kim, "High-stability wavelength-controlled DFB laser sources for WDM applications," in *Proc. OFC '98*, Paper FB5, 1998.

[73] "Broadband (Fabry Perot) wavelength locker, JDS Uniphase, http://www.jdsu.com."

[74] B. Mason, S. P. DenBaars, and L. Coldren, "Tunable sampled-grating DBR lasers with integrated wavelength monitors," *IEEE Photon. Technol. Lett.*, vol. 10, pp. 1085–1087, August 1998.

[75] J. Gripp, P. Bernasconi, C. Chan, K. L. Sherman, and M. Zirngibl, "Demonstration of a 1 Tb/s optical packet switch fabric (80*12.5 Gb/s), scalable to 128 Tb/s (6400*20 Gb/s)," in *Proc. of ECOC'2000*, Paper PD2.7, 2000.

[76] B. Mason, J. Barton, G. A. Fish, L. A. Coldren, and S. P. Denbaars, "Design of sampled grating DBR lasers with integrated semiconductor optical amplifiers," *IEEE Photon. Technol. Lett.*, vol. 12, pp. 762–764, July 2000.

[77] M. Uemukai, T. Suhara, K. Yutani, N. Shimada, Y. Fukumoto, H. Nishihara, and A. Larsson, "Tunable external–cavity semiconductor laser using monolithically integrated tapered amplifier and grating coupler for collimation," *IEEE Photon. Technol. Lett.*, vol. 12, pp. 1607–1609, December 2000.

[78] C. R. Doerr, L. W. Stulz, R. Pafchek, K. Dryer, and L. Zhang, "Potentially low-cost widely tunable laser consisting of a semiconductor optical amplifier connected directly to a silica waveguide grating router," *IEEE Photon. Technol. Lett.*, vol. 15, pp. 1446–1448, October 2003.

[79] D. J. Robbins, G. Busico, L. Ponnampalam, J. P. Duck, P. J. Williams, R. A. Griffin, A. J. Ward, D. C. Reid, N. D. Whitbread, E. Barton, B. Reid, and K. Kasunic, "A high power, broadband tunable laser module based on a DS-DBR laser with integrated soa," in *Proc. OFC 2004*, Paper TuE3, 2004.

[80] S. H. Oh, J. Lee, K. S. Kim, H. Ko, C. Lee, S. Park, and M. Park, "Fabrication of tunable sampled grating DBR-LD using integrated optical semiconductor amplifier with a lateral tapered waveguide," in *Proc. IPRM 2004*, Paper TP31, 2004.

[81] K. Kundo, Yashiki, T. Sasaki, Y. Yokoyama, K. Hamamoto, T. Morimoto, and M. Yamaguchi, "1.55-μm wavelength-selectable microarray DFB-LD's with monolithically integrated MMI combiner, SOA and EA-modulator," *IEEE Photon. Technol. Lett.*, vol. 12, pp. 242–244, March 2000.

[82] T. Kurobe, T. Kimoto, T. Mukaihara, and A. Kasukawa, "High-efficiency heater-loaded wavelength selectable laser," in *Proc. IPRM 2004*, Paper WA2-1, 2004.

[83] L. H. Spiekman, J. M. Wiesenfeld, U. Koren, B. I. Miller, and M. D. Chien, "All-optical mach-zehnder wavelength converter with monolithically integrated preamplifiers," *IEEE Photon. Technol. Lett.*, vol. 10, pp. 1115–1117, August 1998.

[84] G. Morthier, "An accurate rate-equation description fo DFB lasers and some interesting solutions," *IEEE J. Quant. Electron.*, vol. 33, pp. 231–237, February 1997.

[85] P. Lagasse, P. Demeester, A. Ackaert, V. Parys, B. Van Caenegem, M. O'Mahony, K. Stubkjaer, J. Benoit, A. Houghton, K. Fitchew, A. Rawlings, and C. Descamps, "Photonic technologies in europe," *ACTS*, 1999.

[86] V. Jayaraman, Z. M. Chuang, and L. A. Coldren, "Theory, design, and performance of extended tuning range semiconductor-lasers with sampled gratings," *IEEE J. Quant. Electron.*, vol. 29, pp. 1824–1834, June 1993.

[87] Y. Tohmori, Y. Yoshikuni, T. Tamamura, H. Ishii, Y. Kondo, and M. Yamamoto, "Broad-range wavelength tuning in DBR lasers with super structure grating (SSG)," *IEEE Photon. Technol. Lett.*, vol. 5, pp. 126–129, February 1993.

[88] Z. M. Chuang and L. A. Coldren, "Design of widely tunable semiconductor-lasers using grating-assisted codirectional-coupler filters," *IEEE J. Quant. Electron.*, vol. 29, pp. 1071–1080, April 1993.

[89] J.-O. Wesström, G. Sarlet, S. Hammerfeldt, L. Lundqvist, P. Szabo, and P.-J. Rigole, "State–of–the–art performance of widely tunable modulated grating y–branch lasers," in *Proc. OFC 2004*, Paper TuE2, 2004.

[90] Sulur, T. Koonen, I. T. Monroy, H. de Waardt, and J. Jennen, "IP over DWDM networks supported by GMPLS-based LOBS deploying combined modulation format," in *Opticomm, Denver Colorado*, 2001.

[91] B. Tromborg and J. Mørk, "Nonlinear injection locking dynamics and the onset of coherence collapse in external cavity lasers," *IEEE J. Quant. Electron.*, vol. 26, pp. 642–654, April 1990.

[92] M. Osiński and J. Buus, "Linewidth broadening factor in semiconductor lasers - an overview," *IEEE J. Quant. Electron.*, vol. 23, pp. 9–24, January 1987.

[93] J. Mørk, M. Semkow, and B. Tromborg, "Measurement and theory of mode hopping in external cavity lasers," *Electron. Lett.*, vol. 26, pp. 642–654, February 1990.

[94] P. R., M. Meliga, G. Rossi, M. Scofet, and L. Tallone, "15-ghz modulation bandwidth, ultralow-chirp 1.55-mu m directly modulated hybrid distributed bragg reflector (HDBR) laser source," *IEEE Photon. Technol. Lett.*, vol. 10, pp. 1691–1693, December 1998.

[95] N. Chan, C. Shu, and K. Lee, "Performance improvements in high-frequency modulation of a laser diode under enhanced optical feedback," *IEEE Photon. Technol. Lett.*, vol. 14, pp. 2584–2594, December 2002.

[96] "Acreo fibre gratings, http://www.acreo.se/."

[97] M. Born and E. Wolf, *Principles of Optics*. Pergamon Press, Oxford, England, 6 ed., 1980.

[98] K. De Mesel, *Spot-size converters for photonic integrated circuits*. Ghent University, Phd. thesis, 2002.

[99] N. A. Olsson, "Lightwave systems with optical amplifiers," *IEEE J. Lightw. Technol.*, vol. 7, pp. 1071–1082, July 1989.

[100] G. Morthier and B. Moeyersoon, "Intesity noise and linewidth of laser diodes with integrated semiconductor optical amplifier," *IEEE Photon. Technol. Lett.*, vol. 14, pp. 1644–1646, December 2002.

[101] A. Champagne, J. Camel, R. Maciejko, K. J. Kasunic, D. Adams, and B. Tromborg, "Linewidth broadening in a distributed feedback laser integrated with a semiconductor optical amplifier," *IEEE J. Quant. Electron.*, vol. 38, pp. 1493–1502, November 2002.

[102] B. Moeyersoon, M. Zhao, and G. Morthier, "Degradation of the mode suppression in single-mode laser diodes due to integrated optical amplifiers," in *Proc. of Optical Amplifiers and their Applications*, pp. 97–99, 2003.

[103] B. Moeyersoon and G. Morthier, "Degradation of the mode suppression in single-mode laser diodes due to integrated semiconductor optical amplifiers," *IEEE J. Quant. Electron.*, vol. 40, pp. 241–244, March 2004.

[104] A. Champagne, M. Lestrade, J. Camel, R. Maciejko, and B. Tromborg, "Degradation of side-mode suppression ratio in a DFB laser integrated with a semiconductor optical amplifier," *IEEE J. Quant. Electron.*, vol. 40, pp. 1493–1502, July 2004.